COMPLEX THREE-DIMENSIONAL TURBULENT FLOW PHENOMENA OF HIGH-ALPHA PROJECTILE AERODYNAMICS

By

GUANG-WU CHEN

A DISSERTATION PRESENTED TO THE GRADUATE SCHOOL
OF THE UNIVERSITY OF FLORIDA IN PARTIAL FULFILLMENT
OF THE REQUIREMENTS FOR THE DEGREE OF
DOCTOR OF PHILOSOPHY

UNIVERSITY OF FLORIDA

1995

ACKNOWLEDGEMENTS

I wish to express my sincere appreciation to Dr. Chen-Chi Hsu for his guidance and encouragements throughout my research and in working on the dissertation manuscript. I would also like to extend my thanks to other supervisory committee members, Dr. W. Shyy, Dr. D. M. Mikolaitis, Dr. U. H. Kurzweg and Dr. J. Klausner, for their interest and suggestions in this research.

Special thanks are extended to Dr. Shu-Cheng Yang, Dr. Chau-Lin Lee, Dr. Shin-Jye Liang, Dr. Edwin Blosch and Mr. Guobao Guo for their kind assistance since I first joined the CFD family here in the department. I would also like to express my gratitude to my family for their love and support over the years. Last but not least are the people who have helped me many times and made things possible.

This study was partially supported by Florida State University and by Pittsburgh Supercomputing Center through the allocation of supercomputer resources.

TABLE OF CONTENTS

Page

ACKNOWLEDGEMENTS ii

ABSTRACT vi

CHAPTERS

I INTRODUCTION 1

High-α Aerodynamics 3
Role of CFD 6
High-α Projectile Aerodynamics 7
  Crossflow Separation 7
  Three-Dimensional Flow Separation 8
  Topology of Three-Dimensional Flow Separation 9
  High-α Flow Regimes 11
Literature Survey 11
Research Objectives 19

II GOVERNING EQUATIONS 21

Navier-Stokes Equations and Equations of State 21
  Continuity Equation 22
  Momentum Equations 22
  Energy Equation 23
  Governing Equations in Vector Form 24
  Equations of State 25
Non-dimensional Navier-Stokes Equations 26
Transformed Navier-Stokes Equations 28
Thin-Layer Navier-Stokes Equations 35
Turbulence Model 36
Modified Baldwin-Lomax Turbulence Model 41

III FLOW PROBLEM 44

Flow Conditions and Geometrical Model 44
Domain Discretization 45
    Planar Grid Generation 46
    Three-Dimensional Grid Generation 46
Boundary Conditions 47
    Solid Surface Boundary Condition 47
    Outer Domain Boundary Condition 49
    Circumferential Boundary Condition 49
    Singular Plane J=1 49
    Downstream Boundary Condition 50
    Slow Start 51

IV THIN-LAYER NAVIER-STOKES COMPUTATION 55

Thin-Layer Navier-Stokes TVD Code 56
Solution Method and Application 59
    Algorithm and Flow Chart 60
    Residual 62
    Pressure and Shear Stress Coefficients 62
    Aerodynamic Force 66
    Mach Number 67
    Vorticity 68
    Streamtraces and Skin-Friction Lines 68
    Evaluation of the Jacobian J 70
    Integration Time Step $\Delta\tau$ 70

V EFFECTS OF TURBULENCE MODELS 73

Impacts of Excessive Eddy Viscosity 74
    On the Crossflow Plane J=54 74
    On the Surface Flow Properties 78
    On the Development of Crossflow Separation 83
Implication of the Cut-off Constant 87

VI TURBULENT VORTICAL FLOW PHENOMENA 114

Onset of Cross-sectional Vortical Flow Structure 115
Onset and Development of Surface Flow Patterns 118
Three-Dimensional Streamtraces 122
Vortex Shedding Phenomena 123

VII SUMMARY AND CONCLUDING REMARKS 163

APPENDIX: JACOBIAN MATRICES 168

REFERENCES 170

BIOGRAPHICAL SKETCH 175

Abstract of Dissertation Presented to the Graduate School
of the University of Florida in Partial Fulfillment of the
Requirements for the Degree of Doctor of Philosophy

COMPLEX THREE-DIMENSIONAL TURBULENT FLOW PHENOMENA OF HIGH-ALPHA PROJECTILE AERODYNAMICS

By

Guang-Wu Chen

August 1995

Chairperson: Dr. Chen-Chi Hsu
Major Department: Aerospace Engineering, Mechanics and Engineering Science

An impulsively started turbulent flow of Mach 0.96 past a Secant-Ogive-Cylinder-Boattail projectile model with sting at 60-degree angle of attack is considered for investigating the complex three-dimensional vortical flow physics and phenomena. The governing equations used for the vortical flow simulation are the Reynolds-averaged thin-layer Navier-Stokes equations implemented with a modified Baldwin-Lomax algebraic eddy viscosity model for ideal gases. The turbulence model has been shown to provide an acceptably accurate surface pressure distribution in the crossflow separation region by Degani and Schiff. The implication of the turbulence model for a proper description of flow solutions away from the boundary-layer region has been intensively investigated in this study. The comparison of the simulated flow characteristics against those obtained from employing the original Baldwin-Lomax model clearly shows that the modified turbulence model employed in this study can give at least qualitatively correct vortical flow physics and phenomena.

In this study the numerical simulation has revealed a number of interesting and important fundamental characteristics of complex vortical flow. The onset times for primary and secondary crossflow separations are found to be linearly dependent on the diameter of the cross-section. The evolution of the crossflow vortex patterns on the cylinder, boattail and sting sections of the projectile shows a transition from a stable node to an unstable spiral through the appearance of a stable limiting cycle. The unstable spiral vortex on the ogive; however, is formed through an entirely different mechanism, consisting of a two-saddle-point flow structure. It is also shown that the development of primary vortices has induced a high speed axial jet stream in the leeward side of the ogive and cylinder sections. Moreover, the alternating vortex shedding is simulated on the projectile sting and the shedding frequency in terms of the Strouhal number ranges from 0.179 to 0.191 on different cross-sections.

CHAPTER I
INTRODUCTION

In the past few decades, aircraft designers have been continuously creating flight vehicles of improved performance, and with broader flight envelope. Modern jet fighters of the 1990s can fly much faster and higher than their counterparts in World War II. The advancement of avionics and weapon systems allows them to carry out diverse missions. Stealth technology can even make planes invisible to enemy radar. No matter how far and how high a modern jet fighter can go, the most vital part comes back to a simple matter: the traditional "dog fight" (close-in combat) in the range of Mach number 0.8 to 1.2. The modern fighter must be highly maneuverable to counteract its foe in the sky.

In 1989 a Russian demonstrator Su-27 performed a famous "Cobra Maneuver" in an air show and stunned the observers [1]. The airplane's nose pitched up beyond the vertical plane but the airplane was able to maintain a level path and recover its normal flight. The airspeed dropped almost 200 knots ($\approx$230 mph) within a few seconds. Such strong agility can give the plane a great advantage in a dog fight, thanks to its excellent high-angle-of-attack performance. How the Su-27 can maintain control at such an extremely high angle of attack has created much interest for western designers in recent years.

All aerodynamic engineers are familiar with one simple rule: for a given flight condition, the airfoil lift increases when the angle of attack α goes up. But there exists a critical α where the lift reaches its maximum. Above that critical α, the flow on top of the airfoil separates and causes a pressure back up. With the absence of a low pressure suction on the upper airfoil, the lift drops suddenly and leads to a stall. For an airplane the lift can also be contributed from other components such as the nose and fuselage. When α is large, the incoming flow separates from both sides of the slender nose/fuselage configuration and forms a pair of highly counter-rotating vortices on the leeward side. The low pressure region developed by the vortical flow can provide additional lift which improves the airplane's maneuverability and agility. Vortical flow does have some adverse effects on the flight vehicle, such as lateral instability due to the asymmetric vortex pattern. A fundamental knowledge of the vortex dynamics is therefore desirable to fully take advantage of the vortical flow, while in the meantime, minimizing the possible adverse effects. In current study, the general high-α vortical flow phenomena are investigated through a numerical simulation, in particular, a transonic turbulent flow past a projectile configuration. In the following, some general aspects of the high-α vortical flow problem toward an airplane are first addressed. A detailed background of high-α projectile aerodynamics, including three-dimensional flow separation, flow topology, and a literature survey is presented, which is followed by the goal of this study.

High-α Aerodynamics

Aircraft lateral (or directional) stability and control characteristics at high angle of attack can be significantly altered by the presence of vortices developed from the aircraft nose and forward fuselage. Because forebody vortices at high α's are often asymmetric relative to the angle-of-attack plane, their action on body, wing, and tail surfaces can result in large yawing and rolling moments. Such effects may cause conventional stability and control surfaces (rudders, ailerons etc.) to be less effective at high angle of attack. Another example is the tail buffet phenomenon resulting from the tail's interaction with the shedded forebody vortices, exciting the natural frequencies of the fin(s) structure. The interactions between asymmetric forebody vortices with other airplane surfaces at sideslip conditions can also lead to the wing rock phenomenon--a sustained periodic oscillation in pitch and roll. These oscillations may reduce the structural service life, even causing a sudden structural failure during flight. The vortical flow structure can also breakdown such that the lift force generated by the vortices is suddenly lost, causing a possible aircraft stall.

Control of forebody vortex asymmetry is therefore of interest to minimize the adverse effects and to use the associated yawing and rolling moments to enhance actively the aircraft's high-angle-of-attack performance. Nose strakes, chines, or leading-edge-extension (LEX) are found on several aircrafts. These devices provide additional lift due to the vortical flow they develop at moderate-to-high angles of attack. These are useful for minimizing forebody vortex asymmetry; however, the prediction and control of the vortical flow and mutual interactions of the vortices are not well known. Asymmetric nose strakes and asymmetric air jet injection can induce a particular orientation and degree of forebody vortex asymmetry, but such behavior and the resultant effects on the complete aircraft again are not yet understood completely. The combined effect of the LEX or wing-body strake vortices, as well as the forebody vortices on the vehicle aerodynamics, must be considered to avoid the flight stability control and other problems such as tail buffet or wing rock. The appearance of shock waves in the high speed range results in some phenomena associated with shock/boundary-layer, shock/vortex interactions that can also complicate the flowfield.

Recently, there has been growing interest from government agencies and industry to tackle those issues. At NASA Ames Research Center, extensive experimental and computational investigations have been conducted on the High Alpha Research Vehicle (HARV) to determine the effects of three-dimensional separated vortical flow on the aircraft and means of utilizing these effects to the best possible advantages [2]. The F/A-18 was selected as the HARV base configuration because of its exceptional high-angle-of-attack capability. The combination of its complex geometry and the flow physics associated with the vortical flow at high α makes both the experimental and computational processes a great challenge to the engineering society. Significant results have been obtained and reported in several conference papers, for example, Refs. 3-5.

In addition to the F-18 HARV at NASA, the forward-swept-wing X-29 experimental aircraft is also currently under consideration for flight testing of high α forebody vortex control concepts at Dryden Flight Research Center [6,7]. This technology demonstrator was designed to be maneuverable at an angle of attack up to

70°. The issues of the study include (1) the ability to predict asymmetric vortical forebody flow, (2) the use of asymmetric forebody jets to induce formation of asymmetric vortices, and (3) the use of asymmetric forebody jets to reduce vortex asymmetry. The X-31 Enhanced Fighter Maneuverability (EFM) demonstrator is another successful example of high-α aerodynamics [8]. To maintain effective control during a post-stall flight at extremely high angles of attack, the "thrust vector vanes" encircling the engine exhaust nozzle and a pair of "floating" canards were used on a delta-wing fighter configuration. Together with a sophisticated digital flight control system, the X-31 was found to be able to sustain a controlled flight at $\alpha=70°$ for 53 seconds (September 18, 1992). Later it achieved the first "Herbst" maneuver--a 180° reversal of the flight path carried out in a deep stall condition at the speed of 90 knots ($\approx$104 mph) and a minimum 50° angle of attack, after deceleration from a high-speed entry, with subsequent high speed exit in the opposite direction (April 29, 1993). Such super-agility can surely give a fighter aircraft great advantages in close air combat.

Erickson [9] discussed both civil and military airplane high-α aerodynamics with a large variety of configurations. In a much broader sense he defined the high-α as any situation where an airplane or any of its components encounters an off-design, high-lift flight, including attached flows, uncontrolled separated flows, and organized flow separation in the form of vortices, shock waves, or combinations of these flow conditions. For example, the high-α flow phenomena can be seen in the propeller tip vortex system on a light general aviation airplane, blade tip vortex system on a rotorcraft, and wing-mounted engine nacelle and pylon assembly of a transport airplane.

A number of flow control concepts such as airframe shaping or actively controlled mechanical/pneumatic devices which effectively improve the quality of high-α aerodynamics were reviewed.

Role of CFD

For decades, wind-tunnel or flight tests have been major sources of engineering-level data to aircraft designers. The types of data available from wind-tunnel tests are usually limited by the cost and instrumentation restrictions. The measured data often lack resolution and might be affected by the existence of the measuring devices sitting in the flowfield. The flight test costs too much and gives even less data because of larger instrumentation restrictions. For some most interesting cases such as the high-α maneuver, it is simply too dangerous to fly. In addition to the field or flight test, computational fluid dynamics (CFD) is another approach which can provide valuable information in the design process. A qualitative description to capture the dominant flow phenomena is often more important than an absolutely accurate prediction in the preliminary stage. Once we are on a correct track, the code can be improved through the numerical validation which requires comparison with carefully conducted experiments [10]. The validation of a CFD code with experiments can lead to a general confidence in a given methodology to capture the flow phenomena of interest. On the other hand, the more detailed information obtained by a flow simulation can help to interpret and clarify some experimental results. With the advent of supercomputers and the advancement of numerical techniques for nonlinear problems, CFD now can provide more comprehensive flow physics and phenomena than the conventional experiment does if the mathematical model solved is a suitable one for the complex flow problem.

> The creative use of CFD methods can address the flow physics of design problems and configuration concepts for which no design experiences, data base, or test techniques exist. This approach can both yield critical design information and identify areas of high potential for future methodology development and applications programs.[6, pp. 818]

High-α Projectile Aerodynamics

The study of a viscous flow past a projectile geometry (a slender body of revolution) at high angles of attack is essential to the understanding of the high-α aircraft aerodynamics. The complex vortical flow phenomena, such as the three-dimensional flow separation and the development of the symmetric/asymmetric vortical flow in the wake region which arise on a highly maneuverable, geometrically complicated flight vehicle at high α, can also be observed regardless the simplicity of the projectile shape. Besides, it is much easier to apply CFD techniques such as grid generation and graphical representation to a simple geometry like this. The general characteristics of a vortical flow behind an inclined projectile body are described as follows.

Crossflow Separation

A schematic vortical flow structure above a projectile body is shown in Figure 1.1 for a crossflow plane. The outer flow approaching the windward plane of symmetry turns and flows outward along the body from the windward side to the leeward side. A well-attached boundary layer is developed until it separates from the body at a primary separation point S_1; accordingly, a pair of counter-rotating primary vortices on the leeward side of the body is formed. The primary vortices induce a flow downward to the body surface which attaches onto the leeward plane of symmetry at A_1. The induced downflow turns outward along the body surface from the leeward attachment point to the primary separation S_1. The adverse circumferential pressure gradient under the primary vortices, if strong enough, can cause the induced flow to separate at a secondary separation point S_2. The local fluid rolls up behind the body to form the secondary vortex structure. Another point of attachment A_2 is located on the body surface between the primary and secondary separation points. Figure 1.1 shows that the separating flow forms an unstable vortex structure, i.e., the fluid goes away from the vortex center. It is mentioned, however, that the leeward side crossflow structure can consist of either stable/unstable vortices or limiting cycles depending on the various three-dimensional flow development [11].

Three-Dimensional Flow Separation

In the two-dimensional flow case, for example the flow past a cylinder, there exists only one shear stress component along the circumferential direction. The separation or reattachment then can be easily located as the surface points at which the shear stress becomes zero. For three-dimensional flow, in addition to the crossflow shear stress component, an axial component can carry the flow downstream to form a line of separation which is an asymptotic convergence of adjacent surface skin-friction lines. The combined action of the circumferential and axial components on the body surface may be seen in Figure 1.2, which shows the simulated surface skin-friction lines on part of an unwrapped projectile body. The axial component in this graph is to the right hand side. The convergence of surface skin-friction lines toward the primary and secondary separation lines, S_1 and S_2, and the circumferential divergence of the skin-friction lines from the attachment lines, A_1 and A_2, are clearly visible. It should be clarified that the flow does not have to "leave" the surface into the wake region on the separation lines with the circumferential shear stress component zero. In two-dimensional flow the change sign of shear stress simply means the fluid must be elevated and form a recirculation bubble above the surface. In the three-dimensional flow case, the fluid is allowed to escape in the downstream direction to form the skin-friction convergence lines as shown here. This makes the study of the surface flow topology important in viewing and understanding a three-dimensional flow separation.

Topology of Three-Dimensional Flow Separation

One of the approaches to study three-dimensional flow separation is to make use of the topology with the aid of critical-point theory [12]. Also known as the "phase-plane" theory, the critical-point theory was first used in solving autonomous ordinary differential equations. The detailed classifications of various types of separated flow, nomenclature, and topological terminology were described in a review paper by Chapman and Yates [13]. In the following, only materials directly related to the current vortical flow problem are presented.

Mathematically critical points are often referred to as singular points. A singular point in a velocity field implies that the magnitude of the velocity vector at the point is zero, i.e., the slope of particle trajectories is indeterminate. For a viscous flow on the solid surface where the velocity vanishes due to no-slip, the two-component shear stress vector is used instead of a 3-D velocity vector. According to their behavior, critical points are known as either nodal points or saddle points. A nodal point is characterized by an infinite number of trajectories entering (stable node) or leaving (unstable node) the point. It can be further classified as either a regular node or a spiral node. A saddle point has only two lines called separatrixes intersect at the point, one is going toward the point, and the other one away from it. There are rules that can be followed on 3-D body surface or crossflow planes regarding the number of critical points [14]. On the surface of a closed 3-D body, the summation rule states that

$$\sum N - \sum S = 2 \tag{1.1}$$

where N denotes the isolated node and S the saddle point. On a crossflow plane, the summation rule becomes

$$\sum N + \frac{1}{2}\sum N' - \sum S - \frac{1}{2}\sum S' = -1 \tag{1.2}$$

where N' and S' denote half-node and half-saddle that occur on a boundary. There is also a local summation rule for part of surface skin-friction line portrait which can be isolated and enclosed within a smooth curve. This rule says that, within the isolated region, a saddle point must be added or deleted when each node is added or deleted.

The interpretation of surface flow topology can be applied to the 3-D flowfield. For an unstable node on the solid surface, the trajectories are all pointing away from the node which suggests the existence of a source of fluid flow on the wall. This implies that the flow attaches to the node and spreads out along the surface. Such a node is called a node of attachment N_A. A node of separation N_S, therefore, accounts for a stable node which is a sink-like point on the wall. Similarly the saddle of separation S_S and saddle of attachment S_A are defined as detailed in Ref. 13.

High-α Flow Regimes

The leeward side flow pattern on an inclined ogive-cylinder projectile can be usually categorized into three regimes. For α is small, say less than 30°, a symmetric vortical flow pattern is observed with the crossflow topology being similar to Figure 1.1. In general the vortex size grows with the longitudinal distance from the nose. For α is $30° \sim 60°$, the steady asymmetric vortex pattern is observed. For α is 60° and above, vortex shedding becomes essential, with an oblique shedding near the nose and parallel shedding far downstream. With α approaching 90°, the parallel shedding turns out to be dominant over the oblique shedding except very close to the nose tip.

Literature Survey

Over the past decade there were many research efforts into high-α projectile aerodynamics. These works included experimental or computational approaches on laminar or turbulent flows ranging from subsonic to supersonic regime. A number of selected works are discussed in the following.

In 1986, Degani and Schiff [15] used a thin-layer parabolic Navier-Stokes method to compute turbulent supersonic flows around various pointed bodies at large incidence up to 22.75°. Due to the significant crossflow separation, they first tested whether neglecting the circumferential viscous terms in the thin-layer approximation could degrade the solution accuracy. Adding back those terms caused an 11% increase in CPU time, but produced less than 0.5% change in the computed solution. Practically, the circumferential grid resolutions are not sufficient to resolve the circumferential viscous terms. Secondly they proposed a modification of the well-known Baldwin-Lomax turbulence model [16] due to the large crossflow separation, which effectively reduced the over-predicted eddy viscosity. The computed surface pressure distribution matched experimental data much better than the one predicted by the original model. Also in some computed cases, the secondary/tertiary vortices were clearly visible which were absent from the original model computation. They also performed the computation by different circumferential discretization of 5° and 2.5°, respectively. The results showed that a grid size of 2.5° is required to resolve the small-scale secondary vortex structure. The details of the Baldwin-Lomax model and modification are to be discussed in the next chapter.

A further investigation on the effect of the modified Baldwin-Lomax turbulence model and circumferential grid resolution to the vortical flow simulation was conducted by Schiff, Degani and Cummings [17]. In the study they utilized a time-marching thin-layer Navier-Stokes code to compute Mach number 0.2 flow past a projectile with 3.5*D* tangent-ogive forebody and 7.0*D* cylindrical afterbody at $\alpha=20°$, 25° and 30°. The flow was assumed to be symmetric and only half of the domain was solved with the circumferential discretizations of $\Delta\theta=3°$ and 1.5°. The computed surface flow patterns showed the primary crossflow separation line predicted with the modified model was located more upstream than the one predicted by the original model. Furthermore, the modified model computation showed the development of a tertiary separation line near the rear body. On observing the crossflow vortical flow pattern, the modified model computation showed a larger, more complex structure. By using a grid resolution of $\Delta\theta=3°$ at $\alpha=20°$, it was found that the code had trouble in differentiating between the primary and secondary separation lines on the ogive part. Reducing the grid spacing by half cured the problem. However, the requirement of increasing circumferential grid resolution was significantly reduced as the flow physics were altered at larger angles of attack. At $\alpha=25°$ and 30°, the predicted primary and secondary separation lines were further apart due to a stronger circumferential adverse pressure gradient. Therefore a grid spacing of $\Delta\theta=3°$ was sufficient to resolve the crossflow structure. Their experience suggested that at least 4 or 5 circumferential points are needed between primary and secondary separation lines in order to realistically model the flowfield.

As has been mentioned previously, the leeward side flow becomes very unstable at large angles of attack. Degani and Zilliac [18] performed the surface pressure and wake velocity measurements in a low-turbulence wind tunnel past an ogive-cylinder body. The flow was laminar, with a Reynolds number of 26,000. The flow was found to be stable with α less than 15° to 20°. The flowfield at $\alpha=30°$ was found to be highly unsteady by observing some high frequency signals (5000~6000 Hz) with low amplitude, which was associated with the small-scale, three-dimensional vortices in the shear layer. As α increased from 30° to 60°, a low frequency component ($\approx$200 Hz) started to develop and became identifiable at $\alpha=60° \sim 85°$ near the rear of the cylindrical afterbody. The measured frequency was 130~176 Hz which was found to be related to the von Karman vortex shedding. The non-dimensional frequency or Strouhal number was found to be $0.21\sin(\alpha)$ where 0.21 is the classical Strouhal number of the von Karman shedding measured on a two-dimensional cylinder [19].

At a moderate to high α before the vortex-shedding exists, the small unsteadiness is able to trigger the asymmetry and maintains a "steady" asymmetric vortex pattern. How a symmetric body can produce a non-symmetric flow pattern has caused great interest. Degani and Schiff [19] performed a thin-layer Navier-Stokes laminar vortical flow simulation of Mach 0.2 flow past an ogive-cylinder body at 40° angle of attack. The circumferential discretization had $\Delta\theta=3°$ for the whole domain. The computed flow remained symmetric, until a symmetry-breaking perturbation was applied near the nose to induce the asymmetric pattern. When the perturbation was removed, the asymmetric solution returned to symmetric. A space-fixed, time-invariant perturbation was needed to reach and maintain an asymmetric flow pattern. A stronger perturbation was found to result in a greater asymmetry, and so does a perturbation inserted at an upstream location closer to the nose tip. Two pairs of vortices were found which were consistent with what experimentally had been observed [21].

Degani [22] continued the computation for $\alpha=60°$ and $80°$ by inserting a small transient perturbation near the tip. Unlike the $\alpha=40°$ case, the triggered asymmetric flow pattern did not return to symmetry when the perturbation was removed. The flow remained highly asymmetric instantaneously with the computed side force history showing oscillations around a symmetric mean. Once the perturbation stayed, the fluctuating flow resulted in an asymmetric mean side force. The vortices were shed out like von Karman vortex street. He concluded that two kinds of instability can exist in the computation. For 2-D cylinder flow or 3-D finite-length body at very large α (e.g., 80°), the developing of von Karman vortex shedding is a result of absolute instability. A short-time symmetry-breaking perturbation is required to trigger the unsteady vortex shedding phenomenon. For the moderate to high α regime ($\alpha=40°$ and 60°), on the other hand, a permanent disturbance is needed in order to reach a steady, asymmetric vortical flow pattern as has been observed in flow visualization. This is called a convective instability of the symmetric flow. These two instabilities may coexist in a certain range of α, say 60° to 80°.

In fact geometrical perturbation does exist in the experimental model. The imperfection due to the surface roughness simply cannot be completely eliminated. Zilliac, Degani and Tobak [23] conducted a series of experiments of an ogive-cylinder projectile to investigate the sensitivity of the leeward side flow structure to geometrical alteration. The ogive tip was made rotatable by a microstepping motor and the side forces were recorded at different rotating angles $0° \sim 360°$, at various angles of attack. The results showed that the variation of side force with roll angle of the nose was first found when $\alpha \geq 30°$. When α increased, the magnitude of side force variation with roll angle grew from a continuous distribution to one gradually approaching a square-wave distribution. A nearly pure bistable condition was found at $\alpha=53°$, in which the leeside flow structure had only two orientations. At $\alpha=65°$ or larger, a periodic vortex shedding was first found, and the side force variation with the roll angle was becoming virtually zero like in the low-angles-of-attack case. The study showed that the microasymmetry near the nose acts as a permanent geometrical perturbation to trigger the instability at intermediate angles of attack. On studying the surface flow pattern, Degani, Tobak and Zilliac [24] suggested that the bistable nature observed between $\alpha=50°$ and 65° is related to the foci appearing near the ogive-cylinder juncture. In the experiment, oil was attracted to the foci and created thick bubbles only when α was up to 50°. As α further increased, the foci moved forward to the tip and disappeared as α approached 70°. This phenomenon was observed over the testing Reynolds number of 17,000~35,000 in a laminar flow regime.

The computational investigations mentioned above all assert that a symmetry-breaking perturbation must be introduced in order to achieve an asymmetric solution as had been observed in experiments at moderate angles of attack. Siclari and Marconi [25] performed the laminar Navier-Stokes simulation over a 5° circular cone ($\phi=5°$) with the assumption of conical flow solution. The testing case was Mach number 1.8 and Reynolds number 10^5. The grid used had a circumferential discretization of $\Delta\theta=2.25°$. They argued that the assumption of the conical flow will not affect the essential features of the asymmetric vortex flow. For $\alpha/\phi=2$, the solution was able to converge to a symmetric flowfield with the residual dropping to machine zero and staying at that level. For $\alpha/\phi=3$ and up, the residual dropped almost 10 orders with a symmetric solution, then bounced back to its original level and then declined again. Finally the residual reached machine zero and stayed, with the solution being highly asymmetric. When they started the computation with a slightly asymmetric initial condition (a 2° sideslip), it converged monotonically to machine zero, with the identical asymmetric solution obtained from the symmetric initial condition. They also computed the resulting side force and found excellent agreement with the experimental data. The computed flow returned to symmetry when $\alpha/\phi \geq 5$.

Siclari [26] further investigated this problem with various cone angles, Mach numbers and cross-sectional shapes. He found that the existence of the asymmetric solutions was affected by both Mach number and cone angle. When the cone angle increases, the asymmetry declines very rapidly. When Mach number increases, the solution also has a tendency to be symmetric. He concluded that the appearance of the supersonic crossflow region with the increasing free stream Mach number can diminish the communication between the opposing primary vortical flow structures; therefore, the flowfield returns to symmetry. Regarding the effect of the cross-sectional shape, a flatter one (larger aspect ratio) was found to cause less asymmetric behavior. The addition of small strakes also eliminates the asymmetry quite effectively.

The yawing moment generated from the asymmetric vortical flow pattern was usually large enough that the deflected vertical tail/rudder could not produce an effective moment to compensate. A number of forebody vortex control techniques have been reported to eliminate the lateral instability at moderate to high angles of attack. Malcolm [27] reviewed several experimental efforts which include movable strakes, blowing surface jets, blowing and suction through surface slots, suction through surface holes and miniatured rotatable tip strakes. The idea is to control the existing forebody vortex so that the generated yawing moment can be used to enhance the aircraft maneuverability instead of degrading it. Gee, Rizk and Schiff [28] numerically investigated the effect of forebody tangential slot blowing about a F/A-18 aircraft by solving the thin-layer Navier-Stokes equation. The solutions were obtained at $M_\infty=0.243$, $\alpha=30.3°$, and $Re_c=11.0\times10^6$. The original Baldwin-Lomax turbulence model was used through the flowfield except the forebody region, the boundary-layer diverter, and the regions between wing flaps and fuselage. In the forebody region, the modified Baldwin-Lomax model by Degani and Schiff [15] was used. In the boundary-layer diverter and flap-fuselage regions, only the inner eddy viscosity formulation from Baldwin-Lomax model was used. The predicted vortex breakdown and the separation lines were found to be located consistently with the flow visualizations obtained in the wind-tunnel tests. The averaged aircraft yawing moment agreed well with experimental measurements.

Research Objectives

The ultimate goal of this study is to investigate the complex transonic vortical flow dynamics through a time-accurate thin-layer Navier-Stokes computation. The specific flow problem considered is a Mach number 0.96 turbulent flow past a Secant-Ogive-Cylinder BoatTail (SOCBT) projectile at 60° angle of attack. Due to the lack of experimental measurements on the geometrical model and flow conditions, emphasis is placed on the fundamental fluid physics rather than the engineering-level application, i.e., a qualitatively rather than quantitatively accurate solution is sufficient. It is well known that the Reynolds-averaged thin-layer Navier-Stokes equations implemented with the Baldwin-Lomax turbulence model for ideal gases can be accurately simulated in many high speed turbulent flow problems as long as the flow separation is not strong. However, in a flow with large crossflow separation, the predicted eddy viscosity magnitude had been found to be too high to induce the secondary vortical flow phenomena. In order to assure that the mathematical model used in this computation is good enough to represent the physics of the vortical flow, the numerical simulation with both the original Baldwin-Lomax turbulence model [16] and the modified version suggested by Degani and Schiff [15] is conducted. The impact of the strong diffusion predicted by the original model is first investigated. Upon obtaining proper justification to the simulated solution with the modified Baldwin-Lomax turbulence model, a detailed description of the formation and development of the vortical flow is addressed, including a possible onset of asymmetrical vortex shedding.

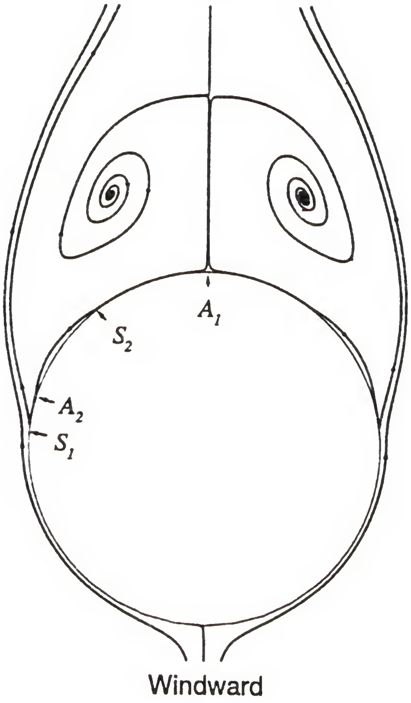

Figure 1.1 A schematic vortical flow structure in a crossflow plane.

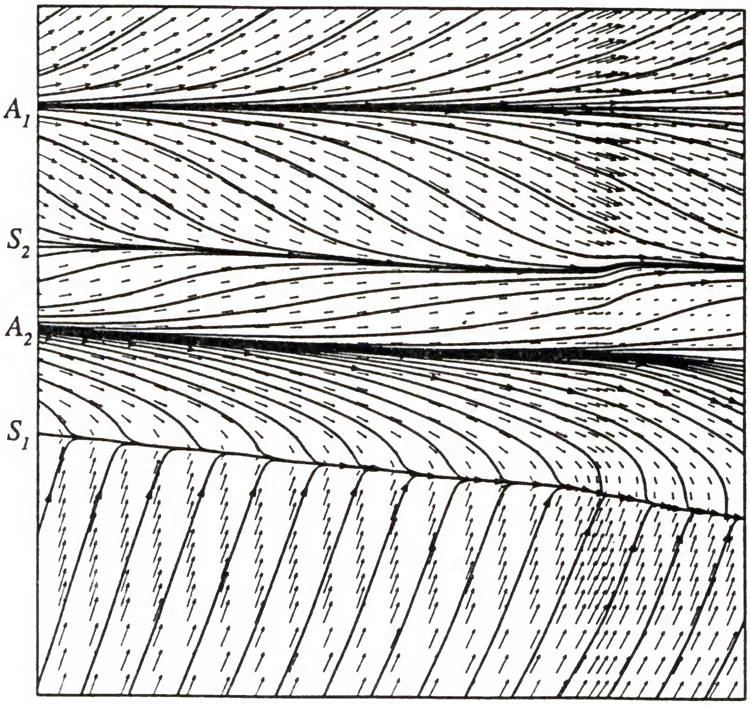

Figure 1.2 Simulated surface skin-friction lines on an unwrapped projectile surface.

CHAPTER II
GOVERNING EQUATIONS

The fundamental equations of fluid dynamics are based on the universal laws of conservation of mass, momentum and energy [29]. Conservation of mass results in an equation called the continuity equation. Conservation of momentum is equivalent to Newton's Second Law which yields a vector equation known as the momentum equation. Conservation of energy is identical to the First Law of Thermodynamics giving a fluid dynamics equation called the energy equation. In addition to the equations developed from these universal laws, it is necessary to establish additional relationships between fluid properties in order to "close" the system of equations. For example, the equation of state relates the thermodynamic variables pressure (p), density (ρ) and temperature (T). For a turbulent flow computation based on the Reynolds-averaged equations, a turbulence model is needed to relate the turbulent flow quantities to the field variables.

Navier-Stokes Equations and Equations of State

Governing equations of unsteady compressible fluid dynamics based on the laws of conservation, or the Navier-Stokes equations, are described in terms of the Cartesian coordinates as follows. All body forces and external heat addition are neglected.

Continuity Equation: Conservation of mass results in

$$\frac{\partial \rho}{\partial t} + \frac{\partial(\rho u)}{\partial x} + \frac{\partial(\rho v)}{\partial y} + \frac{\partial(\rho w)}{\partial z} = 0 \tag{2.1}$$

where ρ is the fluid density and u, v, w are the velocity components in the Cartesian coordinate of the x, y, z directions, respectively.

Momentum Equations: Conservation of momentum in the x, y and z directions can be written as

$$\frac{\partial(\rho u)}{\partial t} + \frac{\partial(\rho u^2 + p)}{\partial x} + \frac{\partial(\rho uv)}{\partial y} + \frac{\partial(\rho uw)}{\partial z} = \frac{\partial \tau_{xx}}{\partial x} + \frac{\partial \tau_{yx}}{\partial y} + \frac{\partial \tau_{zx}}{\partial z} \tag{2.2a}$$

$$\frac{\partial(\rho v)}{\partial t} + \frac{\partial(\rho vu)}{\partial x} + \frac{\partial(\rho v^2 + p)}{\partial y} + \frac{\partial(\rho vw)}{\partial z} = \frac{\partial \tau_{xy}}{\partial x} + \frac{\partial \tau_{yy}}{\partial y} + \frac{\partial \tau_{zy}}{\partial z} \tag{2.2b}$$

$$\frac{\partial(\rho w)}{\partial t} + \frac{\partial(\rho wu)}{\partial x} + \frac{\partial(\rho wv)}{\partial y} + \frac{\partial(\rho w^2 + p)}{\partial z} = \frac{\partial \tau_{xz}}{\partial x} + \frac{\partial \tau_{yz}}{\partial y} + \frac{\partial \tau_{zz}}{\partial z} \tag{2.2c}$$

where p is the thermodynamic pressure. τ_{ij} are the viscous stress tensor components. For a Newtonian fluid they have the form

$$\tau_{xx} = \lambda\left(\frac{\partial u}{\partial x} + \frac{\partial v}{\partial y} + \frac{\partial w}{\partial z}\right) + 2\mu\frac{\partial u}{\partial x} = \frac{2}{3}\mu\left(2\frac{\partial u}{\partial x} - \frac{\partial v}{\partial y} - \frac{\partial w}{\partial z}\right)$$

$$\tau_{yy} = \lambda\left(\frac{\partial u}{\partial x} + \frac{\partial v}{\partial y} + \frac{\partial w}{\partial z}\right) + 2\mu\frac{\partial v}{\partial y} = \frac{2}{3}\mu\left(2\frac{\partial v}{\partial y} - \frac{\partial w}{\partial z} - \frac{\partial u}{\partial x}\right)$$

$$\tau_{zz} = \lambda\left(\frac{\partial u}{\partial x} + \frac{\partial v}{\partial y} + \frac{\partial w}{\partial z}\right) + 2\mu\frac{\partial w}{\partial z} = \frac{2}{3}\mu\left(2\frac{\partial w}{\partial z} - \frac{\partial u}{\partial x} - \frac{\partial v}{\partial y}\right)$$

$$\tau_{xy} = \mu(\frac{\partial u}{\partial y} + \frac{\partial v}{\partial x}) = \tau_{yx}$$

$$\tau_{yz} = \mu(\frac{\partial v}{\partial z} + \frac{\partial w}{\partial y}) = \tau_{zy}$$

$$\tau_{zx} = \mu(\frac{\partial w}{\partial x} + \frac{\partial u}{\partial z}) = \tau_{xz}$$

in which Stokes condition [30] that $\lambda+2/3\mu=0$ has been assumed. Here μ is the coefficient of viscosity (dynamic viscosity) and λ is the second coefficient of viscosity. The coefficient μ is a function of temperature. For air it can be represented accurately by an empirical interpolation formula based on Sutherland theory of viscosity [31]

$$\mu = \mu_\infty(\frac{T}{T_\infty})^{1.5}\frac{T_\infty + S}{T + S} \tag{2.3}$$

where the subscript ∞ denotes the fluid reference state and the constant $S=198.6°R$.

Energy Equation: The conservation of energy yields the energy equation

$$\frac{\partial E}{\partial t} + \frac{\partial[(E+p)u]}{\partial x} + \frac{\partial[(E+p)v]}{\partial y} + \frac{\partial[(E+p)w]}{\partial z} = \frac{\partial \beta_x}{\partial x} + \frac{\partial \beta_y}{\partial y} + \frac{\partial \beta_z}{\partial z} \tag{2.4}$$

with

$$\beta_x = u\tau_{xx} + v\tau_{xy} + w\tau_{xz} + \kappa\frac{\partial T}{\partial x}$$

$$\beta_y = u\tau_{yx} + v\tau_{yy} + w\tau_{yz} + \kappa\frac{\partial T}{\partial y}$$

$$\beta_z = u\tau_{zx} + v\tau_{zy} + w\tau_{zz} + \kappa\frac{\partial T}{\partial z}$$

Here, E, T and κ represent the total energy per unit volume, temperature, and thermal conductivity respectively. The heat transfer by conduction is related to the temperature gradient through the Fourier law as

$$\boldsymbol{q} = -\kappa \nabla T$$

The thermal conductivity κ can be related to the viscosity coefficient μ by the Prandtl number

$$Pr = \frac{\mu}{\kappa}Cp$$

where Cp is the constant pressure specific heat.

Governing Equations in Vector Form

The governing equations for a compressible fluid flow in Cartesian coordinates, Eq.(2.1), (2.2) and (2.4), can be written in the vector form as

$$\frac{\partial \boldsymbol{q}}{\partial t} + \frac{\partial \boldsymbol{E}}{\partial x} + \frac{\partial \boldsymbol{F}}{\partial y} + \frac{\partial \boldsymbol{G}}{\partial z} = \frac{\partial \boldsymbol{E}_v}{\partial x} + \frac{\partial \boldsymbol{F}_v}{\partial y} + \frac{\partial \boldsymbol{G}_v}{\partial z} \tag{2.5}$$

in which $\boldsymbol{q}$ is the unknown vector, $\boldsymbol{E}$, $\boldsymbol{F}$, $\boldsymbol{G}$ are the flux vectors and $\boldsymbol{E}_v$, $\boldsymbol{F}_v$ and $\boldsymbol{G}_v$ are the viscous flux vectors

$$\boldsymbol{q} = \begin{Bmatrix} \rho \\ \rho u \\ \rho v \\ \rho w \\ E \end{Bmatrix}, \quad \boldsymbol{E} = \begin{Bmatrix} \rho u \\ \rho uu + p \\ \rho uv \\ \rho uw \\ (E+p)u \end{Bmatrix}, \quad \boldsymbol{F} = \begin{Bmatrix} \rho v \\ \rho vu \\ \rho vv + p \\ \rho vw \\ (E+p)v \end{Bmatrix}, \quad \boldsymbol{G} = \begin{Bmatrix} \rho w \\ \rho wu \\ \rho wv \\ \rho ww + p \\ (E+p)w \end{Bmatrix},$$

$$\boldsymbol{E}_v = \begin{Bmatrix} 0 \\ \tau_{xx} \\ \tau_{xy} \\ \tau_{xz} \\ \beta_x \end{Bmatrix}, \quad \boldsymbol{F}_v = \begin{Bmatrix} 0 \\ \tau_{yx} \\ \tau_{yy} \\ \tau_{yz} \\ \beta_y \end{Bmatrix}, \quad \boldsymbol{G}_v = \begin{Bmatrix} 0 \\ \tau_{zx} \\ \tau_{zy} \\ \tau_{zz} \\ \beta_z \end{Bmatrix} \tag{2.5a}$$

Equations of State

The time-dependent Navier-Stokes equation Eq.(2.5) consists of a set of five equations with seven unknowns ρ, u, v, w, p, E, and T. Two more equations which relate p, ρ, T and E can be obtained from the equations of state of the fluid. For perfect gas, they are

$$p = \rho R T, \qquad e = C_v T \tag{2.6a}$$

where R is the universal gas constant, e is the internal energy per unit mass and C_v is the constant volume specific heat. Assuming that only internal energy and kinetic energy are important, the total energy E can be written as

$$E = \rho[e + \frac{1}{2}(u^2 + v^2 + w^2)]$$

By applying the following relations,

$$\frac{C_p}{C_v} = \gamma, \qquad C_p - C_v = R \tag{2.6b}$$

we may further develop the two equations of state (Eq. (2.6a)) into the following forms

$$p = (\gamma - 1)[E - \frac{1}{2}\rho(u^2 + v^2 + w^2)] \tag{2.7a}$$

$$T = \frac{\gamma - 1}{R}[\frac{E}{\rho} - \frac{1}{2}(u^2 + v^2 + w^2)] \tag{2.7b}$$

Now the variables p and T are related to the dependent variables ρ, u, v, w, E and therefore the Navier-Stokes equation can be solved for the five unknowns.

Non-dimensional Navier-Stokes Equations

The governing equations are put into non-dimensional form. The advantage of non-dimensionalization is to reduce the number of parameters. By choosing the proper reference quantities, the non-dimensional variables can be defined with an asterisk as

$$x^* = \frac{x}{L}, \quad y^* = \frac{y}{L}, \quad z^* = \frac{z}{L}, \quad t^* = \frac{t}{L/a_\infty}$$

$$u^* = \frac{u}{a_\infty}, \quad v^* = \frac{v}{a_\infty}, \quad w^* = \frac{w}{a_\infty}, \quad \rho^* = \frac{\rho}{\rho_\infty}, \quad \mu^* = \frac{\mu}{\mu_\infty}$$

$$\kappa^* = \frac{\kappa}{\kappa_\infty}, \quad T^* = \frac{T}{T_\infty}, \quad E^* = \frac{E}{\rho_\infty a_\infty^2}, \quad p^* = \frac{p}{\rho_\infty a_\infty^2}, \quad \tau_{ij}^* = \frac{\tau_{ij}}{\rho_\infty a_\infty^2}$$

Here, we denote the free stream condition by the subscript ∞. L is the characteristic length scale and a_∞ is the free stream speed of sound. By using a_∞ as the reference velocity, the Mach number does not appear in the governing equation, thus reducing the number of characteristic parameters. The reference temperature is taken as the free stream temperature T_∞ which can be obtained by the relation $a_\infty^2 = \gamma R T_\infty$, i.e., $T_\infty = a_\infty^2/\gamma R$.

By substituting the non-dimensional variables into Eq.(2.5), we have the non-dimensional Navier-Stokes equations in the vector form as

$$\frac{\partial \boldsymbol{q}^*}{\partial t^*} + \frac{\partial \boldsymbol{E}^*}{\partial x^*} + \frac{\partial \boldsymbol{F}^*}{\partial y^*} + \frac{\partial \boldsymbol{G}^*}{\partial z^*} = \frac{1}{Re}\left(\frac{\partial \boldsymbol{E}_v^*}{\partial x^*} + \frac{\partial \boldsymbol{F}_v^*}{\partial y^*} + \frac{\partial \boldsymbol{G}_v^*}{\partial z^*}\right) \tag{2.8}$$

with the Reynolds number defined as

$$Re = \frac{\rho_\infty a_\infty L}{\mu_\infty}$$

The vectors $\boldsymbol{q}^*$, $\boldsymbol{E}^*$, $\boldsymbol{F}^*$, $\boldsymbol{G}^*$, $\boldsymbol{E}_v^*$, $\boldsymbol{F}_v^*$ and $\boldsymbol{G}_v^*$ now have forms identical to those dimensional vectors in Eq.(2.5a) except that the variables here are non-dimensional (with an asterisk *). However, the explicit expressions for the non-dimensional β are, for example,

$$\beta^*_x = u^*\tau^*_{xx} + v^*\tau^*_{xy} + w^*\tau^*_{xz} + \frac{\kappa^*}{(\gamma-1)Pr}\frac{\partial T^*}{\partial x^*}$$

The equations of state, Eq. (2.7a) and (2.7b), are also given in the non-dimensional forms

$$p^* = (\gamma-1)[E^* - \frac{1}{2}\rho^*(u^{*2} + v^{*2} + w^{*2})] \tag{2.9}$$

$$T^* = \gamma(\gamma-1)[\frac{E^*}{\rho^*} - \frac{1}{2}(u^{*2} + v^{*2} + w^{*2})] \tag{2.10}$$

In subsequent sections the asterisk * is left out from the non-dimensional governing equations for convenience unless otherwise noted.

Transformed Navier-Stokes Equations

In computational fluid dynamics the governing equations are often approximated by a finite-difference method. Previously we have expressed the governing equations in terms of a Cartesian coordinate system. However for many flow problems with complex geometries it is more effective to use a boundary-fitted curvilinear coordinate system. By a proper coordinate transformation, the boundary surfaces in the physical plane can be mapped onto rectangular surfaces in the transformed domain. Moreover, the physical grid points can be clustered in the region with high gradients, yet still can result in a rectangular, uniformly spaced computational domain. This is especially advantageous in simplifying the finite-difference equations, although a set of somewhat more complicated, transformed Navier-Stokes equations is obtained.

Let us denote (x,y,z,t) as the physical domain and introduce a generalized curvilinear coordinate (ξ,η,ζ,τ) as the computational domain such that

$$\xi = \xi(x,y,z,t), \qquad \eta = \eta(x,y,z,t), \qquad \zeta = \zeta(x,y,z,t), \qquad \tau = t$$

where t and τ represent the times which remain unchanged during coordinates transformation. By the chain-rule

$$\frac{\partial}{\partial t} = \frac{\partial}{\partial \tau} + \frac{\partial}{\partial \xi}\xi_t + \frac{\partial}{\partial \eta}\eta_t + \frac{\partial}{\partial \zeta}\zeta_t$$

$$\frac{\partial}{\partial x} = \frac{\partial}{\partial \xi}\xi_x + \frac{\partial}{\partial \eta}\eta_x + \frac{\partial}{\partial \zeta}\zeta_x$$

$$\frac{\partial}{\partial y} = \frac{\partial}{\partial \xi}\xi_y + \frac{\partial}{\partial \eta}\eta_y + \frac{\partial}{\partial \zeta}\zeta_y$$

$$\frac{\partial}{\partial z} = \frac{\partial}{\partial \xi}\xi_z + \frac{\partial}{\partial \eta}\eta_z + \frac{\partial}{\partial \zeta}\zeta_z$$

we can rewrite the non-dimensional Navier-Stokes equation Eq.(2.8) as

$$
\begin{aligned}
&\frac{\partial \boldsymbol{q}}{\partial \tau} + [\xi_t \frac{\partial \boldsymbol{q}}{\partial \xi} + \xi_x \frac{\partial \boldsymbol{E}}{\partial \xi} + \xi_y \frac{\partial \boldsymbol{F}}{\partial \xi} + \xi_z \frac{\partial \boldsymbol{G}}{\partial \xi}] \\
&+ [\eta_t \frac{\partial \boldsymbol{q}}{\partial \eta} + \eta_x \frac{\partial \boldsymbol{E}}{\partial \eta} + \eta_y \frac{\partial \boldsymbol{F}}{\partial \eta} + \eta_z \frac{\partial \boldsymbol{G}}{\partial \eta}] \\
&+ [\zeta_t \frac{\partial \boldsymbol{q}}{\partial \zeta} + \zeta_x \frac{\partial \boldsymbol{E}}{\partial \zeta} + \zeta_y \frac{\partial \boldsymbol{F}}{\partial \zeta} + \zeta_z \frac{\partial \boldsymbol{G}}{\partial \zeta}] \\
&= \frac{1}{Re} \{ [\xi_x \frac{\partial \boldsymbol{E}_v}{\partial \xi} + \xi_y \frac{\partial \boldsymbol{F}_v}{\partial \xi} + \xi_z \frac{\partial \boldsymbol{G}_v}{\partial \xi}] \\
&+ [\eta_x \frac{\partial \boldsymbol{E}_v}{\partial \eta} + \eta_y \frac{\partial \boldsymbol{F}_v}{\partial \eta} + \eta_z \frac{\partial \boldsymbol{G}_v}{\partial \eta}] \\
&+ [\zeta_x \frac{\partial \boldsymbol{E}_v}{\partial \zeta} + \zeta_y \frac{\partial \boldsymbol{F}_v}{\partial \zeta} + \zeta_z \frac{\partial \boldsymbol{G}_v}{\partial \zeta}] \} \qquad (2.11)
\end{aligned}
$$

The metric coefficients ξ_x, ξ_y, etc. appearing in the transformed governing equations (2.11) can be obtained by writing

$$
\begin{Bmatrix} d\tau \\ d\xi \\ d\eta \\ d\zeta \end{Bmatrix} = \begin{bmatrix} 1 & 0 & 0 & 0 \\ \xi_t & \xi_x & \xi_y & \xi_x \\ \eta_t & \eta_x & \eta_y & \eta_z \\ \zeta_t & \zeta_x & \zeta_y & \zeta_z \end{bmatrix} \begin{Bmatrix} dt \\ dx \\ dy \\ dz \end{Bmatrix} \qquad (2.12a)
$$

Or, in the other way,

$$\begin{Bmatrix} dt \\ dx \\ dy \\ dz \end{Bmatrix} = \begin{bmatrix} 1 & 0 & 0 & 0 \\ x_\tau & x_\xi & x_\eta & x_\zeta \\ y_\tau & y_\xi & y_\eta & y_\zeta \\ z_\tau & z_\xi & z_\eta & z_\zeta \end{bmatrix} \begin{Bmatrix} d\tau \\ d\xi \\ d\eta \\ d\zeta \end{Bmatrix} \tag{2.12b}$$

Substituting Eq.(2.12a) into Eq.(2.12b) and rearranging, we have

$$\begin{bmatrix} 1 & 0 & 0 & 0 \\ \xi_t & \xi_x & \xi_y & \xi_x \\ \eta_t & \eta_x & \eta_y & \eta_z \\ \zeta_t & \zeta_x & \zeta_y & \zeta_z \end{bmatrix} = \begin{bmatrix} 1 & 0 & 0 & 0 \\ x_\tau & x_\xi & x_\eta & x_\zeta \\ y_\tau & y_\xi & y_\eta & y_\zeta \\ z_\tau & z_\xi & z_\eta & z_\zeta \end{bmatrix}^{-1} = [\boldsymbol{A}]^{-1} \tag{2.13}$$

Defining the Jacobian of the transformation

$$J \equiv \left| \frac{\partial(\tau,\xi,\eta,\zeta)}{\partial(t,x,y,z)} \right| \equiv \det \begin{bmatrix} 1 & 0 & 0 & 0 \\ \xi_t & \xi_x & \xi_y & \xi_z \\ \eta_t & \eta_x & \eta_y & \eta_z \\ \zeta_t & \zeta_x & \zeta_y & \zeta_z \end{bmatrix} = \frac{1}{\det[\boldsymbol{A}]}$$

Eq.(2.13) gives the relations

$$\xi_x = J(y_\eta z_\zeta - y_\zeta z_\eta), \quad \xi_y = J(z_\eta x_\zeta - z_\zeta x_\eta), \quad \xi_z = J(x_\eta y_\zeta - x_\zeta y_\eta)$$

$$\eta_x = J(y_\zeta z_\xi - y_\xi z_\zeta), \quad \eta_y = J(z_\zeta x_\xi - z_\xi x_\zeta), \quad \eta_z = J(x_\zeta y_\xi - x_\xi y_\zeta)$$

$$\zeta_x = J(y_\xi z_\eta - y_\eta z_\xi), \quad \zeta_y = J(z_\xi x_\eta - z_\eta x_\xi), \quad \zeta_z = J(x_\xi y_\eta - x_\eta y_\xi) \tag{2.14}$$

$$\xi_t = -x_\tau \xi_x - y_\tau \xi_y - z_\tau \xi_z$$

$$\eta_t = -x_\tau \eta_x - y_\tau \eta_y - z_\tau \eta_z$$

$$\zeta_t = -x_\tau \zeta_x - y_\tau \zeta_y - z_\tau \zeta_z$$

with the following identity equations of metric coefficients

$$\frac{\partial}{\partial \tau}\left(\frac{1}{J}\right) + \frac{\partial}{\partial \xi}\left(\frac{\xi_t}{J}\right) + \frac{\partial}{\partial \eta}\left(\frac{\eta_t}{J}\right) + \frac{\partial}{\partial \zeta}\left(\frac{\zeta_t}{J}\right) = 0$$

$$\frac{\partial}{\partial \xi}\left(\frac{\xi_x}{J}\right) + \frac{\partial}{\partial \eta}\left(\frac{\eta_x}{J}\right) + \frac{\partial}{\partial \zeta}\left(\frac{\zeta_x}{J}\right) = 0$$

$$\frac{\partial}{\partial \xi}\left(\frac{\xi_y}{J}\right) + \frac{\partial}{\partial \eta}\left(\frac{\eta_y}{J}\right) + \frac{\partial}{\partial \zeta}\left(\frac{\zeta_y}{J}\right) = 0 \qquad (2.15)$$

$$\frac{\partial}{\partial \xi}\left(\frac{\xi_z}{J}\right) + \frac{\partial}{\partial \eta}\left(\frac{\eta_z}{J}\right) + \frac{\partial}{\partial \zeta}\left(\frac{\zeta_z}{J}\right) = 0$$

where

$$J = [x_\xi(y_\eta z_\zeta - y_\zeta z_\eta) + x_\eta(y_\zeta z_\xi - y_\xi z_\zeta) + x_\zeta(y_\xi z_\eta - y_\eta z_\xi)]^{-1} \qquad (2.15a)$$

Equation (2.11) now can be expressed as [32]

$$\frac{\partial}{\partial \tau}\left(\frac{\boldsymbol{q}}{J}\right) + \frac{\partial}{\partial \xi}\left[\frac{1}{J}(\xi_t \boldsymbol{q} + \xi_x \boldsymbol{E} + \xi_y \boldsymbol{F} + \xi_z \boldsymbol{G})\right]$$

$$+ \frac{\partial}{\partial \eta}\left[\frac{1}{J}(\eta_t \boldsymbol{q} + \eta_x \boldsymbol{E} + \eta_y \boldsymbol{F} + \eta_z \boldsymbol{G})\right]$$

$$+ \frac{\partial}{\partial \zeta}\left[\frac{1}{J}(\zeta_t \boldsymbol{q} + \zeta_x \boldsymbol{E} + \zeta_y \boldsymbol{F} + \zeta_z \boldsymbol{G})\right]$$

$$= \frac{1}{Re}\left\{ \frac{\partial}{\partial \xi}\left[\frac{1}{J}(\xi_x \boldsymbol{E}_v + \xi_y \boldsymbol{F}_v + \xi_z \boldsymbol{G}_v)\right]\right.$$

$$+ \frac{\partial}{\partial \eta}\left[\frac{1}{J}(\eta_x \boldsymbol{E}_v + \eta_y \boldsymbol{F}_v + \eta_z \boldsymbol{G}_v)\right]$$

$$\left.+ \frac{\partial}{\partial \zeta}\left[\frac{1}{J}(\zeta_x \boldsymbol{E}_v + \zeta_y \boldsymbol{F}_v + \zeta_z \boldsymbol{G}_v)\right]\right\}$$

in which the metric identities Eq.(2.15) have been employed. It can be further written in the simple conservation-law form

$$\frac{\partial \hat{\boldsymbol{q}}}{\partial \tau} + \frac{\partial \hat{\boldsymbol{E}}}{\partial \xi} + \frac{\partial \hat{\boldsymbol{F}}}{\partial \eta} + \frac{\partial \hat{\boldsymbol{G}}}{\partial \zeta} = \frac{1}{Re}\left[\frac{\partial \hat{\boldsymbol{E}}_v}{\partial \xi} + \frac{\partial \hat{\boldsymbol{F}}_v}{\partial \eta} + \frac{\partial \hat{\boldsymbol{G}}_v}{\partial \zeta}\right] \tag{2.16}$$

by introducing the new vectors

$$\hat{\boldsymbol{q}} = \frac{\boldsymbol{q}}{J}, \quad \hat{\boldsymbol{E}} = (\xi_t \boldsymbol{q} + \xi_x \boldsymbol{E} + \xi_y \boldsymbol{F} + \xi_z \boldsymbol{G})/J$$

$$\hat{\boldsymbol{F}} = (\eta_t \boldsymbol{q} + \eta_x \boldsymbol{E} + \eta_y \boldsymbol{F} + \eta_z \boldsymbol{G})/J, \quad \hat{\boldsymbol{G}} = (\zeta_t \boldsymbol{q} + \zeta_x \boldsymbol{E} + \zeta_y \boldsymbol{F} + \zeta_z \boldsymbol{G})/J$$

$$\hat{\boldsymbol{E}}_v = (\xi_x \boldsymbol{E}_v + \xi_y \boldsymbol{F}_v + \xi_z \boldsymbol{G}_v)/J, \quad \hat{\boldsymbol{F}}_v = (\eta_x \boldsymbol{E}_v + \eta_y \boldsymbol{F}_v + \eta_z \boldsymbol{G}_v)/J,$$

$$\hat{\boldsymbol{G}}_v = (\zeta_x \boldsymbol{E}_v + \zeta_y \boldsymbol{F}_v + \zeta_z \boldsymbol{G}_v)/J$$

where the vectors $\boldsymbol{q}$, $\boldsymbol{E}$, $\boldsymbol{F}$, $\boldsymbol{G}$, $\boldsymbol{E}_v$, $\boldsymbol{F}_v$ and $\boldsymbol{G}_v$ are defined by Eq.(2.5a) with all related quantities being non-dimensional. Moreover, if we define the contravariant velocity components

$$U \equiv \frac{d\xi}{dt} = \xi_t + \xi_x u + \xi_y v + \xi_z w$$

$$V \equiv \frac{d\eta}{dt} = \eta_t + \eta_x u + \eta_y v + \eta_z w$$

$$W \equiv \frac{d\zeta}{dt} = \zeta_t + \zeta_x u + \zeta_y v + \zeta_z w$$

then the new vectors in Eq.(2.16) can be also written as

$$\hat{\boldsymbol{q}} = \frac{1}{J}\begin{Bmatrix} \rho \\ \rho u \\ \rho v \\ \rho w \\ E \end{Bmatrix}, \quad \hat{\boldsymbol{E}} = \frac{1}{J}\begin{Bmatrix} \rho U \\ \rho u U + \xi_x p \\ \rho v U + \xi_y p \\ \rho w U + \xi_z p \\ (E + p)U - \xi_t p \end{Bmatrix}, \quad \hat{\boldsymbol{F}} = \frac{1}{J}\begin{Bmatrix} \rho V \\ \rho u V + \eta_x p \\ \rho v V + \eta_y p \\ \rho w V + \eta_z p \\ (E + p)V - \eta_t p \end{Bmatrix}$$

$$\hat{G} = \frac{1}{J}\left\{\begin{matrix} \rho W \\ \rho u W + \zeta_x p \\ \rho v W + \zeta_y p \\ \rho w W + \zeta_z p \\ (E + p)W - \zeta_t p \end{matrix}\right\}, \quad \hat{E}_v = \frac{1}{J}\left\{\begin{matrix} 0 \\ \xi_x \tau_{xx} + \xi_y \tau_{yx} + \xi_z \tau_{zx} \\ \xi_x \tau_{xy} + \xi_y \tau_{yy} + \xi_z \tau_{zy} \\ \xi_x \tau_{xz} + \xi_y \tau_{yz} + \xi_z \tau_{zz} \\ \xi_x \beta_x + \xi_y \beta_y + \xi_z \beta_z \end{matrix}\right\}$$

$$\hat{F}_v = \frac{1}{J}\left\{\begin{matrix} 0 \\ \eta_x \tau_{xx} + \eta_y \tau_{yx} + \eta_z \tau_{zx} \\ \eta_x \tau_{xy} + \eta_y \tau_{yy} + \eta_z \tau_{zy} \\ \eta_z \tau_{xz} + \eta_y \tau_{yz} + \eta_z \tau_{zz} \\ \eta_z \beta_x + \eta_y \beta_y + \eta_z \beta_z \end{matrix}\right\}, \quad \hat{G}_v = \frac{1}{J}\left\{\begin{matrix} 0 \\ \zeta_x \tau_{xx} + \zeta_y \tau_{yx} + \zeta_z \tau_{zx} \\ \zeta_z \tau_{xy} + \zeta_y \tau_{yy} + \zeta_z \tau_{zy} \\ \zeta_x \tau_{xy} + \zeta_y \tau_{yz} + \zeta_z \tau_{zz} \\ \zeta_x \beta_x + \zeta_y \beta_y + \zeta_z \beta_z \end{matrix}\right\} \qquad (2.17)$$

Note that for a fixed grid the curvilinear coordinates ξ, η and ζ are invariant with the time t. It follows that $\xi_t = \eta_t = \zeta_t = 0$.

Thin-Layer Navier-Stokes Equations

For high Reynolds number flow, the diffusion processes along the body surface are often negligibly small in comparison with the one normal to the surface. Let the body surface be mapped onto a ζ=constant plane in the transformed domain (ξ, η, ζ), then the viscous derivatives as well as the thermal diffusion derivatives in ξ and η directions are neglected. In contrast to the classical boundary-layer theory, all derivatives in the convective terms are retained to make the simplified equations capable of dealing with separated and reverse flow regions. The thin-layer Navier-Stokes equation in a vector form is written as

$$\frac{\partial \hat{q}}{\partial \tau} + \frac{\partial \hat{E}}{\partial \xi} + \frac{\partial \hat{F}}{\partial \eta} + \frac{\partial \hat{G}}{\partial \zeta} = \frac{1}{Re}\frac{\partial \hat{S}}{\partial \zeta} \tag{2.18}$$

where

$$\hat{S} = \frac{1}{J}\left\{\begin{array}{c} 0 \\ m_1 u_\zeta + m_2 \zeta_x \\ m_1 v_\zeta + m_2 \zeta_y \\ m_1 w_\zeta + m_2 \zeta_z \\ m_1 m_3 + m_2(\zeta_x u + \zeta_y v + \zeta_z w) \end{array}\right\}$$

$$m_1 = \mu(\zeta_x^2 + \zeta_y^2 + \zeta_z^2), \quad m_2 = \frac{\mu}{3}(\zeta_x u_\zeta + \zeta_y v_\zeta + \zeta_z w_\zeta)$$

$$m_3 = \frac{1}{2}(u^2 + v^2 + w^2)_\zeta + \frac{\kappa/\mu}{Pr(\gamma - 1)}\frac{\partial T}{\partial \zeta}$$

Turbulence Model

A direct simulation of a three-dimensional, high speed (high *Re*) turbulent flow is practically not feasible. The main problem lies in that the time and length scales of the turbulent motion are so small that the number of grid points and time steps required usually exceeds present computer's capability [29]. The smallest length scale known to exist in a turbulence motion is the Kolmogorov length scale. The ratio between Kolmogorov length scale to the characteristic length scale in any single direction for a flow problem is to the order of $Re^{-3/4}$ [33]. In three dimensional space it attains a ratio of cubic order, i.e., $Re^{-9/4}$. In order for the mesh size to have the same order as the turbulence length scale, a flow problem with $Re = 10^3$ needs a total number of grid points in the order of $10^{27/4}$, which can take up the available memories in today's most powerful supercomputers. Therefore, in a three-dimensional turbulent flow simulation, we need to increase the computing resources to the order of $10^{9/4}$ if we want to raise the Reynolds number by a factor of 10 times, not to mention the effect of choosing a proper turbulent time scale.

A feasible alternative is to solve the time-averaged Navier-Stokes equations, also referred as the Reynolds averaged equations [29]. The mass-weighted Reynolds averaged equation in this study takes the identical forms as Eq.(2.5), with all dependent variables now becoming time-averaged. For laminar flows the coefficient of viscosity $\mu = \mu_l$ is determined by the Sutherland's law (Eq.(2.3)) and the thermal conductivity κ is defined, assuming a constant Prandtl number, as $\kappa_l = C_p \mu_l / Pr$. For turbulent flows, the "effective" viscosity coefficient μ comprises two parts,

$$\mu = \mu_l + \mu_t$$

where μ_l is the laminar viscosity and μ_t is the turbulent (or eddy) viscosity which can be represented by the well-known Baldwin-Lomax turbulence model [16]. In turbulent flows, an additional transport of heat is caused by the turbulent motion. Accordingly, the thermal conductivity κ has the form

$$\kappa = \kappa_l + \kappa_t = \frac{Cp\,\mu_l}{Pr} + \frac{Cp\,\mu_t}{Pr_t}$$

in which Pr_t is the turbulent Prandtl number with the value of 0.9 for air [29]. The Baldwin-Lomax model is a two-layer algebraic eddy viscosity model which relates turbulent eddy viscosity μ_t to the time-averaged variables in such a way that no additional variables are introduced. This makes the Baldwin-Lomax model an easy one to apply and costs relatively little computer time, which has a great advantage in three-dimensional Navier-Stokes computation. As a matter of fact, the Baldwin-Lomax turbulence model has been applied extensively in many computational cases. The results are accurate and well justified as long as the flow separation is not strong.

The Baldwin-Lomax turbulence model was proposed after Cebeci's two-layer model. In Baldwin-Lomax model, the eddy viscosity μ_t is given by

$$\mu_t = \begin{cases} (\mu_t)_{inner} & y \le y_{crossover} \\ (\mu_t)_{outer} & y \ge y_{crossover} \end{cases} \tag{2.19}$$

where y is the normal distance from the solid wall and $y_{crossover}$ is the value of y which gives $(\mu_t)_{inner} = (\mu_t)_{outer}$.

In the inner region, the Prandtl-Van Driest formulation is applied

$$(\mu_t)_{inner} = \rho l^2 |\omega| \tag{2.20}$$

where l is the mixing length with the form

$$l = ky[1 - \exp(-\frac{y^+}{A^+})]$$

$|\omega|$ is the magnitude of the vorticity vector

$$|\omega| = \sqrt{(\frac{\partial u}{\partial y} - \frac{\partial v}{\partial x})^2 + (\frac{\partial v}{\partial z} - \frac{\partial w}{\partial y})^2 + (\frac{\partial w}{\partial x} - \frac{\partial u}{\partial z})^2}$$

and y^+ is a law-of-wall coordinate defined as

$$y^+ = \frac{\rho_w u_\tau y}{\mu_w} = \frac{\sqrt{\rho_w |\tau_w|}}{\mu_w} y \tag{2.21}$$

The subscript w designates the local flow properties on the wall and $u_\tau = (|\tau_w|/\rho_w)^{1/2}$ is the friction velocity. The viscosity coefficient at wall consists of only the laminar viscosity μ_l, and the wall shear stress $|\tau_w|$ is equal to $\mu_w|\omega|_w$. k and A^+ are two constants set to be 0.4 and 26, respectively.

The Clauser formulation is used for the outer region

$$(\mu_t)_{outer} = K C_{cp} \rho F_{wake} F_{Kleb}(y) \tag{2.22}$$

where K is the Clauser constant which equals to 0.0168. $C_{cp} = 1.6$ is an additional constant, and

$$F_{wake} = \min \left\{ \begin{array}{c} y_{max} F_{max} \\ C_{wk} y_{max} U_{dif}^2 / F_{max} \end{array} \right\}$$

The quantities y_{max} and F_{max} are determined by the function

$$F(y) = y|\omega|[1 - \exp(-\frac{y^+}{A^+})] \tag{2.23}$$

where F_{max} is the maximum F along a radial grid line off a solid surface and y_{max} is the value of y where F_{max} occurs. $C_{wk} = 0.25$ and U_{dif} represents the difference between the maximum and minimum velocity magnitude along the radial line. $F_{Kleb}(y)$ is the Klebanoff intermittency factor given by

$$F_{Kleb}(y) = [1 + 5.5(\frac{C_{Kleb}y}{y_{\max}})^6]^{-1}$$

where $C_{Kleb} = 0.3$.

In application, we first compute the vorticity magnitude $|\omega|$ as well as the mixing length l at each grid point along a radial line from the surface. The computation for $(\mu_t)_{inner}$ is then straightforward. To obtain $(\mu_t)_{outer}$, we need to evaluate F_{wake} which is determined by the profile of the function $F(y)$. The final eddy viscosity distribution along this radial ray is obtained by taking the smaller value from either the inner or the outer eddy viscosity distribution.

The formulations discussed above are all dimensional. The corresponding non-dimensional equations for Eq.(2.20), (2.21) and (2.22) are

$$(\mu_t)_{inner} = Re\rho l^2 |\omega| \tag{2.20a}$$

$$y^+ = \sqrt{Re}\,\frac{\sqrt{\rho_w |\tau_w|}}{\mu_w}y \tag{2.21a}$$

$$(\mu_t)_{outer} = Re K C_{cp} \rho F_{wake} F_{Kleb}(y) \tag{2.22a}$$

in which the vorticity magnitude $|\omega|$ and F_{wake} are normalized by a_∞/L and $a_\infty L$, respectively.

Modified Baldwin-Lomax Turbulence Model

As discussed in Chapter I, the Baldwin-Lomax turbulence model is not suitable for massive crossflow separations in the high-α flow computation. Degani and Schiff [15] have stated that when the crossflow separation is relatively small, the behavior of the function $F(y)$ resembles Case (a) in Figure 2.1. Only one well-defined peak occurs on each of the windward and leeward sides and the determination of F_{max} and y_{max} is straightforward. When α is larger, the characteristics of $F(y)$ does not change on the windward side. However, the underlying vortex structure above the leeward side can cause a second, larger peak as shown in Case (b). A vorticity magnitude jump takes place when the radial ray crosses the vorticity feeding line emanating near the primary separation point. This jump, in conjunction with a much larger distance y from the wall, results directly in the second larger peak. In the original model application, the code searches along the outward ray and determines F_{max}, therefore, picking up the second, larger peak located away from the surface. The eddy viscosity, however, depends only on local flow profiles and should be determined within the attached boundary layer underlying the vortex structures on the leeward side, as well as within the windward-side boundary layer. It concludes that we should pick up the first peak within the attached boundary layer and exclude the second, larger one. Indeed the choice of the larger peak can result in a much larger computed eddy viscosity. Consequently, the turbulence mixing is too strong and the details of the flow physics and phenomena in the thin-layer can be distorted or washed out.

Degani and Schiff then suggested the following modifications on the Baldwin-Lomax turbulence model. First the search for F_{max} is performed circumferentially on a given cross-section from the windward symmetric plane to the leeward symmetric plane. Along each radial ray the code searches for the first peak it encounters then cuts off the searching. The peak is considered to be found when the value of $F(y)$ at the next radial grid point drops more than 10% from the current maximum value. Therefore, choosing F_{max} this way allows us to obtain a more reasonable computed eddy viscosity. It was also mentioned that, when the location of the vortex feeding sheet appears close to the outer edge of the attached boundary layer, i.e., at a very short distance downstream of the crossflow separation point, these two peaks shown in $F(y)$ profile tend to merge. In this case, we cannot assume a drop of more than 10% from the first peak before reaching the second peak. Accordingly, a further modification was made in such a way that, on each ray a cut-off distance is specified in terms of y_{max} from the previous circumferential ray, i.e.,

$$y_{cut-off}(\theta) = c y_{max}(\theta - \Delta\theta) \tag{2.24}$$

where c is a cut-off constant, and θ increases from the windward symmetric plane to the leeward symmetric plane. When a peak does not appear within the assigned cut-off distance, F_{max} and y_{max} simply take their values from the previous ray. Determining the constant c depends very much on the vortical flow structure as well as the radial grid discretization. It must be large enough for the code to detect the desired peak, but cannot be too large with a possibility to pick up the second peak. In this study, the constant c is determined to be 5 through numerical experiments which are described in Chapter V.

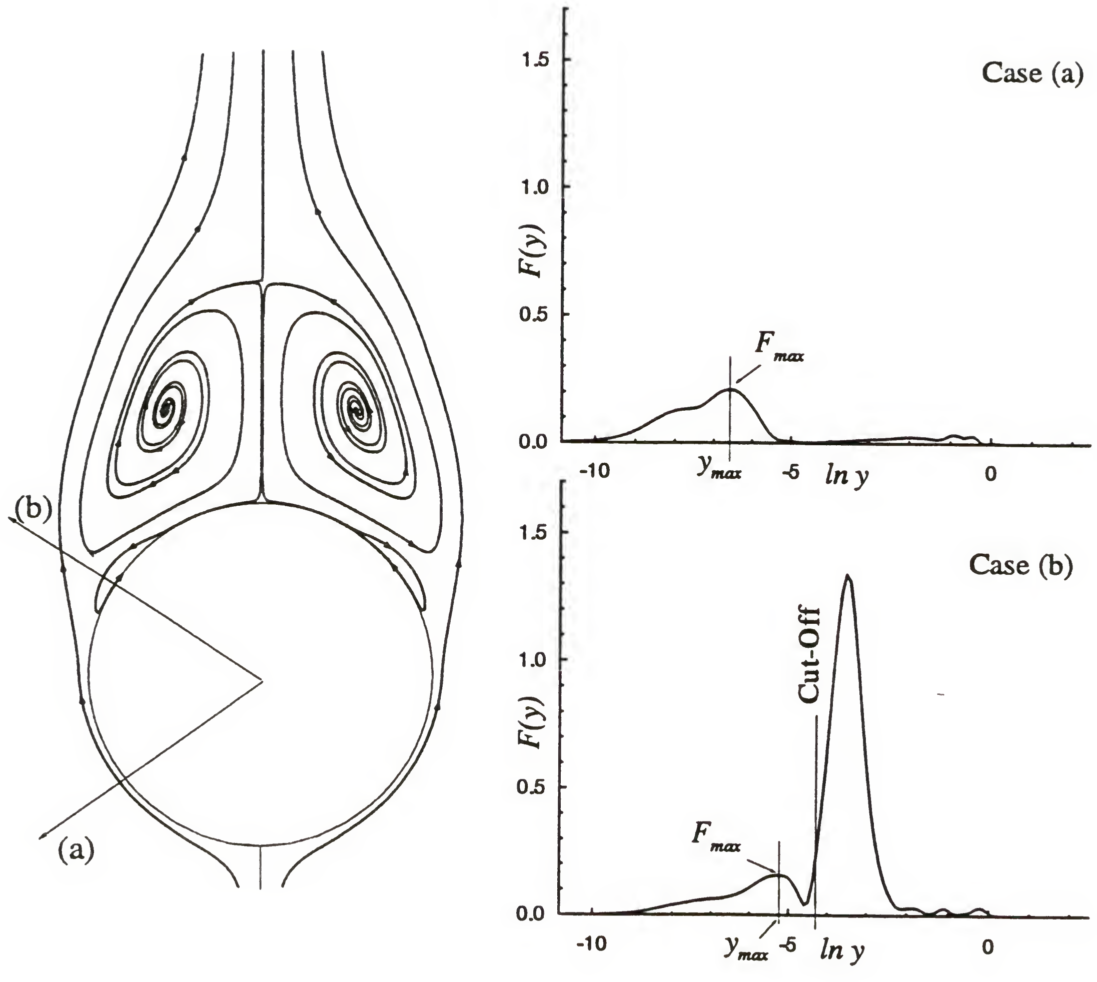

Figure 2.1 Behavior of the function $F(y)$ at windward (Case (a)) and leeward (Case (b)) locations.

CHAPTER III
FLOW PROBLEM

In this chapter the flow problem and geometrical model for numerical simulation are defined. The governing equations are the thin-layer Navier-Stokes equations. The domain discretization (grid generation) is described followed by a discussion on the imposed boundary conditions.

Flow Conditions and Geometrical Model

The specific flow problem considered in this study concerns an impulsively-started Mach number 0.96 turbulent flow past a Secant-Ogive-Cylinder-BoatTail (SOCBT) projectile with sting at 60-degree angle of attack. Defining the 2.25-inch diameter on the cylindrical section as one caliber, the real projectile model consists of a 2.98-caliber forebody, a 1.983-caliber cylinder, and a one-caliber, 7° boattail. There is no measurements available for assessing the numerical simulation of the flow problem. However, the model with a 0.32-caliber cylindrical sting attached to the base had been investigated extensively by the U.S. Army Ballistic Research Laboratory. The surface pressure coefficient on the six-caliber main body had been measured for the angles of attack α at 0°, 4°, 6° and 10°, for the free stream Mach numbers M_∞ at 0.91, 0.94, 0.96, 0.98, 1.10 and 1.20 [34]. The Reynolds number, based on a free stream velocity $V_\infty = 0.96a_\infty$ and the diameter of the projectile cylinder, is 760,000. The stagnation pressure $p_0 = 1$ atm and the stagnation temperature $T_0 = 580°\text{R}$, or $p_\infty = 0.55$ atm and $T_\infty = 489.6°\text{R}$. The Prandtl number for the testing condition is 0.71 [35].

A simplified projectile model for numerical simulation is shown in Figure 3.1. The boattail has been extended for another 1.82 calibers onto the sting to avoid the difficulties in a base flow simulation. The total length is 15.963 calibers. Also shown in Figure 3.1 are the Cartesian and curvilinear coordinates of the flow problem. The Cartesian coordinate system has x as the projectile longitudinal axis, y lies in the right-hand-side direction, and z in an upward direction. The curvilinear coordinates ξ, η and ζ represent the streamwise, circumferential and normal directions, respectively.

Domain Discretization

The three-dimensional grid system employed in this study is obtained by rotating a two-dimensional planar grid with respect to x-axis. It has 92 points in the circumferential direction. The planar grid, which has 110 points in the streamwise direction and 60 points in the normal direction respectively, is a good grid for the transonic flow problem at 10-degree angle of attack. In the following sections, the integers J, K, L are used to denote the grid points in ξ, η and ζ directions, respectively. JMAX, KMAX and LMAX represent the grid dimensions in each direction.

Planar Grid Generation

The two-dimensional planar grid with JMAX=110 in ξ direction and LMAX=60 in ζ direction is generated by a hyperbolic grid generation code and shown in Figure 3.2 [36]. It has an exponential clustering in the ζ direction with the minimum spacing of 2×10^{-5} beiwen the surface (L=1) and first grid lines (L=2) which keeps the law-of-the-wall coordinate y^+ at L=2 within the value of 1 throughout the computation. This spacing is indeed small enough for an accurate turbulent boundary layer flow simulation. The outer domain is approximately 24 calibers away from the projectile and is large enough for an accurate Mach number 0.96 turbulent flow simulation for $\alpha\leq10°$ [37]. A detailed planar grid distribution near the surface is shown in Figure 3.3. A few selected J locations and their local diameters are identified for reference. Note that the 110 points in x-direction are distributed such that 95 points are located on the main body (nose tip to boattail-sting juncture). Accordingly, the largest grid spacing on sting is about 1.03 calibers. It is realized that such a grid resolution may not be sufficient to justify the computational results on the sting segment. Therefore in a subsequent version of the planar grid, some additional 21 points are added to refine sting resolution for more accurate asymmetric vortex shedding simulation. A comparison of these two planar grids on the sting is shown in Figure 3.4.

Three-Dimensional Grid Generation

The three-dimensional grid is obtained by rotating the planar grid with respect to the projectile axis in the circumferential η direction. A cross-sectional grid topology on the cylinder is shown in Figure 3.5. Starting from $\theta=0°$ (K=1) on the windward symmetric plane, a suitable discretization chosen has $\Delta\theta=10°$ for $0° \leq \theta \leq 40°$, $\Delta\theta=5°$ for $40° \leq \theta \leq 65°$, and $\Delta\theta=3°$ all the way to the leeward symmetric plane $\theta=180°$ (K=47). The grid is symmetric with respect to the angle-of-attack plane with a total of 92 K-planes. Previous studies show that $\Delta\theta=10°$ can give an accurate windward flow simulation while $\Delta\theta=3°$ in the crossflow separation region is sufficient to resolve the secondary vortical flow structure on the leeward side.

Boundary Conditions

The three-dimensional grid in the physical domain (x,y,z) is transformed onto a computational domain (ξ,η,ζ) where the thin-layer Navier-Stokes algorithm is applied. The transformed computational domain with a constant discretization is shown in Figure 3.6. The boundary conditions (i.e., the solution vector $[\rho, \rho u, \rho v, \rho w, E]^T$) on the six surface planes must be provided for the computation at every time step and are discussed as follows.

Solid Surface Boundary Condition

The solid surface L=1 (or $\zeta=0$) is mapped onto the plane EFGH on which the "no-slip" condition is enforced for a viscous flow case, i.e., $u=v=w=0$. An adiabatic wall is assumed such that $\partial T/\partial \hat{n}=0$ at L=1 where $\hat{n}=\nabla\zeta/|\nabla\zeta|$ is the unit normal vector on the surface. The density ρ and total energy E on the surface are found by first considering the inviscid normal momentum equation. Knowing that the contravariant velocity components U, V and W also vanish on the solid wall, the three inviscid momentum equations are rewritten from Eq.(2.18) as

$$\frac{\partial}{\partial \xi}[\frac{1}{J}(\xi_x p)] + \frac{\partial}{\partial \eta}[\frac{1}{J}(\eta_x p)] + \frac{\partial}{\partial \zeta}[\frac{1}{J}(\zeta_x p)] = 0$$

$$\frac{\partial}{\partial \xi}[\frac{1}{J}(\xi_y p)] + \frac{\partial}{\partial \eta}[\frac{1}{J}(\eta_y p)] + \frac{\partial}{\partial \zeta}[\frac{1}{J}(\zeta_y p)] = 0$$

$$\frac{\partial}{\partial \xi}[\frac{1}{J}(\xi_z p)] + \frac{\partial}{\partial \eta}[\frac{1}{J}(\eta_z p)] + \frac{\partial}{\partial \zeta}[\frac{1}{J}(\zeta_z p)] = 0$$

Now multiplying these three equations by ζ_x, ζ_y, and ζ_z, respectively, adding them up together and utilizing the metric identities Eq.(2.15), we have the resulting equation in the form

$$(\xi_x\zeta_x + \xi_y\zeta_y + \xi_z\zeta_z)p_\xi + (\eta_x\zeta_x + \eta_y\zeta_y + \eta_z\zeta_z)p_\eta + (\zeta_x\zeta_z + \zeta_y\zeta_y + \zeta_z\zeta_z)p_\zeta = 0$$

or

$$\zeta_x p_x + \zeta_y p_y + \zeta_z p_z = 0 \tag{3.1}$$

This is the same as having $\nabla\zeta\cdot\nabla p = 0$ or $\partial p/\partial\hat{n}=0$ at L=1. By ideal gas law the fluid density is solely a function of pressure and temperature. Therefore we also have $\partial\rho/\partial\hat{n}=0$ at L=1 for an adiabatic wall ($\partial T/\partial\hat{n}=0$). Accordingly, ρ and p at L=1 can have their values directly from L=2. The total energy E at L=1 then can be computed from the equation of state Eq.(2.9).

Outer Domain Boundary Condition

In Figure 3.6, plane ABCD is the outer domain L=LMAX on which the free stream conditions are assumed

$$\rho = \rho_\infty, \quad u = V_\infty \cos\alpha, \quad v = 0, \quad w = V_\infty \sin\alpha, \quad E = E_\infty, \quad p = p_\infty, \quad T = T_\infty$$

where α is the angle of attack.

Circumferential Boundary Condition

The flow domain in the circumferential direction is cut open and "unwrapped" during the coordinate transformation. In order to establish a periodic boundary condition in the cut-off plane, two extra K planes are added to overlap on K=1 and K=2 planes which makes KMAX=94. The boundary conditions at K=1 (plane ABFE) and K=KMAX (plane CDHG) are provided with the solutions at K=KMAX-1 and K=2 from a previous time step. The overlapping is chosen at the windward symmetric plane in order to minimize the adverse effect of updating periodic boundary conditions in the wake region.

Singular Plane J=1

J=1 (or $\xi=0$) is a straight line off the projectile nose in the physical domain. It is mapped onto a singular plane ADHE in the computational domain. Subject to the physical meaning that the solution on this singular plane should be circumferentially invariant, a zero-order extrapolation in J direction is applied to obtain the individual $\boldsymbol{q}|_{J=1}$

for each K and L, i.e.,

$$q|_{J=1} = \frac{4q|_{J=2} - q|_{J=3}}{3} \tag{3.2}$$

Equation (3.3) was obtained in the original 3-D thin-layer Navier-Stokes code by enforcing a zero-slope condition at J=1. It is understood that the assumption is not ideal for an angle-of-attack flow simulation. The local accurary can be improved by using a linear extrapolation

$$q|_{J=1} = q|_{J=2} - (q|_{J=3} - q|_{J=2})\frac{S_{12}}{S_{23}} \tag{3.3}$$

where S_{12} and S_{23} are the distance between the points at J=1 to J=2, and J=2 to J=3, respectively. In this study, however, Eq.(3.3) is used throughout the computation.

A summation/averaging procedure then is taken

$$q|_{\mathrm{J=1}} = \frac{\sum_{\mathrm{K=2}}^{\mathrm{KMAX-1}} q|_{\mathrm{J=1}}}{\mathrm{KMAX-2}} \tag{3.4}$$

to form the singular plane boundary condition at J=1 used in the code.

Downstream Boundary Condition

J=JMAX is mapped onto plane BCGF in Figure 3.6. Due to the fact that the sting has been extended quite far downstream away from the projectile main body, the code in an earlier version simply sets a zeroth-order extrapolation on ρ, ρu, ρv and ρw. For example, $\rho_{\mathrm{JMAX}} = \rho_{\mathrm{JMAX-1}}$ and etc. The total energy E then is computed from Eq.(2.9), assuming that the pressure is equal to free stream pressure p_∞. After analyzing the intermediate computational results near the end of projectile sting, however, some unrealistic pressure and temperature contours were found near J=JMAX by enforcing the free stream pressure at the downstream plane. When the study of the solution on sting segment found to be important at a later time for $\tau \geq 5.0$, the JMAX=131 grid simply replaces the original JMAX=110 grid, along with a zeroth-order extrapolation for all five variables ρ, ρu, ρv, ρw and E to set up the downstream boundary condition, i.e, $p_{\mathrm{JMAX}} = p_{\mathrm{JMAX\text{-}1}}$ which is not equal to p_∞ anymore.

Slow Start

The flow problem is subject to an impulsively started flowfield. To avoid the sudden jump between the initial free stream velocity at L=2 grid lines and the viscous "no-slip" condition on the solid boundary L=1 lines, a slow start technique is applied in the code such that the velocity at L=1 is reduced gradually to zero over the first 30 time steps. This is accomplished by setting the solution vector $\boldsymbol{q}$ on the solid surface as

$$\boldsymbol{q}_n = \omega\, \boldsymbol{q}_{bc} + (1-\omega)\boldsymbol{q}_\infty, \qquad N = 1,30 \tag{3.5}$$

with

$$\omega = (10 - 15\theta + 6\theta^2)\theta^3, \qquad \theta = (N-1)/30$$

where N is the number of time steps over the first 30 steps and $\boldsymbol{q}_{bc}$ is the solid surface boundary conditions previously discussed. The function ω has a distribution which increases very slowly over the first few steps and recovers to one smoothly.

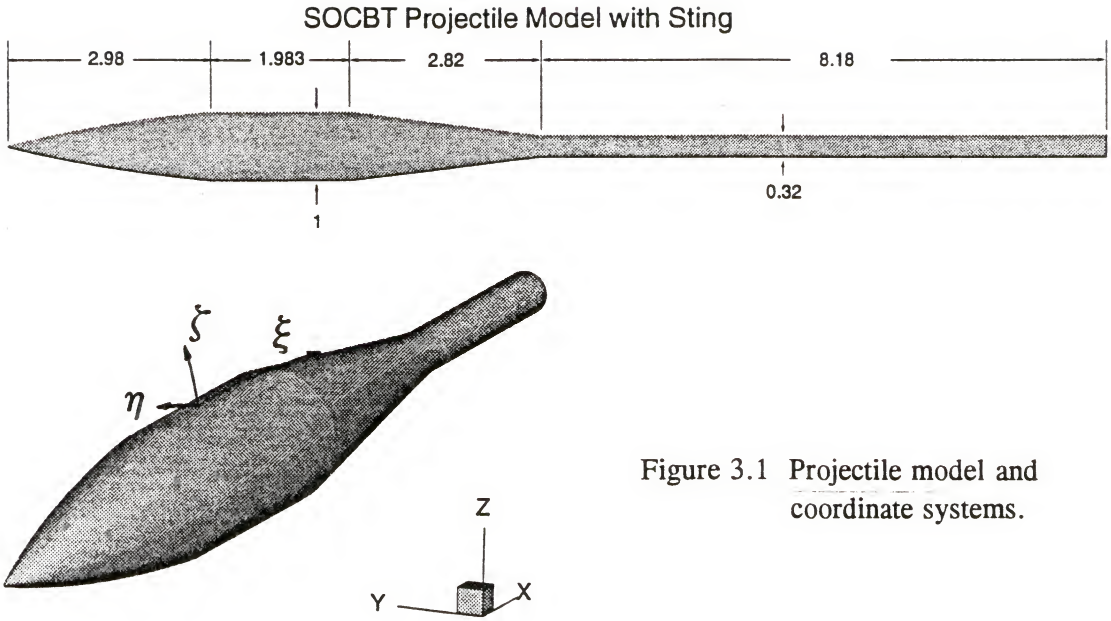

Figure 3.1 Projectile model and coordinate systems.

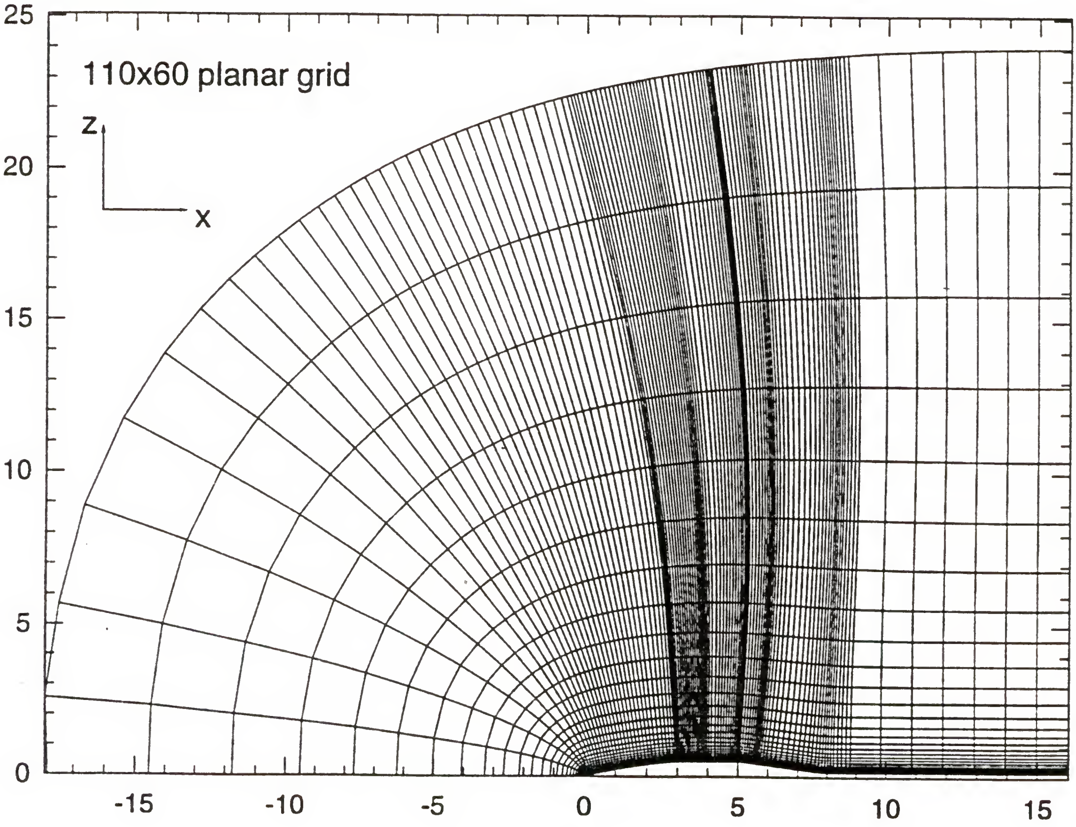

Figure 3.2 2-D planar grid (JMAX=110).

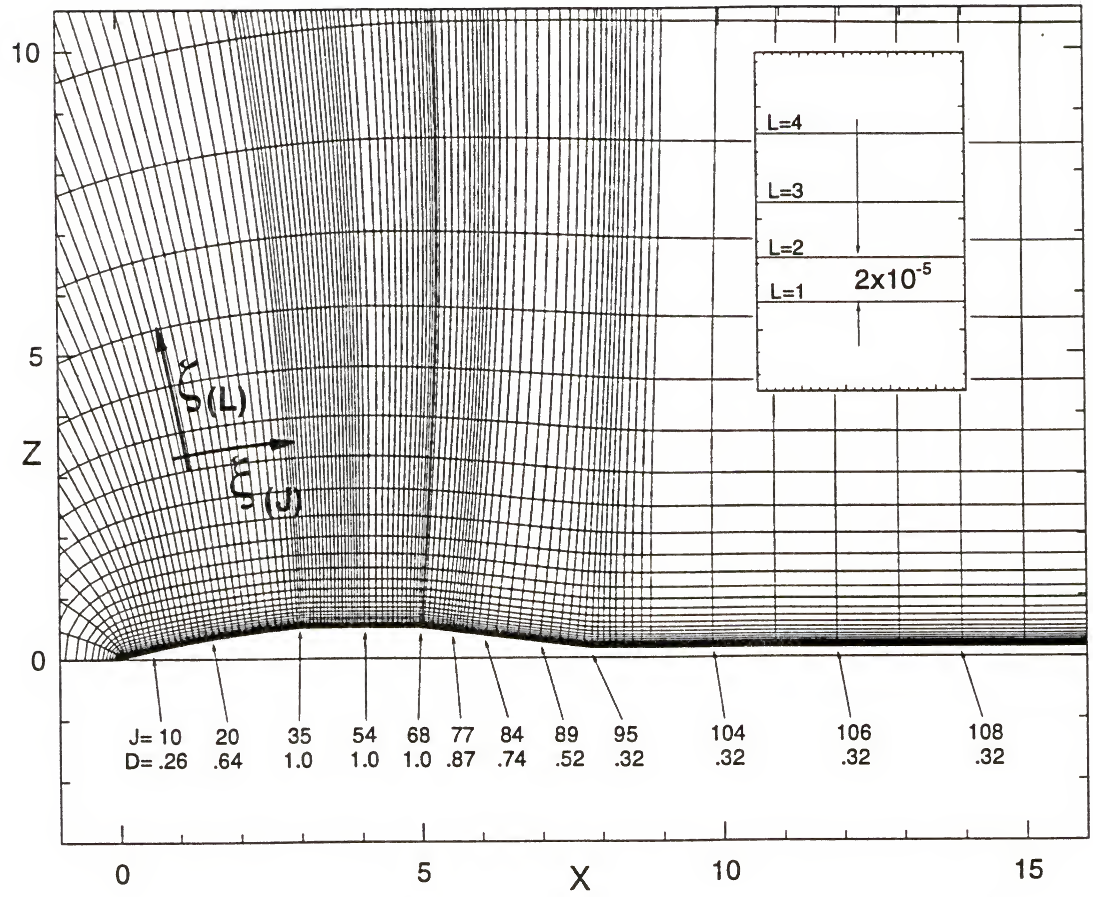

Figure 3.3 Close-up of 2-D planar grid (JMAX=110).

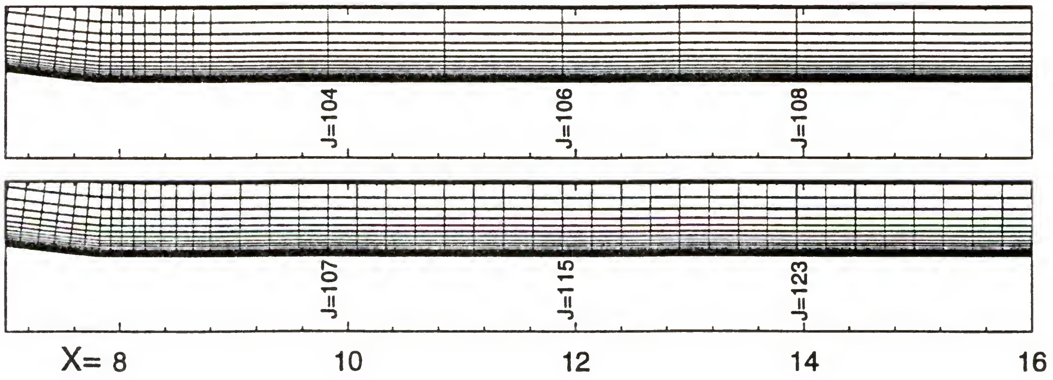

Figure 3.4 JMAX=110 grid (top) and JMAX=131 grid (bottom) on the sting.

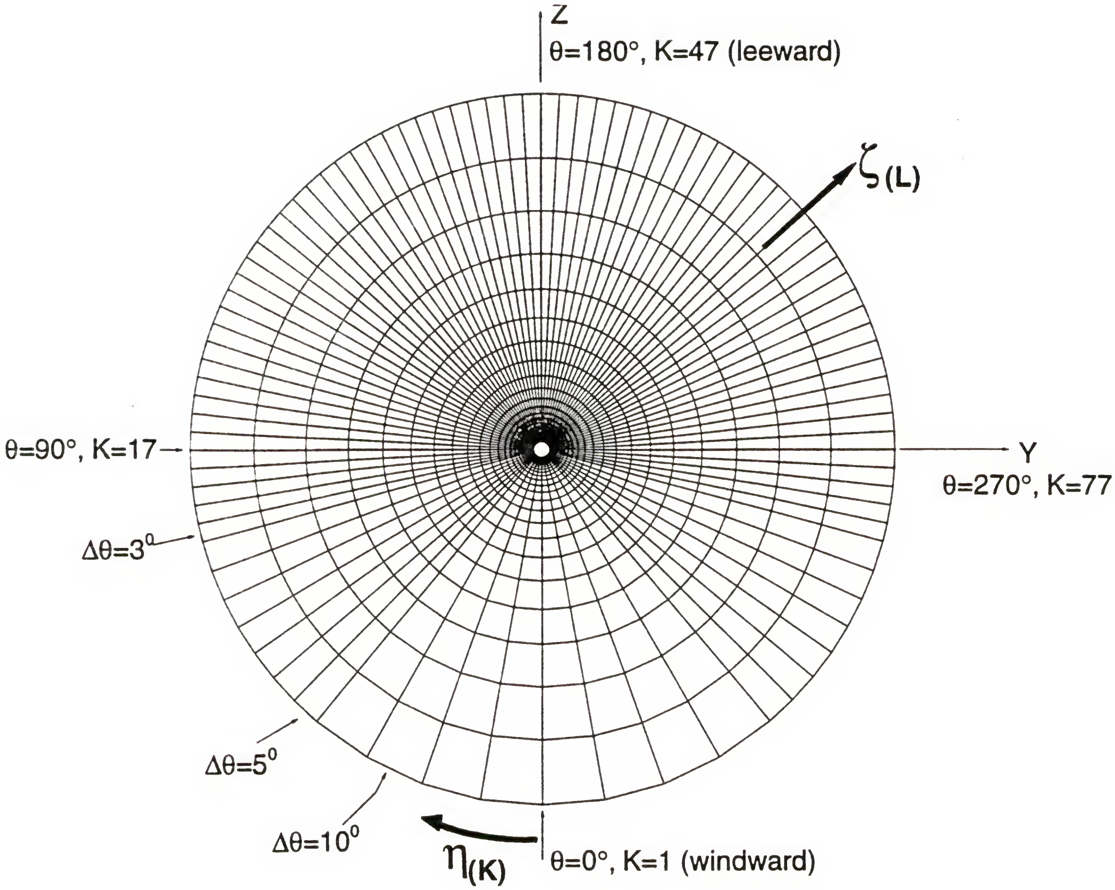

Figure 3.5 Circumferential grid distribution.

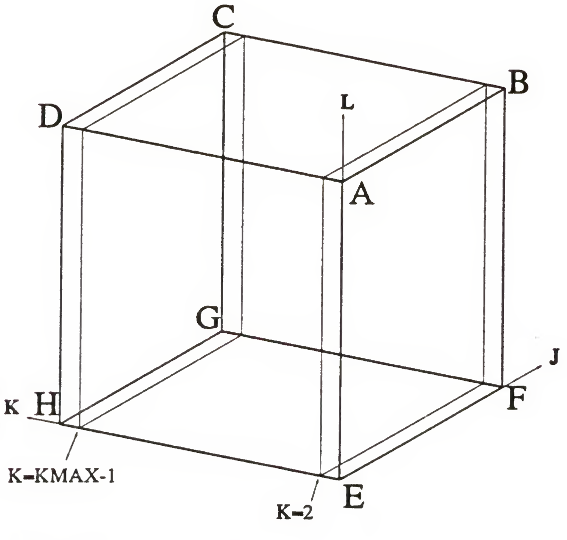

Figure 3.6 Transformed computational (J,K,L) domain.

CHAPTER IV
THIN-LAYER NAVIER-STOKES COMPUTATION

In this chapter the three-dimensional thin-layer Navier-Stokes TVD code used in the study is first discussed. Then a number of algorithms which relate the solution vector $\boldsymbol{q} = [\rho, \rho u, \rho v, \rho w, E]^{\mathrm{T}}$ to other useful flow variables such as the pressure and shear stress coefficients are described. These variables are used to present the results in the next chapter.

The thin-layer Navier-Stokes Total Variation Diminishing (TVD) code is developed for solving the transformed thin-layer Navier-Stokes equation (Eq.(2.18)). The scheme is based on a non-iterative, implicit approximately, factorized finite-difference algorithm described by Beam and Warming [38] which is accurate to the first order in time. Instead of inverting a very large system of equations resulted from all three spatial directions, the implicit operator is factorized into three one-dimensional processes. The TVD code is a modification of an original version of ARC3D thin-layer Navier-Stokes code developed at NASA Ames Research Center [39]. In application the TVD code can be viewed as the same as ARC3D code. It only uses a different way to construct its numerical dissipation terms, and has been shown to be more efficient and robust for the transonic turbulent flow simulation [40,41].

Both schemes had been extensively described in various applications. In the following only the TVD scheme is presented without further elaboration. For simplicity, all vectors in Eq.(2.18) are dropping their hat ^. It is therefore a good reminder that the vector $\boldsymbol{q}$ now represents J^{-1} $[\rho, \rho u, \rho v, \rho w, E]^{T}$ and $J\boldsymbol{q}$ is the physical non-dimensional solution vector.

Thin-Layer Navier-Stokes TVD Code

The transformed unsteady three-dimensional thin-layer Navier-Stokes equation can be approximated by the following finite-difference equation based on the delta form described Beam and Warming

$$L_{\xi}L_{\eta}L_{\zeta}\Delta\boldsymbol{q}^{n} = \boldsymbol{R}^{n} \tag{4.1}$$

where the difference operators L_{ξ}, L_{η} and L_{ζ} and the right-hand-side vector $\boldsymbol{R}^{n}$ are

$$L_{\xi} = [\boldsymbol{I} + \Delta\tau\delta_{\xi}\boldsymbol{A} + D_{I\xi}]^{n}$$

$$L_{\eta} = [\boldsymbol{I} + \Delta\tau\delta_{\eta}\boldsymbol{B} + D_{I\eta}]^{n}$$

$$L_{\zeta} = \{\boldsymbol{I} + \Delta\tau[\delta_{\zeta}\boldsymbol{C} - Re^{-1}\delta_{\zeta}(J^{-1}\boldsymbol{M}J)] + D_{I\zeta}\}^{n}$$

$$\boldsymbol{R}^{n} = [-\Delta\tau(\delta_{\xi}\boldsymbol{E} + \delta_{\eta}\boldsymbol{F} + \delta_{\zeta}\boldsymbol{G} - Re^{-1}\delta_{\zeta}\boldsymbol{S}) + D_{E}]^{n}$$

Here $\Delta\boldsymbol{q}^{n} = \boldsymbol{q}^{n+1} - \boldsymbol{q}^{n}$ is the delta-form unknown to be solved and $\boldsymbol{I}$ is a 5×5 identity matrix. $\boldsymbol{A} = \partial\boldsymbol{E}/\partial\boldsymbol{q}$, $\boldsymbol{B} = \partial\boldsymbol{F}/\partial\boldsymbol{q}$, $\boldsymbol{C} = \partial\boldsymbol{G}/\partial\boldsymbol{q}$ and $\boldsymbol{M} = \partial\boldsymbol{S}/\partial\boldsymbol{q}$ are the Jacobian matrices obtained in the time linearization process of $\boldsymbol{E}$, $\boldsymbol{F}$, $\boldsymbol{G}$ and $\boldsymbol{S}$, respectively [42]. They are all 5×5 matrices and are explicitly expressed in Appendix. δ_ξ, δ_η and δ_ζ in L_ξ, L_η and L_ζ are second-order central difference operators which keep the resulting systems of equations to be solved in a block-tridiagonal matrix form. In $\boldsymbol{R}^n$ a fourth-order central difference approximation is used for the convection terms (**E**, **F** and **G**) in order to keep the convection truncation error from exceeding the one of the viscous terms. For the viscous term **S** the second-order central difference approximation is also used. Notice that the elements of matrix M contain derivatives in ζ direction. For those terms with the form $\delta_\zeta(\alpha\delta_\zeta\beta)$ appeared in $\delta_\zeta(J^{-1}\boldsymbol{M}J)$, they are differenced as [32]

$$\delta_\zeta(\alpha\delta_\zeta\beta) = [(\alpha_{J,K,L+1} + \alpha_{J,K,L})(\beta_{J,K,L+1} - \beta_{J,K,L})$$

$$- (\alpha_{J,K,L} + \alpha_{J,K,L-1})(\beta_{J,K,L} - \beta_{J,K,L-1})]/[2(\Delta\zeta)^2] \tag{4.2}$$

The implicit dissipation operators $D_{I\xi}$, $D_{I\eta}$, $D_{I\zeta}$ and the explicit dissipation term D_E appear in Eq.(4.1) are results of the second-order symmetric TVD scheme [43,44]. These terms are artificially added in order to damp out the spurious oscillations that occur when dealing with flow discontinuities. They are

$$D_{I\xi} = -0.5\Delta\tau(\boldsymbol{\Omega}_{J+\frac{1}{2},K,L} - \boldsymbol{\Omega}_{J-\frac{1}{2},K,L})\epsilon_i$$

$$D_{I\eta} = -0.5\Delta\tau(\boldsymbol{\Omega}_{J,K+\frac{1}{2},L} - \boldsymbol{\Omega}_{J,K-\frac{1}{2},L})\epsilon_i$$

$$D_{I\zeta} = -0.5\Delta\tau(\boldsymbol{\Omega}_{J,K,L+\frac{1}{2}} - \boldsymbol{\Omega}_{J,K,L-\frac{1}{2}})\epsilon_i \tag{4.3}$$

$$D_E = -0.5\Delta\tau(\boldsymbol{T}_{J+\frac{1}{2}}\boldsymbol{\Phi}_{J+\frac{1}{2}} - \boldsymbol{T}_{J-\frac{1}{2}}\boldsymbol{\Phi}_{J-\frac{1}{2}} + \boldsymbol{T}_{K+\frac{1}{2}}\boldsymbol{\Phi}_{K+\frac{1}{2}}$$

$$- \boldsymbol{T}_{K-\frac{1}{2}}\boldsymbol{\Phi}_{K-\frac{1}{2}} + \boldsymbol{T}_{L+\frac{1}{2}}\boldsymbol{\Phi}_{L+\frac{1}{2}} - \boldsymbol{T}_{L-\frac{1}{2}}\boldsymbol{\Phi}_{L-\frac{1}{2}})\epsilon_e$$

where

$$\begin{aligned}
\boldsymbol{\Omega}_{J+\frac{1}{2},K,L} &= \mathrm{diag}[-\max\Psi(\lambda^m_{J+\frac{1}{2}})]\Delta_{J+\frac{1}{2}} \\
\boldsymbol{\Omega}_{J,K+\frac{1}{2},L} &= \mathrm{diag}[-\max\Psi(\lambda^m_{K+\frac{1}{2}})]\Delta_{K+\frac{1}{2}} \qquad (4.4) \\
\boldsymbol{\Omega}_{J,K,L+\frac{1}{2}} &= \mathrm{diag}[-\max\Psi(\lambda^m_{L+\frac{1}{2}})]\Delta_{L+\frac{1}{2}}
\end{aligned}$$

Here $\epsilon_i=1.5$ and $\epsilon_e=1$ are two constants which control the amount of added numerical dissipation. $\lambda_{J+½}{}^m$, $\lambda_{K+½}{}^m$ and $\lambda_{L+½}{}^m$ are the m^{th} eigenvalues ($m=1,5$) of the Jacobian matrices ***A***, ***B*** and ***C***, respectively. The subscripts J+½, K+½ and L+½ imply that the Jacobian matrices are evaluated as $\boldsymbol{q}_{J+½,K,L}$, $\boldsymbol{q}_{J,K+½,L}$ and $\boldsymbol{q}_{J,K,L+½}$, respectively. For example, $\boldsymbol{q}_{J+½,K,L}$ is a symmetric average of $\boldsymbol{q}_{J+1,K,L}$ and $\boldsymbol{q}_{J,K,L}$, i.e.,

$$\boldsymbol{q}_{J+\frac{1}{2},K,L} = \frac{1}{2}(\boldsymbol{q}_{J+1,K,L} + \boldsymbol{q}_{J,K,L}) \qquad (4.5)$$

$\Psi(\lambda)$ is an entropy correction function given by

$$\Psi(\lambda) = \begin{cases} |\lambda| & ,|\lambda| \geq \epsilon = 0.25 \\ (\epsilon^2 + \lambda^2)/2\epsilon & ,|\lambda| \leq \epsilon = 0.25 \end{cases}$$

and diag(z) denotes a 5×5 diagonal matrix with the diagonal elements equal to z. The operators $\Delta_{J+½}$, $\Delta_{K+½}$ and $\Delta_{L+½}$ are defined in the form, for example,

$$\Delta_{J+\frac{1}{2}}\boldsymbol{u} = \boldsymbol{u}_{J+1,K,L} - \boldsymbol{u}_{J,K,L}$$

The ***T***'s in Eq.(4.3) with the subscript J+½, K+½ and L+½ are the eigenvector matrices of Jacobian matrices ***A***, ***B*** and ***C***, respectively. The subscript ½ here has the same meaning as in Eq.(4.5). The Φ's in Eq.(4.3) are 5×1 vectors. For example, the m^{th} element of the vector $\Phi_{J+1/2}$ is

$$\Phi^m_{J+\frac{1}{2}} = \Psi(\lambda^m_{J+\frac{1}{2}})(g^m_J + g^m_{J+1} - 2\alpha^m_{J+\frac{1}{2}}) \tag{4.6}$$

where

$$g_J{}^m = S\ \max[0, \min(|\alpha^m_{J+\frac{1}{2}}|, S\alpha^m_{J-\frac{1}{2}})]$$

$$S = \mathrm{sign}(\alpha^m_{J+\frac{1}{2}})$$

$$\alpha_{J+\frac{1}{2}} = \boldsymbol{T}^{-1}_{J+\frac{1}{2}} \frac{q_{J+1,K,L} J_{J+1,K,L} - q_{J,K,L} J_{J,K,L}}{0.5(J_{J+1,K,L} + J_{J,K,L})}$$

The $\boldsymbol{T}^{-1}$'s are the inverse of corresponding eigenvector matrices. The explicit expression of these eigenvalues and eigenvector matrices can be found in Ref. 45.

Solution Method and Application

The thin-layer Navier-Stokes computation is a time-marching process which calculates the solution vector q^{n+1} along ξ, η and ζ directions at a given time τ from the solution q^n at a previous time step. The computation takes 17.2 Mwords of total memory of Cray Y-MP or Cray C-90 for the $110\times94\times60$ grid. The CPU time required for each 100 time steps is approximately 0.72 hours on Cray Y-MP and 0.37 hours on C-90, which translates into 4.2×10^{-5} and 2.14×10^{-5} seconds per time step, per grid point, respectively. In this section, a flow chart illustrating the time-marching process from the time step n to $n+1$ is first presented. Then a few algorithms which convert the solution vector to other useful flow parameters are described. Finally the evaluation of Jacobian J and the applicable size of time step $\Delta\tau$ are briefly discussed.

Algorithm and Flow Chart

Equation (4.1) shows the delta form of the factorized finite-difference formula for the thin-layer Navier-Stokes code. In application it is split into three block-tridiagonal systems in each spatial direction and is solved in the following sequence

$$L_\xi \Delta \boldsymbol{q}^{**} = \boldsymbol{R}^n \tag{4.7a}$$

$$L_\eta \Delta \boldsymbol{q}^{*} = \Delta \boldsymbol{q}^{**} \tag{4.7b}$$

$$L_\zeta \Delta \boldsymbol{q}^{n} = \Delta \boldsymbol{q}^{*} \tag{4.7c}$$

$$\boldsymbol{q}^{n+1} = \boldsymbol{q}^n + \Delta \boldsymbol{q}^n$$

where $\Delta\boldsymbol{q}^*$ and $\Delta\boldsymbol{q}^{**}$ are two intermediate solutions. A flow chart shown in Figure 4.1 presents the solution algorithm of the thin-layer Navier-Stokes code. A brief description of some subroutines in the main program is provided as follows.

BC	:Set up the boundary conditions described in Chapter III, i.e., the $\boldsymbol{q}$ vector at J=1 and JMAX, K=1 and KMAX, L=1 and LMAX.
VISRHS	:Evaluate the viscous right-hand-side $-Re^{-1}\delta_\zeta \boldsymbol{S}$.
RHS	:Evaluate the rest of the right-hand-side terms.

FILTRX :Fill in the elements of the block-tridiagonal matrix L_ξ.

BTRIX :Solve the block-tridiagonal system Eq.(4.7a).

FILTRY :Fill in the elements of the block-tridiagonal matrix L_η.

BTRIY :Solve the block-tridiagonal system Eq.(4.7b).

VISMAT :Evaluate the viscous term $-Re^{-1}\delta_\zeta(J^{-1}MJ)$ in L_ζ.

FILTRZ :Fill in the elements of the block-tridiagonal matrix L_ζ.

BTRIZ :Solve the block-tridiagonal system Eq.(4.7c).

For the vortical flow simulation, the solution process is divided into separated jobs with every job accounting for 50 time steps computation (i.e., NMAX=50 in Figure 4.1). In each job the thin-layer Navier-Stokes code reads in the grid data and restart data (solution vector $\boldsymbol{q}$ and the time τ at the end of previous job) at the head of the main program. To the end it writes out the restart output $\boldsymbol{q}$-file for the next restart. In the 50-time-step computation, the code computes the residual at each 10 time steps and records them. It also records the surface pressure coefficient *Cp* and the surface shear stress coefficients $\tau_{\zeta\xi}$, $\tau_{\zeta\eta}$ at every 5 time steps. A time history with a good resolution is especially important when we are interested in the transient flow development.

The Baldwin-Lomax turbulence model is employed in the code to evaluate the eddy viscosity, with an option to use either the original or a modified version by Degani and Schiff. In the modified Baldwin-Lomax turbulence model application, it is necessary to search for the quantities F_{max} and y_{max} in the circumferential direction from windward location. To eliminate the unwanted asymmetry in the current study, the searching is made to start from the windward symmetric plane ($\theta=0°$ or K=1) and end at the leeward symmetric plane ($\theta=180°$ or K=47) through both sides of the body.

Residual

The numerical algorithm used is a time-marching scheme. The steady-state solution is obtained as a time asymptotic solution of the unsteady Navier-Stokes equations. In this case we have $\Delta \boldsymbol{q}^n = 0$, or $\boldsymbol{R}^n = 0$ in Eq.(4.1). Therefore, the convergence criterion to the steady-state solution can be represented by the averaged L2 residual of the vector $\boldsymbol{R}^n$ over the internal nodes of the domain, i.e.,

$$\text{L2 residual} = \frac{1}{\Delta\tau}\left\{\frac{\sum_{\mathrm{J,K,L,M}} (\boldsymbol{R}^n_{\mathrm{J,K,L,M}})^2}{(\mathrm{JMAX}-2)(\mathrm{KMAX}-2)(\mathrm{LMAX}-2)}\right\}^{\frac{1}{2}} \tag{4.8}$$

where J=2, JMAX-1, K=2, KMAX-1, L=2, LMAX-1 and M=1, 5. In general the residual drops when the computed solution converges to a stable flow pattern. It is understood, however, the steady-state solution may not exist due to the inherent unsteadiness of the physical flow, for example, the vortex shedding phenomena.

Pressure and Shear Stress Coefficients

By the equation of state, we may have the pressure p and temperature T as well as their non-dimensional quantities p^* and T^* expressed as

$$p = (\gamma - 1)[E - \frac{1}{2}\rho(u^2 + v^2 + w^2)] \tag{2.5}$$

$$T = \frac{\gamma - 1}{R}[\frac{E}{\rho} - \frac{1}{2}(u^2 + v^2 + w^2)] \tag{2.6}$$

$$p^* = (\gamma - 1)[E^* - \frac{1}{2}\rho^*(u^{*2} + v^{*2} + w^{*2})] \tag{2.9}$$

$$T^* = \gamma(\gamma - 1)[\frac{E^*}{\rho^*} - \frac{1}{2}(u^{*2} + v^{*2} + w^{*2})] \tag{2.10}$$

The pressure coefficient *Cp* can be computed, according to its definition

$$Cp = \frac{p - p_\infty}{\frac{1}{2}\rho_\infty U_\infty^2} = \frac{p - p_\infty}{\frac{1}{2}\rho_\infty a_\infty^2}\frac{a_\infty^2}{U_\infty^2} = (\frac{p}{\rho_\infty a_\infty^2} - \frac{p_\infty}{\rho_\infty a_\infty^2})\frac{2}{M_\infty^2}$$

where $p/\rho_\infty a_\infty^2$ is the non-dimensional p^* shown in Eq.(2.9) and $p_\infty/\rho_\infty a_\infty^2 = \rho_\infty RT_\infty/\rho_\infty(\gamma RT_\infty) = 1/\gamma$. Accordingly,

$$Cp = \{\gamma(\gamma-1)[E^* - \frac{1}{2}\rho^*(u^{*2} + v^{*2} + w^{*2})] - 1\}\frac{2}{\gamma M_\infty^2} \tag{4.9}$$

To compute the shear stress components, for example,

$$\tau_{xy} = \mu(\frac{\partial u}{\partial y} + \frac{\partial v}{\partial x})$$

with its non-dimensional form as

$$\tau_{xy}^* = \mu^*(\frac{\partial u^*}{\partial y^*} + \frac{\partial v^*}{\partial x^*})\frac{1}{Re}$$

where $Re = \rho_\infty a_\infty L/\mu_\infty$, we have the shear stress coefficient

$$Cs = \frac{\tau_{xy}}{\frac{1}{2}\rho_\infty U_\infty^2} = \frac{\tau_{xy}^* \rho_\infty a_\infty^2}{\frac{1}{2}\rho_\infty U_\infty^2} = \tau_{xy}^* \frac{2}{M_\infty^2} = \mu^* \left(\frac{\partial u^*}{\partial y^*} + \frac{\partial v^*}{\partial x^*}\right)\frac{2}{M_\infty^2 Re} \tag{4.10}$$

On solid surface the non-dimensional viscosity coefficient μ^* consists of only laminar viscosity which can be computed by the Sutherland's law (Eq.(2.3))

$$\mu^* = \frac{\mu}{\mu_\infty} = \left(\frac{T}{T_\infty}\right)^{1.5}\left(\frac{T_\infty + S}{T+S}\right) = \left(\frac{T}{T_\infty}\right)^{1.5}\left(\frac{1+\frac{S}{T_\infty}}{\frac{T}{T_\infty}+\frac{S}{T_\infty}}\right) = T^{*\,1.5}\left(\frac{1+\frac{S}{T_\infty}}{T^* + \frac{S}{T_\infty}}\right) \tag{4.11}$$

where T^* is shown in Eq.(2.10) and S=198.6°R. The evaluation of velocity gradients can be made by the chain-rule, for example, $u_x = u_\xi \xi_x + u_\eta \eta_x + u_\zeta \zeta_x$. The velocity gradients u_ξ, u_η and u_ζ on the transformed domain are computed by second-order central difference formula at the interior points, and forward/backward difference formula at boundary points.

In order to transform the stress tensor in a Cartesian system to the one in curvilinear system, we have [30]

$$[\tau(\xi,\eta,\zeta)] = [A]^T\ [\tau(x,y,z)]\ [A] \tag{4.12}$$

where $[\tau]$ is the stress tensor and $[A]$ is a transformation matrix defined as

$$[\tau(\xi,\eta,\zeta)] = \begin{bmatrix} \tau_{\xi\xi} & \tau_{\xi\eta} & \tau_{\xi\zeta} \\ \tau_{\eta\xi} & \tau_{\eta\eta} & \tau_{\eta\zeta} \\ \tau_{\zeta\xi} & \tau_{\zeta\eta} & \tau_{\zeta\zeta} \end{bmatrix} \qquad [A] = \begin{bmatrix} a_\xi^x & a_\eta^x & a_\zeta^x \\ a_\xi^y & a_\eta^y & a_\zeta^y \\ a_\xi^z & a_\eta^z & a_\zeta^z \end{bmatrix}$$

Each individual matrix element can be expressed in terms of the metric coefficients, which represents the directional cosine of the corresponding axes. For example,

$$a^{x}_{\xi} = \frac{\hat{i}\cdot\hat{e}_{\xi}}{|\hat{i}|\,|\hat{e}_{\xi}|} = \frac{\xi_x}{\sqrt{\xi_x^2 + \xi_y^2 + \xi_z^2}} = \frac{x_{\xi}}{\sqrt{x_{\xi}^2 + y_{\xi}^2 + z_{\xi}^2}}$$

Therefore, the shear stress components $\tau_{\zeta\xi}$, $\tau_{\zeta\eta}$ and $\tau_{\zeta\zeta}$ can be expressed as

$$\tau_{\zeta\xi} = \frac{(a\xi_x + b\xi_y + c\xi_z)}{\sqrt{\xi_x^2 + \xi_y^2 + \xi_z^2}} = \frac{(ax_{\xi} + by_{\xi} + cz_{\xi})}{\sqrt{x_{\xi}^2 + y_{\xi}^2 + z_{\xi}^2}} \tag{4.13a}$$

$$\tau_{\zeta\eta} = \frac{(a\eta_x + b\eta_y + c\eta_z)}{\sqrt{\eta_x^2 + \eta_y^2 + \eta_z^2}} = \frac{(ax_{\eta} + by_{\eta} + cz_{\eta})}{\sqrt{x_{\eta}^2 + y_{\eta}^2 + z_{\eta}^2}} \tag{4.13b}$$

$$\tau_{\zeta\zeta} = \frac{(a\zeta_x + b\zeta_y + c\zeta_z)}{\sqrt{\zeta_x^2 + \zeta_y^2 + \zeta_z^2}} = \frac{(ax_{\zeta} + by_{\zeta} + cz_{\zeta})}{\sqrt{x_{\zeta}^2 + y_{\zeta}^2 + z_{\zeta}^2}} \tag{4.13c}$$

where

$$a = \frac{\tau_{xx}\zeta_x + \tau_{yx}\zeta_y + \tau_{zx}\zeta_z}{\sqrt{\zeta_x^2 + \zeta_y^2 + \zeta_z^2}} = \frac{\tau_{xx}x_{\zeta} + \tau_{yx}y_{\zeta} + \tau_{zx}z_{\zeta}}{\sqrt{x_{\zeta}^2 + y_{\zeta}^2 + z_{\zeta}^2}}$$

$$b = \frac{\tau_{xy}\zeta_x + \tau_{yy}\zeta_y + \tau_{zy}\zeta_z}{\sqrt{\zeta_x^2 + \zeta_y^2 + \zeta_z^2}} = \frac{\tau_{xy}x_{\zeta} + \tau_{yy}y_{\zeta} + \tau_{zy}z_{\zeta}}{\sqrt{x_{\zeta}^2 + y_{\zeta}^2 + z_{\zeta}^2}}$$

$$c = \frac{\tau_{xz}\zeta_x + \tau_{yz}\zeta_y + \tau_{zz}\zeta_z}{\sqrt{\zeta_x^2 + \zeta_y^2 + \zeta_z^2}} = \frac{\tau_{xz}x_{\zeta} + \tau_{yz}y_{\zeta} + \tau_{zz}z_{\zeta}}{\sqrt{x_{\zeta}^2 + y_{\zeta}^2 + z_{\zeta}^2}}$$

It should be noted that at the singular plane J=1, all derivatives with respect to the circumferential direction η are zero. It leads to that Eq.(4.13b) is indeterminate. Therefore the shear stresses at J=1 are not computed in the code.

The surface points with zero $\tau_{\zeta\eta}$ are defined as the crossflow separation points in a crossflow plane. For a given circumferential $\tau_{\zeta\eta}$ distribution, the zeros can be located by the bi-section method together with second-order Aitken interpolation and are used to identify the crossflow separation and attachment points. It is often misleading that the crossflow separation points are where the flow leaves the solid surface, i.e, three-dimensional flow separation. In fact the three-dimensional flow separation should be associated with the surface singular points on which both the longitudinal and circumferential shear stresses become zero.

Aerodynamic Force

The aerodynamic force vector acting on the projectile can be obtained by integrating surface pressure and shear stresses over projectile surface consisted of panels. Except for those panels between J=1 and 2 which are triangles, all other panels are quadrilaterals. Figure 4.2 shows a typical triangular panel and a quadrilateral panel. The forces due to pressure p and three shear stress components $\tau_{\zeta\xi}$, $\tau_{\zeta\eta}$ and $\tau_{\zeta\zeta}$ on each panel can be assumed to be the geometrically averaged pressure and shear stresses acting on the panel center multiplied by the panel area Ω, i.e.,

$$\bar{p} = \frac{1}{m}\sum_{i=1}^{m} p^{i}, \quad \bar{\tau}_{\zeta\xi} = \frac{1}{m}\sum_{i=1}^{m} \tau^{i}_{\zeta\xi}, \quad \bar{\tau}_{\zeta\eta} = \frac{1}{m}\sum_{i=1}^{m} \tau^{i}_{\zeta\eta}, \quad \bar{\tau}_{\zeta\zeta} = \frac{1}{m}\sum_{i=1}^{m} \tau^{i}_{\zeta\zeta}$$

where m=3 for triangular panel and m=4 for quadrilateral panel. With the (x,y,z)

coordinates of the surrounding nodal points given, it is easy to compute the unit vectors $\boldsymbol{n}_\xi$ and $\boldsymbol{n}_\eta$ pointing to the local ξ and η directions. Also $\boldsymbol{n}_\zeta=\boldsymbol{n}_\xi \times \boldsymbol{n}_\eta$ is the unit normal vector pointing outward from the panel surface. Then the resultant force vector can be expressed as

$$\boldsymbol{F} = \sum_{i=1}^{np} (-\bar{p}\boldsymbol{n}_\zeta + \bar{\tau}_{\zeta\xi}\boldsymbol{n}_\xi + \bar{\tau}_{\zeta\eta}\boldsymbol{n}_\eta + \bar{\tau}_{\zeta\zeta}\boldsymbol{n}_\zeta)\Omega_i = F_x\hat{i} + F_y\hat{j} + F_z\hat{k}$$

where Ω_i is the panel area and *np* is the total number of surface panels. Finally we can decompose the force components to get the lift, drag and side forces, i.e.,

$$\begin{aligned} \text{lift} &= F_z\cos(\alpha) - F_x\sin(\alpha) \\ \text{drag} &= F_z\sin(\alpha) + F_x\cos(\alpha) \\ \text{side force} &= F_y \end{aligned}$$

Mach Number

Due to the fact that all velocity components are normalized by free stream speed of sound a_∞, it is easy to compute the Mach number based on a_∞ as

$$\tilde{M} = \sqrt{u^2 + v^2 + w^2}$$

In order to get the local Mach number M based on the local speed of sound a, we need to correct it by the square root of temperature ratio, i.e.,

$$M = \tilde{M}\frac{a_\infty}{a} = \tilde{M}\sqrt{\frac{T_\infty}{T}}$$

where T is the local temperature.

Vorticity

Vorticity of a velocity field V is defined as

$$\bar{\omega} = \nabla \times V = \begin{vmatrix} \hat{i} & \hat{j} & \hat{k} \\ \dfrac{\partial}{\partial x} & \dfrac{\partial}{\partial y} & \dfrac{\partial}{\partial z} \\ u & v & w \end{vmatrix} = \omega_x \hat{i} + \omega_y \hat{j} + \omega_z \hat{k}$$

where

$$\omega_x = \frac{\partial w}{\partial y} - \frac{\partial v}{\partial z}, \quad \omega_y = \frac{\partial u}{\partial z} - \frac{\partial w}{\partial x}, \quad \omega_z = \frac{\partial v}{\partial x} - \frac{\partial u}{\partial y}$$

The magnitude of vorticity then is

$$|\bar{\omega}| = \sqrt{\omega_x^2 + \omega_y^2 + \omega_z^2}$$

Streamtraces and Skin-Friction Lines

It is often useful to have the streamline plot to study the flow topology. For unsteady flow problem, there exists only instantaneous streamline, or the streamtrace. Keep in mind that those lines are different from the steady-state streamlines or particle traces.

The basic idea to generate a streamtrace is to move a massless particle through a series of small steps in the direction tangential to the local vector field, either two or three-dimensional [46]. A predictor-corrector integration algorithm is used for the calculation of streamtraces. At each intermediate step the local velocity vector can be obtained by a linear interpolation from the surrounding nodal vectors. The step size is controlled which typically results in 10 to 20 integration steps through each grid cell, depending on the grid density in the domain interested. The starting point is selected interactively by try-and-error such that we may have the best interpretation of the flow structure. By reversing the velocity vector we can have a backward streamtrace.

There are several occasions that the streamtraces could be terminated. The first one is when the streamtrace hits the preset maximum number of integration steps. We can increase the number of maximum steps to avoid the situation. The second one is when the streamtrace goes into a stable limiting cycle and terminates there, no matter how large the number of integration step is. The third one is when the streamtrace moves outside the domain boundary, in which it cannot obtain the interpolated velocity vector and is terminated on the boundary. This is often seen near the solid boundary for a simulated viscous flowfield. Theoretically the velocity vector very next to a non-permeable wall should be tangent to the local surface. In a numerical computation, however, a slightly inward velocity component normal to the surface could be developed through numerical interpolation or integration which terminates the streamtrace on solid boundary.

On the solid surface where velocity vanishes, streamtraces can be represented by the surface skin-friction lines which are lines tangent to the two-dimensional surface shear stress vector field. By a proper selection of starting points, the surface flow topology can be clearly presented.

Evaluation of the Jacobian J

The Jacobian is evaluated according to Eq.(2.15a) in which the spatial derivatives x_ξ etc. are computed by second-order central difference formula at interior nodes and forward/backward difference formula on boundaries. It is noticed that the Jacobian at the singular plane J=1 is computed by an linear extrapolation from the Jacobian at J=2 and J=3.

Integration Time Step $\Delta\tau$

In the time marching process, a time spacing $\Delta\tau$ is used where τ is the non-dimensional time defined in Chapter II. If we consider one caliber as the length of 2.25 inches for the projectile cylindrical diameter and the speed of sound as 1085 *ft/s* (at sea level and T_0=580°R), one unit of τ is approximately equal to 1.73×10^{-4} seconds in real time. To reduce the cost of computation resources, it is desired to speed up the time-marching process as fast as possible. Although the linear analysis shows that the numerical scheme is unconditionally stable, the nonlinear equations are subject to a time-step limitation. In general $\Delta\tau$ must be smaller when the flowfield is subject to a rapid transition, for example, higher speed or higher angle-of-attack flow. A most-often-seen error suffered from a larger $\Delta\tau$ is that the computed total energy E turns out to be less than the amount of dynamic energy such that the internal energy e is negative. The temperature then is negative so the evaluation of the laminar viscosity (Eq.(2.3) or (4.11)) causes a mathematical error (negative square root). To avoid such difficulties, the maximum $\Delta\tau$ allowed is in the order of 10^{-3}.

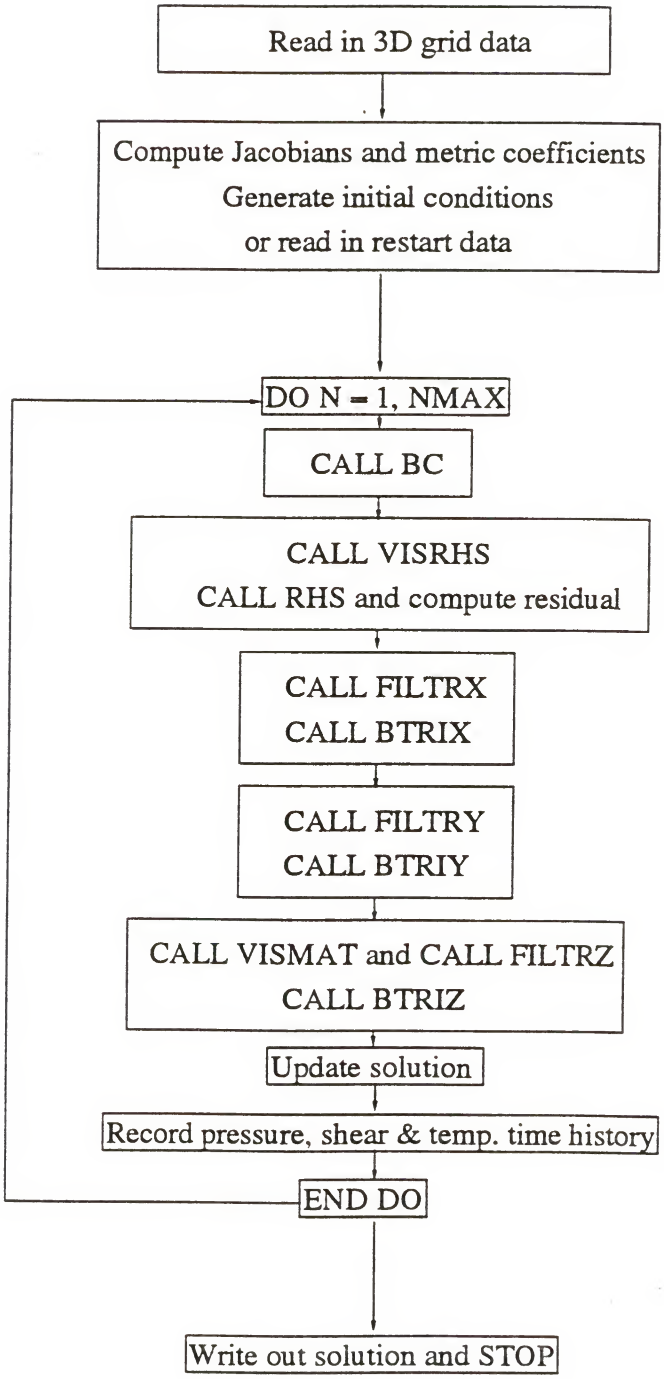
Read in 3D grid data
Compute Jacobians and metric coefficients
Generate initial conditions
or read in restart data
DO N = 1, NMAX
CALL BC
CALL VISRHS
CALL RHS and compute residual
CALL FILTRX
CALL BTRIX
CALL FILTRY
CALL BTRIY
CALL VISMAT and CALL FILTRZ
CALL BTRIZ
Update solution
Record pressure, shear & temp. time history
END DO
Write out solution and STOP

Figure 4.1 Flow chart of thin-layer Navier-Stokes code.

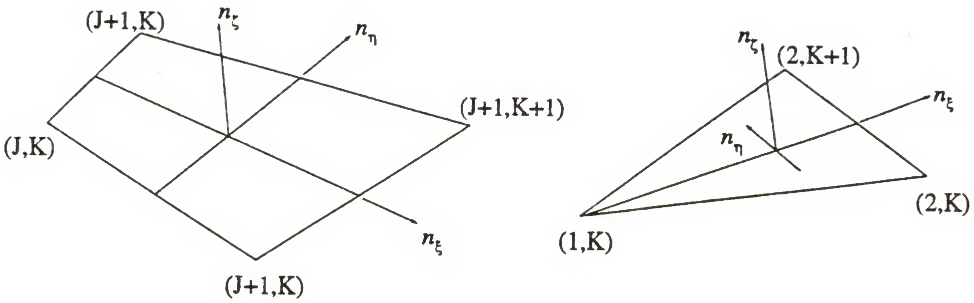

Figure 4.2 Quadrilateral and triangular panels used to computed aerodynamic forces.

CHAPTER V
EFFECTS OF TURBULENCE MODELS

The evolution of projectile vortical flow based on the original Baldwin-Lomax turbulence model for JMAX=110 grid has been simulated to $\tau=14.475$ with $\Delta\tau \cong 10^{-3}$ (Case A). The flow problem has also been solved by the modified Baldwin-Lomax model with JMAX=110 grid for $\tau \leq 6.8$, and with JMAX=131 grid for $5.0 \leq \tau \leq 11.1$ (Case B). Accordingly, a tremendous amount of three-dimensional, time-dependent flowfield data has been generated for analysis. It is understood in literature that the modified model can give acceptably accurate surface pressure distribution for subsonic and supersonic vortical problems, especially in the secondary flow region [15,47]. In this chapter, quantitative implications of both turbulence models are explored and discussed. The impact of strong diffusive process of the original model upon the flow solution on the solid surface as well as in the wake region is investigated. The effect of cut-off distance to the computed eddy viscosity distribution in the modified model is also examined through a series of numerical experiments.

It should be mentioned that the flow pattern remains symmetric with respect to the angle-of-attack plane except for the very downstream region on sting with $x \geq 10$. Therefore only half-of-the-domain results are presented throughout most of the chapter. When referring to a longitudinal J location, the JMAX=110 grid in Figure 3.3 is used, unless otherwise mentioned. All flow quantities presented are non-dimensionalized as defined in Chapter II except when the dimensional units are explicitly shown.

Impacts of Excessive Eddy Viscosity

On the Crossflow Plane J=54

Results simulated at $\tau=9.325$ for the J=54 cross-section (near the middle of the cylinder at $x=4.042$) by both turbulence models are first selected to illustrate the effects of excessive eddy viscosity in Case A. The crossflow vortex pattern is found to be in steady state for both cases. Figure 5.1 shows the eddy viscosity contour in the (y,z) plane (rear view of the projectile). Apparently the original Baldwin-Lomax model has resulted in a much larger amount of eddy viscosity in the order of $10^2 \sim 10^3$, compared to the near-zero values of modified model solution in the separated region. Figure 5.2 shows the corresponding instantaneous streamtraces in a crossflow plane. A streamtrace is a line tangent to the velocity vector. Here only the Cartesian velocity components v and w are used to generate the streamtraces. Since the streamtraces are constructed by using small-step integrations over the velocity field, a small change of transverse velocity component can cause a considerable deviation to the resulting plot. Taking Figure 5.2 for example where the v-component in y-direction is nearly zero on the leeward symmetric plane $\theta=180°$. Even the starting points of streamtraces are completely symmetric, a small disturbance in the v-component during the spatial integration has caused the streamtrace to move significantly to one side of the symmetric plane as shown. It should be emphasized that such asymmetry in a streamtraces plot does not necessarily represent a significant quantitative difference. In Figure 5.2 we can clearly see that the primary vortices are about the same for both cases, while the secondary separations are formed close to the leeward side surface only for Case B. This complies with the results obtained by Degani and Schiff [15] that the excessive computed eddy viscosity predicted by original Baldwin-Lomax model can suppress the onset of secondary separation. Figure 5.3 and 5.4 show the vorticity magnitude and $F(y)$ (Eq.(2.23)) contours. Away from secondary flow regions, the excessive eddy viscosity of Case A as shown in Figure 5.1 seems to have little effect upon general characteristics of the function $F(y)$ as well as vorticity distributions outside the thin-layer region. Figure 5.5 and 5.6 show the Mach number and Cp contours. Only minor shifts of the contour lines are observed except near the secondary separation regions. Although the flow is found supersonic before the primary separation point in both Mach contour plots, the sonic line ($M=1$) close to surface associated with the decelerated flow from $M>1$ to $M<1$ is almost parallel to the local flow direction. An enlarged portion of Mach contour for Case B with identified thick streamtraces is shown in Figure 5.5 for illustration. Accordingly the velocity component normal to the sonic line $M=1$ is subsonic rather than supersonic, which means no shock wave is detected in the computed solution. In fact the sonic line in Figure 5.5 looks very similar to the slip line observed in a supersonic boundary layer flow which sits in between the free stream supersonic flow and the subsonic boundary layer flow.

It is clear from Figure 5.1 to 5.6 that the use of a physical (y,z) plane fails to bring out quantitatively the secondary flow phenomena close to the projectile surface. With highly-stretched grid lines near the body, a transformed (K,L) plane, on the other hand, can clearly provide important flow characteristics in the thin layer. Figure 5.7 to 5.12 show the corresponding field plots in the (K,L) plane, compared to Figure 5.1 through 5.6. Only one-half of the cross-section is presented since the flow is symmetric with respect to the angle-of-attack plane. Here K=1 and K=47 represents, respectively, the circumferential location $\theta=0°$(windward symmetric plane) and $\theta=180°$(leeward symmetric plane), while the ordinate L is a node along an exponentially stretched line from the surface. The normal distance at node L, y_L measured in caliber from the solid surface (the same y used in the Baldwin-Lomax turbulence model described in Chapter II) at J=54 is listed in Table 5.1 for reference. The difference of eddy viscosity near the surface (e.g., $L \leq 30$) in both cases is now clearly presented in the stretched (K,L) plane as shown in Figure 5.7. The existence of secondary flow region in case B is clearly visible in Figure 5.8. The secondary flow separates at about K=35 ($\theta=144°$) and reattaches at K=28 ($\theta=123°$), with a size about 0.183 calibers in span and 0.009 calibers in height (L=23). From the streamtraces plot we can easily verify the crossflow topology summation rule by considering the entire cross-section, i.e., K=1 to 93. For example in Case B of Figure 5.8, there is one saddle point (*S*) near (K,L)=(47,46), 4 nodal points (*N*) at two primary and two secondary vortex centers (two in the other corresponding half are not shown), and 8 half-saddle points (*S'*) corresponding to the crossflow separation/attachment locations on the solid surface at K=1, 18, 28, 35, 47,

Table 5.1 Normal distance y_L at node L at J=54

L	y_L	L	y_L	L	y_L	L	y_L
1	0	16	1.970×10^{-3}	31	4.995×10^{-2}	46	1.218×10^{0}
2	2.000×10^{-5}	17	2.457×10^{-3}	32	6.182×10^{-2}	47	1.505×10^{0}
3	4.474×10^{-5}	18	3.060×10^{-3}	33	7.650×10^{-2}	48	1.858×10^{0}
4	7.536×10^{-5}	19	3.805×10^{-3}	34	9.467×10^{-2}	49	2.294×10^{0}
5	1.132×10^{-4}	20	4.729×10^{-3}	35	1.172×10^{-1}	50	2.830×10^{0}
6	1.601×10^{-4}	21	5.870×10^{-3}	36	1.450×10^{-1}	51	3.490×10^{0}
7	2.181×10^{-4}	22	7.282×10^{-3}	37	1.794×10^{-1}	52	4.303×10^{0}
8	2.898×10^{-4}	23	9.030×10^{-3}	38	2.219×10^{-1}	53	5.304×10^{0}
9	3.786×10^{-4}	24	1.119×10^{-2}	39	2.746×10^{-1}	54	6.535×10^{0}
10	4.884×10^{-4}	25	1.387×10^{-2}	40	3.398×10^{-1}	55	8.048×10^{0}
11	6.242×10^{-4}	26	1.718×10^{-2}	41	4.204×10^{-1}	56	9.905×10^{0}
12	7.923×10^{-4}	27	2.127×10^{-2}	42	5.201×10^{-1}	57	1.218×10^{1}
13	1.000×10^{-3}	28	2.634×10^{-2}	43	6.435×10^{-1}	58	1.496×10^{1}
14	1.258×10^{-3}	29	3.260×10^{-2}	44	7.961×10^{-1}	59	1.837×10^{1}
15	1.576×10^{-3}	30	4.036×10^{-2}	45	9.847×10^{-1}	60	2.402×10^{1}

59, 66 and 76 (K=59, 66 and 76 are not shown). The number of critical points satisfies the summation rule Eq.(1.2) such that $4+\frac{1}{2}(0)-1-\frac{1}{2}(8)=-1$.

In Figure 5.9 we notice a vorticity feeding line in both cases that emanates from the primary separation point near K=18 and ends near the primary vortex center. Unlike an attached boundary layer within which the vorticity magnitude rapidly drops to almost zero near the edge, here the vorticity feeding line away from the surface has created a small bump of vorticity in the wake region along L-direction. This bump, combined with the effect of a large distance y from the surface, directly results in a ridge of $F(y)$ along the feeding line as shown in Figure 5.10. For the original Baldwin-Lomax turbulence model application the code picks up the peak F_{max} and corresponding y_{max} on each L-line, thus producing the excessive eddy viscosity distribution shown in Case A of Figure 5.7. The modified model in Case B chooses the first peak close to the edge of boundary layer and results in a much smaller eddy viscosity magnitude, especially near the secondary flow region shown in Case B of Figure 5.7. In Figure 5.11 the reduced eddy viscosity does produce shifts in some Mach contour lines in the secondary flow region. Also the Mach number near primary vortex core in case B seems to have a smaller value. In Figure 5.12, a slightly broader range of high pressure area ($Cp \geq -0.7$) near the leeward side surface is observed from K=23 to 32, which is apparently associated with the secondary flow separation around K=35. In general the large eddy viscosity has a negligible effect for large L (or y_L) outside the thin-layer region.

On the Surface Flow Properties

In addition to the cross-sectional view, surface flow patterns are also used to illustrate the turbulence models effects. Figure 5.13 and 5.14 show the surface skin-friction lines and corresponding pressure/temperature contours at $\tau=9.325$. These are side views of the projectile model covering the circumferential domain from 0° to 180°. We can observe distinctly developed primary and secondary separation lines as well as a secondary attachment line for Case B, as opposed to a much simpler skin-friction lines pattern in Case A. Note that the starting points for skin-friction lines are selected by try-

and-error in order to obtain a proper interpretation to the surface flow topology. It should be mentioned in passing that the density of skin-friction lines shown in this study does not possess any quantitative meaning. A further investigation of the solution at a later time shows that the results at $\tau=9.325$ are approaching a steady-state solution upon most of the surface for $x \leq 10$, except for a small portion near the cylinder-boattail juncture in the leeward separated region.

Again, for convenience of analysis, skin-friction lines are plotted on a stretched surface (x,θ) which is obtained by unwrapping the circumferential domain to a uniform span for all longitudinal locations. Recall that the ogive-cylinder, cylinder-boattail, and boattail-sting junctures are located at $x=3.017$, 5.0 and 7.82. In Figure 5.15 the primary separation line sits approximately on the same circumferential location in both cases, ranging from over 110 degrees on the ogive section to less than 90 degrees on boattail. In contrast to Case B, secondary separation and attachment lines in Case A are only observed near the $x \geq 10$ region on sting. In Case B we also see a separated region in the longitudinal x-direction in addition to the usually observed crossflow separation in θ-direction. It covers approximately from $x=4.8$ (longitudinal primary separation) to 5.5 (longitudinal primary attachment) and from $\theta=90°$ to $110°$. Details of the longitudinal separated flow are discussed in a later section. The existence of such an axially reverse flow in Case B indicates that the over-predicted eddy viscosity in Case A does produce a strong turbulent mixing to suppress the flow separation, although a 7° downslope boattail is indeed prone to form a longitudinally reverse flow. For Case B in Figure 5.15, a nodal point attracting neighboring skin-friction lines is found near $(x,\theta)=(4.8,$

90°) which is related to the longitudinal primary separation line mentioned above. Accordingly, a saddle point connecting the longitudinal primary attachment line is located near $(x,\theta)=(5.3,\ 80°)$ to balance the surface flow topology. One more point of interest observed in Figure 5.15 is the off-centering of primary attachment line (near $\theta=180°$) after $x=8.5$, which indicates a loss of symmetry with respect to the angle-of-attack plane. This can be noticed in both cases, implying the vortical flow simulation implemented with the original Baldwin-Lomax turbulence model can also trigger vortex asymmetry regardless of the excessive eddy viscosity it predicted.

Figure 5.16 and 17 show the corresponding surface *Cp* and temperature contours at $\tau=9.325$, with a few selected streamtraces added for reference. On the windward side before the primary separation, pressure in both cases drops rapidly, due to the accelerated flow in a circumferential direction and reaches a minimum value right before the primary separation line. In the separated region, a pressure rise is observed in Case B on seeing the secondary attachment line. Situated between the primary attachment (near $\theta=180°$) and secondary attachment lines is another small pressure trough that appears right before the secondary separation. Although the skin-friction lines pattern in Case A does not show a secondary flow structure over the projectile mainbody, computed surface pressure contour turns out to be very comparable to the one in Case B. The surface temperature distribution, on the other hand, is more correlated to the skin-friction lines pattern, as shown in Figure 5.17. Primary separation lines sit right on top of the temperature ridge in both cases. In general the modified Baldwin-Lomax turbulence model gives a higher surface temperature over the separated region by a range of 20° to 80°R, especially on the ogive and cylinder.

The circumferential surface *Cp* distributions at τ=9.325 for both turbulence model computations are presented in Figure 5.18 for quantitative comparisons. Solid lines represent results of the modified model (Case B) and circles are for the original model (Case A). Since the computed solution becomes slightly asymmetric after x=6, only cross-sections up to J=77 (x= 5.521) are selected for presentation. Other chosen J's are J=10 (x=0.554), J=20 (x=1.555), J=35 (x=3.017), J=54 (x=4.042) and J=68 (x=5.0). In general the modified Baldwin-Lomax turbulence model only yields a slightly more pressure back up in the secondary separation region, indicating that the generated secondary vortices may be too weak to make significant pressure changes. A larger deviation of circumferential *Cp* is shown at J=68 and 77, which is apparently caused by the rather complex flow pattern in the separated region observed in Case B (Figure 5.15).

Effects of excessive eddy viscosity in Case A are also observed at earlier times during the vortical flow developing stage. Figure 5.19 to 21 show the surface skin-friction lines, *Cp* and temperature contours at τ=2.0. The primary separation is located further to the leeward side compared to the one at τ=9.325. The secondary flow exists in Case A, even a tertiary vortex structure is found on boattail in Case B. Unlike the solutions at τ=9.325, *Cp* and temperature contours at τ=2.0 show large disparity between two cases due to very different surface flow patterns. Figure 5.22 to 24 present the same field plots at τ=6.8. The flow pattern now resembles more to the τ=9.325 case, except for a difference in the longitudinal flow separation near cylinder-boattail juncture in the crossflow separated region. Locally the flow seems to be still in transition where only a smaller reverse flow area in x-direction is observed.

Time history of non-dimensional forces acting on the projectile model is computed and presented. Lift, drag and side forces resulting from both the pressure and viscous shear forces are shown in Figure 5.25(a). Dash and solid lines represent original Baldwin-Lomax turbulence model (Case A) and modified model (Case B) results, respectively. The tiny circles on solid lines after τ=5.0 indicate that the solution is obtained by using JMAX=131 grid with an extrapolated downstream boundary condition as discussed in Chapter IV. Due to the incorrect simulation near the end of sting by previously fixing a downstream boundary pressure in Case A as well as in Case B for $\tau \leq 6.8$ with JMAX=110 grid, the forces presented are only computed up to half of sting at x=11.88 (J=106 in JMAX=110 grid, or J=115 for JMAX=131 grid). In Figure 5.25(a) only little difference can be seen regarding the lift and drag forces, especially when they converge at a larger time. Drag forces are considerably large at such high speed and high angle of attack. The asymmetric vortex shedding on sting has caused fluctuating side forces as shown for both turbulence models, despite of certain phase shift is observed. The oscillations are around a zero mean, with an amplitudes of only 4% to 5% of the lift forces. The modified model seems to give a smaller non-dimensional period of 1.9 rather than 2.2 from the original model, or in terms of the Strouhal number as 0.152 for the original model and 0.176 for the modified model. The Strouhal number is defined as fd/V_∞, where f, d and V_∞ are the dimensional frequency, diameter and free stream velocity, respectively. As mentioned in Chapter I the Strouhal number for an inclined cylinder flow can be evaluated as 0.21sin(α) which gives the value of 0.182 for α=60°. Notice that the classical Strouhal number of 0.21 is based on the measurements performed by Roshko [19,31]. Apparently the modified Baldwin-Lomax model has predicted a more comparable shedding frequency. Figure 5.25(b) shows the force history due to viscous skin-friction only. They consist of barely 1% of total forces in terms of the magnitude, causing little change to the overall lift and drag forces.

On the Development of Crossflow Separation

As mentioned previously in Chapter IV that the crossflow separation or attachment points on the solid surface are defined with their circumferential shear stress component $\tau_{\xi\eta}$ as zero. In Figure 5.26 the time history of crossflow separation and attachment points are presented at six selected J cross-sections. The horizontal axis has a non-dimensional time τ ranging from 0 to 2 for earlier flow development. The vertical axis covers a circumferential domain from 60° to 300°, with the absence of the windward attachment point near the symmetric plane $\theta=0°$. Hollow circles are used to represent the original model computation Case A, while solid dotted lines stand for the modified model computation Case B. Local diameters for J=10, 20, 54, 84, 95, 106 are 0.261, 0.641, 1.0, 0.737, 0.32 and 0.32, respectively. Figure 5.26 shows that the primary separation initiates at the leeward symmetric plane $\theta=180°$. The primary separation points immediately move upstream on either side to allow the primary vortex recirculation region to form behind the body. The onset of primary separation is found to be dependent on the local diameter. For a smaller cross-section, the time required is less. With the primary vortices further developing and moving away from the surface, the secondary separations and attachments are initiated. In general the secondary separation region in Case B covers a larger circumferential span than it does in Case A, which appropriately reflects the effect of modified Baldwin-Lomax turbulence model. The secondary flows in Case B expand in size as time grows; accordingly, pushing the primary separation points further upstream in the circumferential direction. For a smaller cross-section near the sting, development of tertiary separations in Case B is clearly visible, for example, $0.8 \leq \tau \leq 1.2$ at J=95. It is interesting to observe a temporary vanishing of secondary flow regions in Case B at J=95 and 106, bringing the primary separation points slightly back toward the $\theta = 180°$ plane. The secondary flow regions re-appear after a short period of time with the primary separation points moving back to their previous upstream locations. Figure 5.27 shows the time history of crossflow separation/attachment development we have simulated for the above J cross-sections. The modified model Case B has resulted in larger and more sustained crossflow secondary flows due to less amount of eddy viscosity. At J=106 both models predict alternating vortex shedding, regardless of the much larger eddy viscosity magnitude in Case A. The vortex shedding phenomena are further discussed in the next chapter.

In Figure 5.28 the onset time for crossflow separation is given as a function of the cross-sectional diameter. Since different cross-sections on the ogive and boattail-sting may have identical diameters, solid geometrical symbols and thick lines are used to highlight the locations on boattail and sting. Evidently we can see a linear behavior of the onset time to the local diameter. All symbols lie on the same line for the primary separation, regardless of different locations on projectile or different turbulence models.

As a matter of fact the modified model does not play a role until the primary separation is formed, therefore the onset time for primary separation is not affected. In Figure 5.28 the modified model shows an earlier onset of secondary separation on the ogive and cylinder (large hollow squares) than the original model does (large hollow triangles). On boattail and sting (small solid squares and triangles), on the other hand, the difference seems to be limited, which implies that the onset of secondary separation is also affected by the local geometry and flow characteristics as well as by the turbulence models. Notice that some of original model results for the onset of secondary separation (large hollow and small solid triangles) are isolated with dotted lines for τ near 1 and up. Due to the relatively large $\Delta\tau$ we have used in the original model computation within that time span, the results inside the dotted-line region might have possessed larger truncation errors.

With the help of time history plots shown in Figure 5.26 and 27 we can easily visualize the impact of excessive eddy viscosity on the crossflow topology at any instant time. For example, Figure 5.29 and 30 show the streamtraces by two different turbulence models at J=54 cross-section. In Figure 5.29 streamtraces are plotted at τ=2.0 during the vortical flow development. The primary separation points in Case B are observed at slightly upstream locations than those found in Case A. The primary vortex structure is larger, with secondary separation regions clearly visible near the surface. In Figure 5.30 the crossflow structure becomes nearly steady at τ=6.8, in comparison to the streamtraces at τ=9.325 in Figure 5.2. Again the primary vortices are about the same in both cases, and the secondary flows can be only seen in Case B due to the less amount of eddy viscosity. It seems that the effects of turbulence models upon the primary vortex structure (location of primary separation and size of primary vortex) are more significant in the flow developing stage. Figure 5.31 shows the streamtraces for the cross-section J=106 on sting at an earlier time (τ=0.4) before the secondary separation occurs. As expected the primary vortical flow structure in Case B is slightly larger. Figure 5.32 shows the streamtraces at τ=0.9. Unlike in Case A where simple secondary flow regions are observed, the instantaneous streamtraces in Case B exhibit a more complex crossflow structure. Figure 5.33(a) shows the enlarged secondary flow structure for Case B at J=106 and τ=0.9. Within the crossflow plane there are 6 nodal points (*N*), 3 saddle points (*S*), 8 half-saddle points (*S*') but no half-nodes (*N*'). Note that a half-saddle point on the windward symmetric surface is not shown in either Figure 5.32 or 5.33(a). Also in Figure 5.33(a) only half the domain is presented due to symmetry. A pair of nodes and a saddle point associated with the primary vortex structure that are not shown in the enlarged Figure 5.33(a) can be located in Figure 5.32. Substituting the numbers of critical points into Eq.(1.2) we obtain $6+\frac{1}{2}(0)-3-\frac{1}{2}(8)=-1$ which satisfies the crossflow summation rule. Referring to Figure 5.26 for the crossflow separation time history, however, we can deduce that the crossflow topology should consist of a tertiary flow region inside the secondary flow near the surface, which is not seen in Figure 5.33(a). The streamtraces are redrawn in one half of the stretched (K,L) plane and the tertiary separation region is clearly identified in Figure 5.33(b). We now have 8 nodal points, 7 saddle points, 8 half-saddle points and 4 half-nodal points. Again critical points on the other symmetric half and the half-saddle at K=1 are not shown. Although the number of critical points are different, the summation rule states $8+\frac{1}{2}(4)-7-\frac{1}{2}(8)=-1$ which is still satisfied. In addition to the discrepancy found in the number of critical points, the two vortices near the surface in the (y,z) plane Figure 5.33(a) are found to be unstable spiral nodes. In the (K,L) plane of Figure 5.33(b), however, they are apparently stable. It is mentioned in Chapter IV that the streamtraces are obtained through a series of numerical interpolation and integration in the vector field. An equally-spaced (K,L) domain in general is believed to yield a more accurate streamtraces distribution than a physical (y,z) domain does in a numerical point of view when discrepancies arise.

Implication of the Cut-off Constant

The cut-off constant c in Eq. (2.24) determines an appropriate length scale across the turbulent boundary layer in the modified Baldwin-Lomax turbulence model to reject excessive eddy viscosity in the separated region. The resulting eddy viscosity distribution based on a given cut-off constant is found to be very dependent on the local solution profile and grid characteristics. Degani and Schiff [15] first proposed $c=1.5$ for their supersonic flow case ($M=1.8\sim3.0$, $\alpha=6.3°\sim22.75°$, $\Delta\theta=2.5°\sim5°$) to match measured pressure distribution and surface flow direction. After that, the modification has been used in a number of applications, yet no explicit values of cut-off constant were reported in the literature. In general the cut-off distance must be at least large enough to accommodate the boundary layer thickness on the leeward side. If the cut-off distance is too small, on the other hand, the length scale y_{max} is limited within part of the turbulent boundary layer and the resulting eddy viscosity could become too low. As a consequence the leeward suction peak generated by the vortical flow structure is over-predicted [47]. In this section the author wishes to examine how the amount of cut-off constant can affect the resulting eddy viscosity distribution. The computed solutions based on $c=5$ are provided to obtain corresponding eddy viscosity contours for various cut-off constants, according to the modified formulation suggested by Degani and Schiff.

The effect of cut-off constant can be demonstrated by the following numerical experiment. Based on the simulated flowfield at J=54 and $\tau=9.325$ from Case B, a number of constant c's are selected to compute the corresponding eddy viscosity coefficient. Figure 5.34 shows the eddy viscosity contours on a partial (K,L) domain with small circles representing the location of chosen F_{max} (i.e., y_{max}). Refer to Figure 5.10 for the corresponding $F(y)$ contour plot. Recall that if the peak value F_{max} is not found within the cut-off distance, values of F_{max} and y_{max} at a given K-plane are assumed to be the same from the previous circumferential K-location. In Figure 5.34 we use shaded circles to represent such locations. The primary and secondary separations S_1, S_2, and the secondary attachment A_2 are also shown in each plot on the horizontal axis for reference. Streamtraces pattern for this case can be referred to Figure 5.8. It is understood that flow inside the thin layer has a direction from attachment points A_i to separation points S_i, where $i=1$ or 2. In Figure 5.34 the predicted eddy viscosity magnitude is found to be strongly dependent on the location of chosen F_{max} and y_{max}. In "upstream" flow regions before S_1 ($1 \leq K \leq 18$) and S_2 ($36 \leq K \leq 47$), the computed eddy viscosity contours are identical for different cut-off constants. The eddy viscosity magnitude "behind" the separation points S_1 and S_2 grows rapidly as the constant c increases. The terms "upstream" and "behind" used here are relative to the local flow direction in the thin layer. For example, a "upstream" region of S_1 and S_2 are located in the negative and positive K-direction, respectively. When c is greater than 6, the cut-off distance simply does not play any role in finding the peak values F_{max} and y_{max} (no shaded circles are present). It is evident that a smaller value of c (2.0 or 2.5) is effective in reducing large amount of eddy viscosity between S_1 and S_2. When c advances from 2.5 to 3.0, the predicted eddy viscosity magnitude "behind" S_1 jumps up 1 to 2 orders and then remains constant thereafter. The eddy viscosity magnitude behind S_2, on the other hand, does not change by switching c from 2.5 to 3.0, but picks up slowly and steadily with increasing c's. In Figure 5.10 (the $F(y)$ contour) it is noticed that the peak value of $F(y)$ for Case B is elevated off the surface significantly from K=19 to 24 behind primary separation S_1, with corresponding L indices as 22, 23, 26, 28, 29 and 31. In Degani and Schiff's modification the cut-off distance on current K-plane is set to be the constant c multiplied by the chosen y_{max} from the previous K-plane. Notice that F_{max} and y_{max} at K=18 are located at L=18. For a smaller c such as 2.5 the cut-off distance at K=19 has a value of $2.5 \times y_{18}$ (y at L=18) which confines the search of F_{max} within L=21. Therefore the peak $F(y)$ at L=22 is not reached and therefore we have a shaded circle at K=19. Apparently the F_{max}'s at K=20 to 24 all fall out of the cut-off distance that assumes the value from previous K in a similar situation and the circles are shaded. With a slight increase of c to 3.0, the peak $F(y)$ at K=19 is reached at L=22. The cut-off distance at K=20 then has a value of $3.0\times y_{22}$ within which the peak $F(y)$ at L=23 can be easily found. The effective cut-off distance grows rapidly on subsequent K-planes due to an increasing chosen y_{max}, which results in a jump up of eddy viscosity distribution shown in Figure 5.34. In the region "behind" secondary separation, however, the cut-off distance is limited to a relatively small value from previous K-plane. For example, K=24 to 31 in $c=5.0$ case. In fact, the shaded circles after K=27 for various c's are all caused by a local peak $F(y)$ with the approximate value of 0.14 around K=25 to 27 (Figure 5.10). At K=27, y_{max} has a value of 0.00473 located at L=20. With the cut-off constant $c=5$ the search of F_{max} at K=28 is limited within $y_{cut\text{-}off}=5\times0.00473=0.02365$ which is greater than y_{27} but smaller than y_{28}. Although in Figure 5.10 the first peak of $F(y)$ at K=28 seems to be located at L=26, $F(y)$ at L=27 did not drop more than 10% from the local peak value at L=26. Therefore y_{max} and F_{max} are taking their values from K=27, since no local $F(y)$ peak is determined for L less than 28. Similar conditions hold for K=29, 30, 31 and 32. Unless a cut-off constant c greater than 5 is specified, the resulting eddy viscosity magnitude near the secondary flow region is restricted to a lower value as shown. It seems that the contour plots for $c=2.0$ and 2.5 can give a smoother eddy viscosity variation along the circumferential K-direction. For $c=3.0$ and up the sharp drops of eddy viscosity magnitude across K=25 and K=27~34 are apparently inevitable by using the modified Baldwin-Lomax turbulence model with Eq.(2.24). Due to the limited computing resources, we have not simulated the flow problem with different c's in the modified model computation. However, it is believed that by effectively reducing the eddy viscosity magnitude in the separated region, a qualitatively correct solution can be accomplished by using the modified Baldwin-Lomax turbulence model with a cut-off constant c=5.

Not only the modified model can give quite a different μ_t-distribution at different time as the flow develops, the dependency of computed eddy viscosity to the cut-off constant c is also varied with different crossflow topology. Figure 5.35 shows the $F(y)$ contour plots for Case B at J=54 with τ=2.0, and J=106 with τ=0.9. The top graph represents an earlier vortical flow structure shown in Figure 5.29, compared to the τ=9.325 solution at J=54 in Figure 5.2 and 5.8. The secondary vortex exists with its center closer to the solid surface. Accordingly, the first peak of $F(y)$ in the secondary flow region near K=30 is located at L=22, compared to L=27 in the τ=9.325 case. The bottom $F(y)$ contour in Figure 5.35 represents a flowfield consisting of both secondary and tertiary flows (Figure 5.32 and 33). The peak $F(y)$'s associated with secondary and tertiary vortices are observed near L=25 and L=14, respectively. Figure 5.36 shows the eddy viscosity contours for the case with J=54 and τ=2.0 by applying different cut-off constants in modified Baldwin-Lomax model, based the solution computed with c=5. Since the first peak $F(y)$ is now located closer to the surface, a cut-off distance with c=5 is large enough to accommodate the first peak $F(y)$ in the separated region, hence no cut-offs (shaded circles) are detected. It is also noticed that the eddy viscosity within secondary flow region jumps up more than one order in magnitude around L=20 when c advances from 4.5 to 5.0. This implies that eddy viscosity magnitude in the separated region is very sensitive to small changes of c in this specific flow condition. For the other case at τ=0.9 and J=106, however, the change of c from 2.5 to 5.5 all give identical eddy viscosity distribution as shown in Figure 5.37.

In 1993 Chaderjian [47] conducted a study for the comparison of two Navier-Stokes codes in simulating high-incidence vortical flow. The specific flow problem solved is a Mach number 0.2 flow past an ogive-cylinder with $\alpha=20°$ and $Re_D=5\times10^6$. The turbulence model used was based on the Baldwin-Lomax model modified by Degani and Schiff, but with a different way to specify the cut-off distance which is a constant throughout the circumferential K-direction, i.e.,

$$y_{cut\text{-}off} = Cy_{max}|_w \tag{5.1}$$

where $y_{max}|_w$ is the value of y_{max} at the windward plane of symmetry K=1. C is a user-specified cut-off constant with a suggested value of 3 to 5. For the J=54 and $\tau=9.325$ case, y_{max} at the windward plane of symmetry is approximately 2.3×10^{-3} around L=17. A cut-off distance of 3 to 5 times therefore lies between L=22 to 26. The resulting eddy viscosity contour is similar to the $c=3$ case in Figure 5.34, but with a smoother variation in K-direction and smaller computed eddy viscosity near S_1 and S_2. Both Eq.(2.24) and Eq.(5.1) used in the modified Baldwin-Lomax turbulence model are able to effectively reduce the amount of eddy viscosity in the separated region. Accordingly, a realistic vortical flowfield is obtained without sacrificing the advantage of using the simple algebraic Baldwin-Lomax model. In order to achieve a quantitatively accurate solution, on the other hand, the cut-off constant (either c or C) must be validated through carefully conducted measurements.

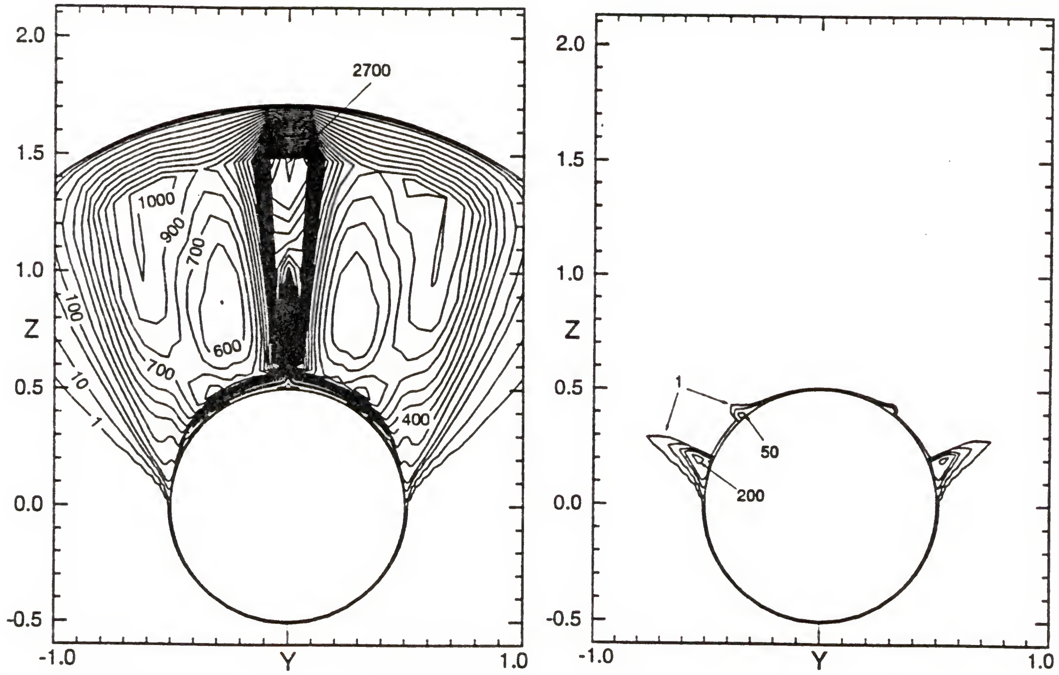

Figure 5.1 Eddy viscosity contour at J=54, τ=9.325 - Case A (left) and Case B (right).

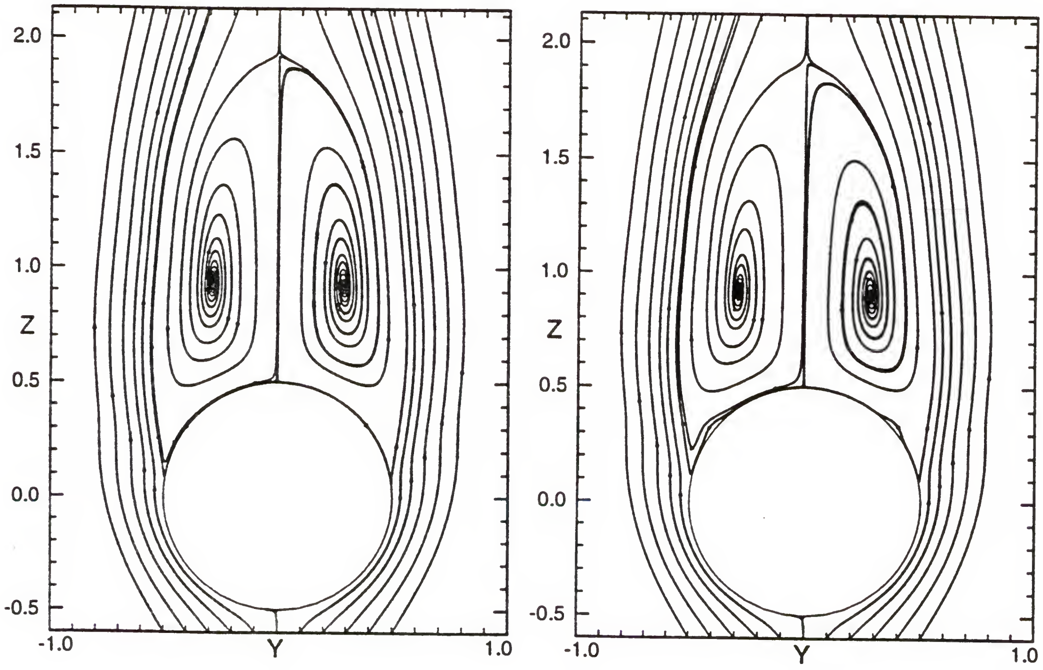

Figure 5.2 Instantaneous streamtraces at J=54, τ=9.325 - Case A (left) and Case B (right).

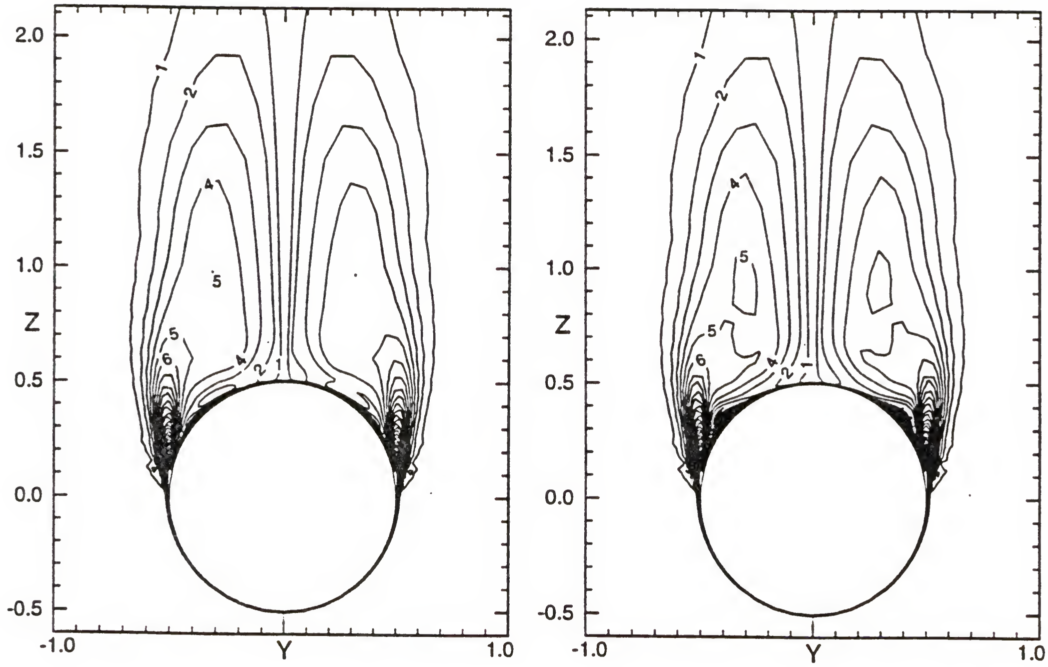

Figure 5.3 Total vorticity contour at J=54, τ=9.325 - Case A (left) and Case B (right).

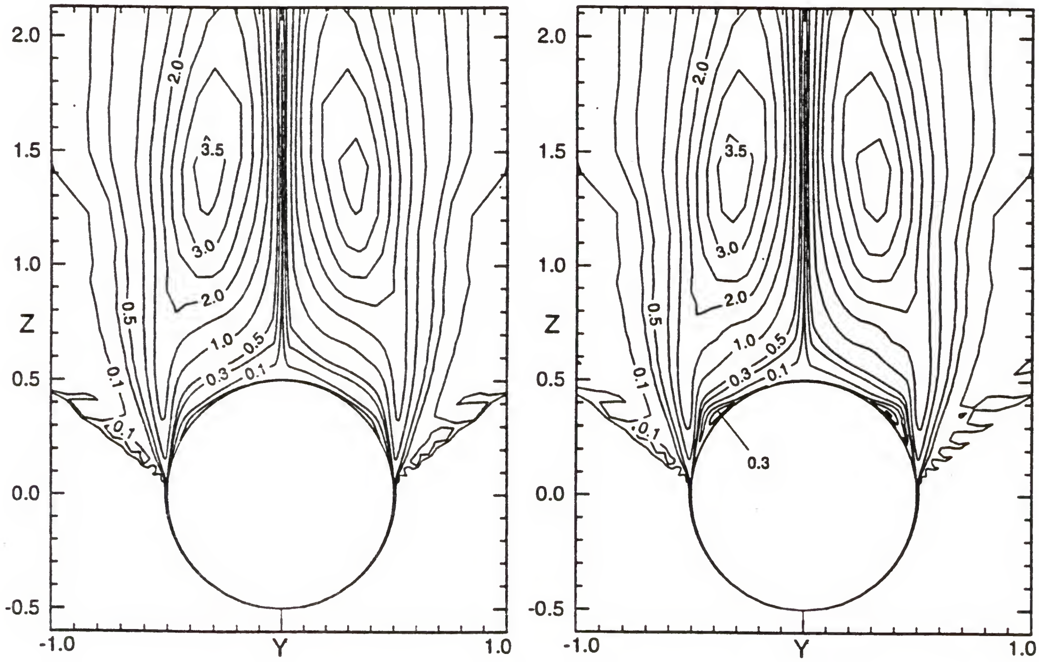

Figure 5.4 $F(y)$ contour at J=54, τ=9.325 - Case A (left) and Case B (right).

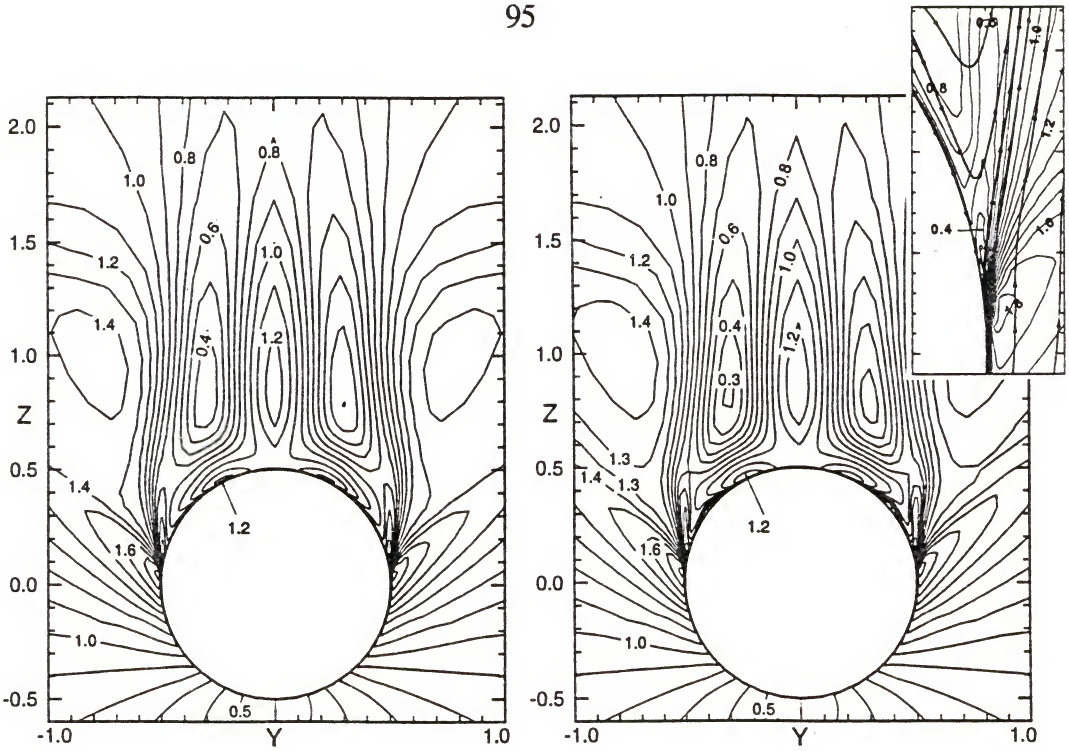

Figure 5.5 Mach contour at J=54, τ=9.325 - Case A (left) and Case B (right).

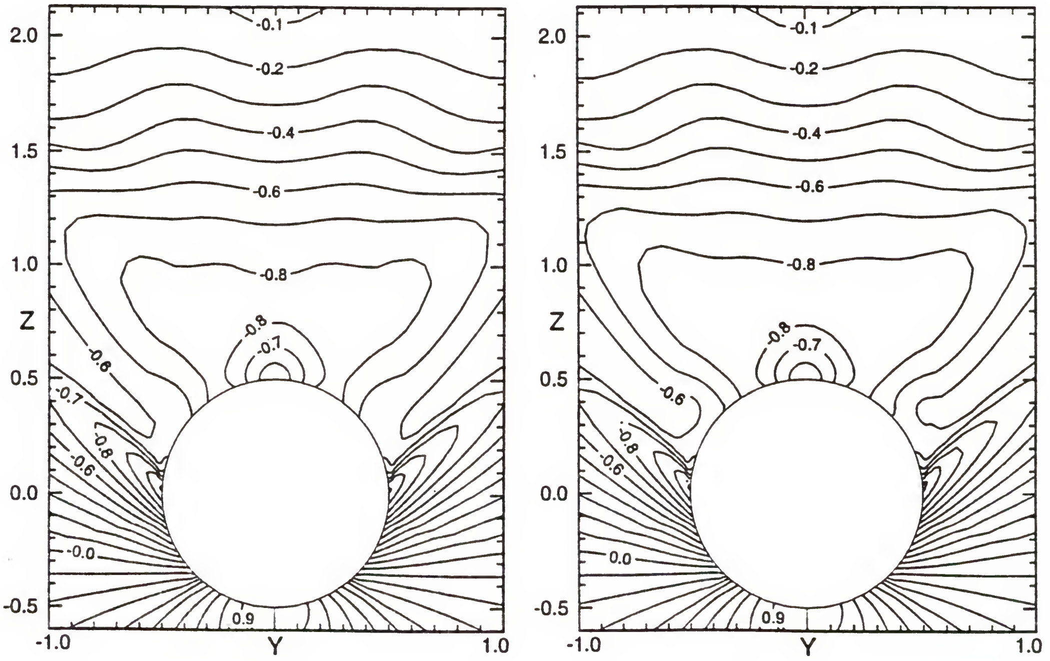

Figure 5.6 *Cp* contour at J=54, τ=9.325 - Case A (left) and Case B (right).

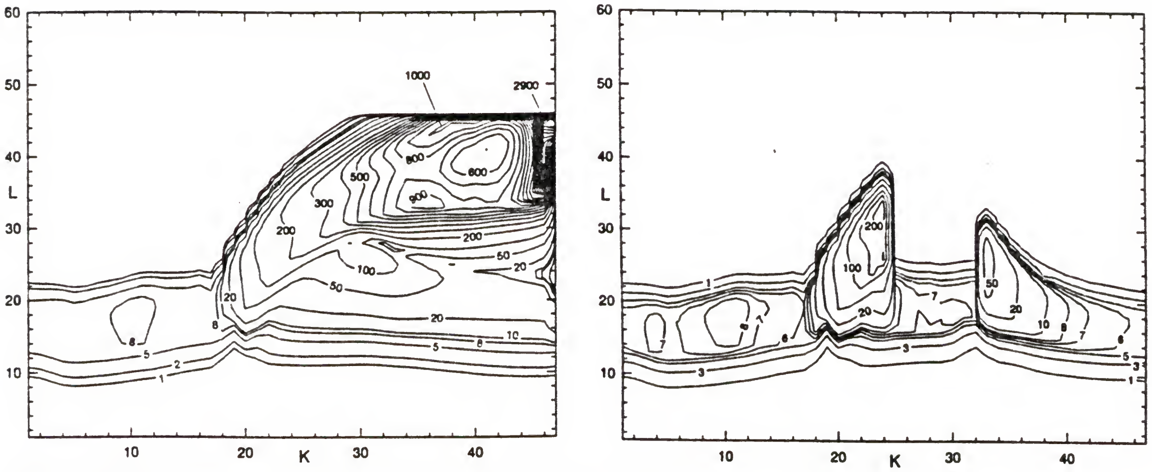

Figure 5.7 Eddy viscosity contour at J=54, τ=9.325 - Case A (left) and Case B (right).

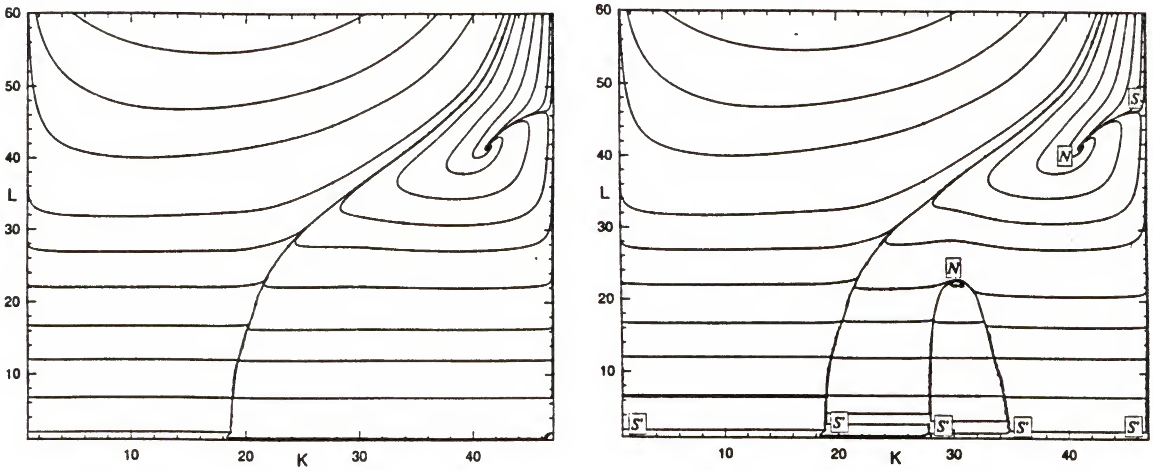

Figure 5.8 Instantaneous streamtraces at J=54, τ=9.325 - Case A (left) and Case B (right).

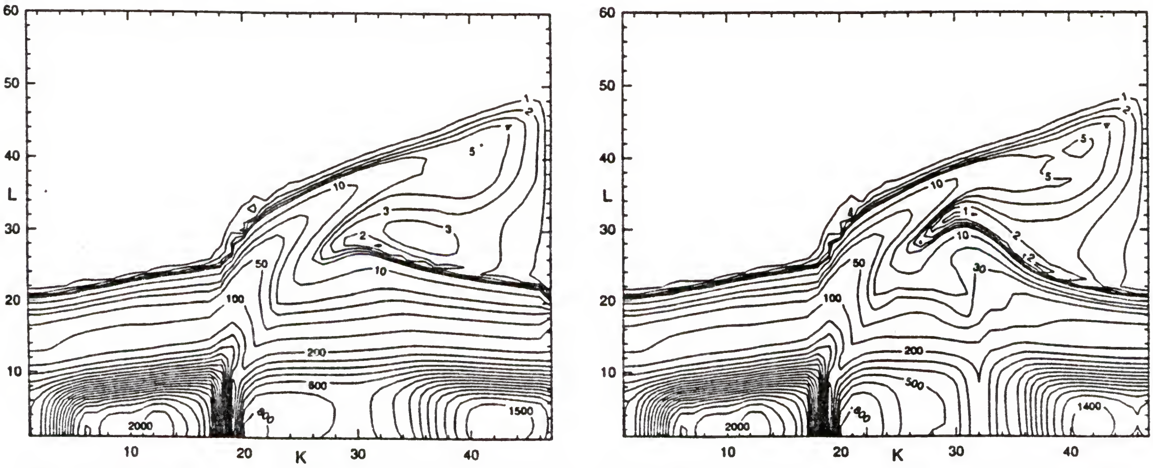

Figure 5.9 Total vorticity contour at J=54, τ=9.325 - Case A (left) and Case B (right).

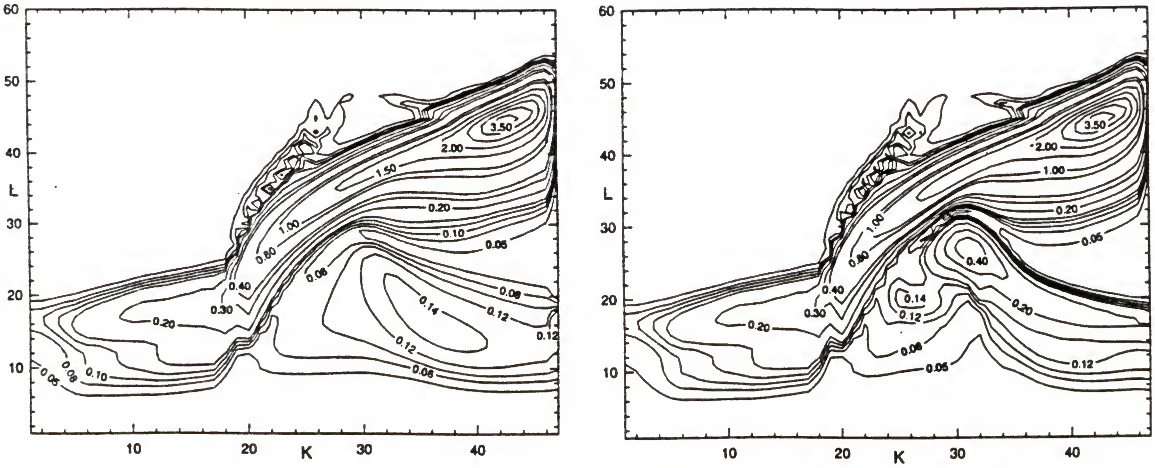

Figure 5.10 *F*(*y*) contour at J=54, τ=9.325 - Case A (left) and Case B (right).

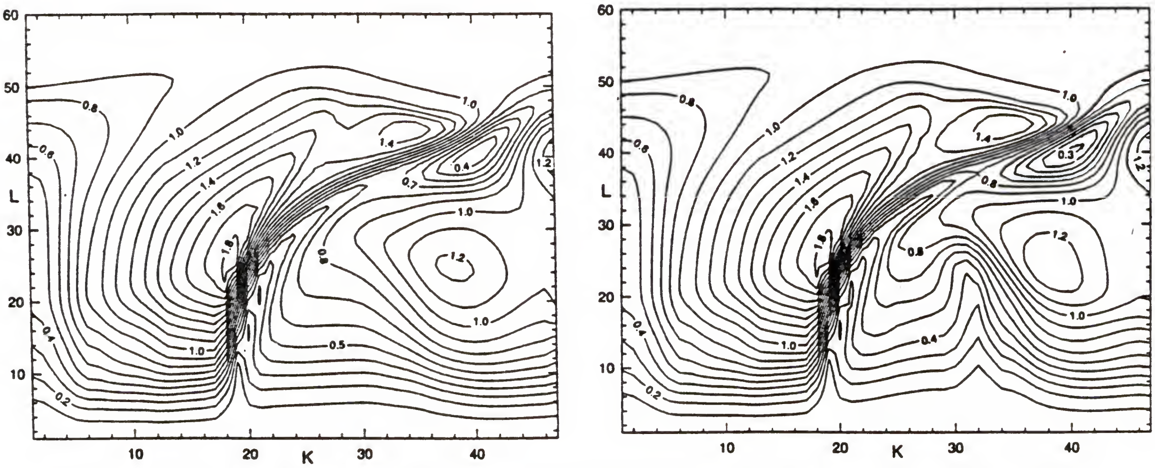

Figure 5.11 Mach contour at J=54, τ=9.325 - Case A (left) and Case B (right).

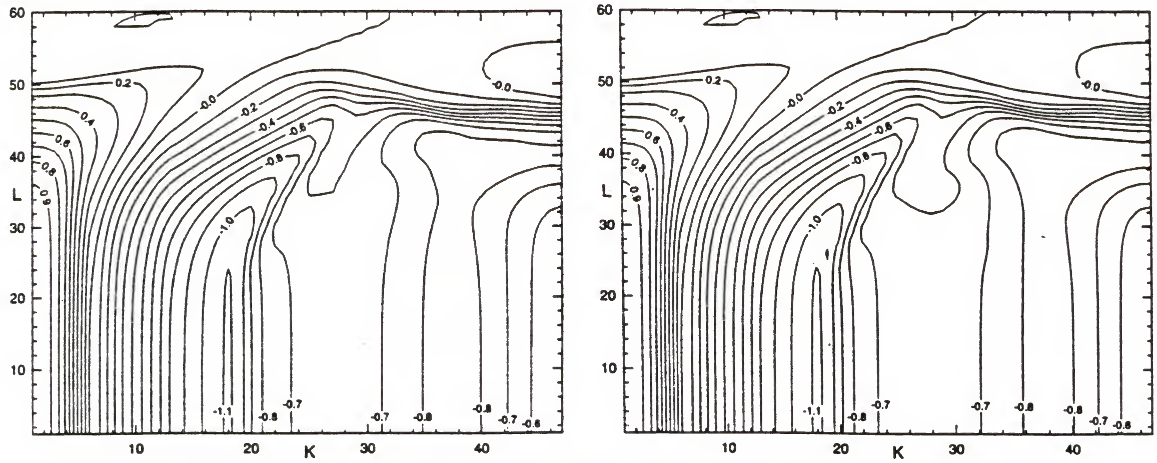

Figure 5.12 *Cp* contour at J=54, τ=9.325 - Case A (left) and Case B (right).

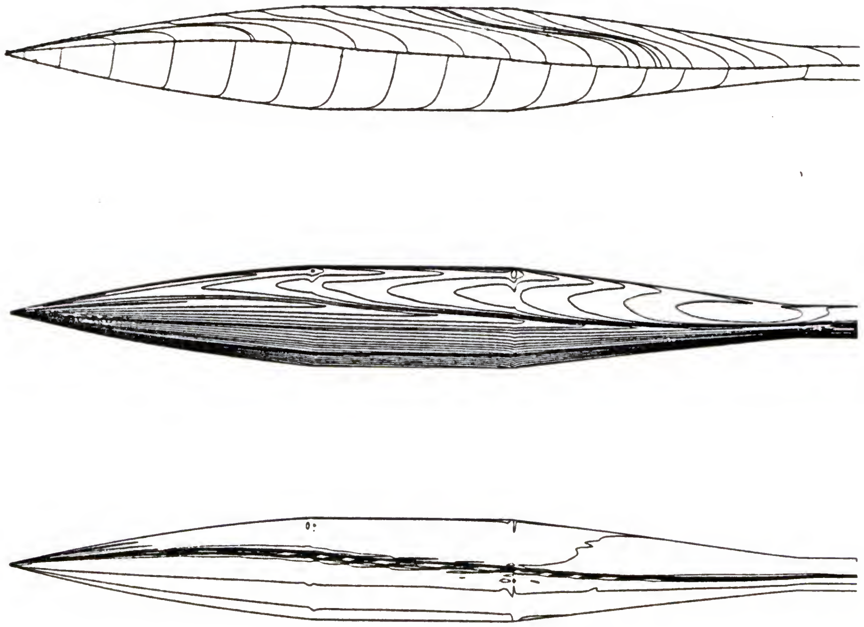

Figure 5.13 Surface skin-friction lines (top), Cp (middle) and temperature contours (bottom) at τ=9.325 for Case A. ΔCp=0.1 and ΔT=20°R.

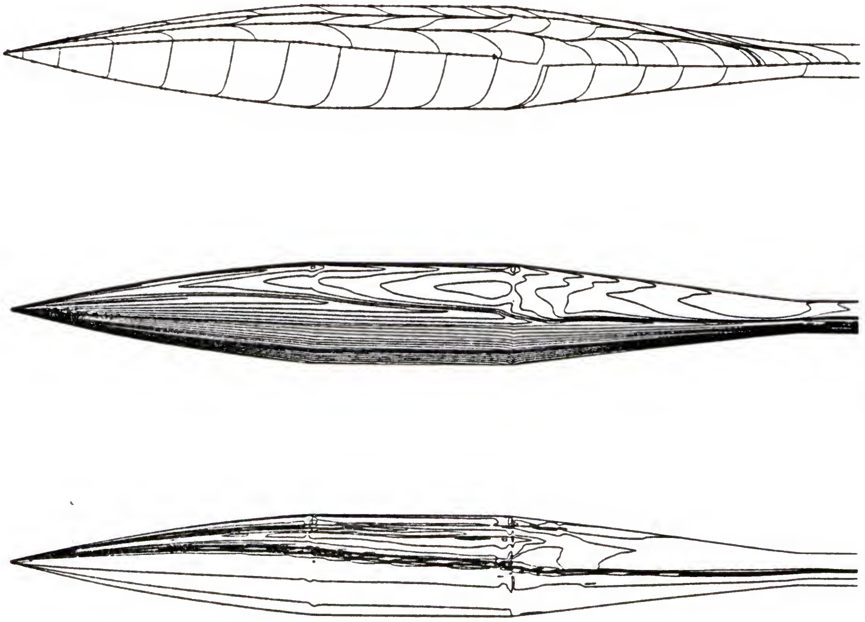

Figure 5.14 Surface skin-friction lines (top), Cp (middle) and temperature contours (bottom) at τ=9.325 for Case B. ΔCp=0.1 and ΔT=20°R.

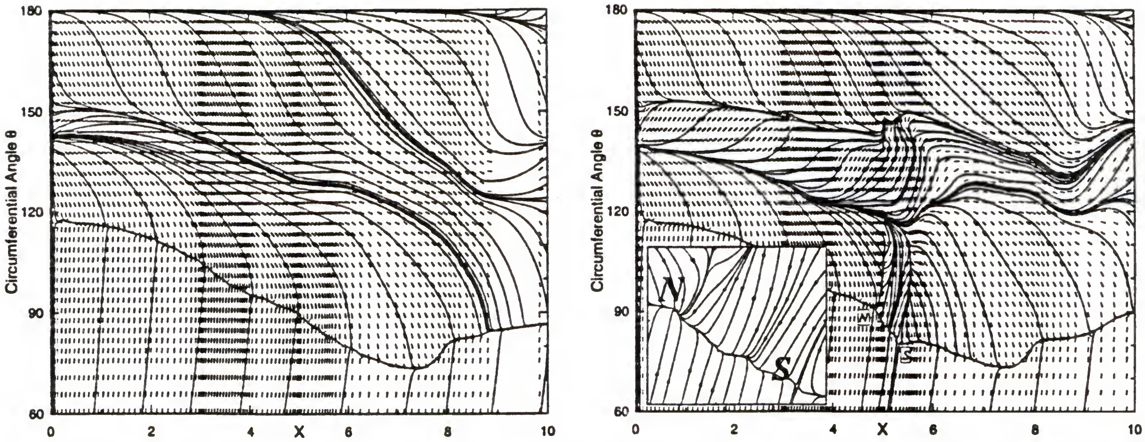

Figure 5.15 Surface skin-friction lines at τ=9.325 - Case A (left) and Case B (right).

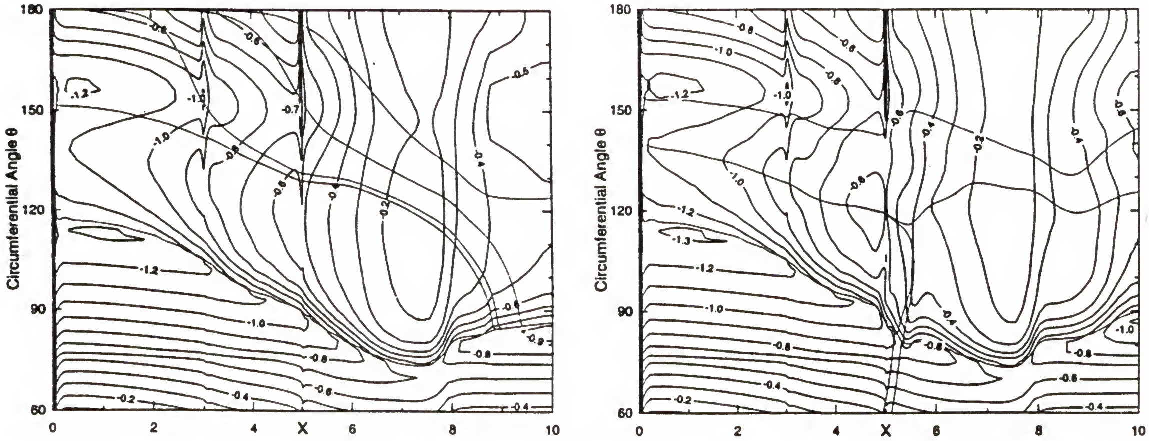

Figure 5.16 Surface *Cp* contour at τ=9.325 - Case A (left) and Case B (right).

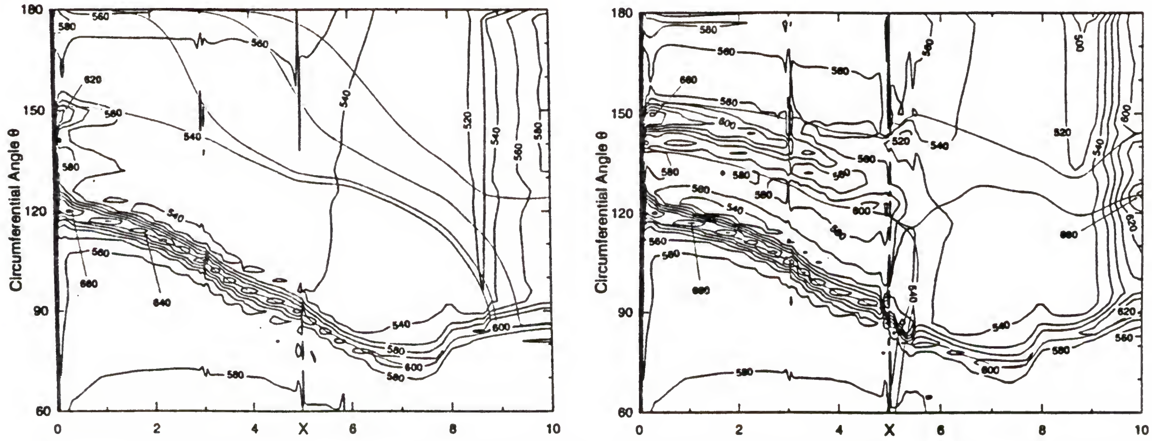

Figure 5.17 Surface temperature contour at τ=9.325 - Case A (left) and Case B (right).

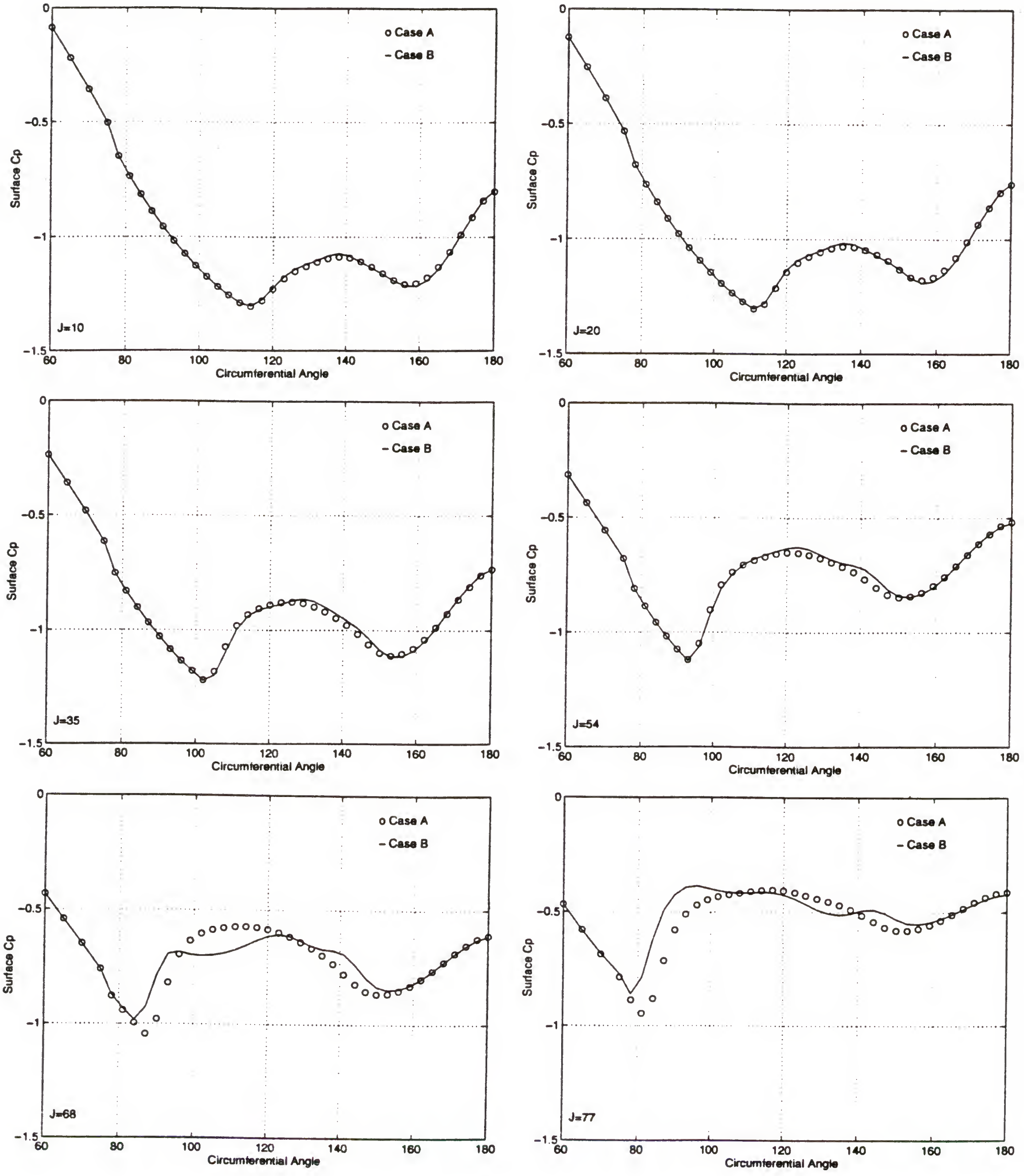

Figure 5.18 Circumferential surface *Cp* distribution at τ=9.325.

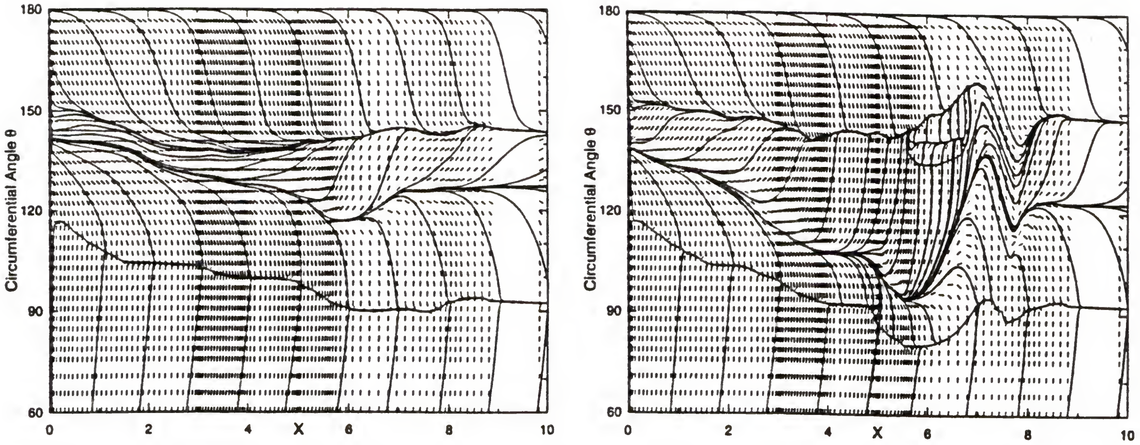

Figure 5.19 Surface skin-friction lines at τ=2.0 - Case A (left) and Case B (right).

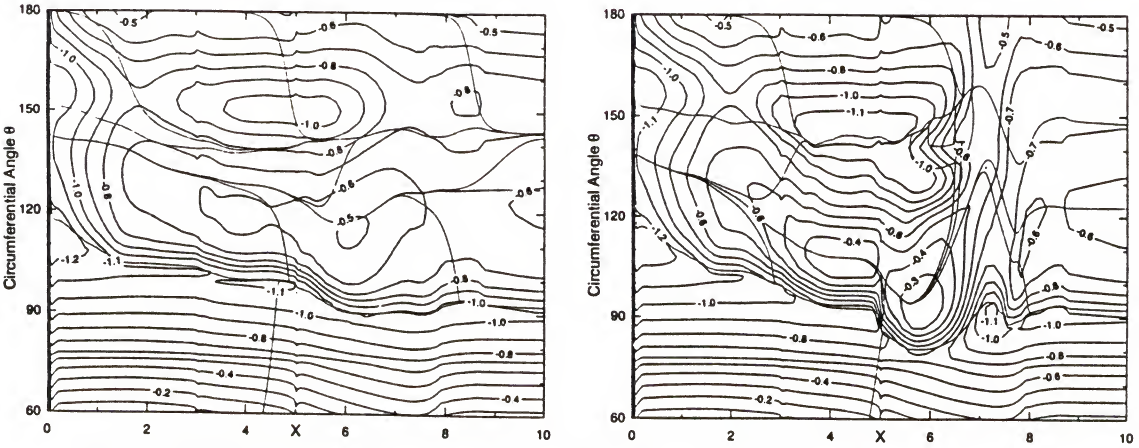

Figure 5.20 Surface *Cp* contour at τ=2.0 - Case A (left) and Case B (right).

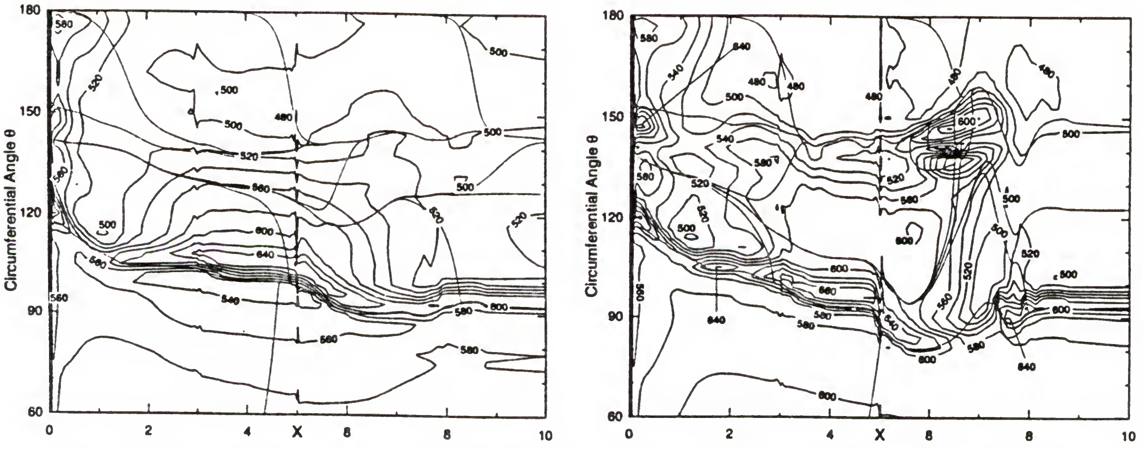

Figure 5.21 Surface temperature contour at τ=2.0 - Case A (left) and Case B (right).

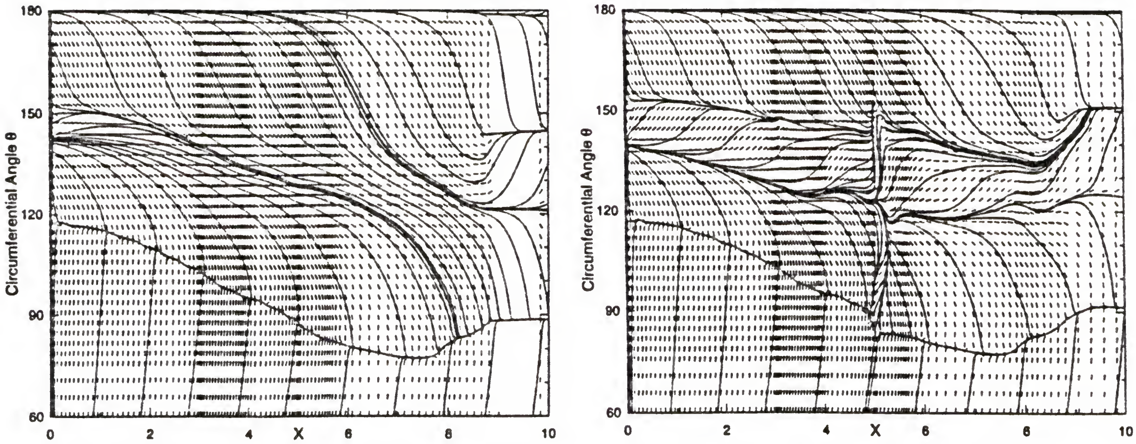

Figure 5.22 Surface skin-friction lines at τ=6.8 - Case A (left) and Case B (right).

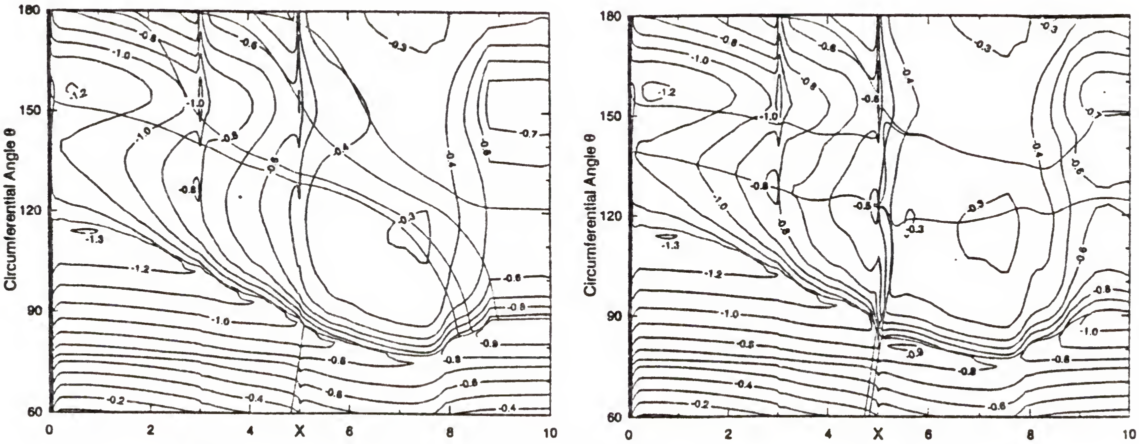

Figure 5.23 Surface *Cp* contour at τ=6.8 - Case A (left) and Case B (right).

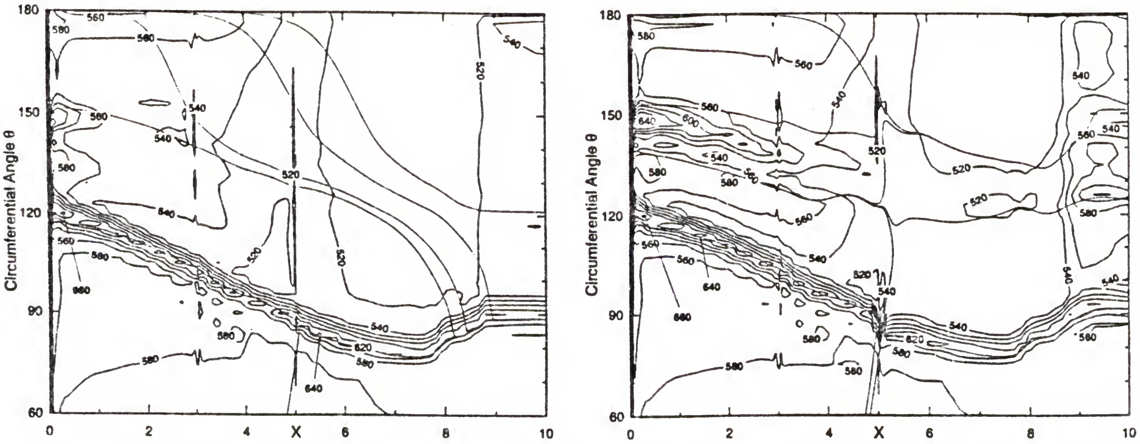

Figure 5.24 Surface temperature contour at τ=6.8 - Case A (left) and Case B (right).

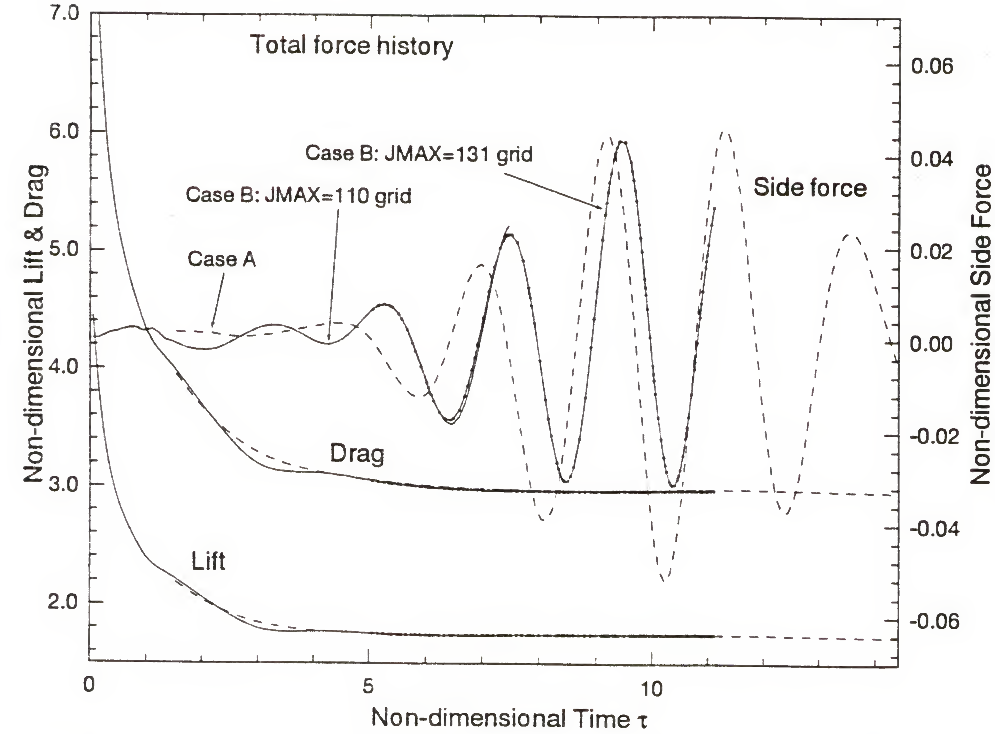

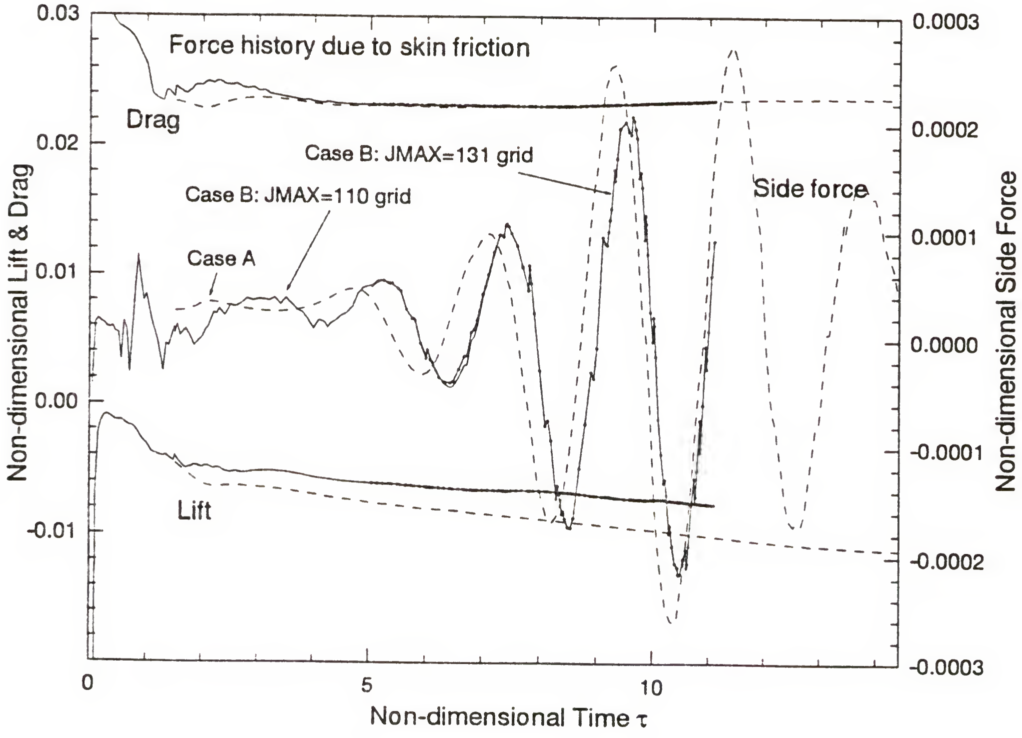

Figure 5.25 (a) Total force time history. (b) Skin-friction force history.

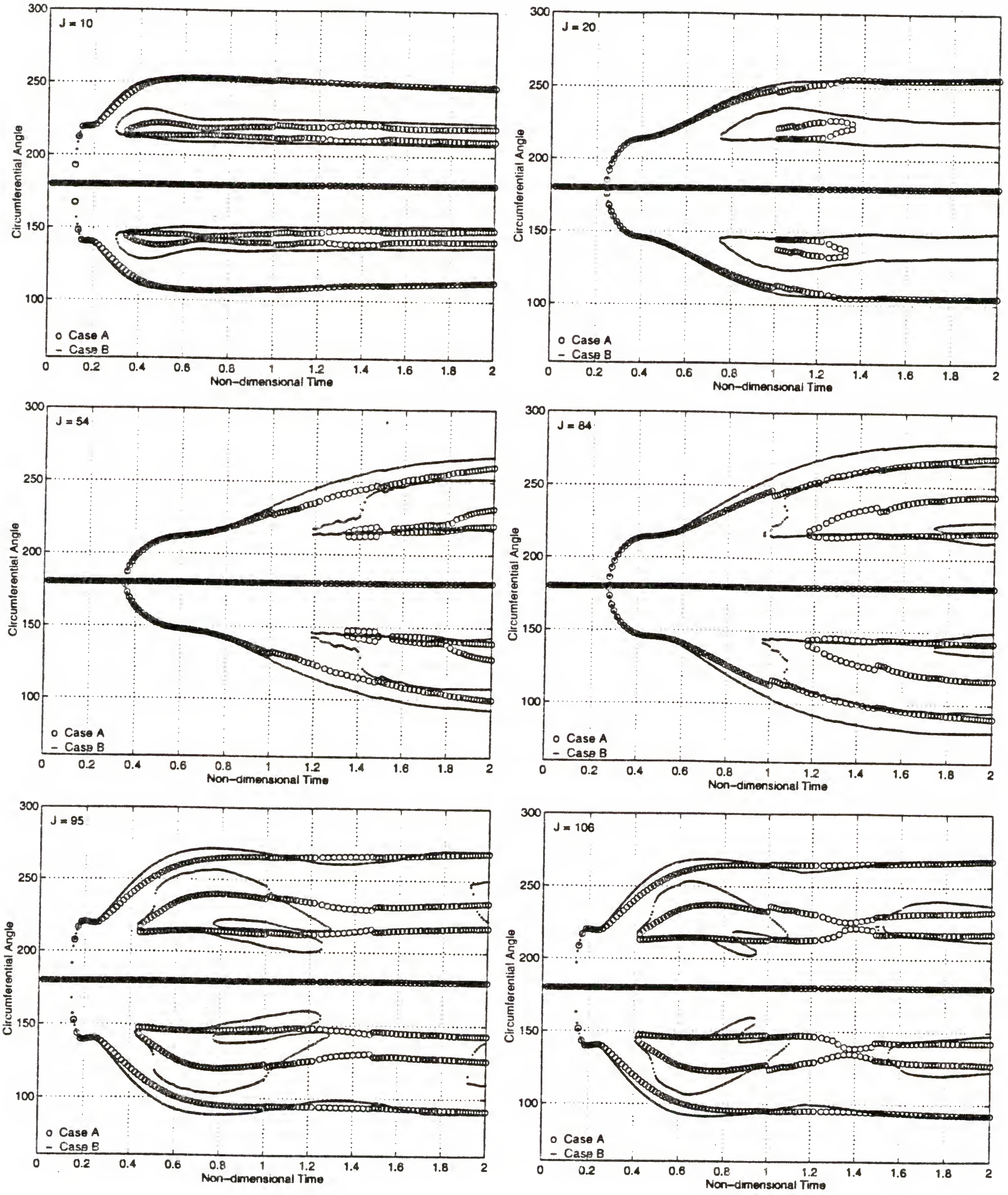

Figure 5.26 Time history of crossflow separation/attachment points in earlier stage.

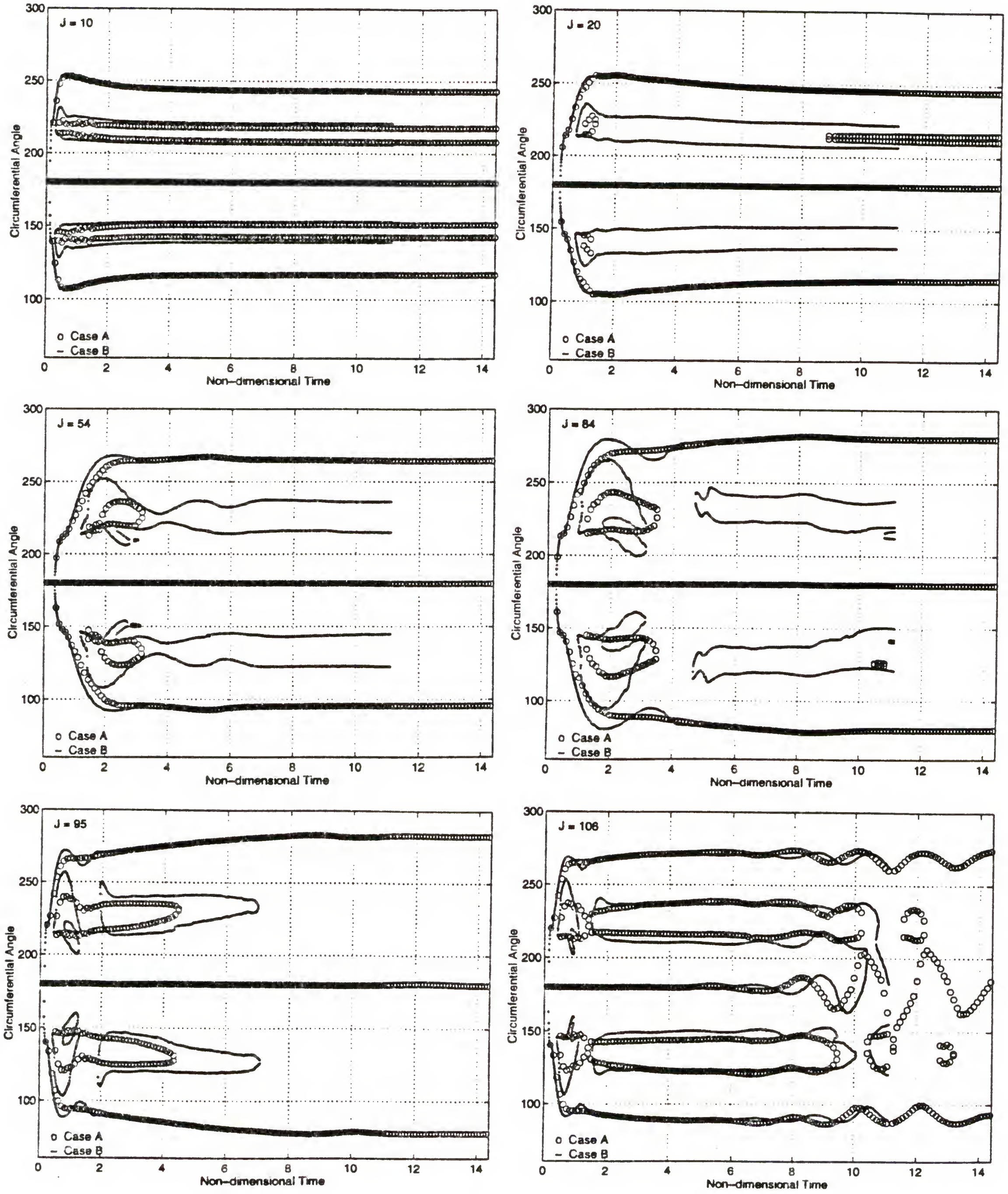

Figure 5.27 Time history of crossflow separation/attachment points.

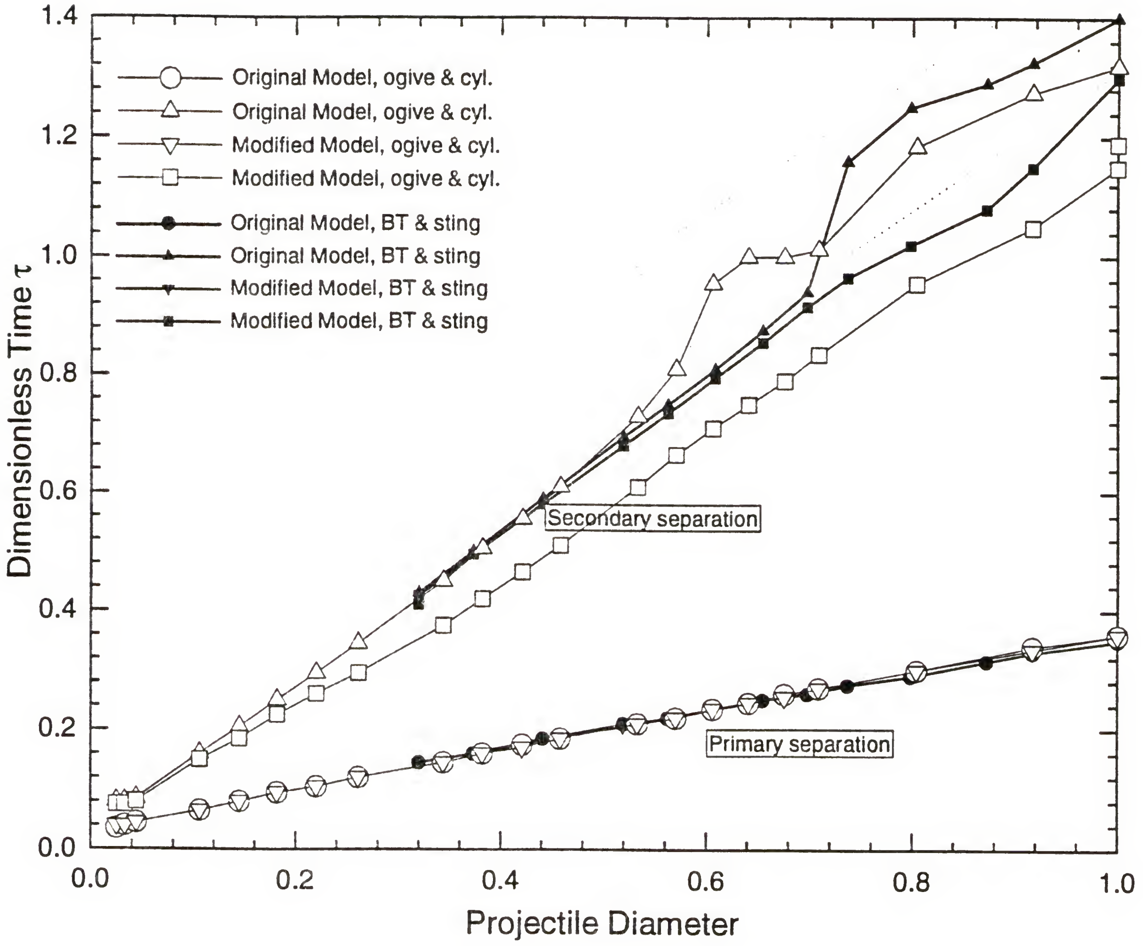

Figure 5.28 Onset time for crossflow separation *vs* projectile diameter.

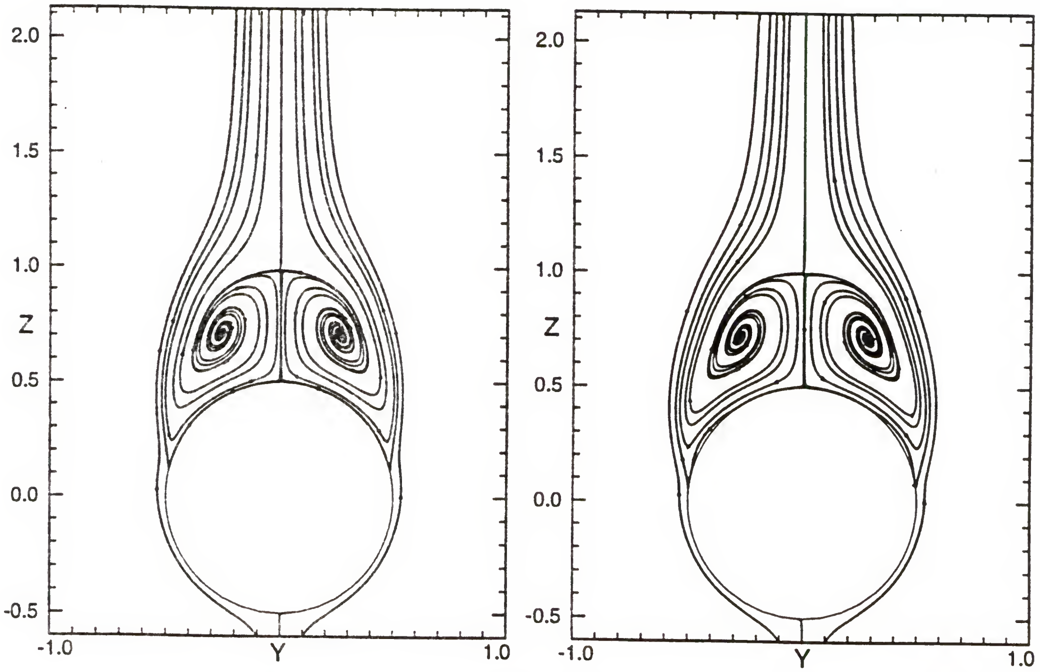

Figure 5.29 Instantaneous streamtraces at J=54, τ=2.0 - Case A (left) and Case B (right).

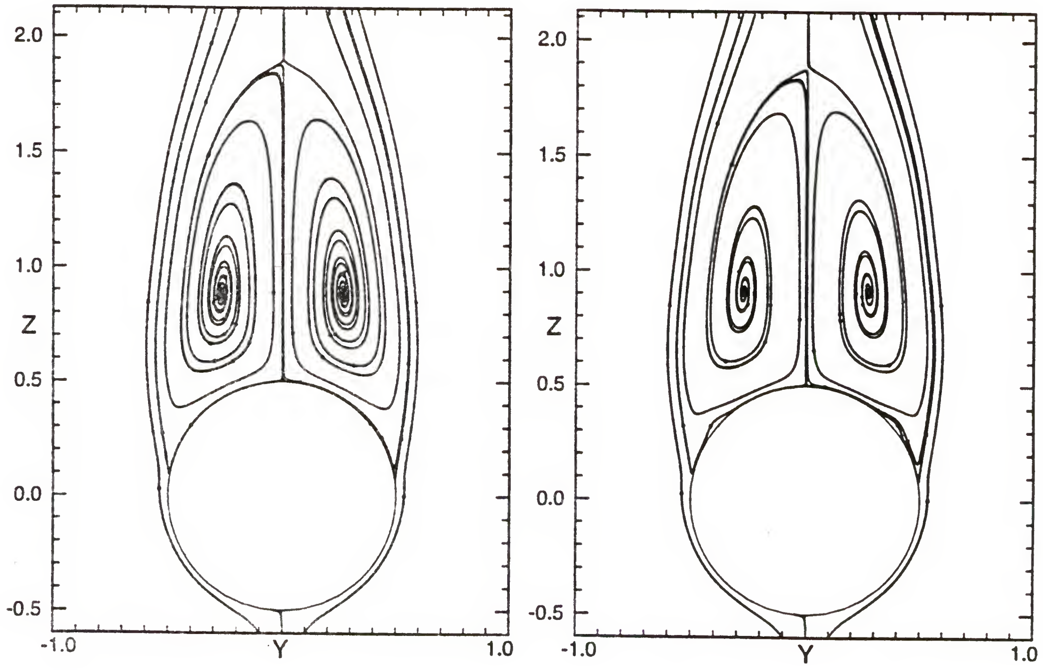

Figure 5.30 Instantaneous streamtraces at J=54, τ=6.8 - Case A (left) and Case B (right).

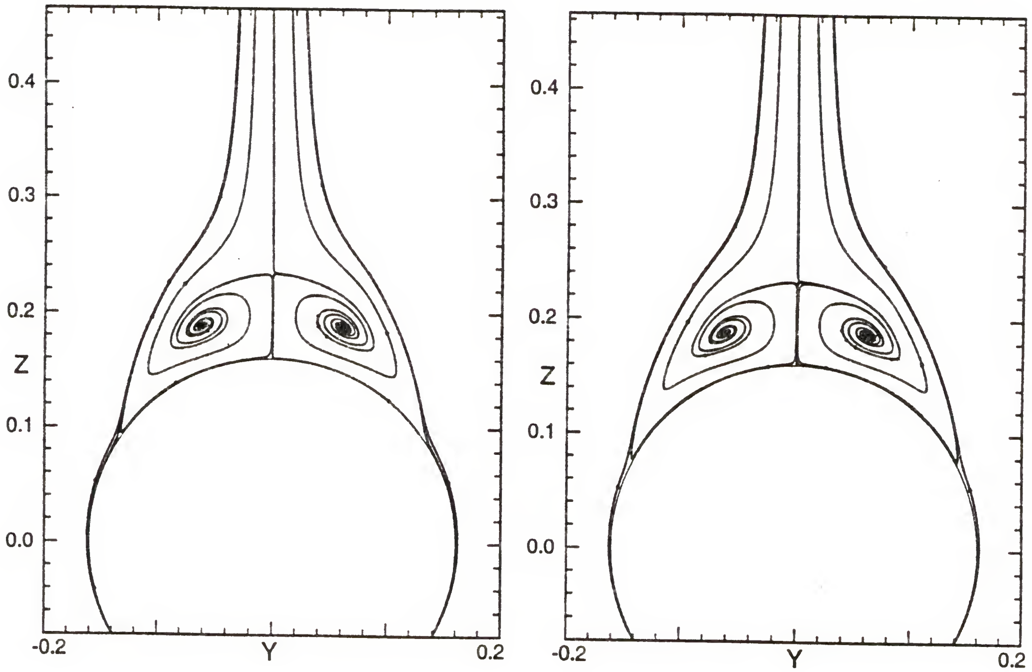

Figure 5.31 Instantaneous streamtraces at J=106, $\tau=0.4$ - Case A (left) and Case B (right).

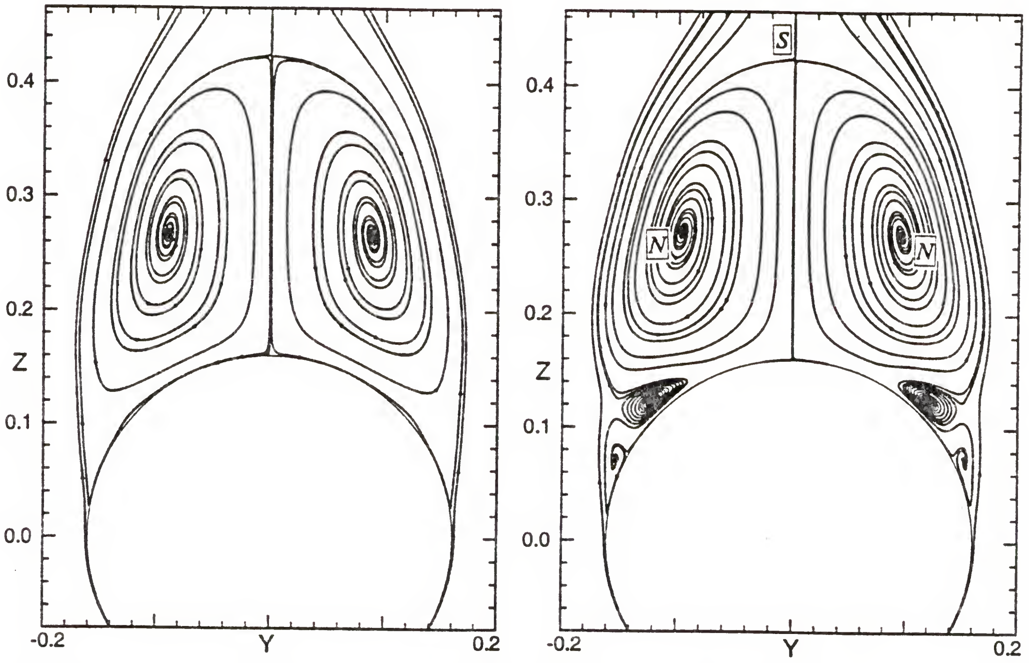

Figure 5.32 Instantaneous streamtraces at J=106, $\tau=0.9$ - Case A (left) and Case B (right).

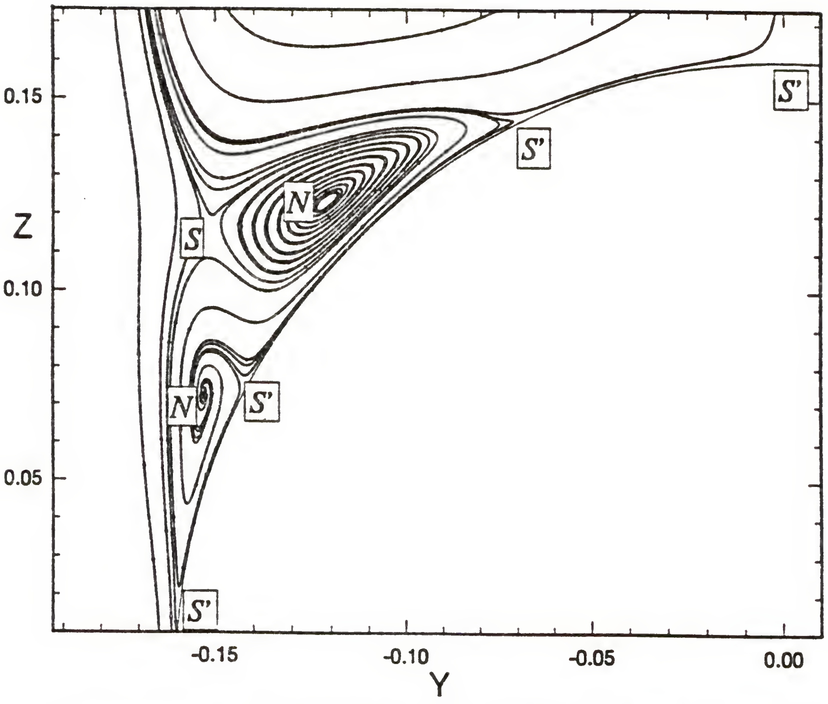

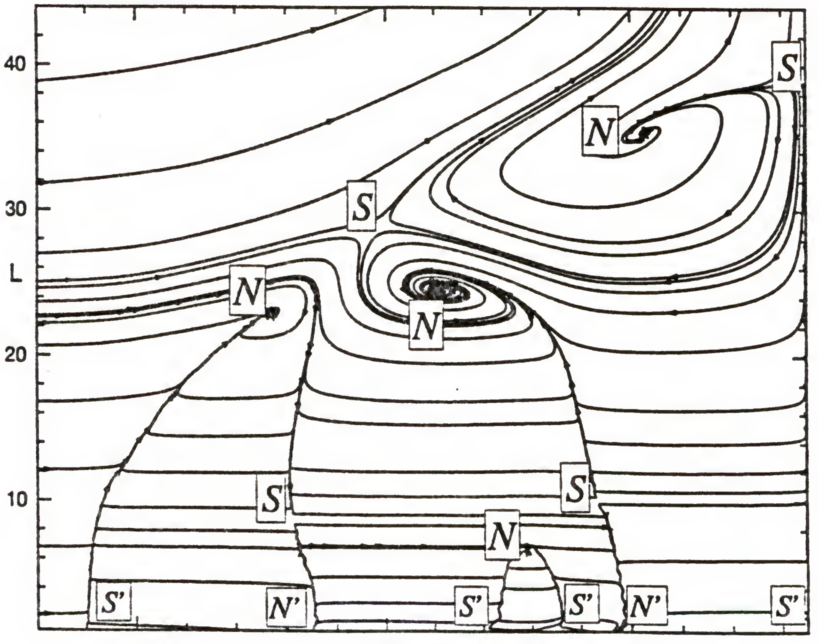

Figure 5.33 Instantaneous streamtraces at J=106 and τ=0.9 for Case B. (a) In (y,z) plane (upper). (b) In (K.L) plane (bottom).

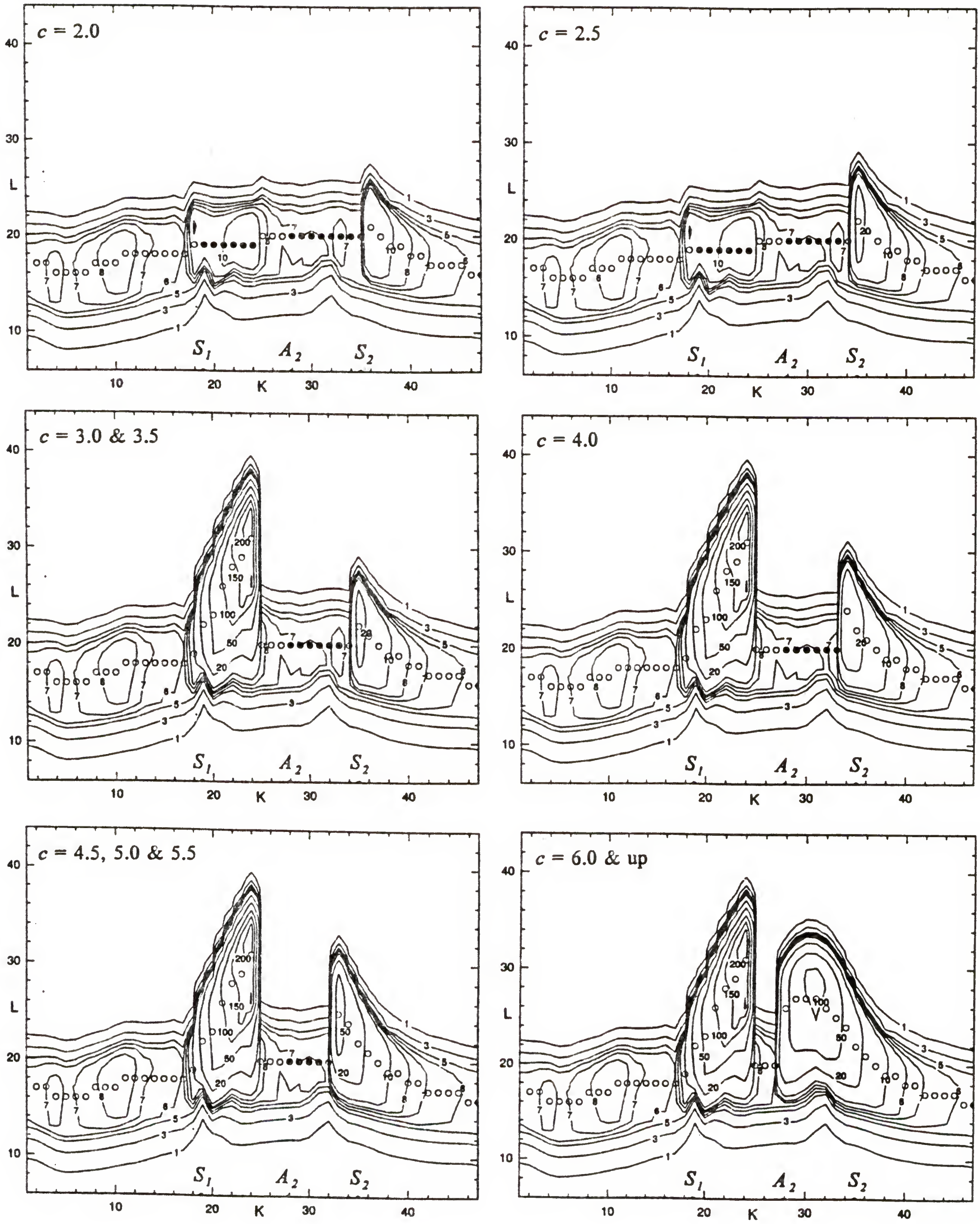
c = 2.0

c = 2.5

c = 3.0 & 3.5

c = 4.0

c = 4.5, 5.0 & 5.5

c = 6.0 & up

Figure 5.34 Computed eddy viscosity contours at J=54 and τ=9.325.

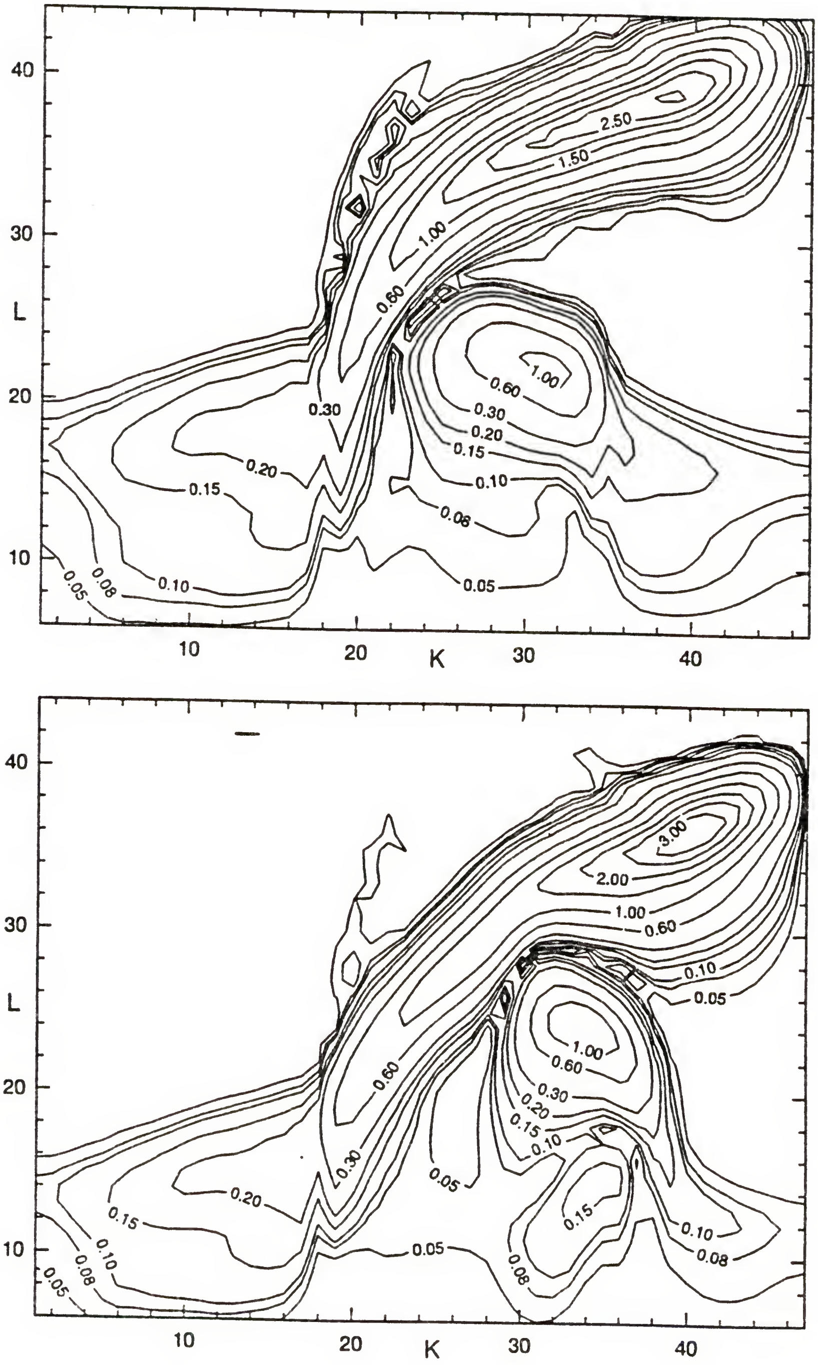

Figure 5.35 $F(y)$ contours for $J=54$, $\tau=2.0$ (top) and $J=106$, $\tau=0.9$ (bottom).

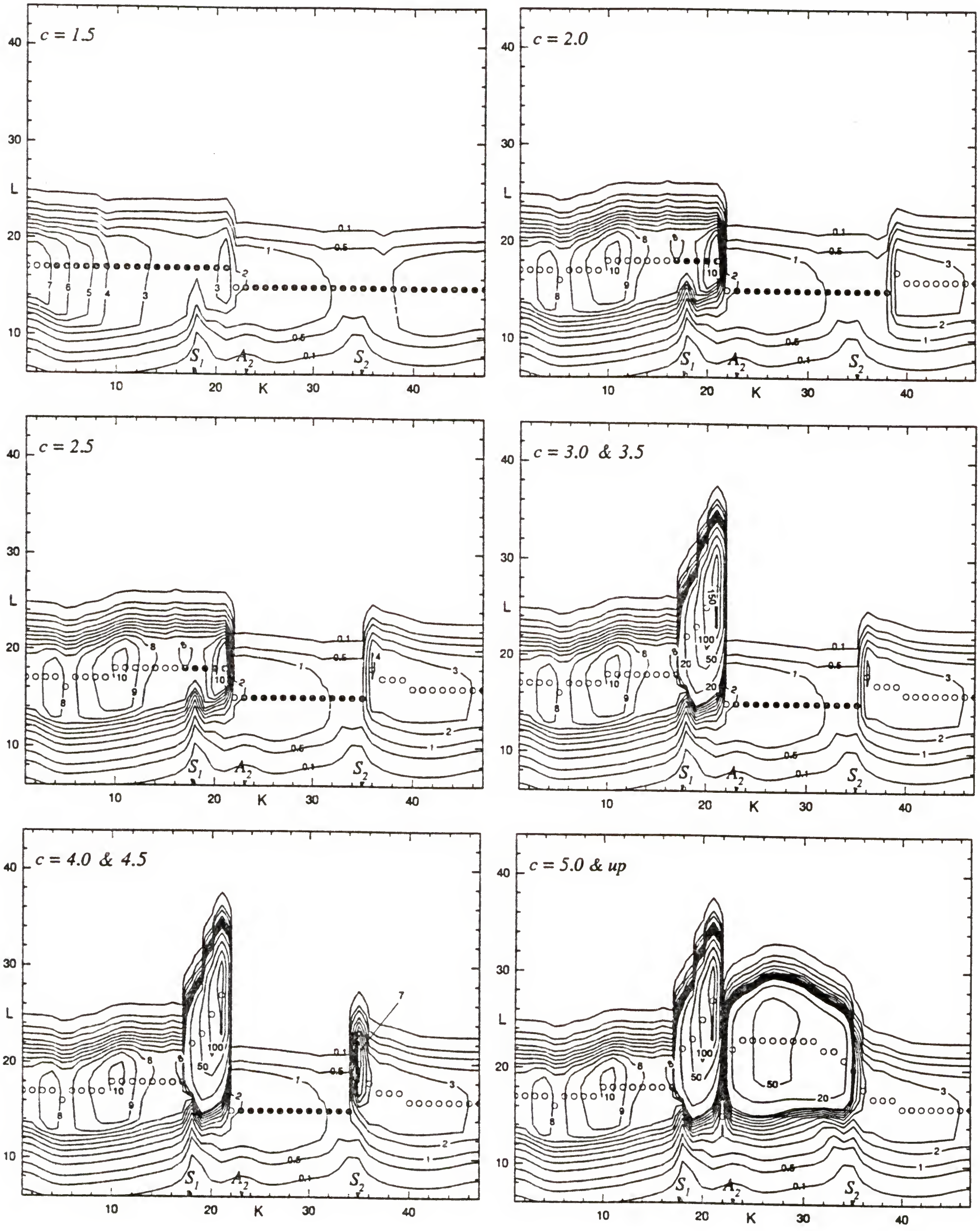

Figure 5.36 Computed eddy viscosity contours at J=54 and τ=2.0.

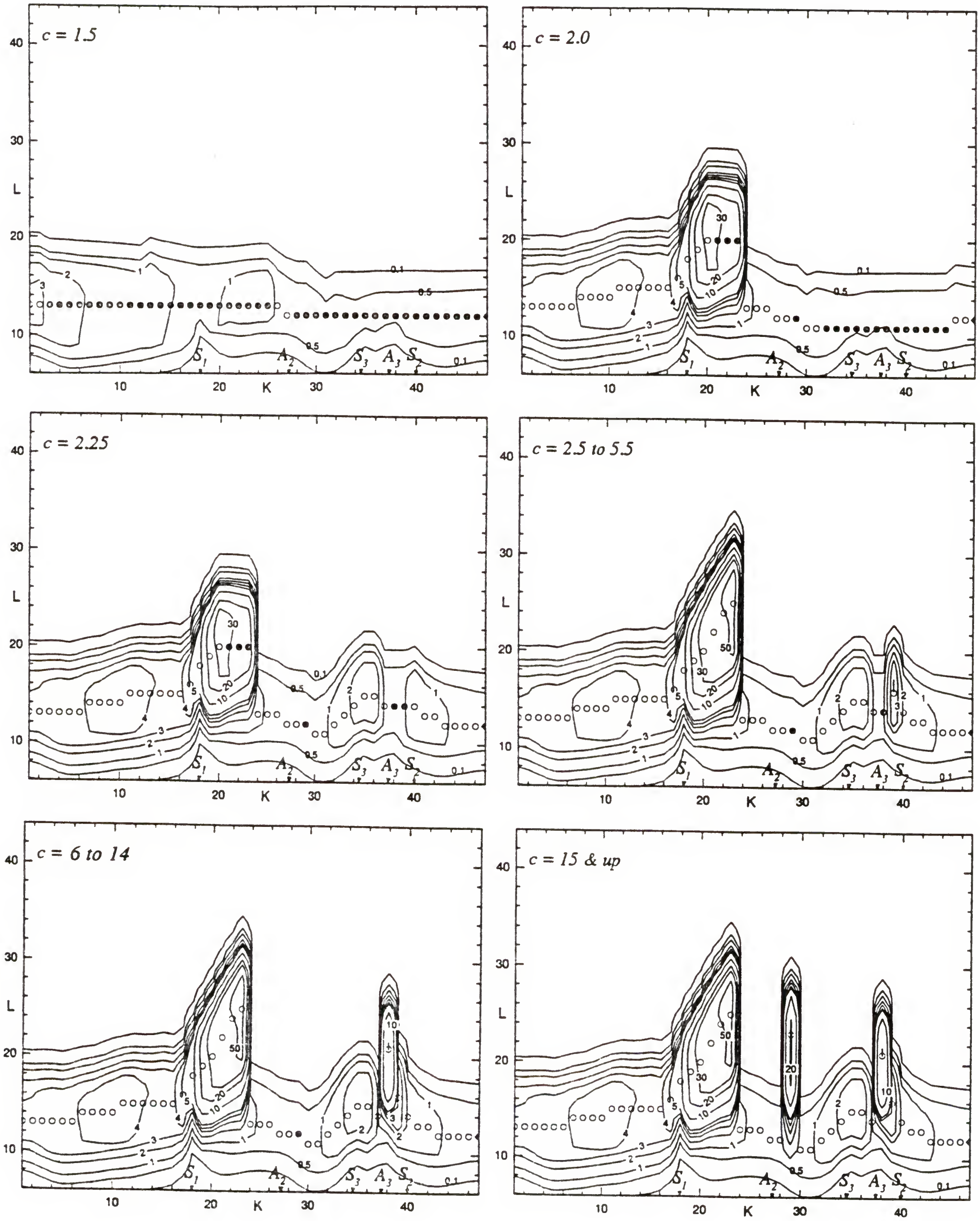

Figure 5.37 Computed eddy viscosity contours at J=106 and τ=0.9.

CHAPTER VI
TURBULENT VORTICAL FLOW PHENOMENA

In the previous chapter we have demonstrated that the modified Baldwin-Lomax turbulence model can bring out physically realistic secondary flow phenomena in the near wake region. Results obtained also show that the strong diffusive process in the original Baldwin-Lomax model computation has little qualitative effect upon the vortical flow solution in the outer layer. It is therefore concluded that the modified model can indeed represent turbulent vortical flow physics and phenomena.

In this chapter, the simulated results by modified Baldwin-Lomax turbulence model are used to investigate complex three-dimensional vortical flow phenomena. The crossflow streamtraces at selected J cross-sections are first presented to illustrate the evolution of cross-sectional vortical flow. The surface skin-friction lines and related contours are shown to demonstrate the flow development on projectile body up to $x=10$. A visualization of three-dimensional flowfield is presented with the aid of 3-D streamtraces. Finally, the vortex shedding phenomena simulated on sting section are examined through a series of cross-sectional streamtraces and surface skin-friction lines plots.

Cross-sectional Vortical Flow Structure

The evolution of cross-sectional vortical flow structure of the impulsively-started 60-degree angle-of-attack turbulent flow at J=54 is shown in a portion of (K,L) plane in Figure 6.1. A saddle point which separates the upward and downward flow at K=47 ($\theta=180°$) is observed near L=26 ($y=0.0172$) before the cross-sectional reverse flow starts at $\tau=0.36$ (refer to Figure 5.26). As soon as the crossflow separation point begins to appear, a separation line originating from the surface is formed which extends further into the wake region at a later time. The flow direction on the separation line is toward the surface, until a stable node is observed at $\tau=0.45$. The stable node moves toward the end of the separation line at $\tau=0.60$ and is to develop into a stable spiral. Figure 6.2 shows an enlargement of the spiral vortex development at J=54. The spiral remains stable until about $\tau=0.90$ when a stable limiting cycle is formed within which the spiral is an unstable one. As the unstable spiral is fully grown, the stable limiting cycle simply disappears and the unstable vortex pattern takes over. It is understood that the crossflow topology can be transformed from a stable spiral to an unstable one through the appearance of limiting cycle, and vice versa. Visbal and Gordnier [11] suggested that a stable crossflow spiral vortex is associated with a positive axial velocity gradient (vortex stretching) at the core, if the flow is assumed to be effectively incompressible, while an unstable vortex is present due to the negative axial velocity gradient (vortex compression). Such correlations, however, are not observed in the current flow problem which is highly compressible. As a matter of fact, the axial velocity gradient $\partial u/\partial \xi$ contour plots reveal that the flow is decelerating in the separated region at all times ever since the stable spiral pattern is formed at $\tau=0.7$.

Depending on various external flow conditions the evolution of primary vortex can be very different from the one at J=54. The cross-section J=19 (x=1.45) on ogive and J=87 (x=6.59) on boattail which have approximately the same diameter (D=0.606 and 0.608, respectively) are selected with their crossflow streamtraces presented in Figure 6.3. Unlike the crossflow vortex evolution at J=54, the one at J=19 consists of only an unstable spiral pattern for $\tau \geq 0.6$. The velocity component at leeward symmetric plane K=47 is pointing outward from the surface L=1, due to a surface curvature from the axially-increasing ogive diameter. Immediately after the formation of an unstable vortex at $\tau=0.6$, a pair of saddle points are found at K=47 to balance the crossflow topology. The existence of the lower saddle point connecting the upward and downward flows due to surface curvature effect was also reported by Ward and Katz [48] in their experiments, in which the flow visualization of an inclined body of revolution was obtained in a towing tank with $\alpha=40° \sim 45°$ and $Re_D=0.8\times10^4 \sim 2.7\times10^5$. The vortex evolution at J=87, on the other hand, looks very similar to the one at J=54. A limiting cycle is also observed at $\tau=0.6$ which transforms the stable vortex pattern into an unstable one at a later time.

The crossflow streamtraces for τ=6.8 and 11.1 at J=19, 54 and 87 are presented in Figure 6.4. Despite of the appearance of some secondary flow regions, the primary vortex remains unstable. Flow patterns at J=19 and 54 are very similar from τ=6.8 to 11.1, indicating that a good convergence has been achieved. The flow pattern at J=87, on the other hand, shows a slower convergence due to its rather downstream location as well as the inclined 7° boattail. The secondary flow region collapses at τ=11.1, although it is still seen at $\tau=6.8$. Figure 6.4 also shows a growing cross-sectional primary vortex in the longitudinal J direction. The axial velocity component (u) and crossflow plane velocity magnitude (square root of v^2+w^2) contour plots for J=19, 54 and 87 at $\tau=11.1$ are presented in Figure 6.5. The free stream axial velocity component has a value of 0.48 which is normalized by the free stream speed of sound. It is noticed that the axial velocity near primary vortex core decreases dramatically from J=19 to J=87. In the region above primary attachment point K=47, on the other hand, the axial velocity slows down gradually but maintains a relative high speed compared to the free stream value of 0.48. The slowing down of crossflow plane velocity magnitude is also observed, especially in the near wake region under primary vortex around L=20. Figure 6.6 shows the corresponding $\partial u/\partial\xi$ and Cp contour plots. In contrast to the mostly negative $\partial u/\partial\xi$ in the separated region at J=19 and J=54, the one at J=87 is found to be positive near the primary vortex center and above the vanishing secondary flow region. On the other hand, $\partial u/\partial\xi$ is apparently negative along the primary separation line at J=87, while they are positive at J=19 and J=54. The Cp contour at J=19 is found to be in close pattern as the one at J=54, only with a higher surface pressure at the windward symmetric plane K=1 and a lower one in the wake region. The surface pressure at J=87, however, leaves a rather flat distribution in the wake region. Without a proper circumferential adverse pressure, the development of secondary separation is simply constrained.

Figure 6.7 shows a variation of crossflow topology along the projectile at $\tau=11.1$. The size of primary vortex increases in axial direction on ogive, cylinder and boattail. Near the boattail-sting juncture, the primary vortices are found to be elevated away from the surface with the shrinking cross-sectional area, while small recirculations are formed in the near wake region. Eventually the primary vortices breakdown in the far wake region and the ones near the surface simply take over as the new primary vortices. The crossflow pattern on the rear sting exhibits alternating vortex shedding which is to be discussed in a separate section.

Development of Surface Flow Patterns

The development of surface flow pattern is illustrated through a series of skin-friction lines plots as shown in Figure 6.8. Again the unwrapped and stretched (x,θ) surface is used which covers the projectile from $x=0\sim 10$, and $\theta=60°\sim 180°$. The flow at $\tau=0.05$ remains attached on most of the projectile surface when the impulsive flow is initiated, except a small portion of circumferentially reverse flow is observed near the nose tip. The reverse flow soon propagates onto the ogive along the longitudinal direction at $\tau=0.2$, while in the meantime a primary separation line is formed on the sting. Recall that the onset time of crossflow primary separation was found to be linearly proportional to the local diameters in previous discussion. Eventually the primary separation lines on ogive and sting join together at $\tau=0.4$, and the secondary flow region starts to develop on the ogive section as well as on the sting ($\tau=0.8$). A tertiary separation region is formed at $\tau=0.8$ right behind the boattail-sting juncture ($x=7.82$) and immediately develops onto the entire sting section ($\tau=0.9$). When the primary separation line on the cylinder moves toward the windward side, the tertiary separation on the sting section begins to disappear around $\tau=1.0$. The tertiary separation located in front of the boattaill-sting juncture, however, is maintained and propagates upslope along the boattail at a later time. The secondary separation line from ogive then ties together with the one from boattail ($\tau=1.2$) and the secondary flow region is formed on cylinder section ($3 \leq x \leq 5$) while the secondary flow on sting is temporarily gone ($\tau=1.1$, 1.2 and 1.4). In subsequent development the secondary attachment line promptly moves upstream in the circumferential direction together with the primary separation line, which allows the tertiary flow region on boattail to further merge into the secondary flow. The secondary separation and attachment lines re-appear on the sting section after the secondary flow region is formed on the cylinder at $\tau=1.8$. It is noticed that the initial flow development on cylinder is mostly under circumferential flow action rather than in the longitudinal direction. This can be seen from the plots before $\tau=1.2$ on which the skin-friction lines are joining separation lines in an almost perpendicular direction. The axial flow development is not obvious until a jet stream is formed above the leeward plane of symmetry after the secondary flows on ogive and boattail merging together, which creates a more complex transient pattern before a relatively steady surface flow topology is formed at $\tau=6.0$.

Figure 6.9 shows the development of surface *Cp* contours in a time sequence associated with skin-friction lines plots shown in Figure 6.8. In the circumferentially upstream region prior to the primary separation line, the pressure declines as the flow accelerates toward the leeward side. Small pressure drops are found longitudinally on both the ogive-cylinder (x=3.017) and cylinder-boattail junctures (x=5.0) due to local flow expansions at the corners. On the other hand a pressure rise is found on the boattail-sting juncture due to a flow compression. Pressure troughs are located slightly ahead the primary and secondary separation lines in the circumferential direction throughout the flow development, which are apparently the important mechanisms to accelerate the flow before reaching the separation lines. The pressure ridge, on the other hand, coincides well with the secondary attachment line when the flow pattern is getting steady (τ=4.8 and up). In general the pressure distribution is not quite sensitive to the apparently weak secondary and tertiary flow motions. The corresponding surface temperature contours are presented in Figure 6.10. Similar to the pressure distribution, the temperature drops from the windward side to the leeward side before the primary separation line. A temperature ridge is observed right on top of the primary separation line for $\tau \geq 3.0$, which is apparently associated with the pressure rise across the separation line. Unlike the pressure contour, the temperature distribution is more sensitive to the corresponding flow topology, for example, the tertiary flow development for $1.0 \leq \tau \leq 3.0$.

A number of transient critical points observed in the skin-friction line plots are helpful to describe the formation and development of the surface flow topology. For example, Figure 6.11 shows the earlier flow development on the first half of ogive section for $100° \leq \theta \leq 160°$, in terms of the skin-friction lines and surface *Cp* contour plots. In the very beginning (τ=0.05), a saddle point is found close to the ogive tip at $\theta \approx 135°$ which effectively divides the surface flow into four regions. To the left and top of the saddle point are the longitudinally and circumferentially reverse flows, respectively. A nodal point then shows up at $\tau=0.1$ bringing a longitudinally downstream flow from its left. The pair of nodal-saddle points move to the right rapidly and merge together at $\tau=0.4$, leaving the secondary flow developed behind. Eventually the secondary flow is formed at $\tau=0.8$ which continues to propagate onto the rear part of ogive and cylinder. In the corresponding pressure contours the formation of two low pressure centers associated with both sides of primary separation line and a high pressure center associated with the secondary attachment line are clearly observed from $\tau=0.2$ to 0.4. The high pressure center cuts into those two low pressure regions at a later time which sets up an overall circumferential pressure distribution we have seen in Figure 5.18.

Another example is the evolution of longitudinally reverse flow shown in Figure 6.12. When the general flow pattern is nearly stable on the projectile surface, a secondary flow region in the longitudinal direction near the cylinder-boattail juncture starts to develop. The transformed domain presented has the ranges $4 \leq x \leq 6$ and $60^\circ \leq \theta \leq 180^\circ$. Recall that at $x=5$ the projectile begins to see a 7° downslope boattail from the cylinder section, which is in favor of forming a longitudinal recirculation pattern. Indeed the reverse flow is observed at $\tau=7.0$ between the circumferential primary and secondary separation lines. After going through a rather complex transition only the reverse flow between primary separation line and secondary attachment line is maintained at $\tau=11.0$. The remaining two pairs of nodal-saddle points formation allows the recirculation area to reside, while in the meantime, sets up a proper link between the crossflow primary separation and secondary attachment lines.

The surface flow pattern appears to be quite steady at the end of the modified Baldwin-Lomax model computation ($\tau=11.1$). Figure 6.13 shows the skin-friction lines and the *Cp*/temperature contours at $\tau=10.6$ and 11.1. Very much resemblance is observed except on the sting section where the flow pattern is in transition associated with the alternating vortex shedding. Compare Figure 6.13 to the skin-friction lines at $\tau=6.8$ (Figure 5.22) and $\tau=9.325$ (Figure 5.15), we can see the diminishing of crossflow secondary flow structure for $5.5 \leq x \leq 10$. In fact at $\tau=11.1$ there is no cross-sectional secondary flow region detected in the range $6.78 \leq x \leq 9.05$ (J=88 to 104).

Three-Dimensional Streamtraces

The three-dimensional instantaneous streamtraces are presented in a time sequence to visualize the vortical flow development. Due to the hardware limitation, the plotting is made by using only upper half of the domain with every other grid points included in all three directions. In Figure 6.14 the particles are released at J=4 ($x=0.086$) right above the surface (L=2), from 13 circumferential locations ranging from $\theta=90°$ to 270° with $\Delta\theta=15°$. At earlier times when the axial flow has not well developed, for example, $\tau=1.0$ and 2.0, the streamtraces are only able to reach part of the projectile then elevated from the surface in a direction parallel to the free stream flow. When the streamtraces arrive onto the boattail at a later time, they are first found to stay close to the surface then take off. Referring back to Figure 6.9 for the pressure distribution from $\tau=3.0$ to 6.0 and Figure 6.13 with $\tau=10.6$ and 11.1 reveals that the surface pressure on boattail exhibits a low value of -0.5 at $\tau=3.0$ then gradually goes up to -0.1 at $\tau=11.1$. The low pressure suction formed during the initial boattail flow development around $\tau=3.0$ is believed to attract the streamtraces close to the surface as shown. Figure 6.15 shows the streamtraces at $\tau=11.1$, with the particles released from J=35, 54, 68 and 77, respectively. The numbered labels 1 to 6 attached to the individual streamtrace imply that the particles are released at $\theta=90°$, 120°, 150°, 210°, 240° and 270°, respectively. Note that the projectile body is made transparent in order to see the streamtraces on the other side. From these plots it is evident that the particles released near $\theta=90°$ (negative *y*-direction) and 270° (positive *y*-direction) have carried mostly circumferential momentum, therefore depart from the surface immediately. The particles released near the leeward symmetric plane (number 3 and 4), on the other hand, have more axial momentum to transport the particles downstream. At the cross-section J=77 the traces number 1 and 6 are missing because of the spatial integration based on local velocity vectors, which has caused the trajectories to fall outside of the current plotting domain, therefore terminates the tracing.

Vortex Shedding Phenomena

As mentioned in previous discussion that the simulated vortical flow pattern lost the symmetry with respect to the angle-of-attack plane and the alternating vortex shedding is observed on the sting section. Although the mechanisms that lead to the vortex shedding phenomena are not well understood at the present time, a number of suggestions have been made by Degani [22] to relate the asymmetry to instabilities in the flowfield. In order to simulate the von Karman vortex shedding street observed behind a 2-D cylinder flow, a symmetry-breaking perturbation must be applied for a short period of time to break the symmetric solution. The perturbation then is removed and the flow was able to advance to a self-sustained oscillatory solution. This is called an absolute instability of the symmetric flow, which means the disturbance will grow in time and space once it is introduced. Similarly in a 3-D ogive-cylinder flow simulation performed by Degani at very high angles of attack (60° and 80°), a small temporal disturbance of finite duration was found sufficient to trigger the unsteadiness that evolved to an alternating vortex shedding in the wake region of the cylindrical afterbody. The vortical flow was instantaneously highly asymmetric, but was fluctuating around a symmetric mean, revealed by the total side force time history.

In this study it is believed that the asymmetric vortex shedding observed is a result of absolute instability. Due to the one-sided sweeping from K=1 to KMAX in solving block-tridiagonal system along η-direction (Eq.(4.7b)) in the thin-layer Navier-Stokes code, an asymmetric truncation error is introduced in the transient solution which triggers the instability. The Strouhal number of the simulated vortex shedding is found to be quite comparable to an empirical value 0.182 (as discussed in previous chapter) which gives a good quantitative assessment to the numerical accuracy.

The onset of vortex asymmetry is first observed on the surface skin-friction line pattern, which is especially visible near the leeward symmetric plane. In Figure 6.16 the primary attachment line is shown in a time sequence on a transformed (x,θ) surface with

$160° \leq \theta \leq 200°$ for the overall projectile length. The oscillation pattern on sting section appears like the undulating of a string from one constrained end (boattail-sting juncture at $x=7.82$) while keeping the other end free. Observe that the attachment line on sting is all in the upper half until a bump near boattail-sting juncture is developed at $\tau=6.6$ to drive it down. At $\tau=7.8$ a similar bump is again seen near the juncture but to pull the string up. Note that when such a bump is formed to move the string to one side, the rear part of the string is still gaining its magnitude to the other side. Two cycles later the amplitude on rear sting is large enough to interact with the secondary flow region as shown on the top-right corner at $\tau=10.6$. The oscillation of skin-friction lines associated with vortex shedding, including the primary/secondary separation and attachment lines are shown in Figure 6.17 on part of the boattail and sting. As indicated by the time history of crossflow separation in Figure 5.27 and the ones from other related J cross-sections, the crossflow secondary flows are not detected for $x \leq 9.0$ at the interested times in Figure 6.17. Observe the merging of secondary separation and attachment lines at $\tau=9.5$ on top half of the plot after $x \approx 13$. With the primary attachment line swinging to the lower half and interacting with secondary flow for $\tau=9.9 \sim 10.2$, the secondary flow region on the top half shows up again. The process reverses itself such that the upper secondary flow fades away and the lower one re-appears. Note that the plot at $\tau=11.1$ happens to be very close to the mirror image of the one at $\tau=10.2$.

The crossflow streamtraces at $J=111$ ($x=10.85$) based on $JMAX=131$ grid are presented in Figure 6.18 to visualize the vortex shedding phenomena. At $\tau=10.2$ it is clear that the secondary flow does not exist under the left, smaller vortex which stays close to the surface. The left vortex grows in size and pushes the right vortex away from the surface ($\tau=10.2\sim10.6$), while in the meantime, a secondary flow region is formed under the left vortex. Although the size of left-hand-side secondary flow is practically invisible at this moment, it can be identified by the surface skin-friction lines in Figure 6.17. From $\tau=10.6\sim10.9$ it appears that a right-hand-side sub-vortex center is left alone near the surface and merges into the secondary flow to form a new primary vortex, while the previous primary vortex is dissipating into the wake region. The streamtraces shown in Figure 6.18 is close to half a cycle by observing that the flow pattern at $\tau=11.1$ is similar to the mirror image of the one at $\tau=10.2$. Similarly the vortex shedding patterns at J=115 ($x=11.88$) and 119 ($x=12.91$) are presented in Figure 6.19 and 6.20. They are found to be almost the same as the ones at J=111, but apparently with a phase lag. Observe that the flow pattern at $\tau=10.5$ and J=115 is very close to the one at $\tau=10.3$ and J=111 regarding the locations of primary vortices, indicating that a lag of approximately 0.2 units of non-dimensional time is present. Similarly the flow pattern at J=119 clearly falls behind the one at J=115 by $\Delta\tau=0.2\sim0.3$. These phase lags suggest that the vortex shedding on boattail is not parallel to the x-axis, but rather inclined with a small angle to the sting. The vortical flow patterns for $\tau=11.1$ at the cross-sections J=107 ($x=9.83$), 111, 115 and 119 are shown in Figure 6.21. Although the shedding is not seen at J=107, the streamtraces at the other 3 cross-sections clearly show the phase lag mentioned above. The dense streamtraces within the left primary vortex at J=107 is actually an unstable limiting cycle, in which a stable vortex center is not shown. Figure 6.22 presents the crossflow streamtraces at $\tau=11.1$ along the sting, on which the oblique shedding is clearly observed. Toward the end of sting the shedding becomes more parallel. As a matter of fact the oblique shedding was also shown in Ramberg's experiments [19] which was found to be related to the upstream tip vortices.

Finally in Figure 6.23 the oscillation period is presented along the sting axis. The period is obtained from the time history of crossflow separation points based on the latest simulated oscillation cycle. For those locations with $x < 10.5$ the periodic oscillation is also observed associated with mutual interaction between two primary vortices, which apparently gives a much larger period. The shedding period in non-dimensional time falls between 1.75 to 1.9, or 0.191 to 0.176 in terms of the Strouhal number, which is very comparable to the value 0.182 given by Roshko's empirical relation.

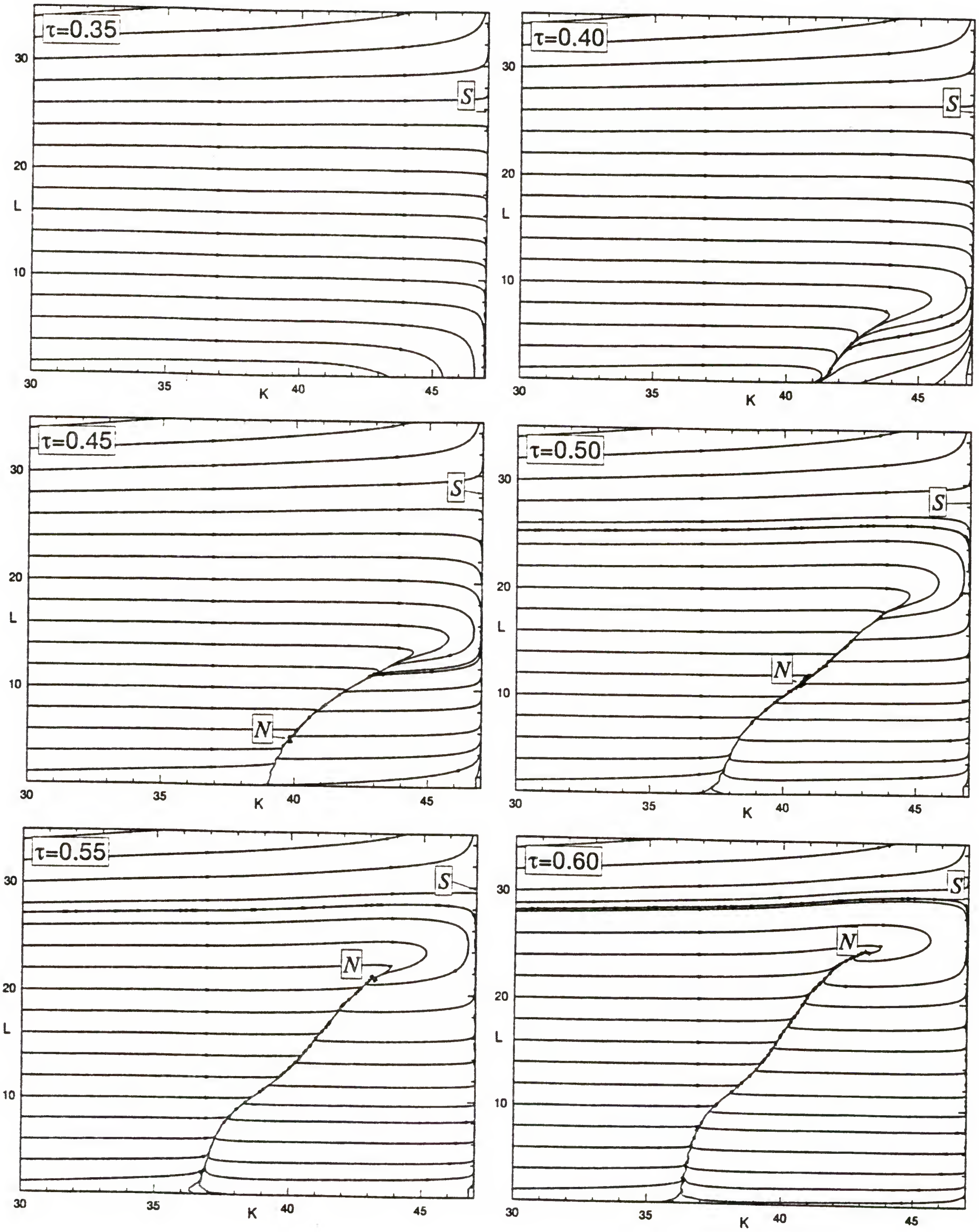

Figure 6.1 Evolution of crossflow vortical flow at J=54.

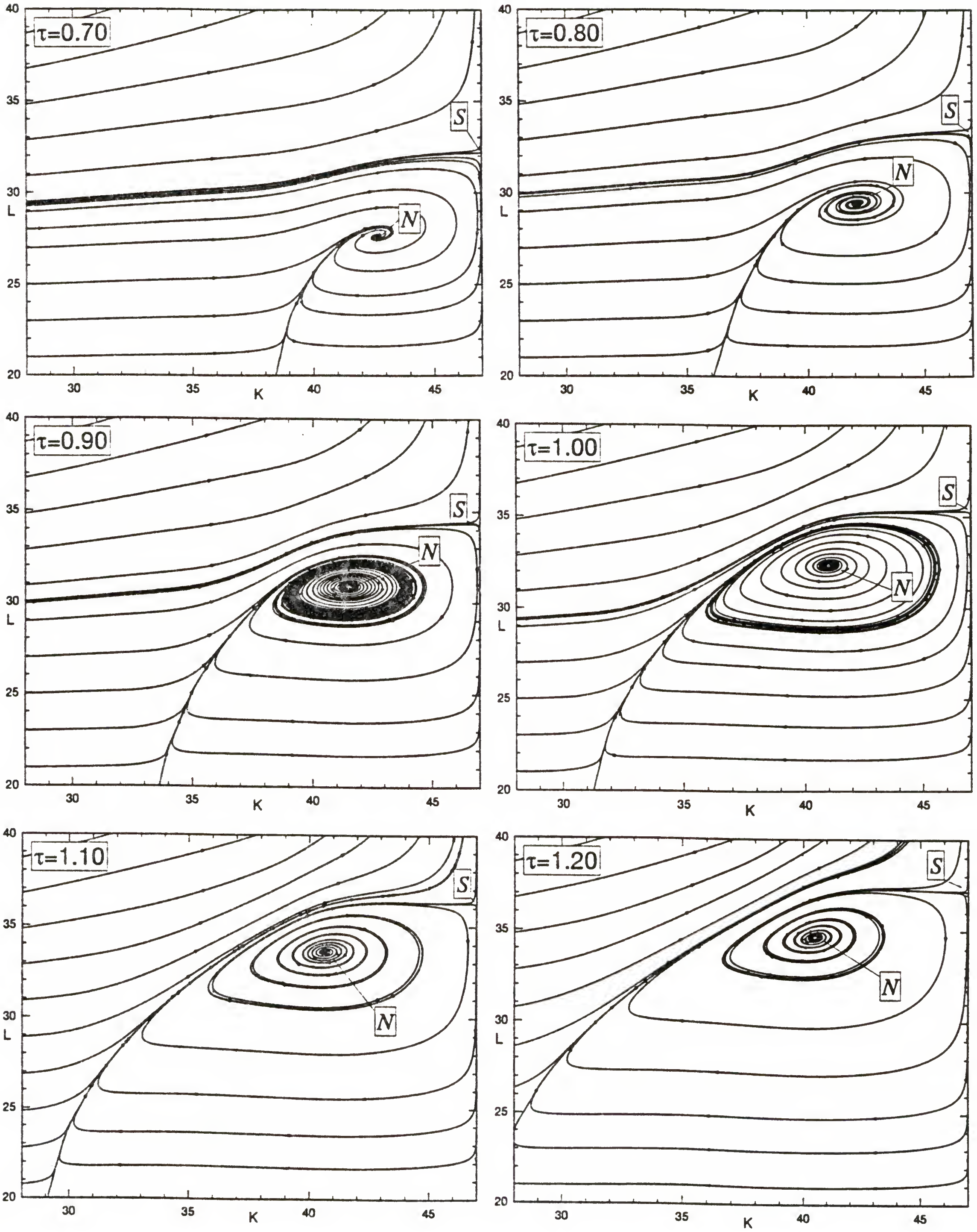

Figure 6.2 Development of crossflow spiral vortex pattern at J=54.

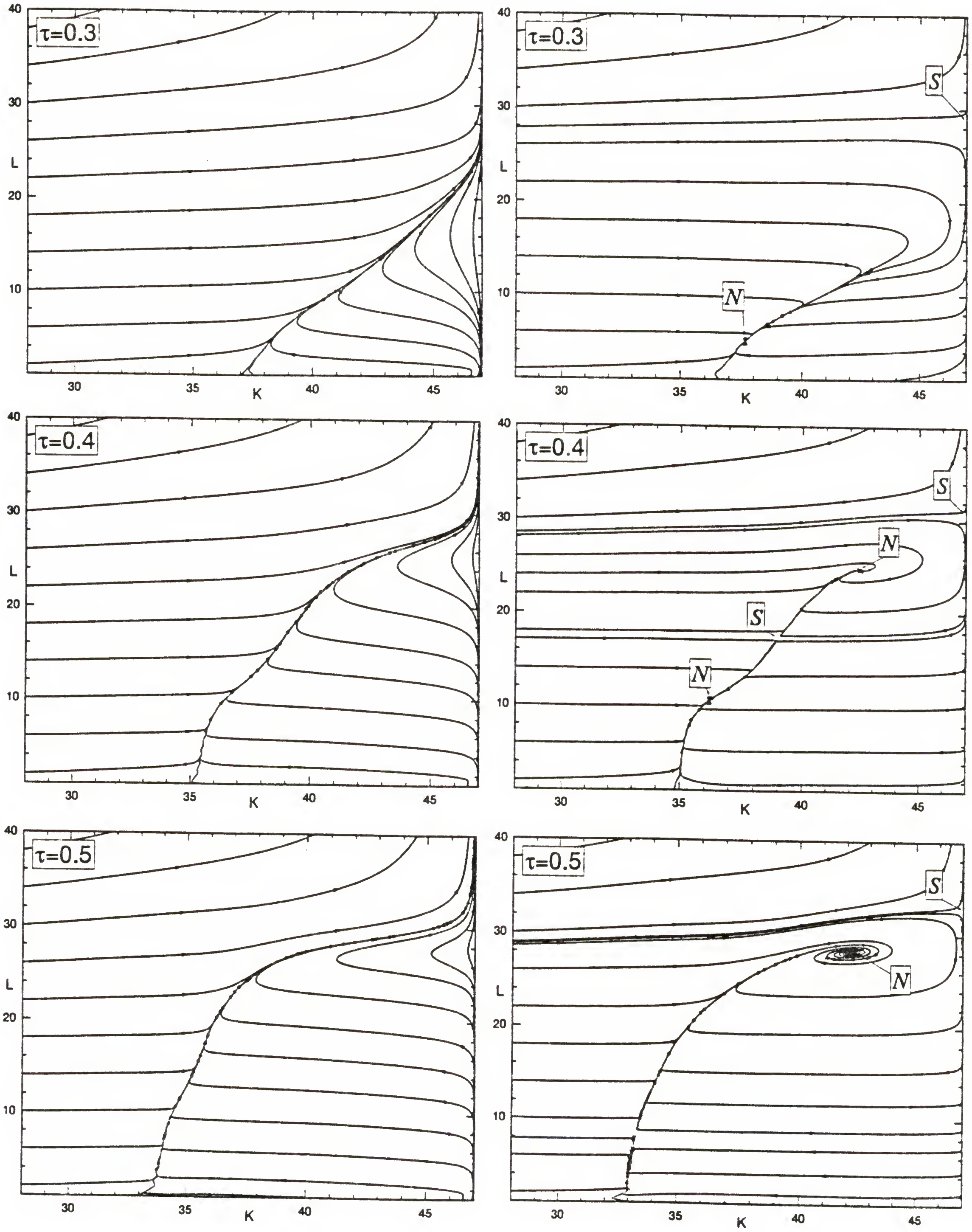

Figure 6.3 Evolution and development of crossflow vortical flow at J=19 (left) and J=87 (right).

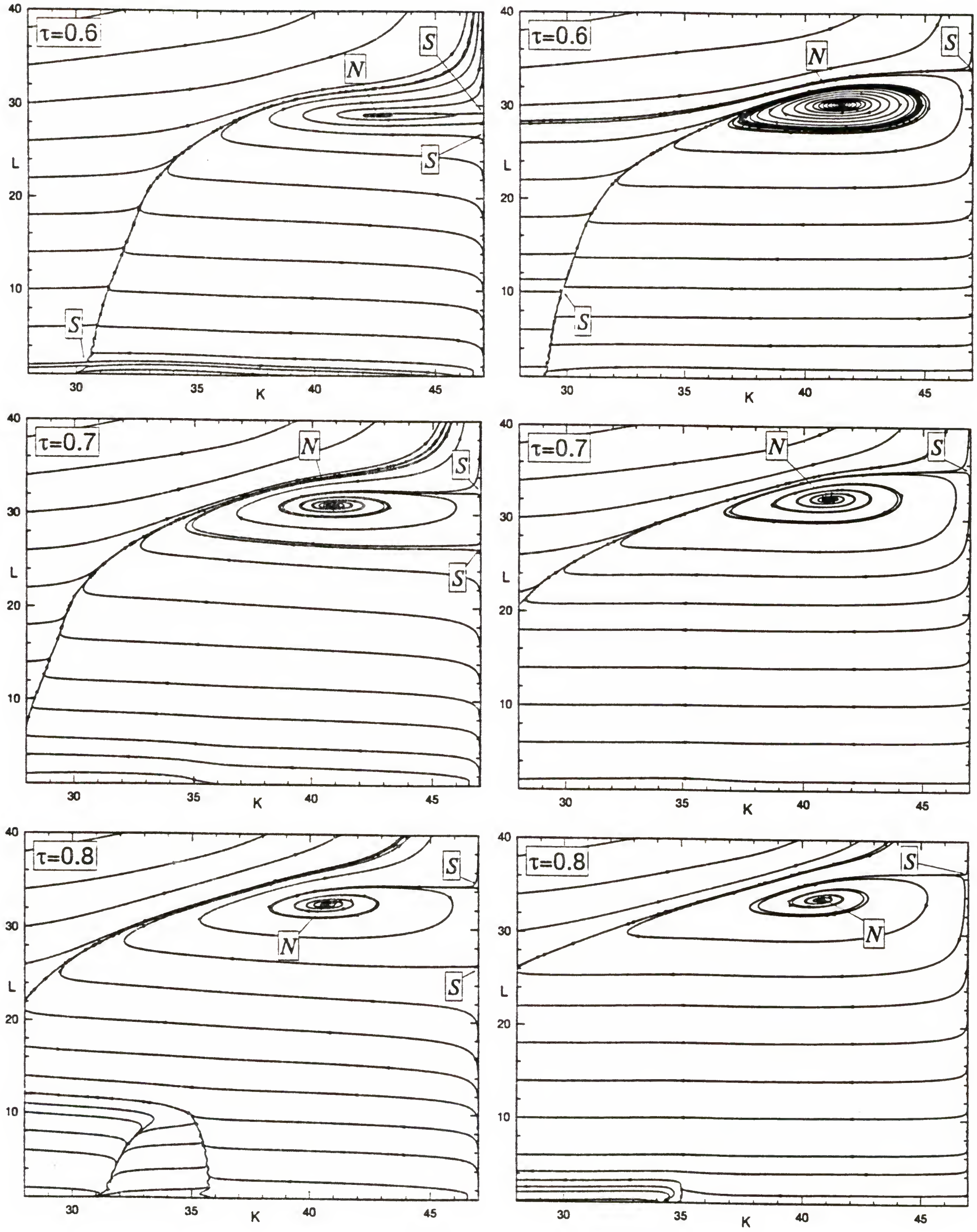

Figure 6.3 - continued.

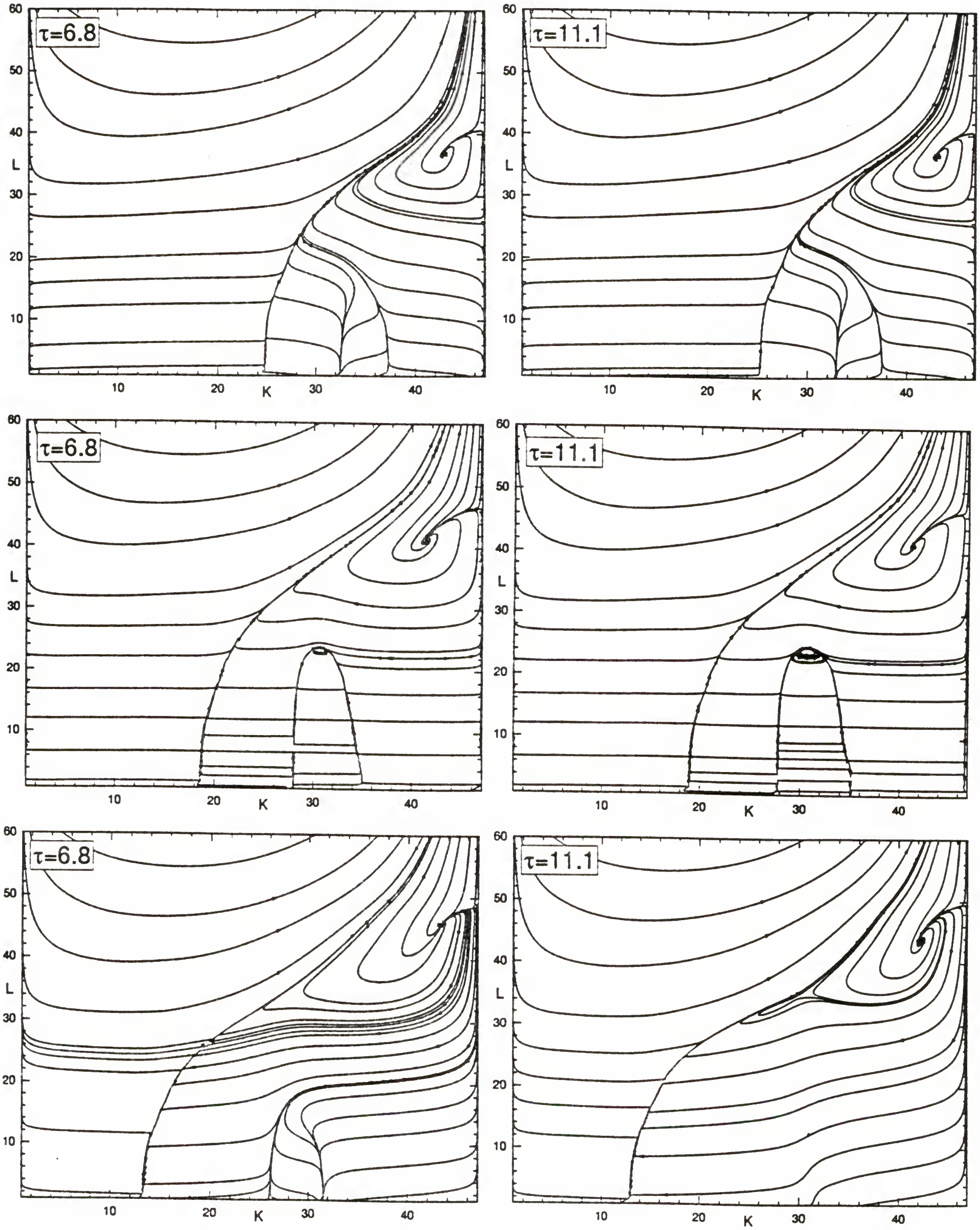

Figure 6.4 Crossflow streamtraces at J=19 (top), J=54 (middle) and J=87 (bottom) for τ=6.8 and 11.1.

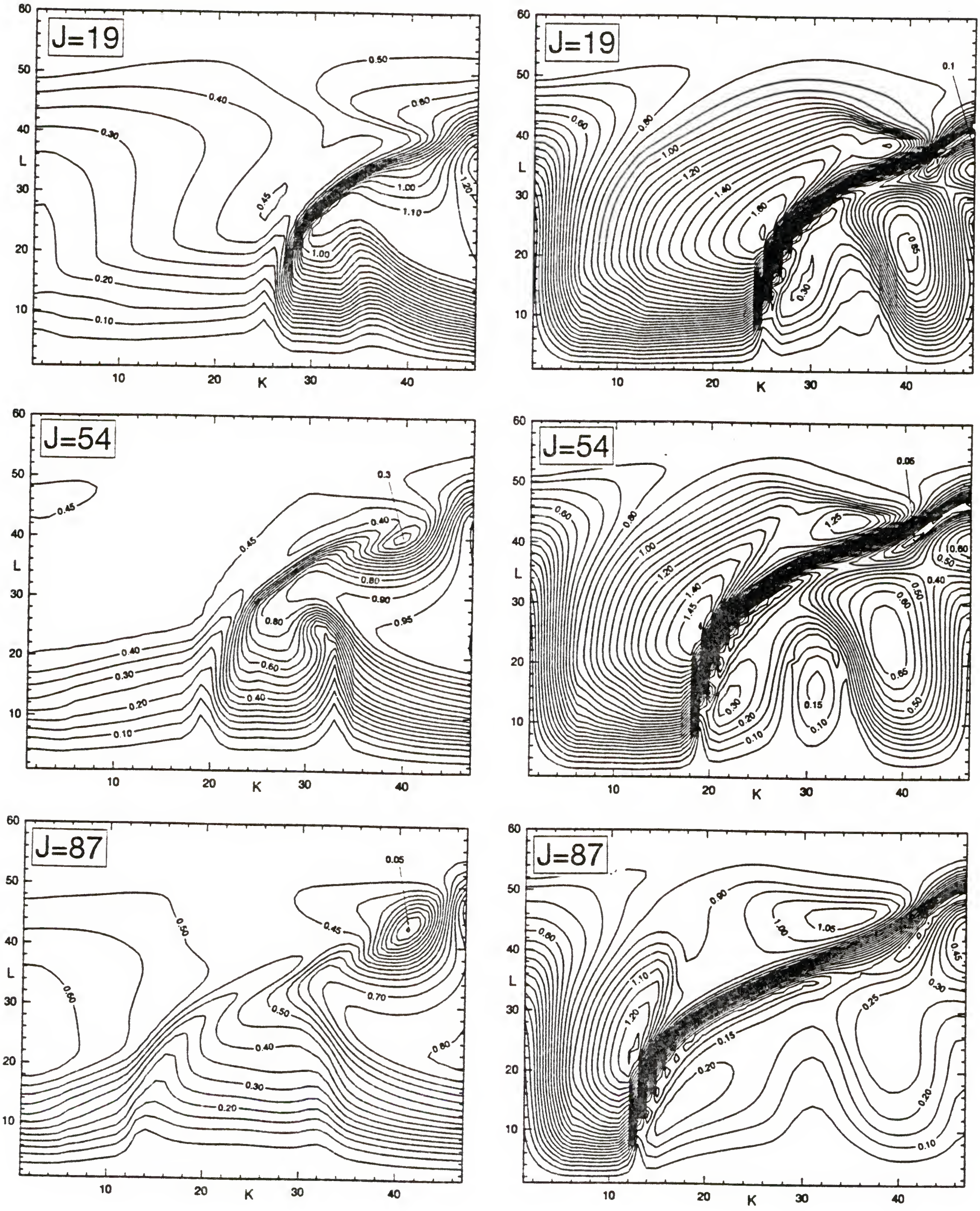

Figure 6.5 Contour plots for axial velocity component (left) and crossflow velocity magnitude (right) at $\tau = 11.1$.

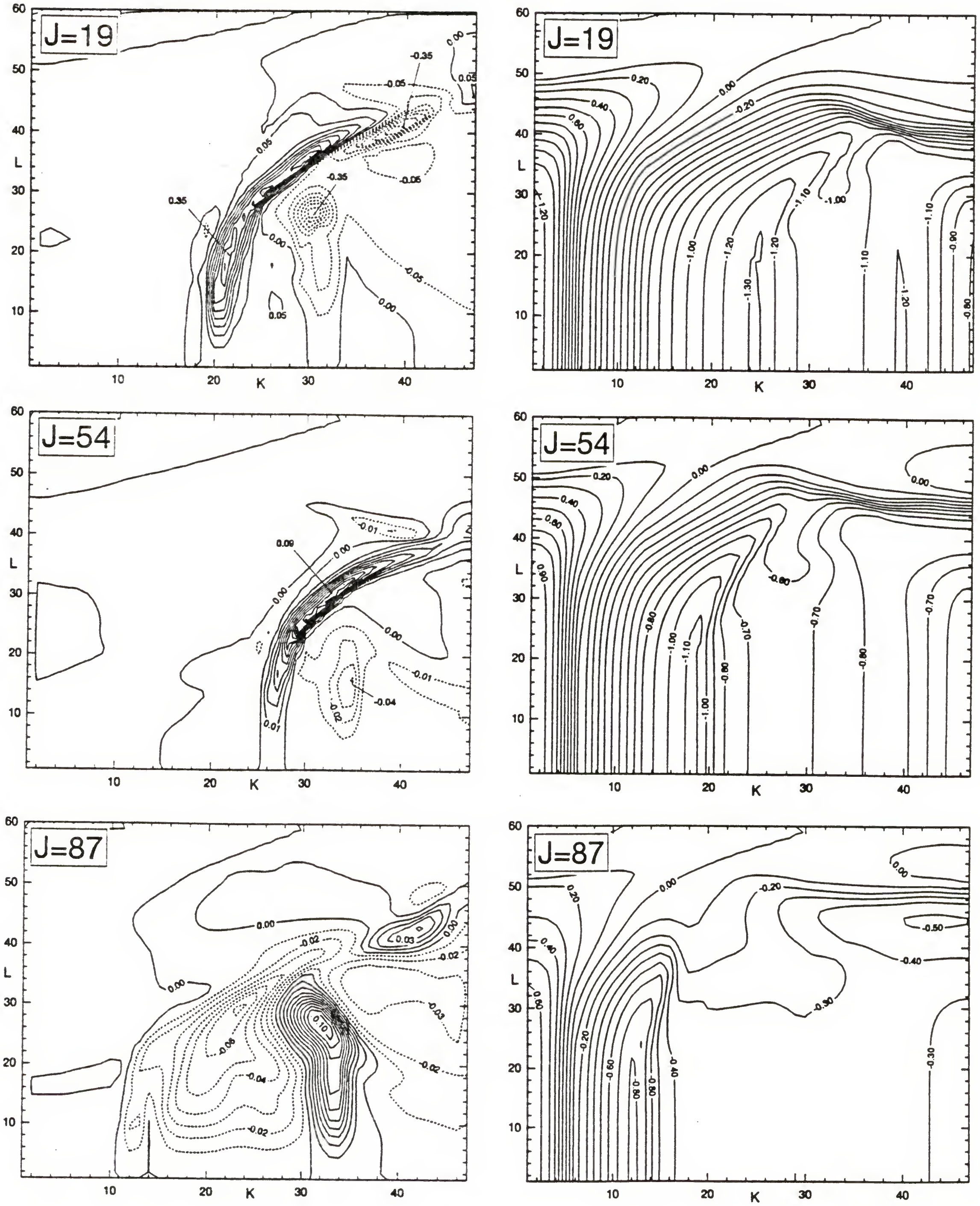

Figure 6.6 Contour plots for $\partial u/\partial \xi$ (left) and pressure coefficient Cp (right) at $\tau=11.1$.

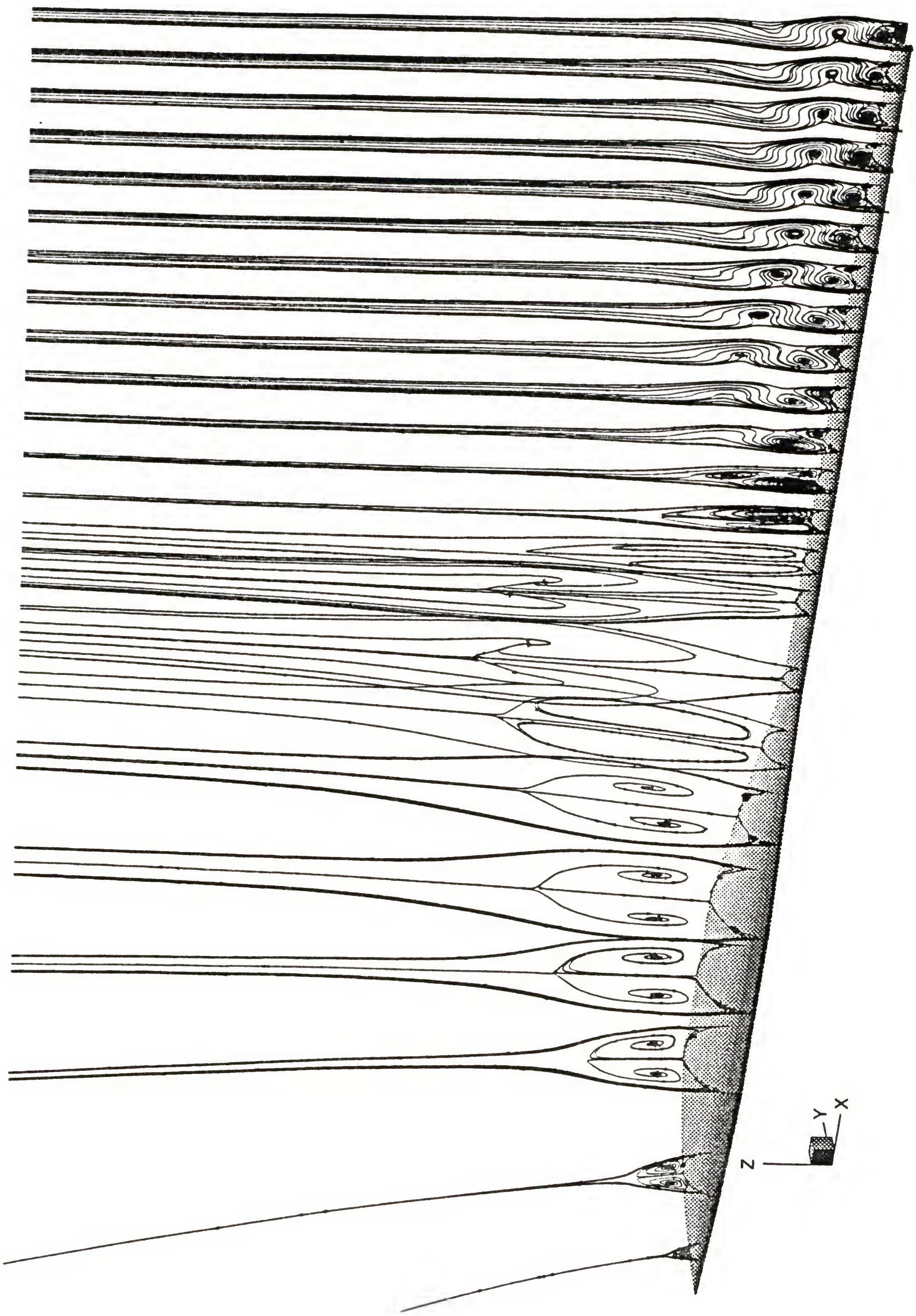

Figure 6.7 Variation of cross-sectional flow topology along the projectile at $\tau = 11.1$.

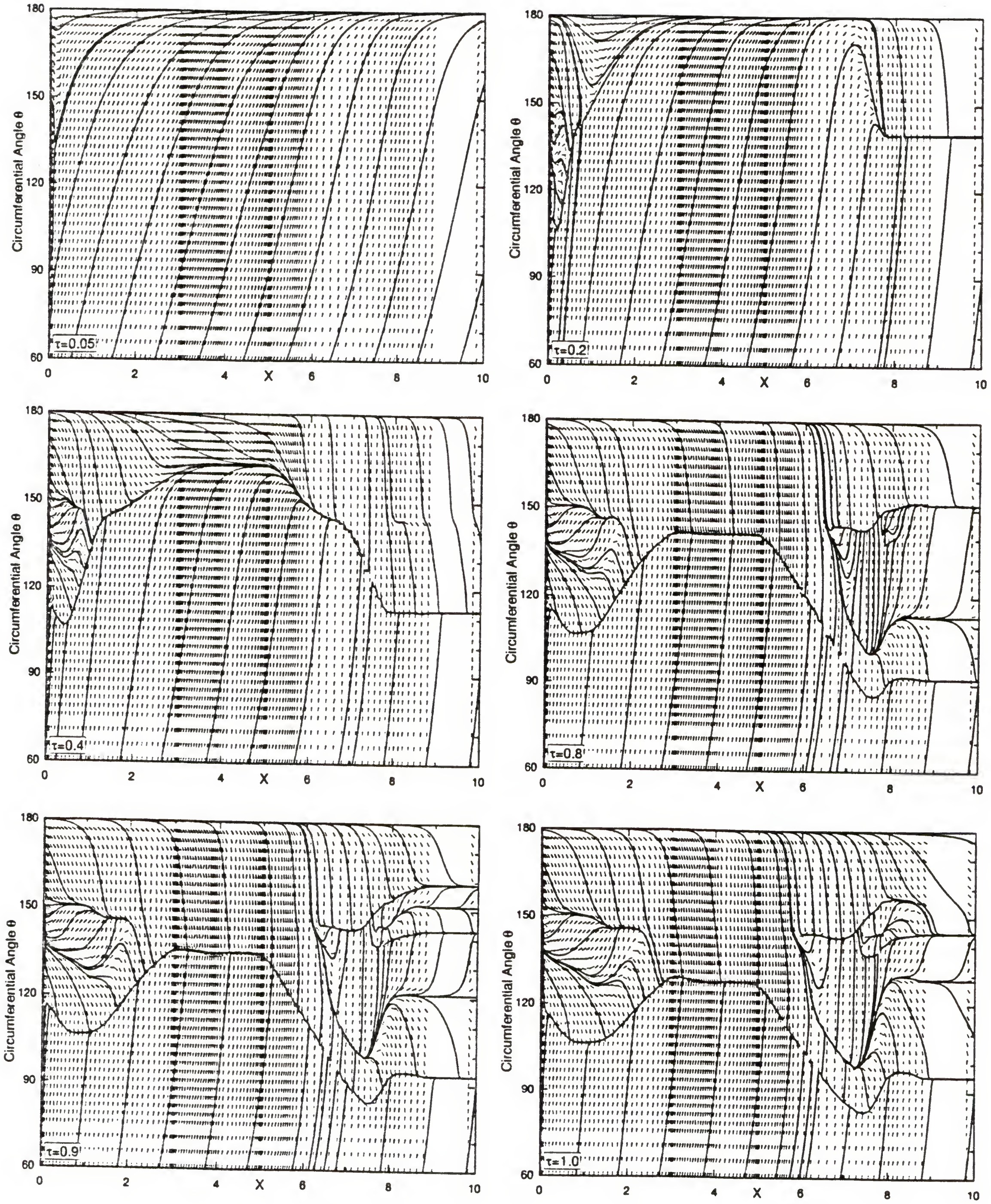

Figure 6.8 Time-sequence of surface skin-friction lines.

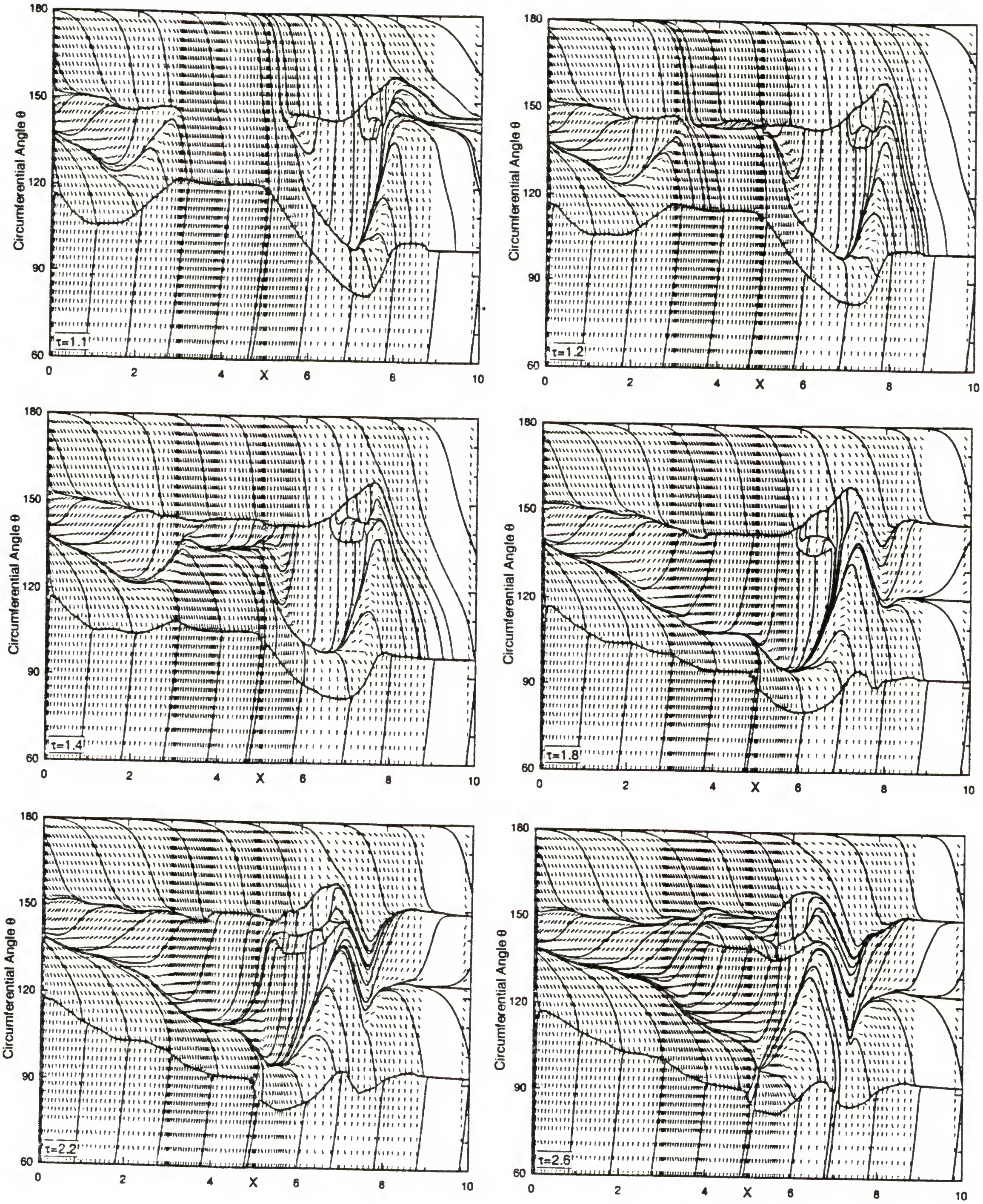

Figure 6.8- continued.

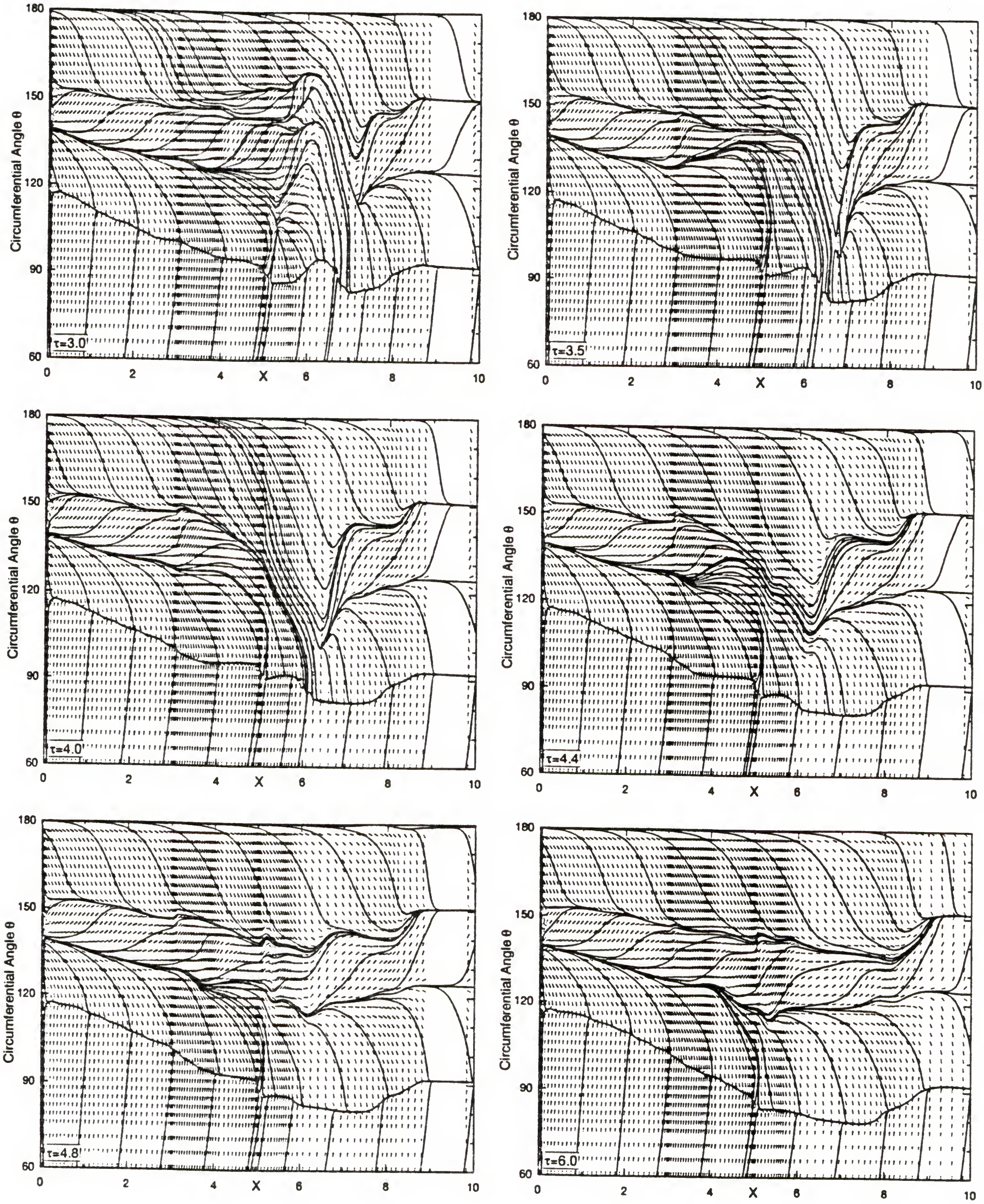

Figure 6.8 - continued.

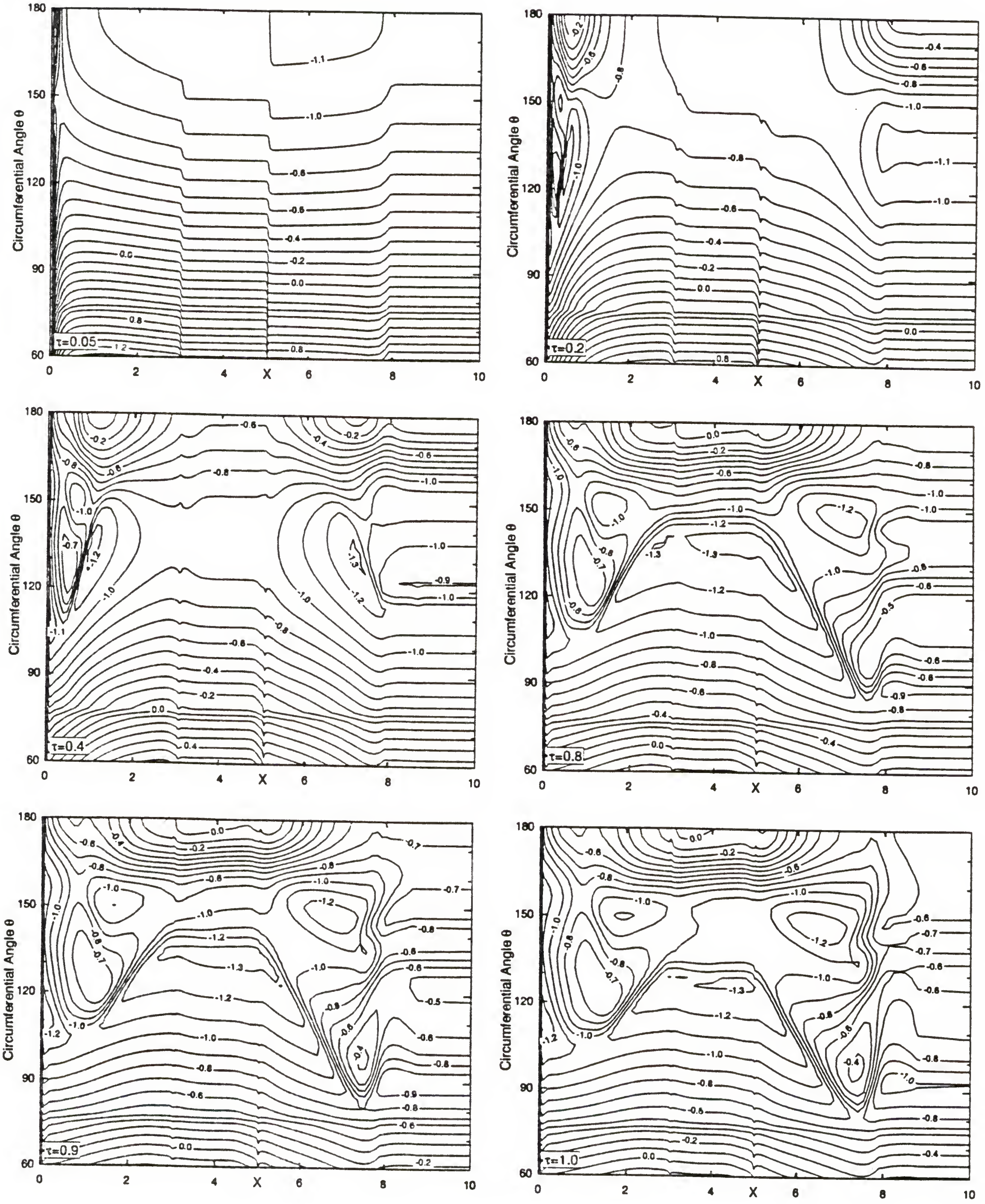

Figure 6.9 Time-sequence of surface *Cp* distribution.

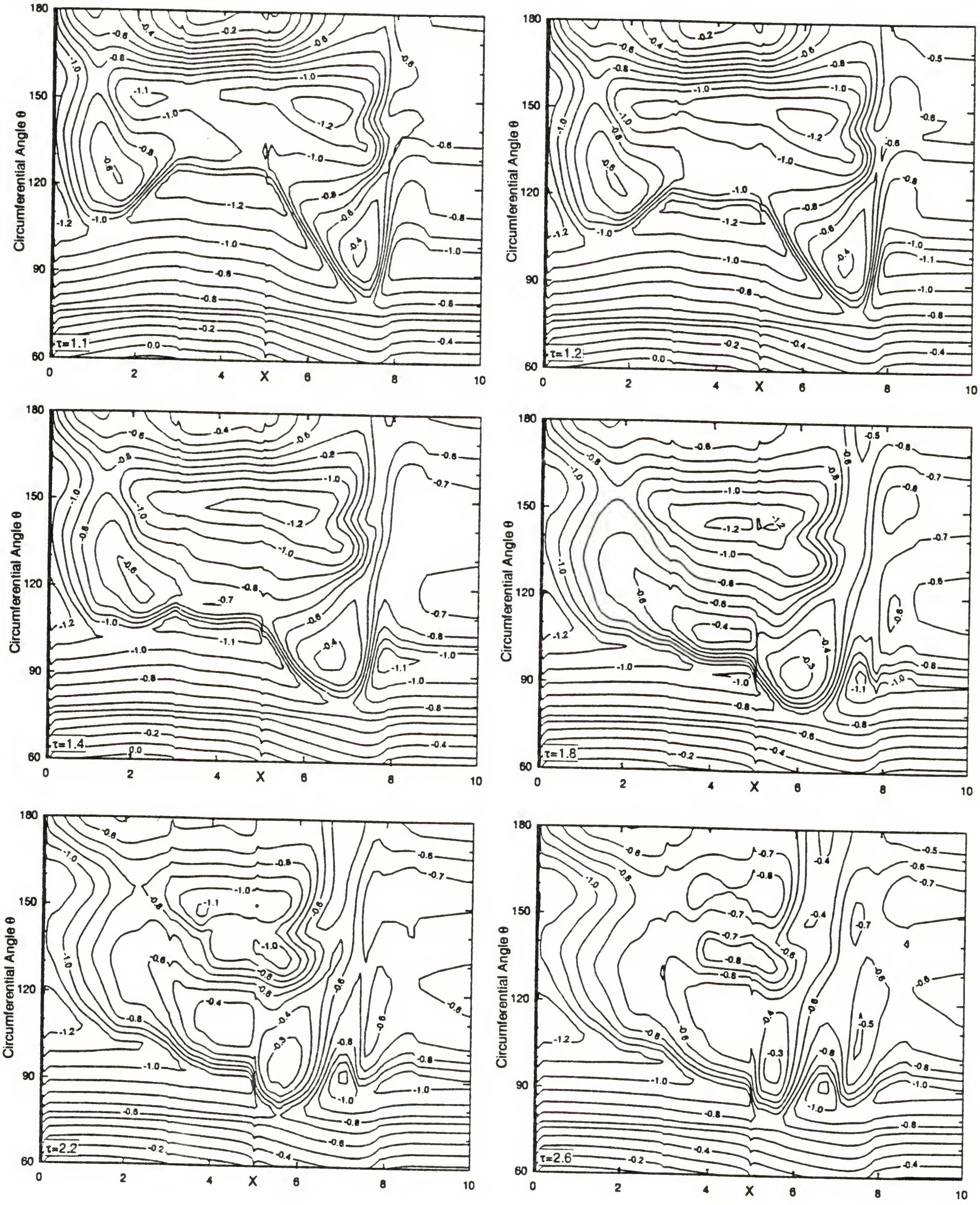

Figure 6.9 - continued.

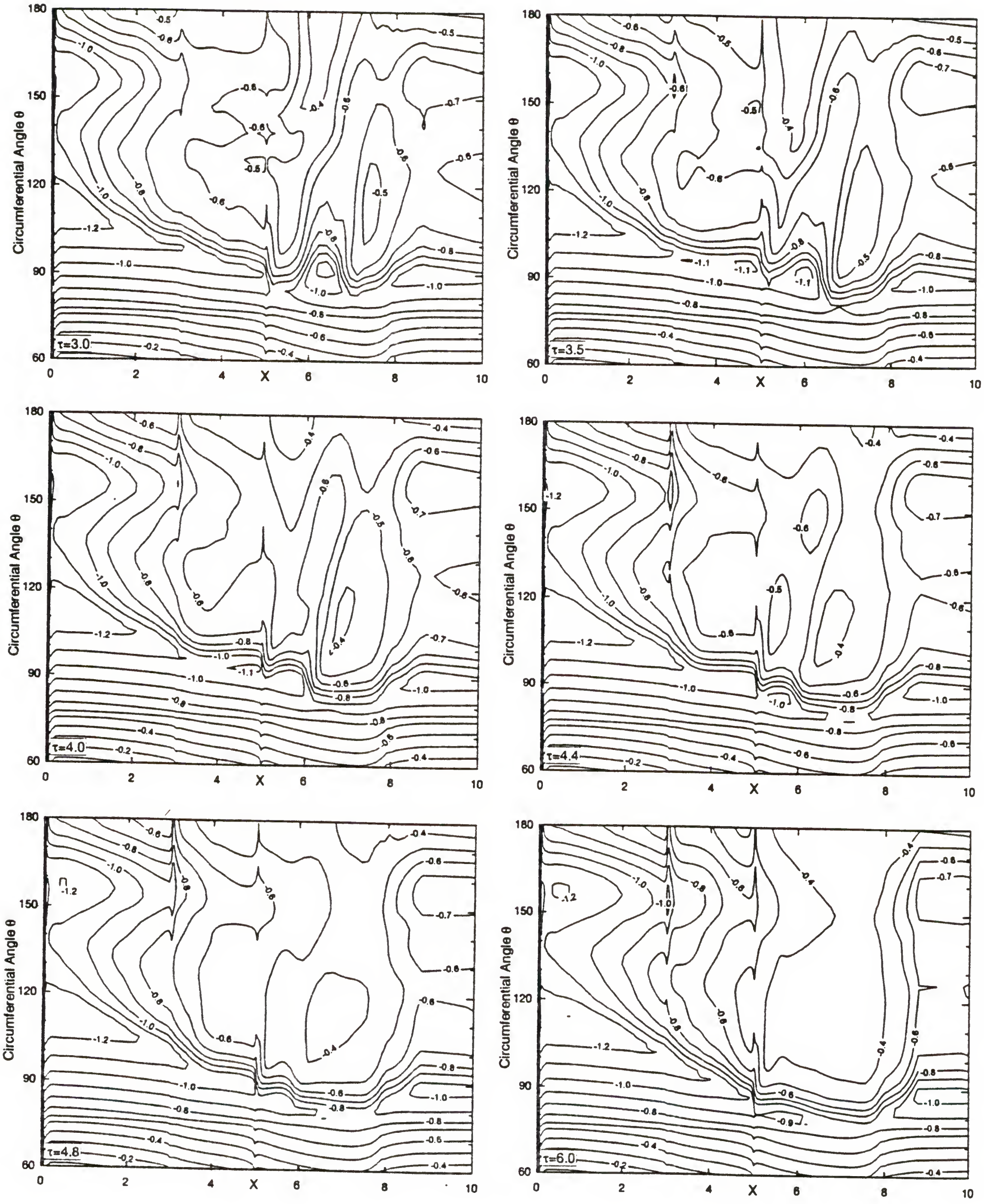

Figure 6.9 - continued.

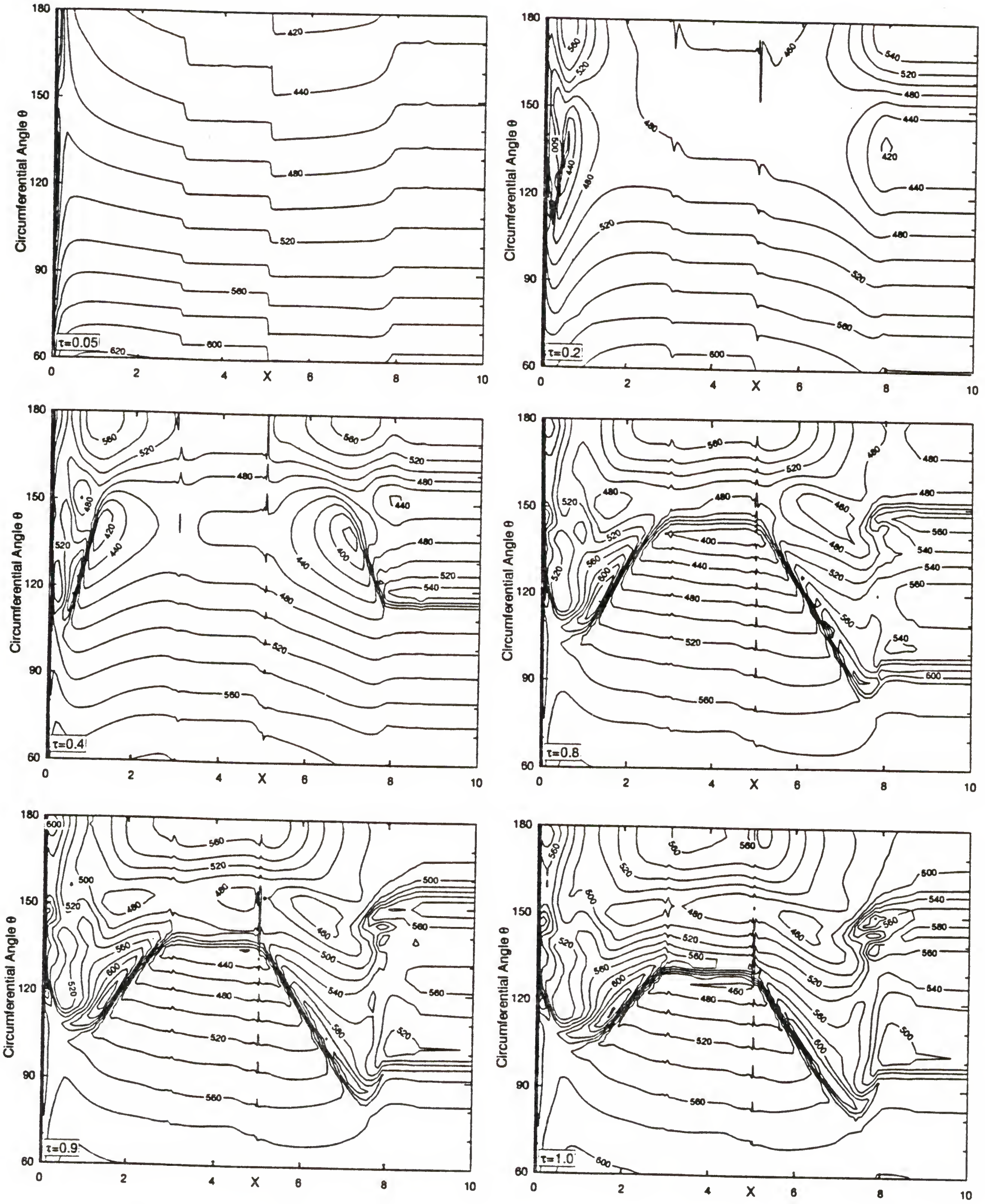

Figure 6.10 Time-sequence of surface temperature (°R) distribution.

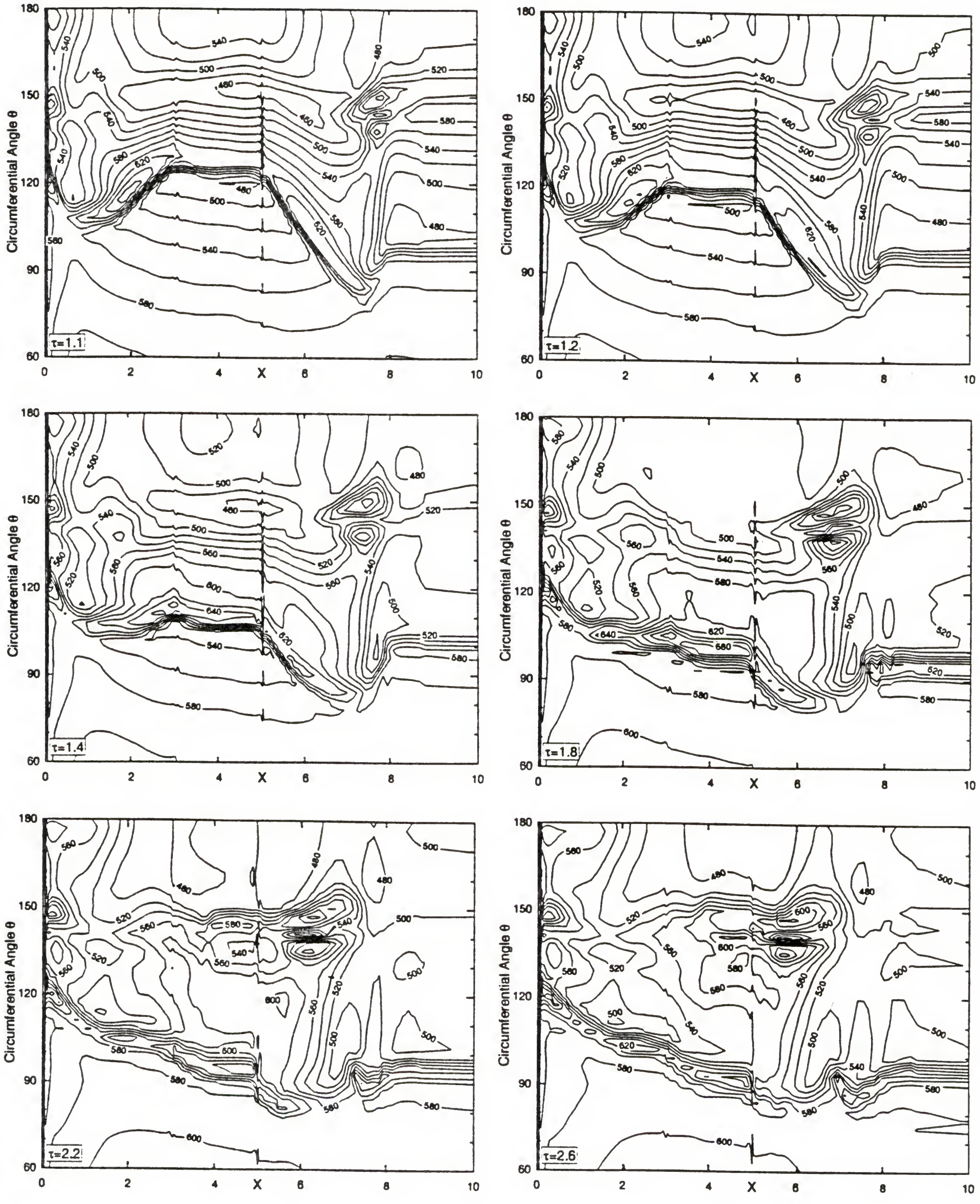

Figure 6.10 - continued.

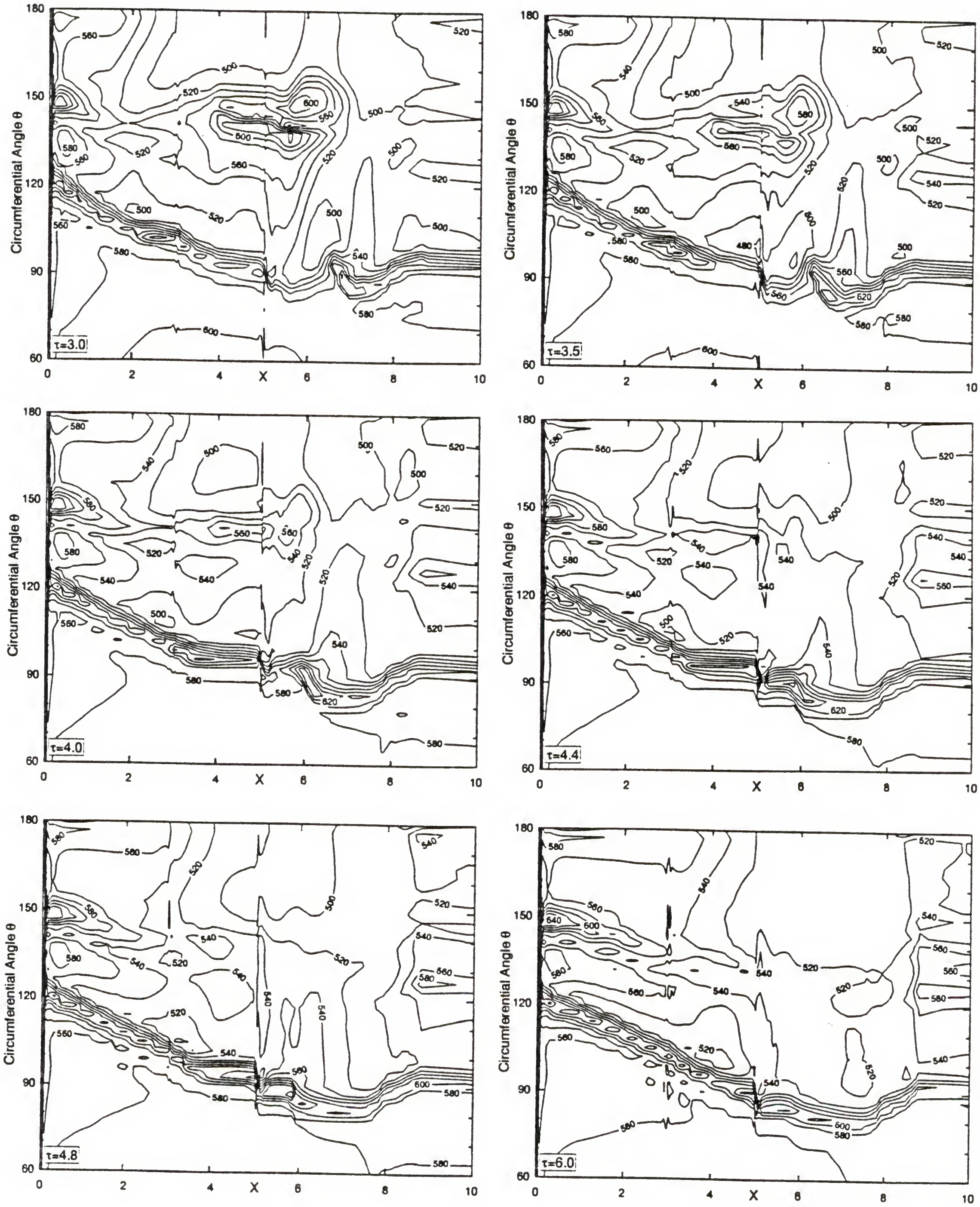

Figure 6.10 - continued.

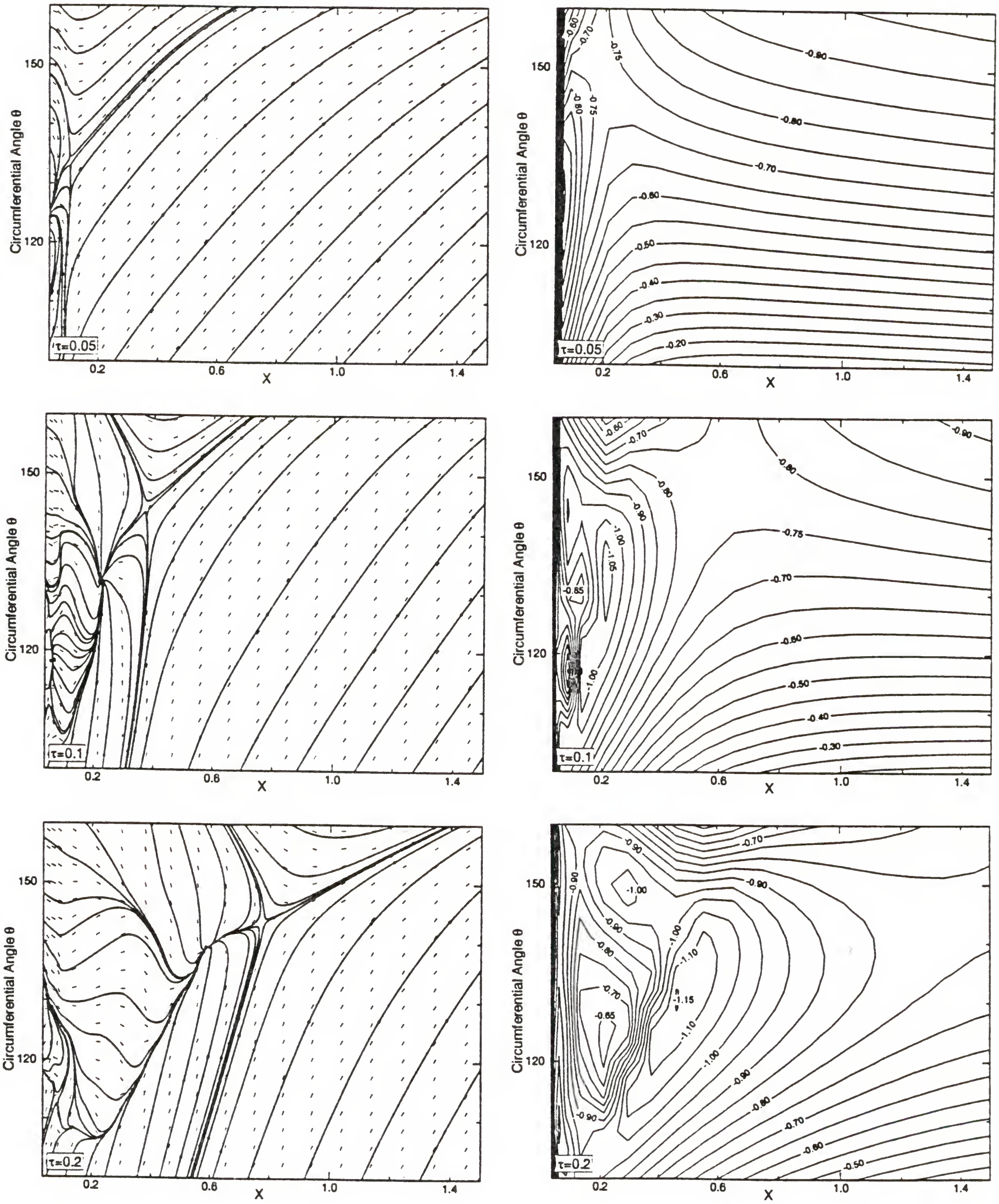

Figure 6.11 Ogive flow development - skin-friction lines (left) and surface Cp distribution (right).

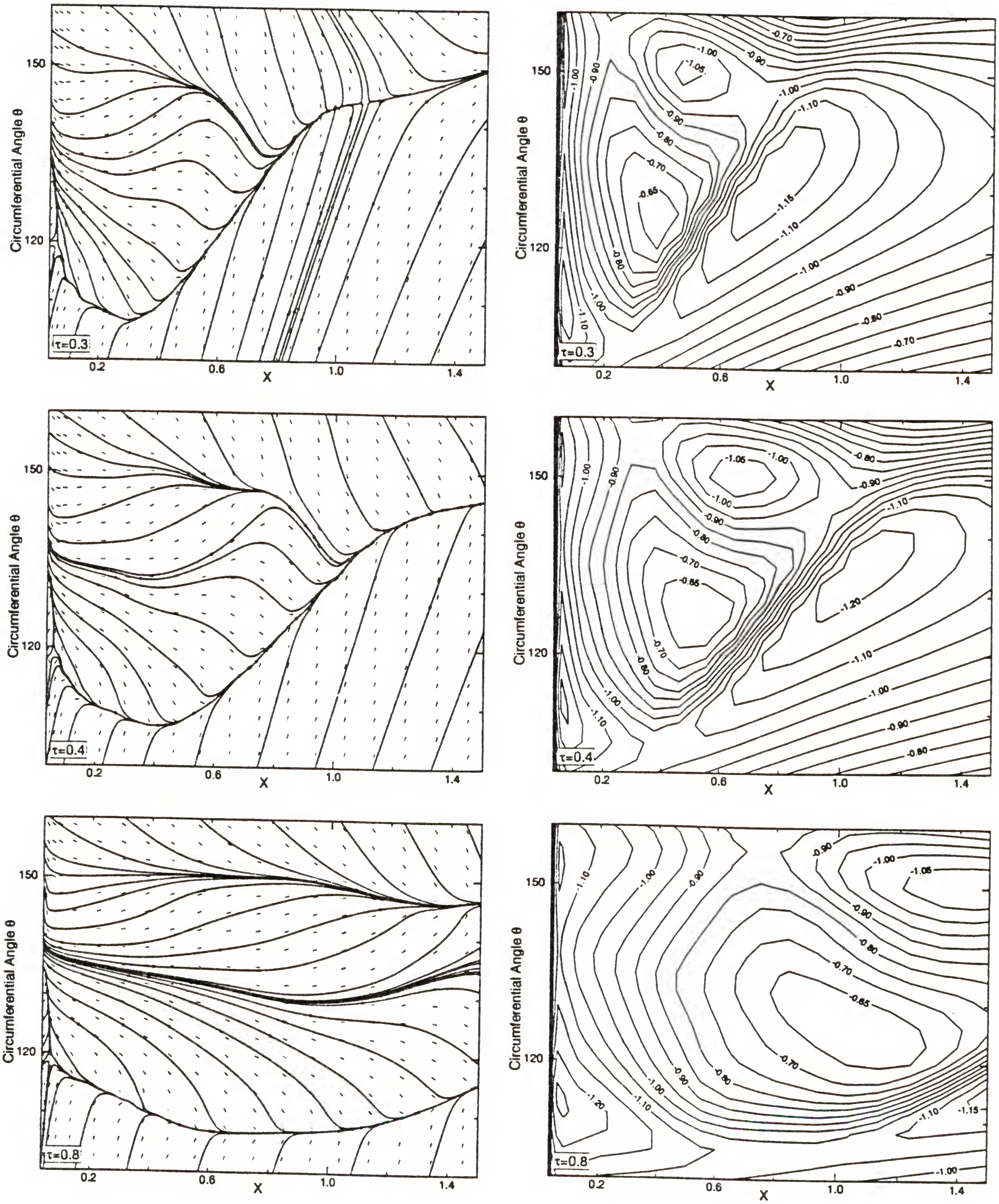

Figure 6.11 - continued.

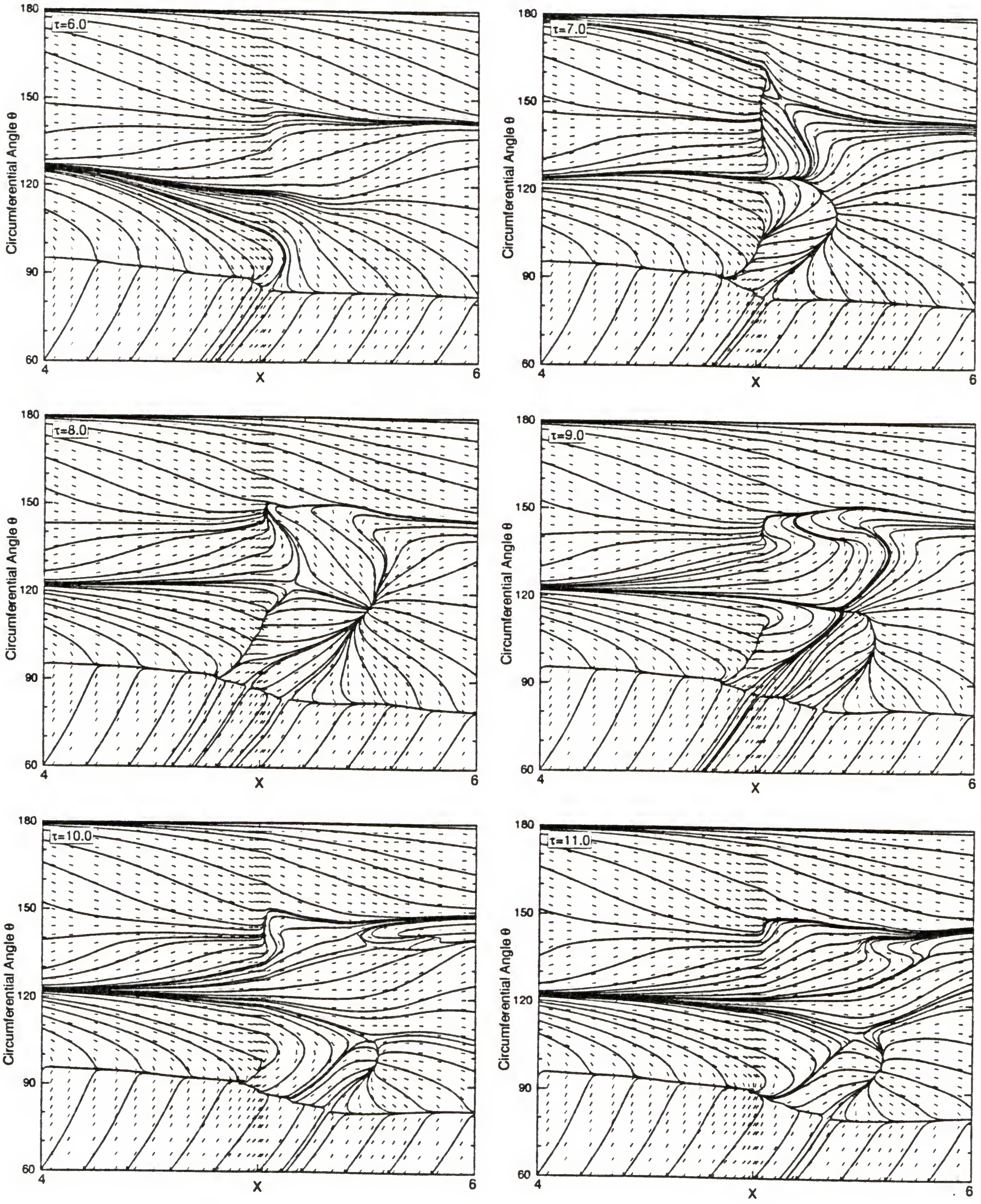

Figure 6.12 Transition of longitudinal flow separation.

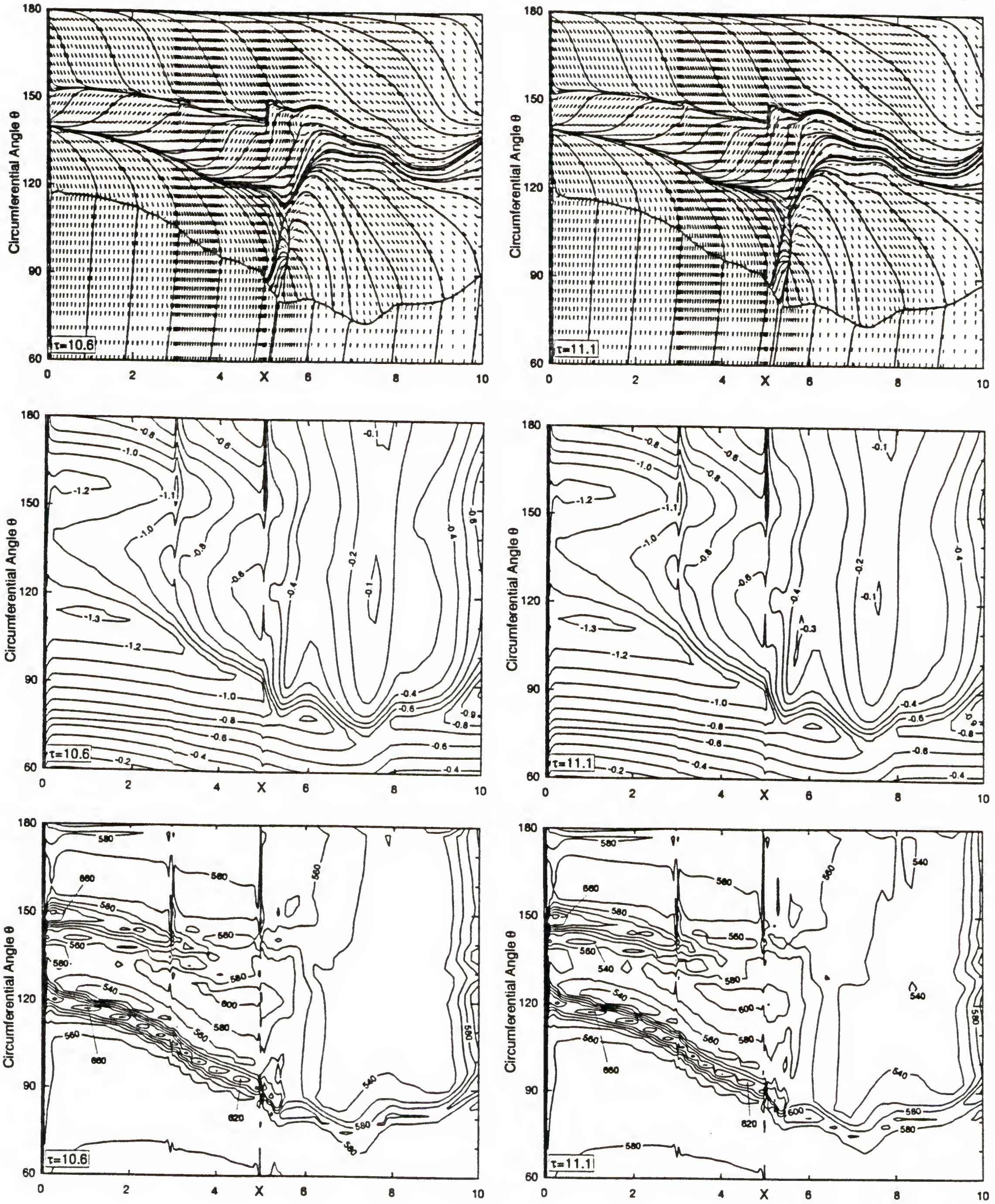

Figure 6.13 Convergence of surface flow patterns - skin-friction lines (top), *Cp* (middle), and temperature (°R) (bottom).

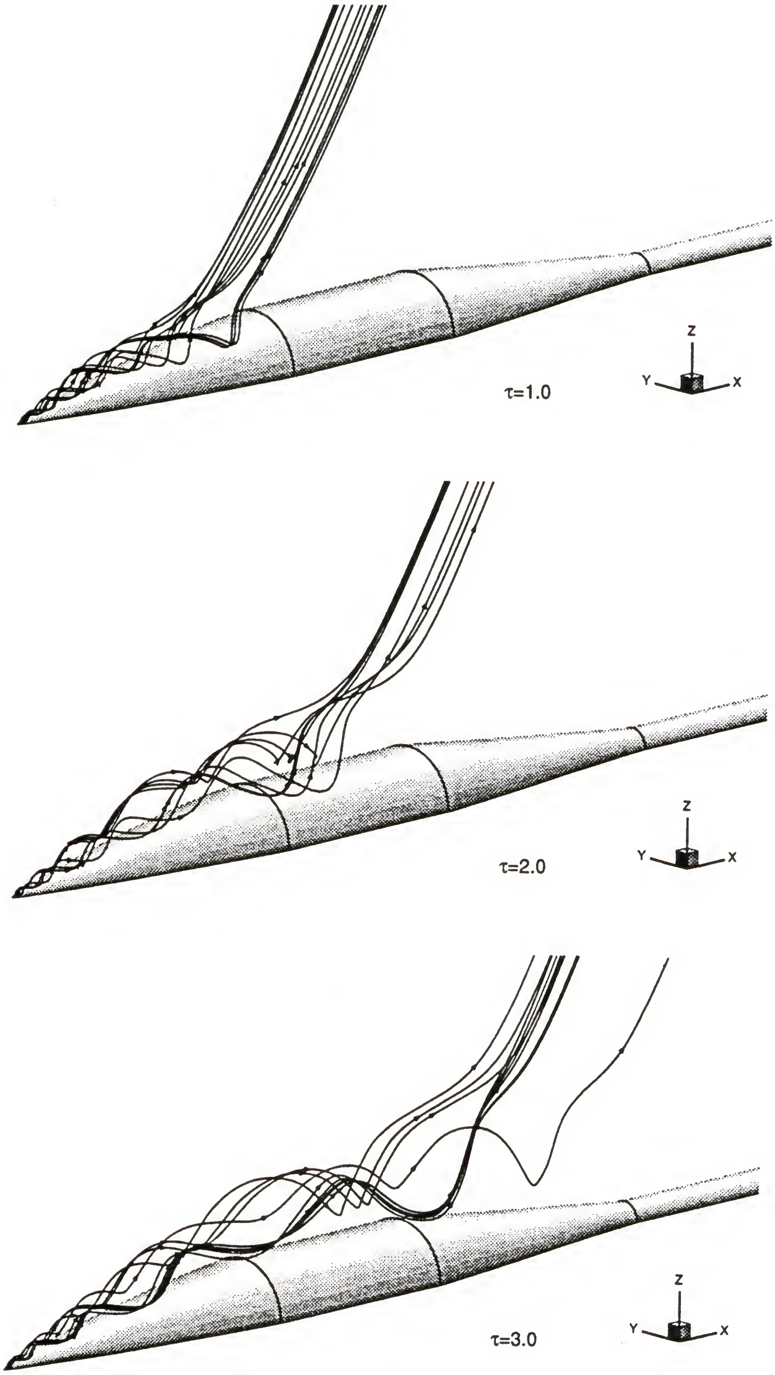

Figure 6.14 3-D instantaneous streamtraces from J=4 (x=0.086).

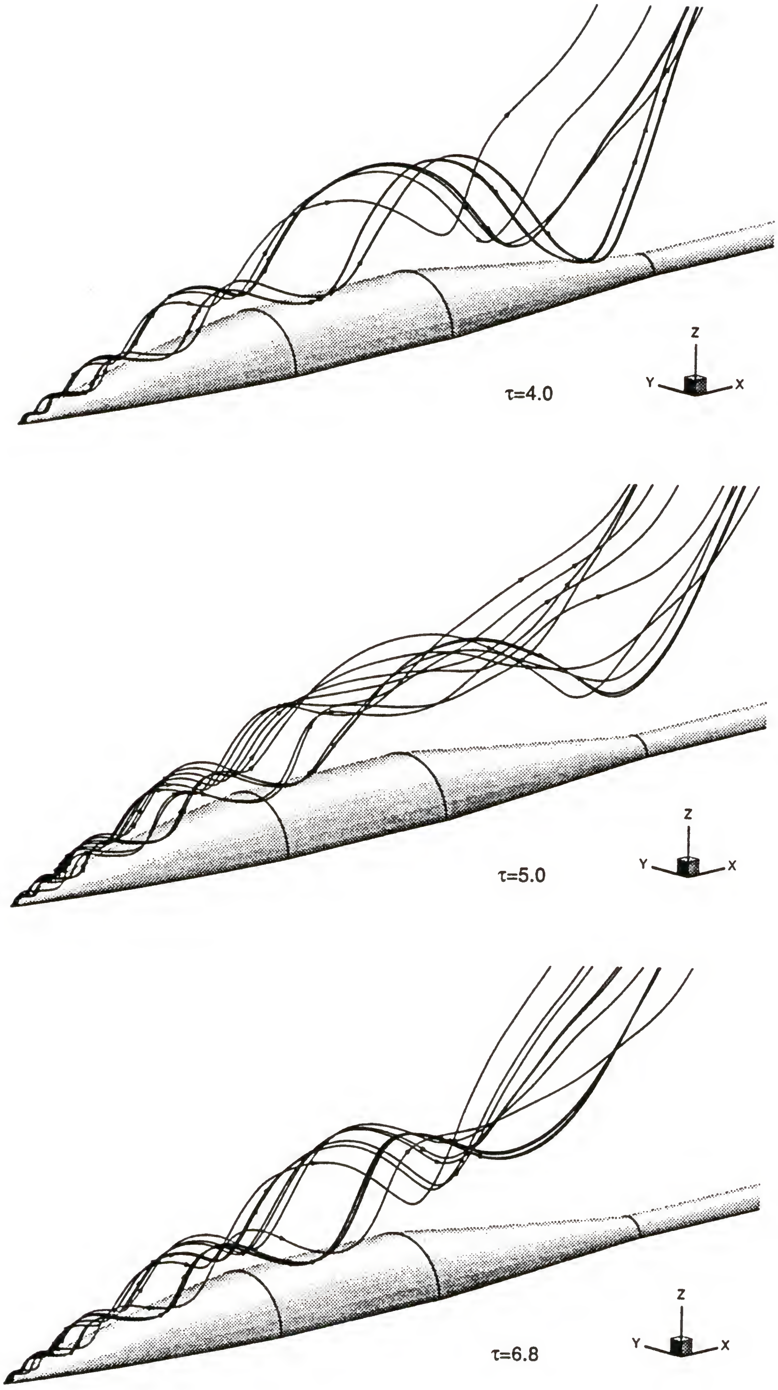

Figure 6.14 - continued.

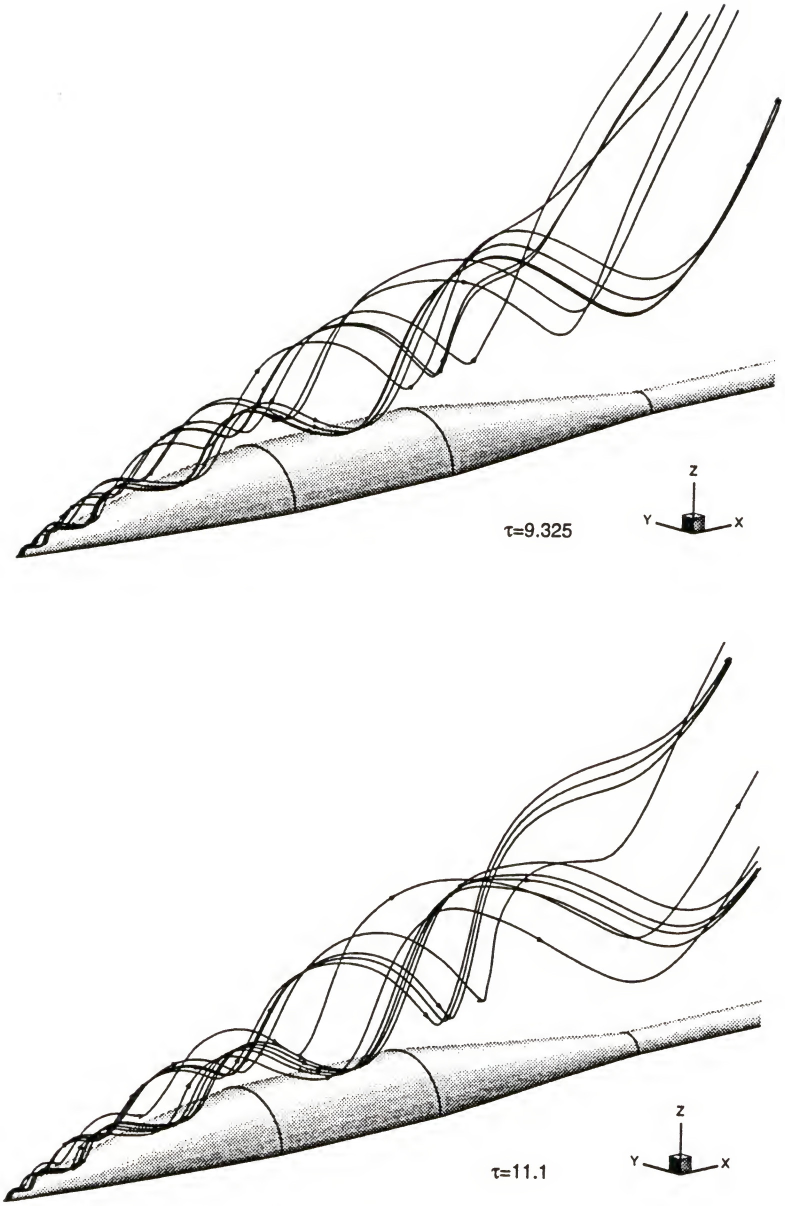

Figure 6.14 - continued.

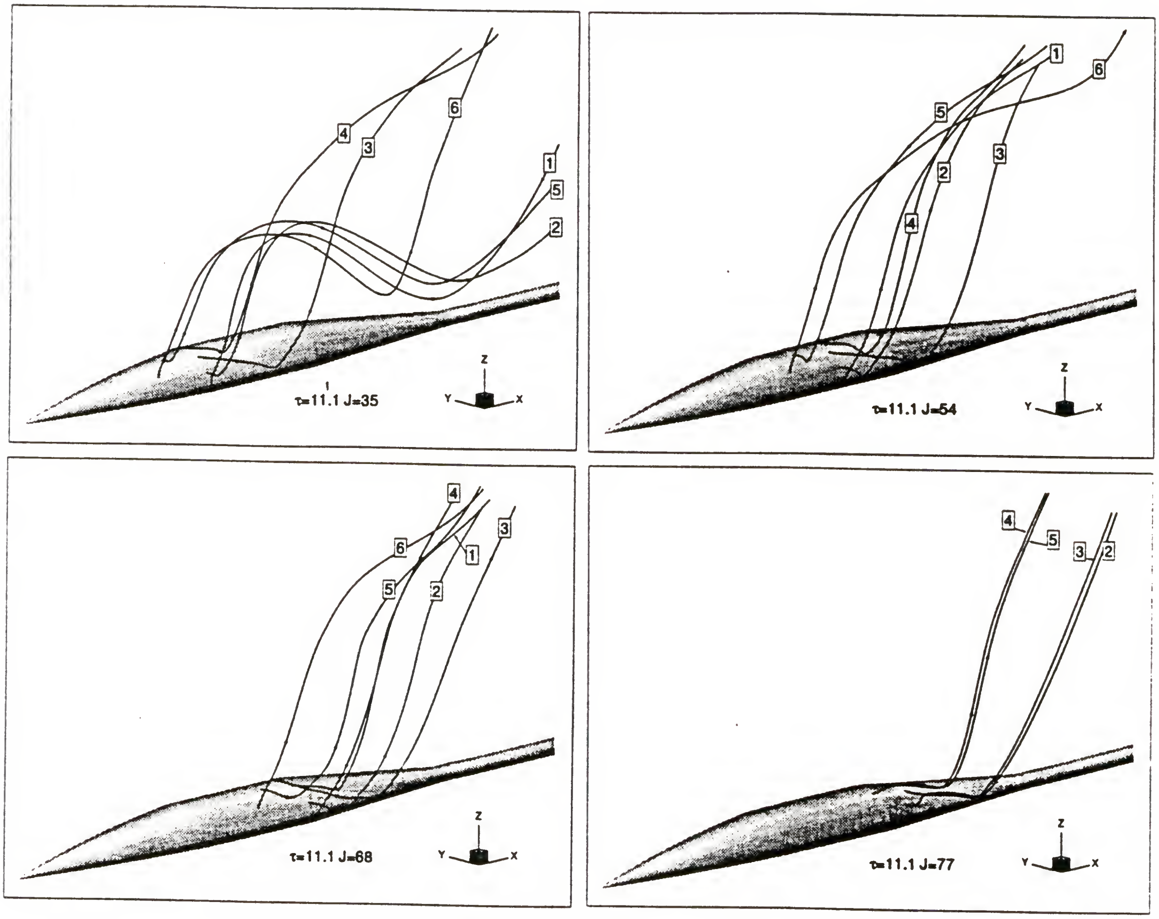

Figure 6.15 3-D streamtraces from J=35, 54, 68 and 77 at τ=11.1.

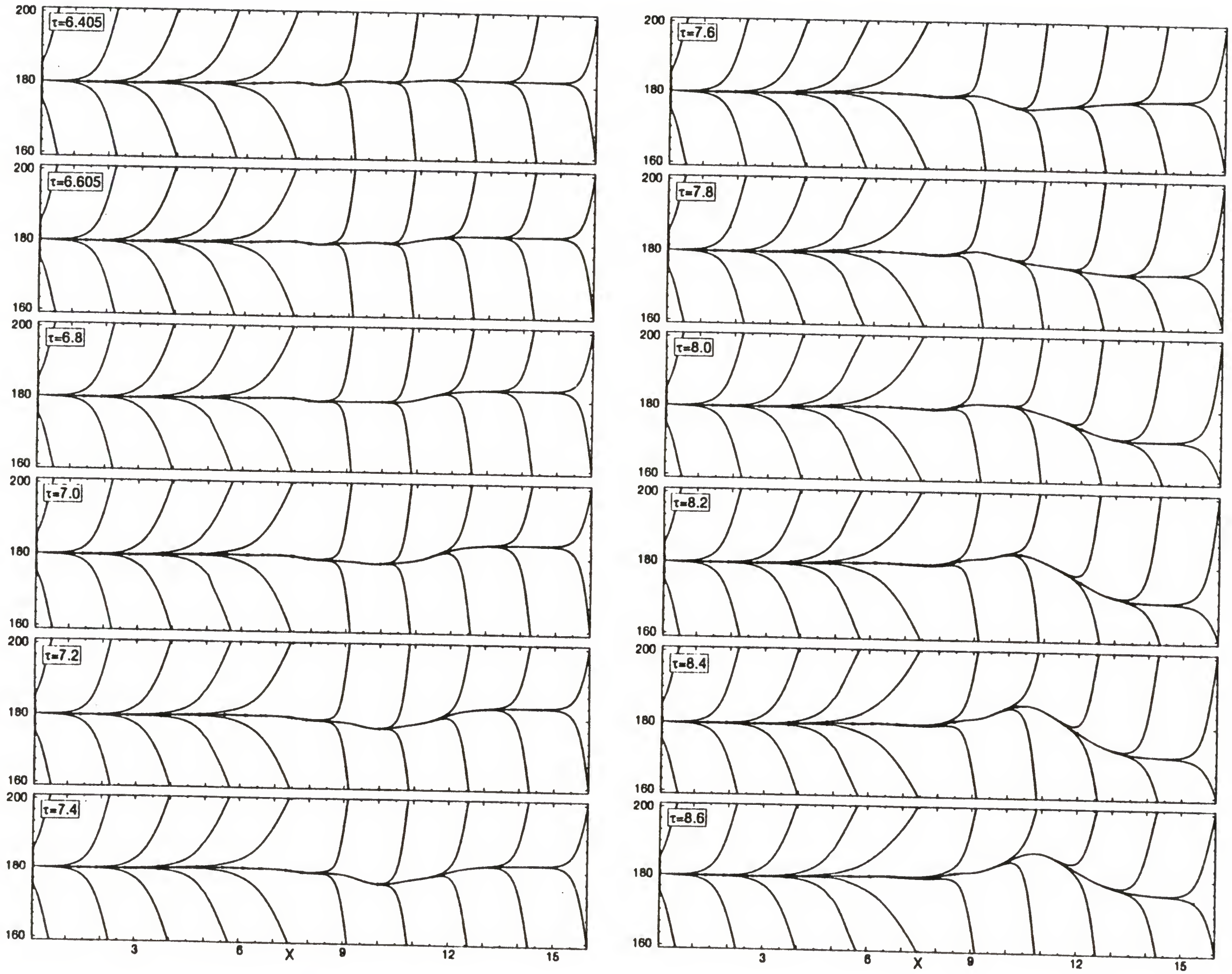

Figure 6.16 Oscillation of primary attachment line near $\theta = 180°$.

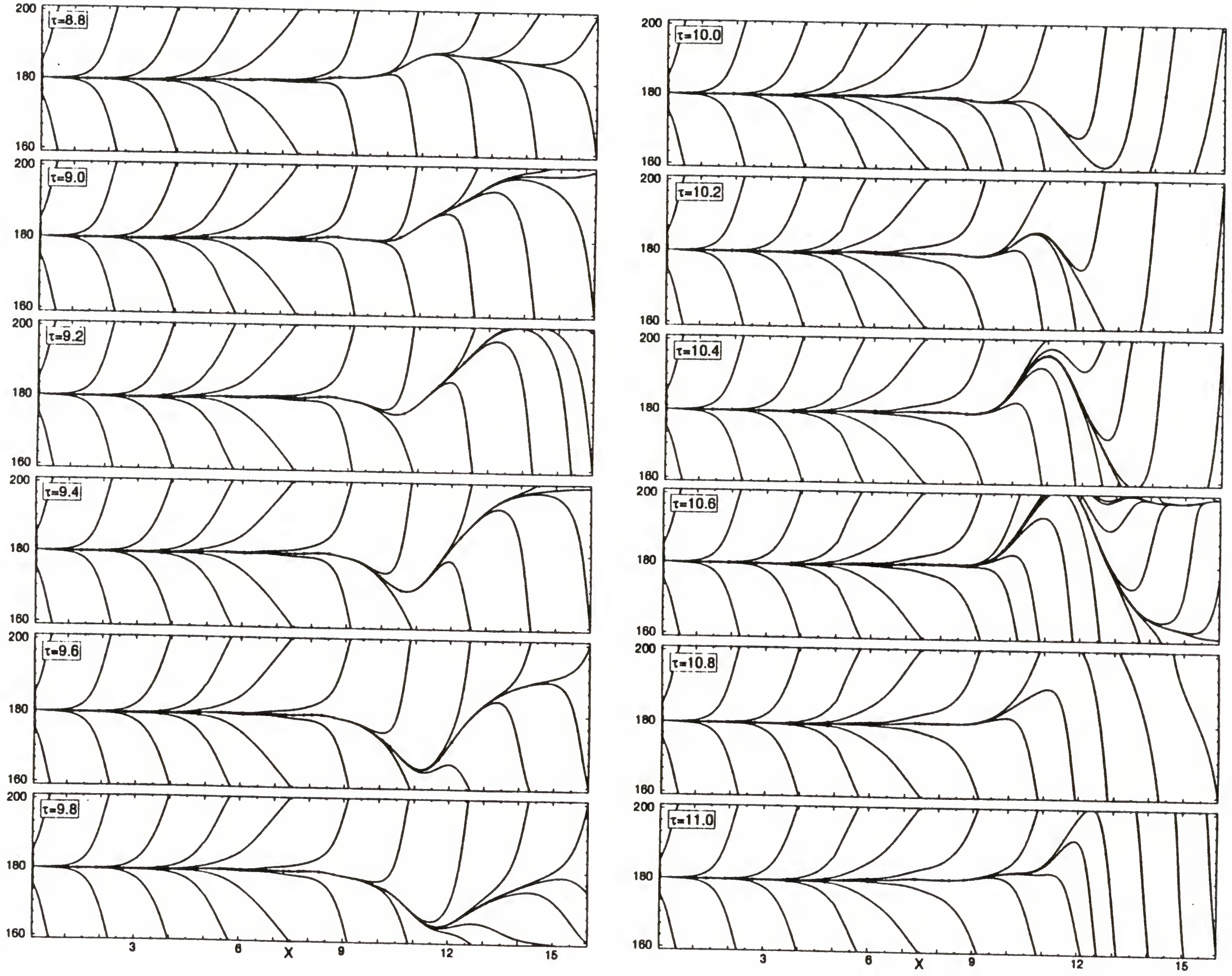

Figure 6.16 - continued.

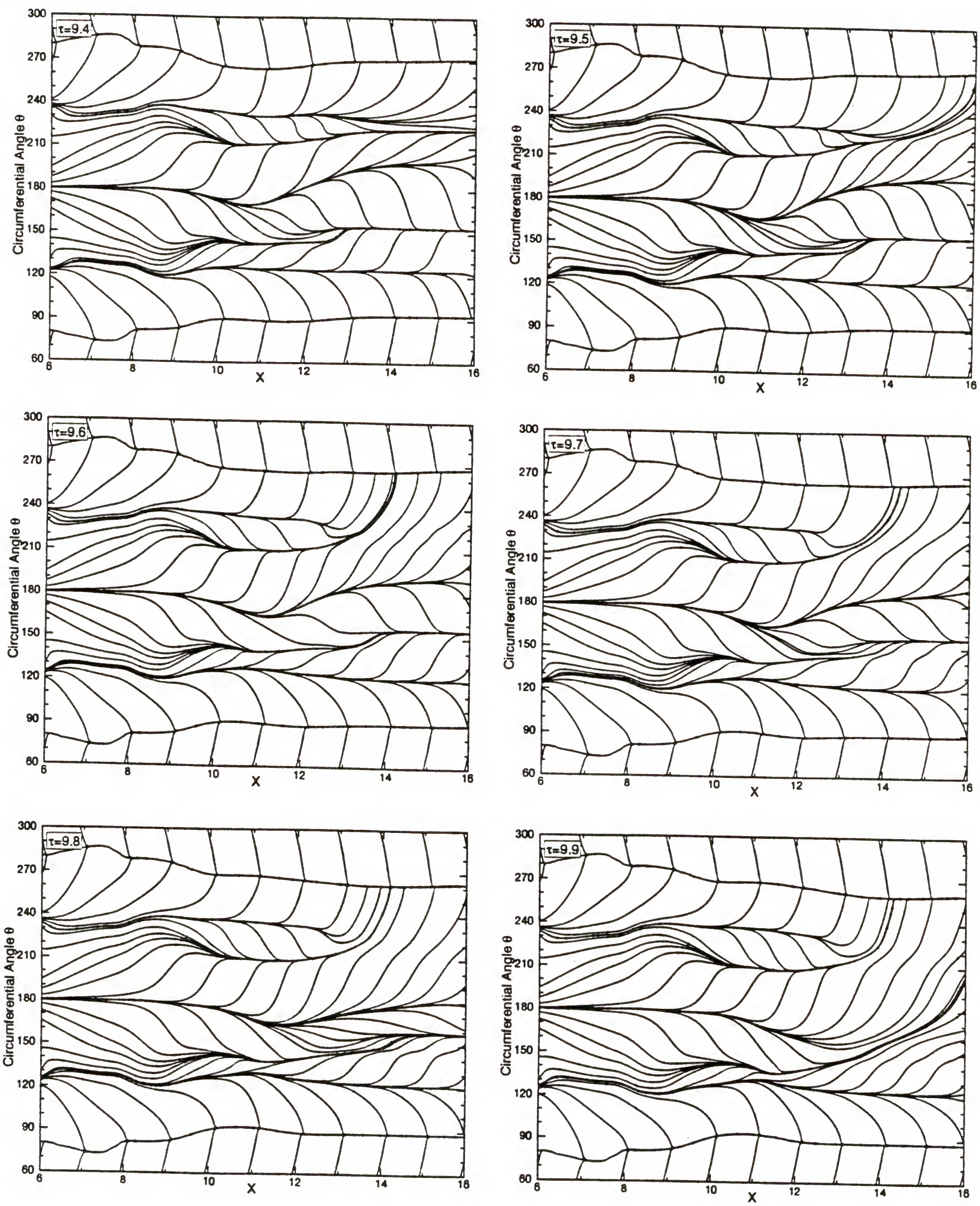

Figure 6.17 Oscillation of skin-friction lines on boattail ($x \leq 7.82$) and sting ($x \geq 7.82$).

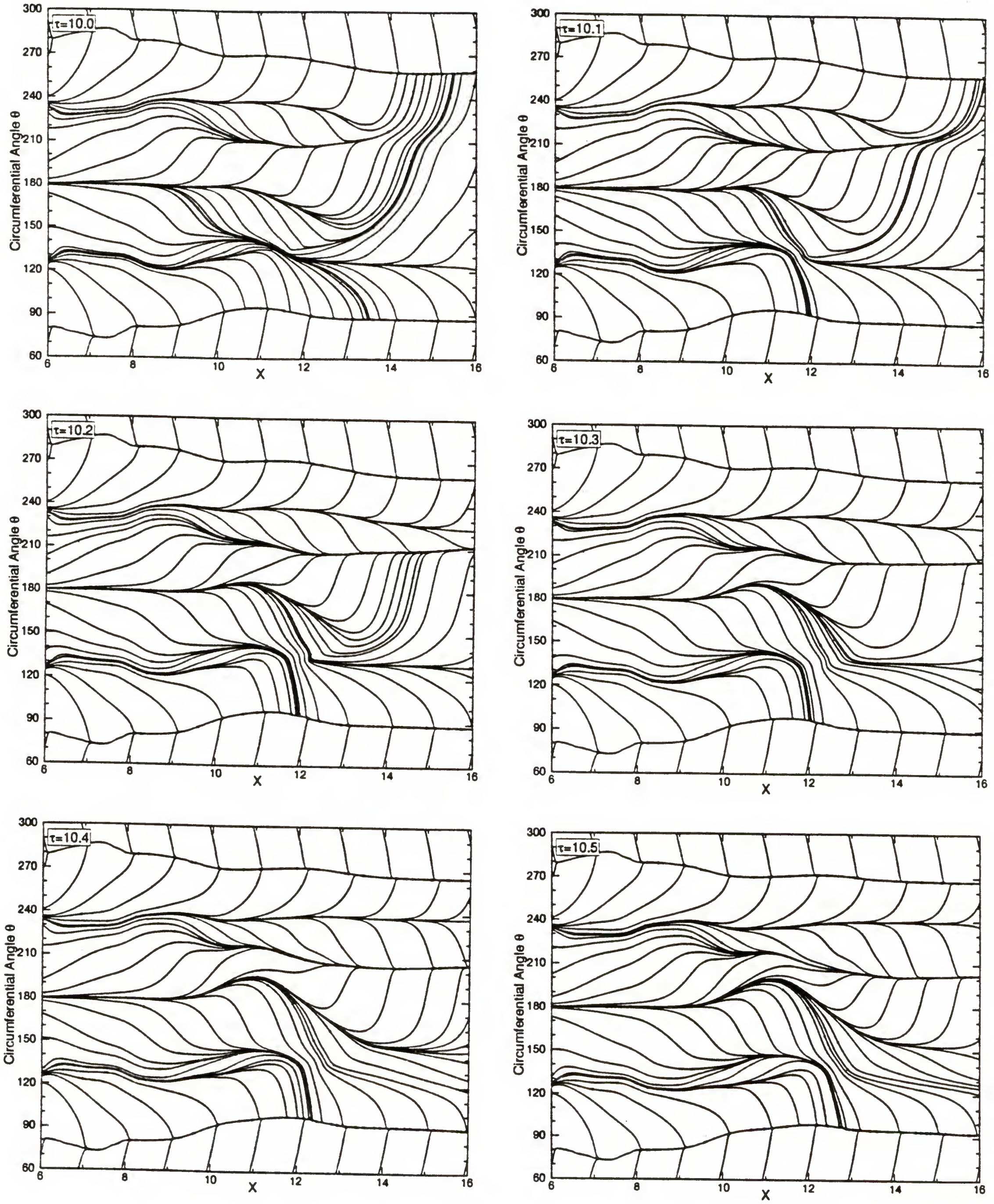

Figure 6.17 - continued.

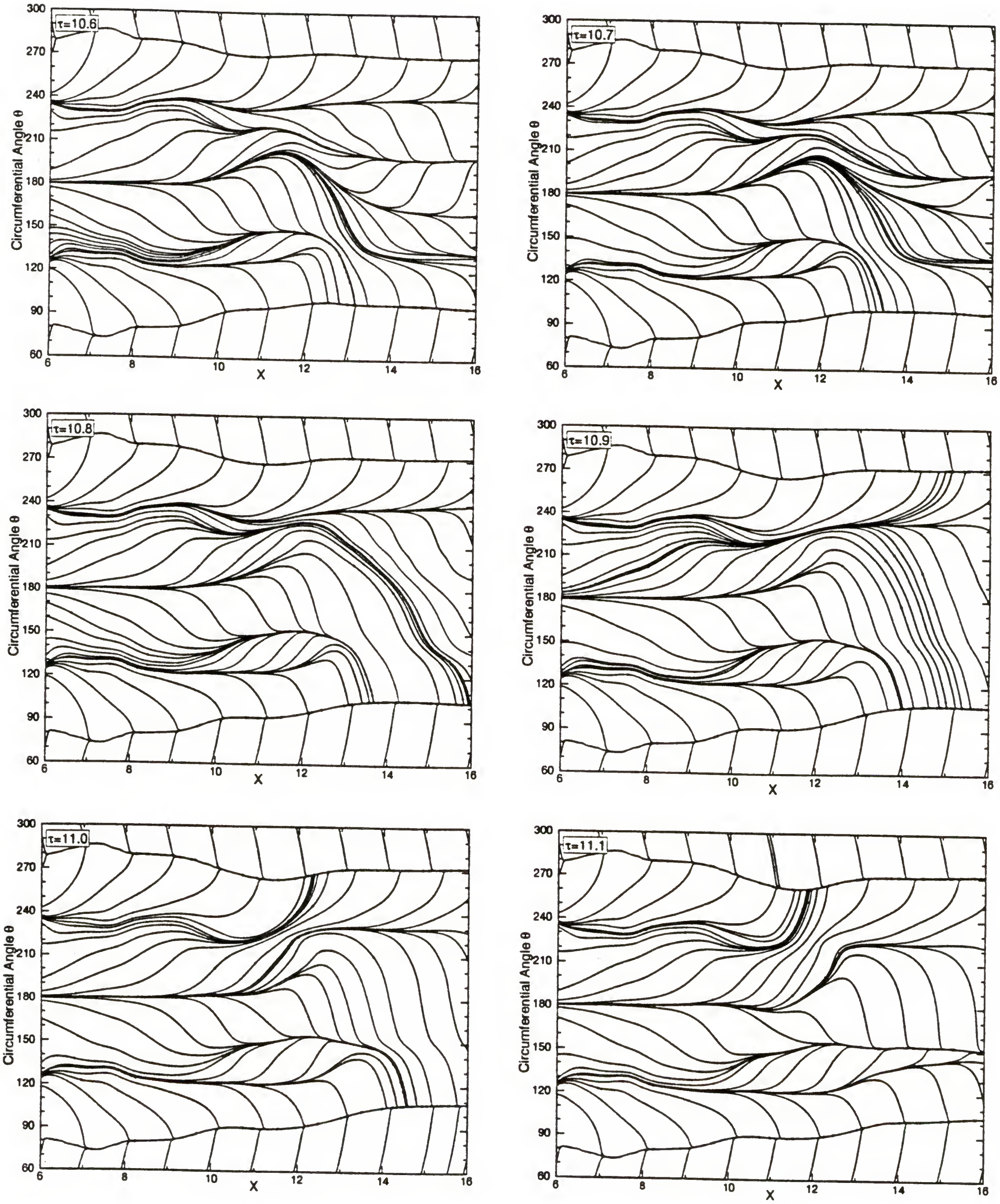

Figure 6.17 - continued.

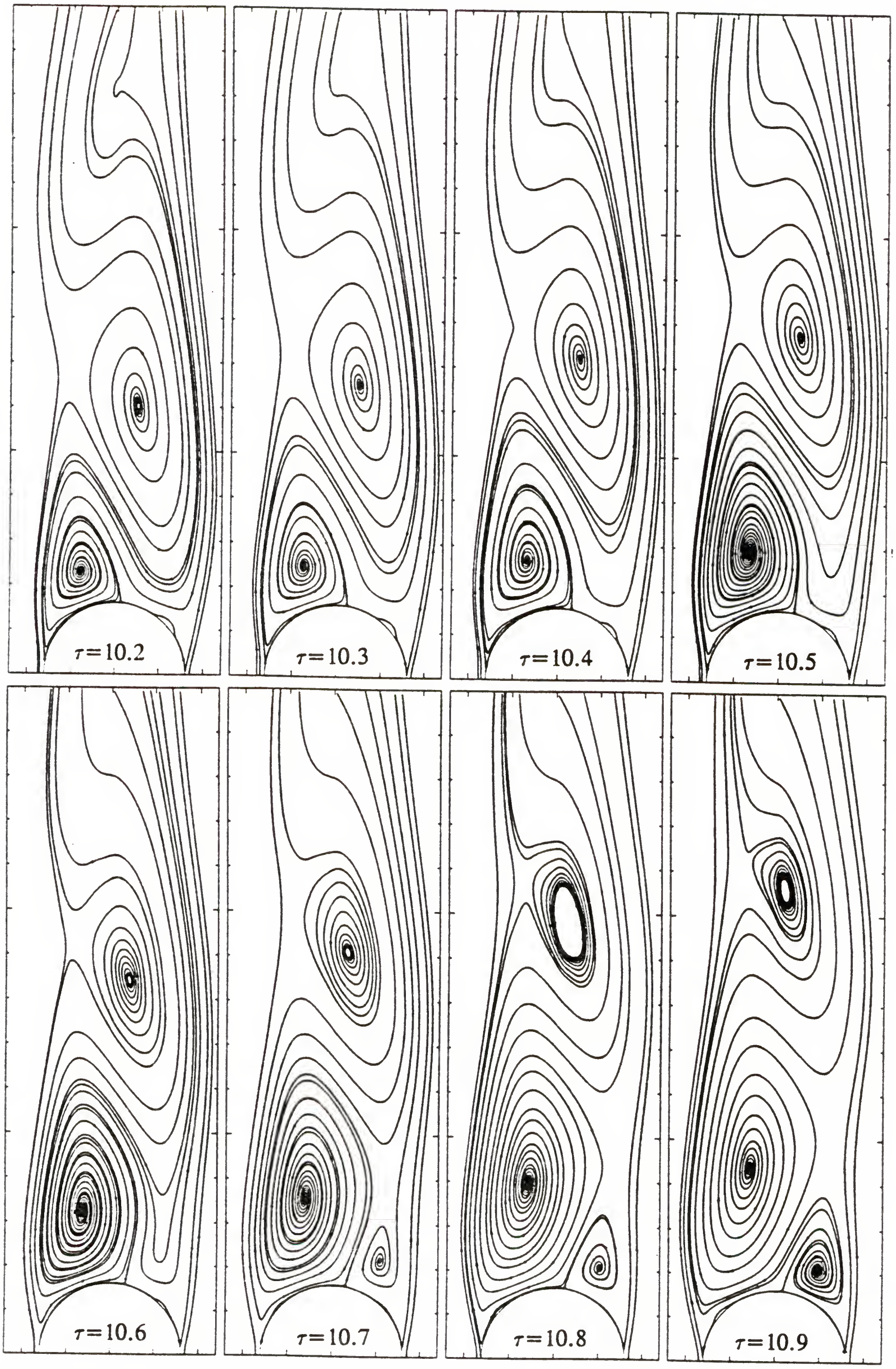

Figure 6.18 Alternating vortex shedding at J = 111 ($x=10.85$) on JMAX = 131 grid.

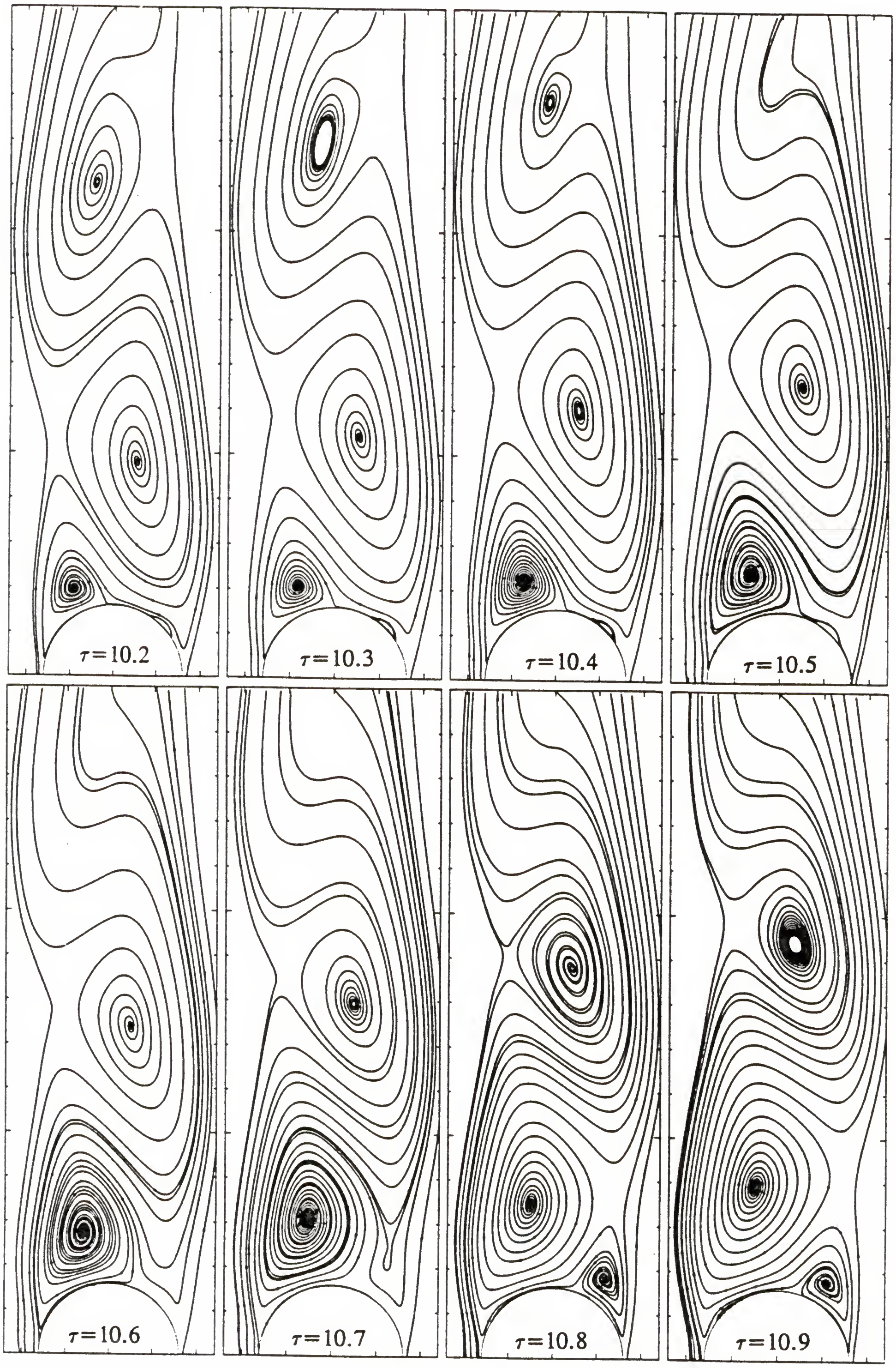

Figure 6.19 Alternating vortex shedding at J=115 (x=11.88) on JMAX=131 grid.

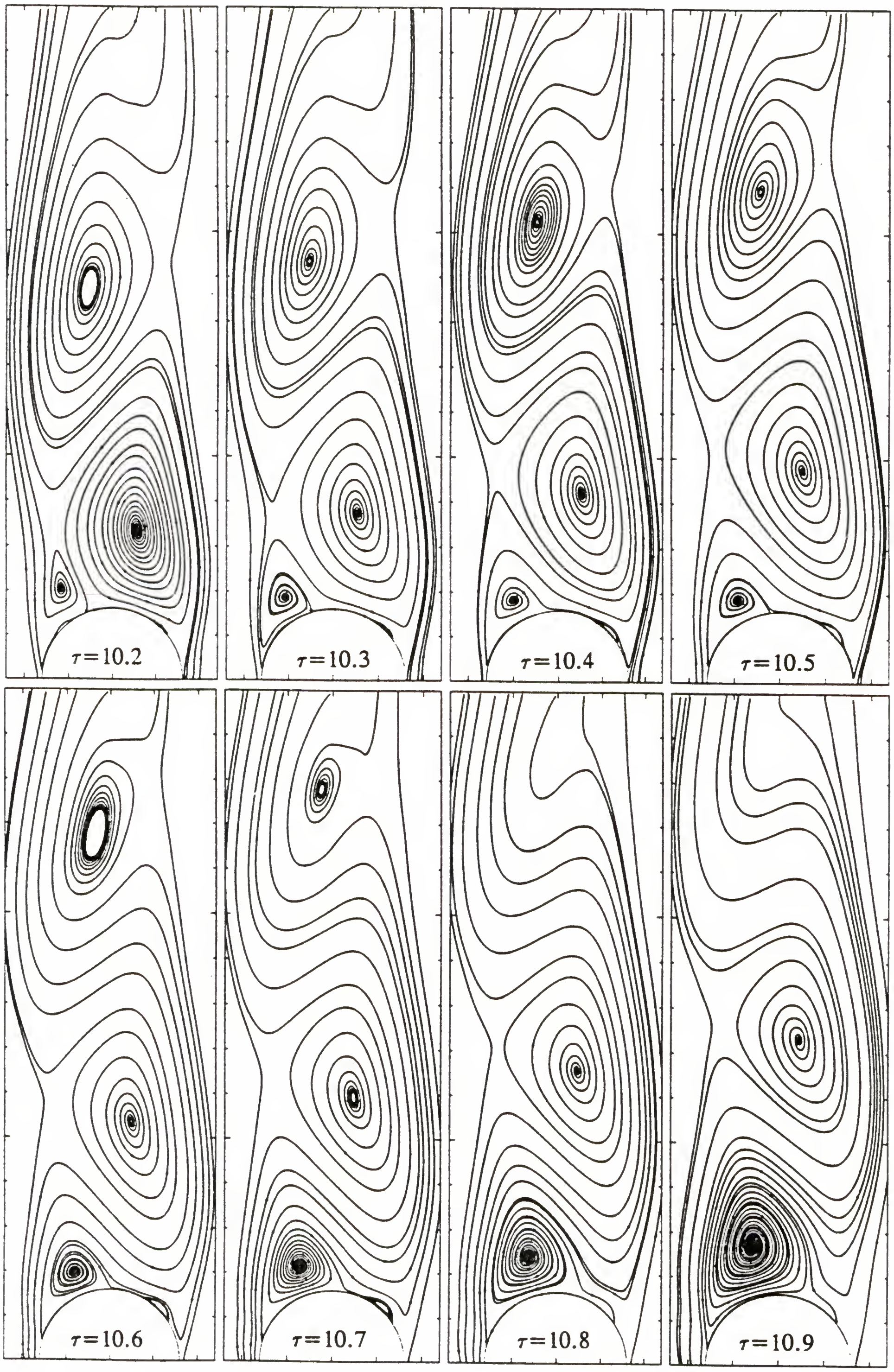

Figure 6.20 Alternating vortex shedding at J = 119 (x = 12.91) on JMAX = 131 grid.

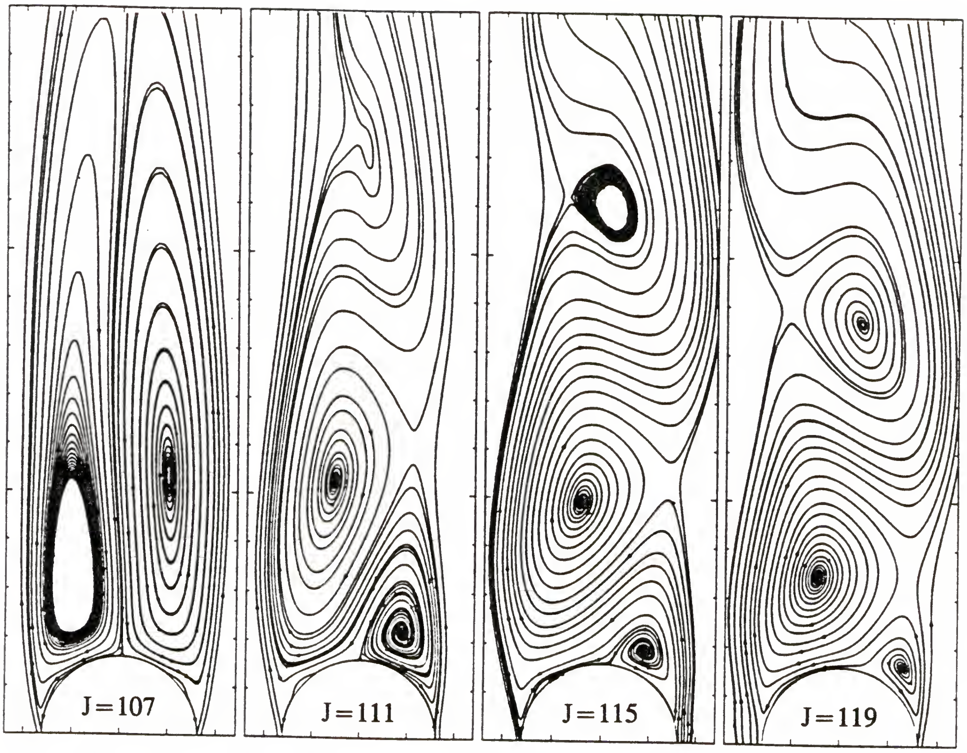

Figure 6.21 Instantaneous vortical flow pattern on sting at $\tau=11.1$.

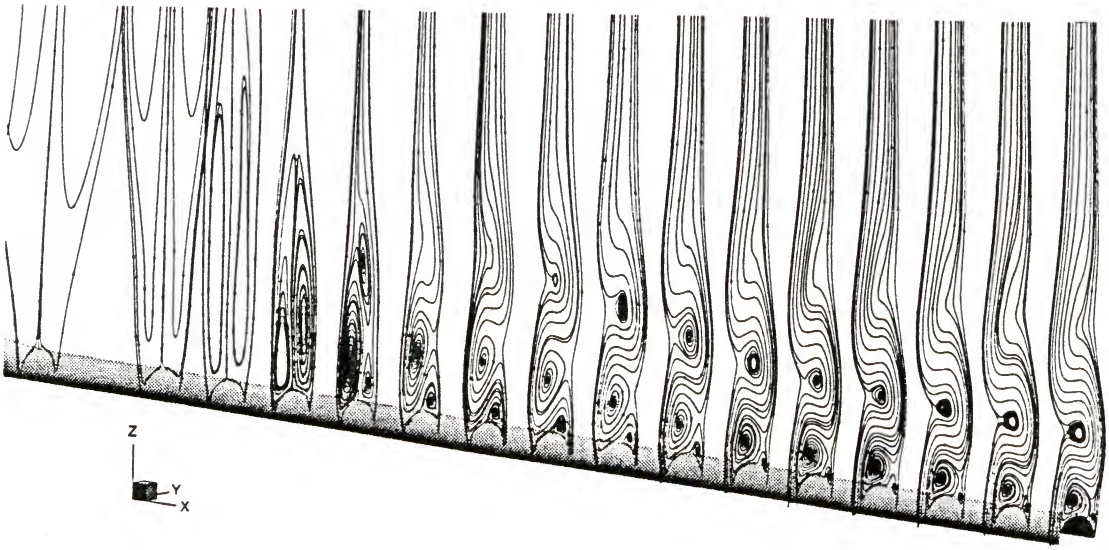

Figure 6.22 Variation of crossflow vortex shedding pattern on sting at $\tau=11.1$.

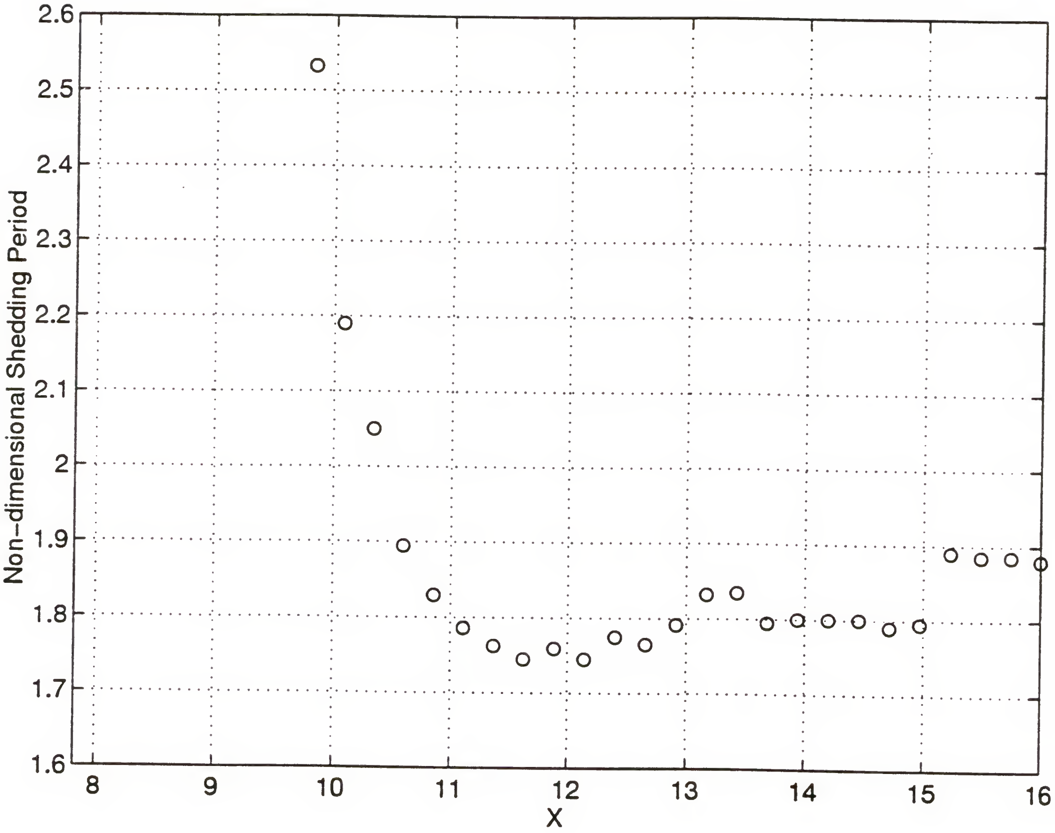

Figure 6.23 Oscillation period computed on projectile sting.

CHAPTER VII
SUMMARY AND CONCLUDING REMARKS

The thin-layer Navier-Stokes simulation of an impulsively-started Mach 0.96 turbulent flow past a SCOBT projectile with sting at 60-degree angle-of-attack has been conducted by implementing the original Baldwin-Lomax turbulence model and a modified Baldwin-Lomax model proposed by Degani and Schiff. The original Baldwin-Lomax model is an algebraic model which needs not to solve additional equations like other one- or two-equation models do, therefore costs little extra computer time which is especially advantageous in a large-scale three-dimensional flow simulation. It is known that many high speed flow problems can be accurately simulated by the thin-layer Navier-Stokes computation with the use of original Baldwin-Lomax turbulence model, provided that the flow separation is not very strong. In the high-α vortical flow simulation involving large crossflow separations, however, the original Baldwin-Lomax model was found to over-predict the eddy viscosity in the separated region, which can suppress or distort the secondary flow phenomena near the surface. The idea behind the modified Baldwin-Lomax model is to make the model capable of differentiating the leeward side vortical flow structure by properly determining a turbulent mixing length within the turbulent boundary layer, therefore effectively reduce the eddy viscosity to a reasonable magnitude in the separated region. The fundamental formulations in the original Baldwin-Lomax model are retained such that the vortical flow physics and phenomena can be realistically modelled without requiring further computer resources or tedious coding procedure. The improvement of the modified Baldwin-Lomax turbulence model has been demonstrated through a number of subsonic and supersonic flow simulations with various incidences in the past decade. The similar investigations for transonic high-α flows, however, were very limited.

Although there are no experimental measurements available to justify the numerical accuracy of the current computational work, a study to the effects of original Baldwin-Lomax turbulence model and the modified model upon the general vortical flow characteristics has revealed that the modified model is indeed capable of bringing up the complex secondary flow phenomena. The simulated flowfield by modified Baldwin-Lomax model has been shown to be quite comparable in quality to the results from other high-α projectile flow studies. Some of the important findings are summarized as follows.

(1) The amount of computed eddy viscosity is significantly reduced in the separated region by using the modified Baldwin-Lomax turbulence model. The secondary crossflow separations are simulated over the projectile surface which are mostly absent from the original Baldwin-Lomax model computation. The diminishing of strong diffusive process in the separated region has altered the general flow characteristics in the boundary layer. The flow in the primary vortex region away from the surface, on the other hand, is almost unaffected despite of the substantial reduction of eddy viscosity magnitude in the modified model computation.

(2) Although the modified Baldwin-Lomax model has predicted a more complex surface flow pattern, the resulting surface pressure distribution is found to be very comparable to the one obtained from original model computation for an established flow. The simulated secondary flows are apparently too weak to induce significant surface pressure difference. The viscous force does change with a different surface skin-friction lines distribution for modified Baldwin-Lomax model results, but consists of barely 1% of the pressure force in magnitude. Accordingly, the overall lift and drag forces are less affected. A fluctuating side force time history is observed due to the development of alternating vortex shedding on sting. The oscillation is about a zero mean, with an amplitude of 4% to 5% of the lift forces.

(The followings are based on modified Baldwin-Lomax model only.)

(3) The primary crossflow separation starts to develop from the leeward symmetric plane and moves upstream along the circumferential direction. The onset time for primary separation is found to be linearly dependent to the local projectile diameter. The crossflow secondary separation is brought into existence when enough adverse pressure gradient is developed under the primary vortex structure. The onset time for secondary separation is also linearly dependent to the diameter, with a slight delay for those cross-sections on boattail compared to the ones on ogive having the same diameters.

(4) The evolution of crossflow topology on the cylinder, boattail and sting sections involves transition of a stable spiral vortex to an unstable one through the appearance of a stable limiting cycle. Only one saddle point is located on the leeward symmetric plane

to separate the upward and downward flows. The evolution on the ogive section, on the other hand, consists of two saddle points on the leeward symmetric plane and one unstable spiral vortex. The two-saddle-point structure is found to be related to the surface curvature in conjunction with the local flow direction.

(5) The circumferential velocity component dominates the surface flow pattern on the windward side before crossflow primary separation. Accordingly, the surface skin-friction lines are almost perpendicular to the primary separation line. The induced crossflow secondary flows in the early flow development are only found on smaller cross-sections on ogive and boattail-sting, which gradually propagate onto the cylindrical section and merge together as time grows. A high speed jet stream having large axial velocity (almost twice of the free stream axial velocity) is induced above the leeward symmetric plane over ogive and cylinder, which provides an effective "channel" to bring massive longitudinal flow from the ogive to the boattail and sting.

(6) The particular boattail geometry has caused a longitudinally reverse flow right after the cylinder-boattail juncture in the crossflow separated region. Behind that the secondary flow structure collapses due to a relatively weak circumferential flow action until $x \approx 10$ on sting where the circumferential component becomes strong enough to induce the adverse pressure gradient and the secondary flow separation re-appears.

(7) The vortex shedding is simulated only on the last 2/3 of sting section, which is believed to be a result of absolute instabilities. The Strouhal number is in excellent agreement to a classical empirical value of 0.182. The shedding is found to be slightly oblique near the boattail and gradually becomes parallel near the end of sting.

The investigation in this study has revealed some important information to the high-α projectile aerodynamics. The modified Baldwin-Lomax turbulence model is justified to be capable of representing the high speed turbulent vortical flow physics and phenomena. The choice of cut-off constant needs to be properly resolved in order to have more quantitatively accurate solution. In order to gain a more comprehensive understanding to the complex three-dimensional vortical flow phenomena, it is desired to have further computational investigations to the flow cases with various angles of attack, Mach numbers and Reynolds numbers.

APPENDIX
JACOBIAN MATRICES

The Jacobian matrices ***A***, ***B*** and ***C*** have the following form

$$\begin{bmatrix} k_t & k_x & k_y & k_z & 0 \\ k_x\phi - u\theta & k_t + \theta + (2-\gamma)k_x u & k_y u - (\gamma-1)k_x v & k_z u - (\gamma-1)k_x w & (\gamma-1)k_x \\ k_y\phi - v\theta & k_x v - (\gamma-1)k_y u & k_t + \theta + (2-\gamma)k_y v & k_z v - (\gamma-1)k_y w & (\gamma-1)k_y \\ k_z\phi - w\theta & k_x w - (\gamma-1)k_z u & k_y w - (\gamma-1)k_z v & k_t + \phi + (2-\gamma)k_z w & (\gamma-1)k_z \\ (-\frac{\gamma E}{\rho} + 2\phi)u & k_x(\frac{\gamma E}{\rho} - \phi) - (\gamma-1)u\theta & k_y(\frac{\gamma E}{\rho} - \phi) - (\gamma-1)v\theta & k_z(\frac{\gamma E}{\rho} - \phi) - (\gamma-1)w\theta & k_t + \gamma\theta \end{bmatrix}$$

where

$$\theta = uk_x + vk_y + wk_z, \quad \phi = \frac{1}{2}(\gamma - 1)(u^2 + v^2 + w^2)$$

Here $k = \xi, \eta$ and ζ to represent ***A***, ***B*** and ***C***, respectively. Note that $k_t = 0$ for a fixed grid case.

The Jacobian matrix $\boldsymbol{M}$ has the following form

$$\begin{bmatrix} 0 & 0 & 0 & 0 & 0 \\ m_{21} & \alpha_1\delta_\zeta(1/\rho) & \alpha_2\delta_\zeta(1/\rho) & \alpha_3\delta_\zeta(1/\rho) & 0 \\ m_{31} & \alpha_2\delta_\zeta(1/\rho) & \alpha_4\delta_\zeta(1/\rho) & \alpha_5\delta_\zeta(1/\rho) & 0 \\ m_{41} & \alpha_3\delta_\zeta(1/\rho) & \alpha_5\delta_\zeta(1/\rho) & \alpha_6\delta_\zeta(1/\rho) & 0 \\ m_{51} & m_{52} & m_{53} & m_{54} & \alpha_0\delta_\zeta(1/\rho) \end{bmatrix}$$

where

$$m_{21} = \alpha_1\delta_\zeta(-u/\rho) + \alpha_2\delta_\zeta(-v/\rho) + \alpha_3\delta_\zeta(-w/\rho)$$

$$m_{31} = \alpha_2\delta_\zeta(-u/\rho) + \alpha_4\delta_\zeta(-v/\rho) + \alpha_5\delta_\zeta(-w/\rho)$$

$$m_{41} = \alpha_3\delta_\zeta(-u/\rho) + \alpha_5\delta_\zeta(-v/\rho) + \alpha_6\delta_\zeta(-w/\rho)$$

$$m_{51} = \alpha_1\delta_\zeta(-u^2/\rho) + \alpha_2\delta_\zeta(-2uv/\rho) + \alpha_3\delta_\zeta(-2uw/\rho) + \alpha_4\delta_\zeta(-v^2/\rho) + \alpha_5\delta_\zeta(-2vw/\rho)$$

$$+ \alpha_6\delta_\zeta(-w^2/\rho) + \alpha_0\delta_\zeta(-E/\rho^2) + \alpha_0\delta_\zeta[(u^2 + v^2 + w^2)/\rho]$$

$$m_{52} = -m_{21} - \alpha_0\delta_\zeta(u/\rho), \quad m_{53} = -m_{31} - \alpha_0\delta_\zeta(v/\rho), \quad m_{54} = -m_{41} - \alpha_0\delta_\zeta(w/\rho)$$

$$\alpha_0 = \gamma\kappa Pr^{-1}(\zeta_x^2 + \zeta_y^2 + \zeta_z^2)$$

$$\alpha_1 = \mu(\frac{4}{3}\zeta_x^2 + \zeta_y^2 + \zeta_z^2), \quad \alpha_2 = \frac{\mu}{3}\zeta_x\zeta_y, \quad \alpha_3 = \frac{\mu}{3}\zeta_x\zeta_z$$

$$\alpha_4 = \mu(\zeta_x^2 + \frac{4}{3}\zeta_y^2 + \zeta_z^2), \quad \alpha_5 = \frac{\mu}{3}\zeta_y\zeta_z, \quad \alpha_6 = \mu(\zeta_x^2 + \zeta_y^2 + \frac{4}{3}\zeta_z^2)$$

REFERENCES

1. Hot Flying, video tape produced by McGraw-Hill Aviation Week Group, McGraw-Hill Inc., New York, NY, 1990.

2. Rizk, Y. M., Schiff L. B. and Gee, K., "Numerical Simulation of the Viscous Flow Around a Simplified F/A-18 at High Angles Of Attack," AIAA-90-2999-CP, AIAA 8th Applied Aerodynamics Conference Proceeding, Part 1, Portland, Oregon, August 1990, pp. 36-58.

3. Fisher, D. F., Banks, D. W. and Richwine, D. M., "F-18 High Alpha Research Vehicle Surface Pressures: Initial In-Flight Results and Correlation with Flow Visualization and Wind-Tunnel Data," AIAA-90-3018-CP, AIAA 8th Applied Aerodynamics Conference Proceeding, Part 1, Portland, Oregon, August 1990, pp. 421-451.

4. Ghaffari, F., Luckring, J. M., Thomas, J. L., Bates, B. L. and Biedron, R. T., "Multiblock Navier-Stokes Solutions about the F/A-18 Wing-LEX-Fuselage Configuration," Journal of Aircraft, Vol. 30, No. 3, May-June 1993, pp. 293-303.

5. Gee, K., Rizk, Y. M. and Schiff, L. B., "Forebody Tangential Slot Blowing on an Aircraft Geometry," Journal of Aircraft, Vol. 31, No. 4, July-August 1994, pp. 922-928.

6. Davis, W. H., "The Role of CFD Applied to High Performance Aircraft," AIAA-90-3071-CP, AIAA 8th Applied Aerodynamics Conference Proceeding, Part 2, Portland, Oregon, August 1990, pp. 818-828.

7. Rosen, B. S. and Davis, W. H., "Numerical Study of Asymmetric Air Injection To Control High Angle-Of-Attack Forebody Vortices on the X-29 Aircraft," AIAA-90-3004-CP, AIAA 8th Applied Aerodynamics Conference Proceeding, Part 1, Portland, Oregon, August 1990, pp. 89-99.

8. Francis, M. S., "X-31: An International Success Story," Aerospace America, Vol. 33, No. 2, February 1995, pp. 22-27.

9. Erickson, G. E., "High Angle-of-Attack Aerodynamics," Annual Review in Fluid Mechanics, Vol. 27, 1995, pp. 45-88.

10. Marvin, J. G. and Holst, T. L., "CFD Validation for Aerodynamic Flows--Challenge for the '90's," AIAA-90-2995-CP, AIAA 8th Applied Aerodynamics Conference Proceeding, Part 1, Portland, Oregon, August 1990, pp. 1-13.

11. Visbal, M. R. and Gordnier, R. E., "Crossflow Topology of Vortical Flows," AIAA Journal, Technical Notes, Vol. 32, No. 5, May 1994, pp. 1085-1087.

12. Perry, A. E. and Chong M. S., "A Description of Eddying Motions and Flow Patterns Using Critical-Point Concepts," Annual Review in Fluid Mechanics, Vol. 19, 1987, pp. 125-155.

13. Chapman, G. T. and Yates, L. A., "Topology of flow separation on three-dimensional bodies," Applied Mechanics Review, Vol. 44, No. 7, July 1991, pp. 329-334.

14. Hunt, J. C. R., Peterka, J. A. and Woo, H., "Kinematical Studies of the Flows Around Free or Surface-Mounted Obstacles; Applying Topology to Flow Visualization," Journal of Fluid Mechanics, Vol. 86, pp. 179-200, 1978.

15. Degani, D. and Schiff, L. B., "Computation of Turbulent Supersonic Flows around Pointed Bodies Having Crossflow Separation," Journal of Computational Physics, Vol. 66, 1986, pp. 173-196.

16. Baldwin, B. S. and Lomax, H., "Thin Layer Approximation and Algebraic Model for Separated Turbulent Flows," AIAA-78-257, AIAA 16th Aerospace Sciences Meeting, Huntsville, AL, January 16-18, 1978.

17. Schiff, L. B., Degani, D. and Cummings, R. M., "Computation of Three-Dimensional Turbulent Vortical Flows on Bodies at High Incidence," Journal of Aircraft, Vol. 28, No. 11, November 1991, pp. 689-699.

18. Degani, D. and Zilliac, G. G., "Experimental Study of Nonsteady Asymmetric Flow Around an Ogive-Cylinder at Incidence," AIAA Journal, Vol. 28, No. 4, April 1990, pp. 642-649.

19. Ramberg, S. E., "The Effect of Yaw and Finite-Length Upon the Vortex Wakes of Stationary and Vibrating Circular Cylinders," Journal of Fluid Mechanics, Vol. 128, 1983, pp. 81-107.

20. Degani, D. and Schiff, L. B., "Numerical Simulation of the Effect of Spatial Disturbance on Vortex Asymmetry," AIAA Journal, Vol. 29,No. 3, March 1991, pp. 344-352.

21. Lamont, P. J, "Pressure Around an Inclined Ogive Cylinder with Laminar, Transitional, or Turbulent Separation," AIAA Journal, Vol. 20, No. 11, November 1982, pp. 1492-1499.

22. Degani, D., "Instabilities of Flows over Bodies at Large Incidence," AIAA Journal, Vol. 30, No. 1, January 1992, pp. 94-100.

23. Zilliac, G. G., Degani, D.and Tobak M., "Asymmetric Vortices on a Slender Body of Revolution," AIAA Journal, Vol. 29, No. 5, May 1991, pp. 667-675.

24. Degani, D., Tobak, M. and Zilliac, G. G., "Surface Flow Patterns on an Ogive-Cylinder at Incidence," AIAA Journal, Technical Notes, Vol. 30, No. 1, January 1992, pp. 272-274.

25. Siclari, M. J. and Marconi, F., "Computation of Navier-Stokes Solutions Exhibiting Asymmetric Vortices," AIAA Journal, Vol. 29, No. 1, January 1991, pp. 32-42.

26. Siclari, M. J., "Asymmetric Separated Flows at Supersonic Speeds," AIAA Journal, Vol. 32, No. 1, January 1992, pp. 124-133.

27. Malcolm, G. N., "Forebody Vortex Control," Progress in Aerospace Sciences, Vol. 28, 1991, pp. 171-234.

28. Gee, K., Rizk, Y. M. and Schiff, L. B., "Forebody Tangential Slot Blowing on an Aircraft Geometry," Journal of Aircraft, Vol. 31, No. 4, July-August 1994, pp. 922-928.

29. Anderson, D. A., Tannehill, J. C. and Pletcher, R. H., Computational Fluid Dynamics and Heat Transfer, McGraw-Hill Book Company, New York, 1984.

30. Malvern, L. E., Introduction to the Mechanics of a Continumm, Prentice-Hall Inc., Englewood Cliffs, New Jersey, 1969.

31. Schlichting, H., Boundary Layer Theory, 7th edition, McGraw-Hill Book Company, New York, 1979.

32. Steger, J. L., "Implicit Finite-Difference Simulation of Flow about Arbitrary Two-Dimensional Geometries," AIAA Journal, Vol. 16, No. 7, July 1978, pp. 679-686.

33. Hinze, J. O., Turbulence, 2nd edition, McGraw-Hill Book Company, New York, 1975, pp. 223-226.

34. Kayser, L. D. and Whiton, F., "Surface Pressure Measurements on a Boattailed Projectile Shape at Transonic Speeds," ARBRL-MR-03161, Army Ballistic Research Laboratory, Aberdeen Proving Ground, Maryland, March 1982.

35. White, F. M., Viscous Fluid Flow, McGraw-Hill Book Company, New York, 1979, pp. 46.

36. Chen, G. W., "On High Speed Turbulent Flow over a Projectile Configuration," Proceeding, Vol. 2, AIAA 42nd South-Eastern Student Conference, Altamonte Springs, Florida, April 1990, pp. 446-477.

37. Shiau, N. H., "Numerical Simulation of the Aerodynamics of Turbulent Transonic Flow Past a Projectile," Ph.D. Dissertation, University of Florida, Gainesville, 1987.

38. Beam, R. M. and Warming, R. F., "An Implicit Finite-Difference Algorithm for Hyperbolic Systems in Conservation-Law Form," Journal of Computational Physics, Vol. 22, September 1978, pp. 87-110.

39. Pulliam, T. H. and Steger, J. L., "Recent Improvements in Efficiency, Accuracy, and Convergence for Implicit Approximation Algorithms," AIAA-85-0360, AIAA 23rd Aerospace Sciences Meeting, Reno, Nevada, January 1985.

40. Shiau, N. H. and Hsu, C. C., "A Diagonalized TVD Scheme for Turbulent Transonic Projectile Aerodynamics Computation," AIAA-88-0217, AIAA 26th Aerospace Sciences Meeting, Reno, Nevada, January 1989.

41. Shiau, N. H., Hsu, C. C. and Chyu, W., "Numerical Simulation of 3-D Transonic Turbulent Projectile Aerodynamics by TVD Scheme," AIAA-89-0335, AIAA 27th Aerospace Sciences Meeting, Reno, Nevada, January 1989.

42. Pulliam, T. H., and Steger, J. L., "Implicit Finite-Difference Simulation of Three-Dimensional Compressible Flow," AIAA Journal, Vol 18, No. 2, Feburary 1980, pp. 159-167.

43. Yee, H. C., "Construction of Explicit and Implicit Symmetric TVD Schemes and Their Applications," Journal of Computational Physics, Vol. 68, 1987, pp. 151-179.

44. Yee, H. C., "Linearized Form of Implicit TVD Schemes for the Multi-dimensional Euler and Navier-Stokes Equations," International Journal on Computers and Mathematics with Application, Vol. 12A, December 1985, pp. 413-432.

45. Yang, S. C., "Numerical Simulation of Transonic Turbulent Flows over a Complex Configuration," Ph.D. Dissertation, University of Florida, Gainesville, 1990.

46. Tecplot™ User's Manual, version 6, Amtec Engineering Inc., Bellevue, WA, 1993.

47. Chaderjian, N. M., "Comparison of Two Navier-Stokes Codes for Simulating High-Incidence Vortical Flow," Journal of Aircraft, Vol. 30, No. 3, May-June 1993, pp. 357-364.

48. Ward, K. C. and Katz, J., "Topology of the Flow Structures Behind an Inclined Projectile: Part A," Journal of Aircraft, Vol. 26, No. 11, November 1991, pp. 1016-1022.

BIOGRAPHICAL SKETCH

Guang-Wu Chen was born in 1965 in Taichung, Taiwan, the Republic of China. He received his bachelor's degree in aeronautical and astronautical engineering in 1987 from the National Cheng-Kung University in Tainan, Taiwan. After two-year military service in the ROC Air Force, he came to the United States to work on his doctoral degree in the Department of Aerospace Engineering, Mechanics and Engineering Science at the University of Florida.

I certify that I have read this study and that in my opinion it conforms to acceptable standards of scholarly presentation and is fully adequate, in scope and quality, as a dissertation for the degree of Doctor of Philosophy.

Chen Chi Hsu

Chen-Chi Hsu, Chairperson
Professor of Aerospace Engineering,
Mechanics and Engineering Science

I certify that I have read this study and that in my opinion it conforms to acceptable standards of scholarly presentation and is fully adequate, in scope and quality, as a dissertation for the degree of Doctor of Philosophy.

Wei Shyy

Wei Shyy
Professor of Aerospace Engineering,
Mechanics and Engineering Science

I certify that I have read this study and that in my opinion it conforms to acceptable standards of scholarly presentation and is fully adequate, in scope and quality, as a dissertation for the degree of Doctor of Philosophy.

U. H. Kurzweg

Ulrich H. Kurzweg
Professor of Aerospace Engineering,
Mechanics and Engineering Science

I certify that I have read this study and that in my opinion it conforms to acceptable standards of scholarly presentation and is fully adequate, in scope and quality, as a dissertation for the degree of Doctor of Philosophy.

David W. Mikolaitis
Associate Professor of Aerospace
Engineering, Mechanics and
Engineering Science

I certify that I have read this study and that in my opinion it conforms to acceptable standards of scholarly presentation and is fully adequate, in scope and quality, as a dissertation for the degree of Doctor of Philosophy.

James F. Klausner

James F. Klausner
Associate Professor of
Mechanical Engineering

This dissertation was submitted to the Graduate Faculty of the College of Engineering and to the Graduate School and was accepted as partial fulfillment of the requirements for the degree of Doctor of Philosophy.

August 1995

Winfred M Phillips

Winfred M. Phillips
Dean, College of Engineering

Karen A. Holbrook
Dean, Graduate School